

Computational Investigation of Short Pulse Laser Interaction with Metals



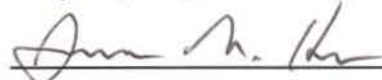
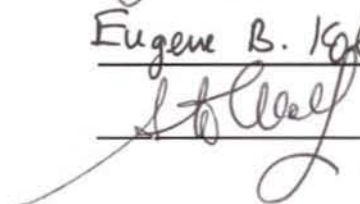
Zhibin Lin
Longhai, Fujian, P.R. China

B.S., Peking University, Beijing, 2002

A Dissertation presented to the Graduate Faculty
of the University of Virginia in Candidacy for the Degree of
Doctor of Philosophy

Department of Physics

University of Virginia
August, 2008




Eugene B. Glensk


© Copyright by
Zhibin Lin
All Rights Reserved
August 2008

Abstract

Recent developments of short (femtosecond or picosecond) pulse laser techniques for probing and modifying materials provide an intriguing opportunity to study the material behavior and properties under extreme conditions that can hardly be achieved by any other means. The highly non-equilibrium nature of the transient processes occurring in the laser-irradiated targets, however, hinders the interpretation of the experimental results.

In this work, the microscopic mechanisms of the ultrafast structural and phase transformations induced in the irradiated metal targets are investigated in a computational model combining classical molecular dynamic method with a continuum description of the electronic excitation and electron-phonon equilibration. The atomic-level structural rearrangements predicted in the simulations are analyzed through the calculation of the diffraction profiles and density correlation functions, and related to the diffraction spectra observed in time-resolved electron diffraction experiments. Computational investigation of the laser-induced generation of crystal defects in bcc and fcc metal targets suggests that a large number of vacancies can be created in the surface regions of the irradiated targets. Moreover, the emission of partial dislocations from the melting front is observed for Ni, where the interaction among the dislocations propagating along different glide planes leads to the formation of complex dislocation configurations. For Cr, the stacking faults, generated during the initial stage of the relaxation of the laser-induced stresses, disappear shortly after the laser-induced tensile stress wave leaves the surface region of the target.

The connections between the electronic structure and the electron temperature dependences of the thermophysical properties, namely the electron-phonon coupling and the electron heat capacity, under strong laser-induced electron-phonon non-equilibrium are established through *ab initio* electronic structure calculations for several representative metals. As a direct consequence of the thermal excitation of lower d band electrons, the thermophysical properties of noble and transition metals investigated in this study exhibit significant deviations from the commonly accepted descriptions for the range of electron temperatures typically realized in femtosecond laser material processing applications. The comparison of computational predictions with experimental observations demonstrates that the transient modifications of the thermophysical properties have important practical implications for quantitative computational description of laser-materials interactions.

Acknowledgements

This work will not be possible without the help of a lot of people around me. First of all, I would like to express my deepest gratitude to my advisor, Prof. Leonid V. Zhigilei for his guidance throughout my study. During the four years in the computational materials group, Leo has been helping me in many aspects to move my research forward. He always makes himself available for discussing problems that I encounter in my study, and provides me with opportunities to present my study at professional conferences and to establish international collaborations. His patience and kindness, as well as suggestions and supports to my graduate study and future career, have made him not only a great advisor but also a wonderful friend in my life.

I also would like to thank Prof. Eugene Kolomeisky, Prof. Despina Louca, Prof. James Howe and Prof. Stuart Wolf for serving on my defense committee and providing valuable suggestions to my dissertation. I am grateful to Prof. Vittorio Celli and Prof. Robert A. Johnson for the collaborations and insightful discussions of the research.

I would like to thank current and former members of Computational Materials Group: Alexey Volkov, Kiril Simov, Derek, Thomas, Avinash Dongare, Bill Duff, Elodie Leveugle, Dmitriy Ivanov, Orenthal Tucker, Carlos Sevilla, Stephen Guy and Benjamin Jessup for their generous helps in my study. I would like to thank all my friends at UVA who have made my life during these six years at UVA very enjoyable.

Finally, I would like to thank my parents and parents-in-law in China for their continuous support to my study. I would like to thank my wife, Zhen, for her patience and understanding. I feel so blessed to have you in my life.

TABLE OF CONTENT

1. Introduction.....	1
1.1 Background	1
1.2 Motivation of the dissertation	5
1.3 Outline of the dissertation.....	8
References for Chapter 1	11
2. Investigation of Short Pulse Laser Induced Structural Transformations in Metals.....	13
2.1 Time-resolved diffraction profiles and atomic dynamics in short pulse laser induced structural transformations.....	13
2.1.1 Introduction.....	13
2.1.2 Computational setup for simulations of laser interactions with Au thin films	15
2.1.3 Numerical methods for calculation of structure function from atomic configurations	19
2.1.4 Results and discussion	26
2.1.4.1 Kinetics and mechanisms of laser melting	26
2.1.4.2 Structure function calculations	40
2.1.4.3 Splitting of the peaks - the uniaxial lattice expansion.....	43
2.1.4.4 Thermal effects.....	48
2.1.4.5 Real space correlations	52
2.1.5 Conclusion and connections to experiments.....	62

References for Chapter 2.1	67
2.2 Time-resolved diffraction profiles and structural dynamics of Ni film under short laser pulse irradiation.....	72
2.2.1 Introduction.....	72
2.2.2 Computational model: MD simulation setup and calculation of diffraction profiles	72
2.2.3 Results and discussion	75
2.2.4 Conclusions.....	80
References for Chapter 2.2	82
2.3 Molecular Dynamic Simulation of Laser-induced Melting of Nanocrystalline Au	83
2.3.1 Introduction.....	83
2.3.2 Computational setup for simulations of laser interaction with Au nanocrystalline films	84
2.3.3 Results and discussion	88
2.3.4 Summary	108
References for Chapter 2.3	109
3. Electron-phonon Coupling and Electron Heat Capacity of Metals under Conditions of Strong Electron-phonon Nonequilibrium.....	111
3.1 Introduction.....	111
3.2 Theory and computational methods.....	114
3.2.1 Electronic structure calculations	116
3.2.2 Electron heat capacity $C_e(T_e)$	116

3.2.3	Electron thermal conductivity	117
3.2.4	Electron-phonon coupling factor $G(T_e)$	118
3.3	Results	123
3.3.1	Aluminum and the free electron gas model	124
3.3.2	Silver, copper and gold	128
3.3.3	Nickel and platinum	137
3.3.4	Tungsten and titanium	141
3.4	Summary	147
3.5	Appendix	149
	References for Chapter 3	153
4.	Practical Implication of Thermal Excitation of Electrons in Short Pulse Laser	
	Interaction with Metals	158
4.1	Thermal excitation of d band electrons in Au: implications for laser-induced phase transformations	158
4.1.1	Introduction	158
4.1.2	The effect of DOS and thermal excitation of electrons on thermophysical properties	160
4.1.2.1	Electron DOS, chemical potential, and electron heat capacity ...	161
4.1.2.2	Temperature dependence of the electron-phonon coupling factor	167
4.1.3	TTM-MD Simulations of laser melting of a thin Au film	173
4.1.3.1	Computational model	173
4.1.3.2	Transient evolution of electron and lattice temperatures	175
4.1.3.3	Ultrafast melting process	182

4.1.4	Summary	187
References for Chapter 4.1		189
4.2	Temperature dependences of the electron-phonon coupling, electron heat capacity and thermal conductivity in Ni under femtosecond laser irradiation	193
4.2.1	Introduction.....	193
4.2.2	The effect of thermal excitation of electrons on thermophysical properties of Ni	195
4.2.3	TTM results and discussion	203
4.2.3.1	Transient evolution of the electron and lattice temperatures	205
4.2.3.2	Fluence threshold for surface melting	206
4.2.4	Summary	208
References for Chapter 4.2		211
5.	Generation of Crystal Defects in a BCC Metal Target Irradiated by Short Laser Pulses	212
5.1	Introduction.....	212
5.2	TTM-MD model for laser interactions with a Cr target	213
5.3	EAM interatomic potential for Cr.....	216
5.4	TTM-MD simulations: Results and discussion.....	224
5.4.1	Laser-induced stresses, surface melting.....	224
5.4.2	Transient generation of stacking faults.....	230
5.4.3	Generation of vacancies and self-interstitials	241
5.4.4	Long-term evolution of the vacancy configuration	246
5.4.5	Simulation at laser fluence below the threshold for surface melting..	251

5.5	Summary	253
References for Chapter 5		257
6.	Generation of Crystal Defects in Short Pulse Laser Interaction with FCC Ni	263
6.1	Introduction.....	263
6.2	TTM-MD model for laser interaction with Ni.....	265
6.3	Simulation results and discussions.....	270
6.3.1	Generation of crystal defects during resolidification.....	272
6.3.2	Emission of partial dislocation at higher laser fluences.....	283
6.4	Summary	293
References for Chapter 6		300
7.	Summary.....	305

1. Introduction

1.1 Background

Short pulse laser interaction with metals is a subject of fundamental scientific interest as well as significant practical importance. Recent advances in the development of femtosecond laser technology open up an exciting opportunity to study the materials under extreme conditions that can hardly be achieved by any other means. For instance, short pulse laser irradiation can create a cascade of coupled transient events consisting of strong electron/lattice superheating, fast structural and phase transformations, generation of defects, surface modification, and/or material removal from the target. At the same time, short pulse lasers are finding an increasing use in a diverse range of applications ranging from advanced materials processing, cutting, drilling, surface micro- and nano-structuring, to laser surgery and artwork restoration. Further optimization of experimental parameters in current applications, the emergence of new techniques, and interpretation of the results of probing the transient atomic dynamics and electronic phenomena in materials requires a better fundamental understanding of the ultrafast processes induced by the short pulse laser excitation.

In metals, the laser energy is absorbed by the conduction band electrons, leading to the promotion of electrons located below the Fermi level to levels above the Fermi energy. As a result, the electron distribution in irradiated metals could deviate away from the Fermi-Dirac distribution right after the laser excitation. This is shown schematically in Figure 1-1.

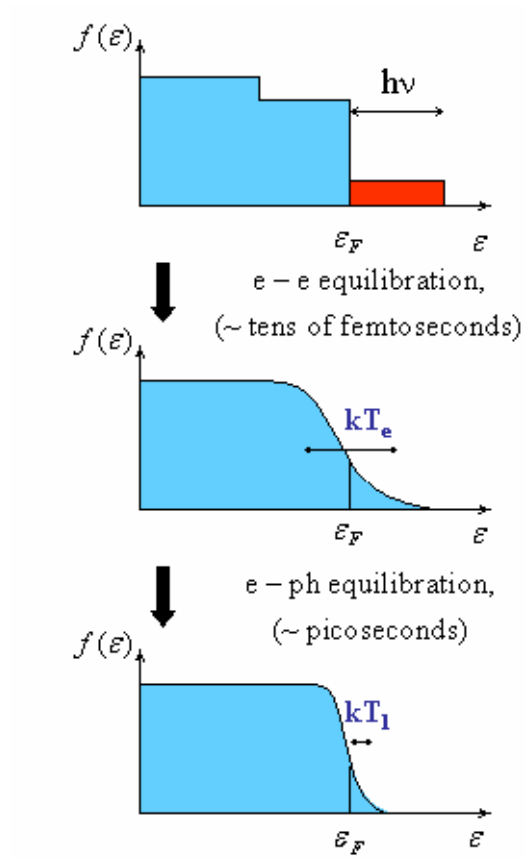


Figure 1-1. A schematic drawing of the modification of the Fermi-Dirac distribution of electrons in metals following the laser irradiation.

The nonequilibrium electrons created by the laser excitation thermalize within a few hundred femtoseconds through electron-electron collisions, leading to the establishment of the Fermi-Dirac distribution [1,2,3,4]. On the other hand, due to the fact that the electrons have a much smaller heat capacity as compared to the lattice, excitation by a short laser pulse can create a highly nonequilibrium state between the electrons and the lattice. In this nonequilibrium state, the electron temperature, determined by the Fermi-Dirac distribution after the electron thermalization, can reach up to tens of thousands of Kelvins, comparable to the Fermi energy, while the lattice still remains cold.

The electron-lattice equilibration process proceeds through the electron-phonon collisions and takes place on a much longer timescale, as compared to the electron thermalization. The timescale of the equilibration between the hot electrons and the lattice is on the order of picoseconds and is determined by the strength of the electron-phonon coupling which could vary by more than an order of magnitude for different metals [5,6,7,8,9]. After the equilibration between the electrons and the lattice is achieved, the energy redistribution from the irradiated surface region into the bulk of the target can be described in terms of the common heat diffusion.

Based on the concepts described above, a continuum approach, called two-temperature model (TTM), was proposed by Anisimov et al. in 1974 [10]. The TTM considers the distinction in the timescales of electron-electron and electron-phonon thermalization processes and assumes that the electron thermalization takes place instantaneously upon the laser pulse irradiation. This assumption is later justified by theoretical calculations presented in [11] in which a set of Boltzmann equations, accounting for nonequilibrium electron distribution, was solved for both electrons and phonons. It was found that for short, sub-picosecond and picosecond, laser pulses, the difference between the solutions of the Boltzmann equations and TTM calculations is negligible for sufficiently strong laser excitations, e.g. near the threshold for laser melting or damage.

The TTM describes the temporal and spatial evolution of the lattice and electron temperatures, T_l and T_e , in the irradiated target by two coupled non-linear differential equations:

$$C_e(T_e) \frac{\partial T_e}{\partial t} = \nabla [K_e(T_e, T_l) \nabla T_e] - G(T_e)(T_e - T_l) + S(\vec{r}, t) \quad (1.1)$$

$$C_l(T_l) \frac{\partial T_l}{\partial t} = \nabla [K_l(T_l) \nabla T_l] + G(T_e)(T_e - T_l) \quad (1.2)$$

where C and K are the heat capacities and thermal conductivities of the electrons and the lattice as denoted by subscripts e and l , $G(T_e)$ is the electron-phonon coupling factor related to the rate of the energy exchange between the electrons and the lattice, and $S(\vec{r}, t)$ is a source term describing the local energy deposition by the laser pulse.

The TTM accounts for the laser excitation of the conduction band electrons and subsequent energy relaxation processes, i.e. the energy transfer from the hot electrons to the lattice vibrations due to the electron-phonon interaction and the electron heat conduction from the irradiated surface to the bulk of the target. In Eq. (1.2), the term describing the lattice heat conduction is often omitted as it is typically negligible as compared to the electron heat conduction in metals.

While the TTM has been widely employed in many theoretical/computational studies of laser interactions with metals, the natural limitation of this continuum model is its inability to adequately describe the kinetics and mechanisms of structural and phase transformations occurring in the target material irradiated by a short laser pulse.

In order to overcome this limitations, a combined atomistic-continuum model that incorporates the classical molecular dynamics (MD) method into the general framework of the TTM model, named TTM-MD, has been developed [12], and applied for investigation of the microscopic mechanisms of laser melting and photomechanical damage in metal films and bulk targets [13,14,15]. In this combined TTM-MD model,

MD substitutes the TTM equation for the lattice temperature in the region of irradiated target affected by laser-induced structural transformations, Eq. (1.4). The diffusion equation for the electron temperature is solved simultaneously with MD integration of the equations of motion of atoms and an additional coupling term is added to the conventional MD equations of motion in order to account for the energy exchange between the electrons and the lattice [12].

$$C_e(T_e) \frac{\partial T_e}{\partial t} = \frac{\partial}{\partial z} \left(K_e(T_e) \frac{\partial}{\partial z} \right) - G(T_e - T_l) + S(z, t) \quad (1.3)$$

$$m_i \frac{d^2 \vec{r}}{dt^2} = \vec{F}_i + \xi m_i \vec{v}_i^T \quad (1.4)$$

$$\text{where } \xi = \frac{\frac{1}{n} \sum_{k=1}^n G V_N (T_e^k - T_l)}{\sum_i m_i (\vec{v}_i^T)^2}$$

In Eq. (1.4), m_i , \vec{v}_i^T , and \vec{r}_i are the mass, thermal velocity, and position of an atom i , and \vec{F}_i is the force acting on atom i due to the interatomic interaction between atoms. A complete description of the TTM-MD model is given in [12].

1.2 Motivation of the dissertation

Recent advances in time-resolved x-ray and electron diffraction techniques provide an intriguing opportunity to directly explore the ultrafast phase transformations under extreme conditions created by the short pulse laser irradiation [16,17]. Although these time-resolved pump-probe experiments can offer important atomic-level insights into the fast laser-induced processes, the complexity of the non-equilibrium phase

transformations makes the reliable interpretation of the diffraction profiles in terms of the transient atomic dynamics challenging. Results from MD simulations contain complete atomic-level information on the mechanisms of laser-induced phase transformations. In addition, diffraction profiles and density correlation functions can be readily obtained from the transient atomic configurations generated in MD simulations, providing a direct link between the results of MD simulations and time-resolved diffraction experiments. Therefore, in this study, MD simulations of metal films irradiated with short laser pulses are carried out and the structural analysis techniques are applied to study the characteristics of laser-induced melting processes in irradiated targets. At the same time, the microscopic processes responsible for the generation and evolution of defect configurations in the irradiated targets have been largely unexplored so far in MD simulations. A detailed analysis of the crystal defects introduced by short pulse irradiation could provide important information for short pulse laser materials processing applications.

One of the major challenges in quantitative description of laser-materials interactions is the lack of understanding of the transient behavior and properties of metals under conditions of strong electronic excitation, when the electron temperature rises up to tens of thousands of Kelvins. Furthermore, the accuracy in the application of the models based on TTM for quantitative description of the kinetics of the energy redistribution in the irradiated target relies on the choice of adequate temperature dependent thermophysical properties of the target material. These thermophysical properties, namely the electron-phonon coupling factor, the electron heat capacity, and the heat conductivity, are important parameters in the TTM equation for the electron temperature,

Eq. (1.1). Due to the small heat capacity of the electrons in metals and the finite time needed for the electron-phonon equilibration, irradiation by a short laser pulse can transiently bring the target material to a state of strong electron-lattice nonequilibrium, in which the electron temperature can rise up to tens of thousand of Kelvins, comparable to the Fermi energy, while the lattice still remains cold. At such high electron temperatures, the thermophysical properties of the material can be affected by the thermal excitation of the lower band electrons, which, in turn, can be very sensitive to the details of the spectrum of electron excitations specific for each metal. Indeed, it has been shown by a simple model of the density-of-states (DOS) for Au, that in the range of electron temperatures typically realized in femtosecond laser material processing applications, thermal excitation of d band electrons, located ~ 2 eV below the Fermi level, can lead to a significant, up to an order of magnitude, increase in the strength of the electron-phonon coupling and positive deviations of the electron heat capacity from the commonly used linear dependence on the electron temperature [18,19]. The question that arises from this is how the thermophysical properties of different metals would vary under conditions of strong laser-induced excitation of electrons? In particular, while the approximations of a linear temperature dependence of the electron heat capacity and a temperature independent electron-phonon coupling are used in most of the current TTM calculations, it is important to investigate to what degree the changes in the transient material properties would affect the quantitative predictions of the transient atomic structural dynamics and the kinetics of the energy redistribution in the irradiated target upon short pulse laser irradiation.

1.3 Outline of the dissertation

This dissertation is organized as follows. In Chapter 2, short pulse laser interaction with single crystalline and nanocrystalline metal targets is investigated through MD simulations based on the TTM-MD method. In Chapter 3, the dependence of thermophysical material properties, namely the electron-phonon coupling and the electron heat capacity, on the electron temperature is investigated for eight representative metals, Al, Cu, Ag, Au, Ni, Pt, W, and Ti, for the conditions of strong electron-phonon nonequilibrium induced by short pulse laser irradiation through first principles electronic structure calculations. In Chapter 4, practical implications of the thermal excitation of lower band electrons in short pulse laser interaction with metals are revealed in TTM-MD and TTM simulations performed with thermophysical material properties predicted in Chapter 3. In Chapters 5 and 6, the microscopic mechanisms of the generation of crystal defects in BCC Cr and FCC Ni irradiated by a short laser pulse are investigated in TTM-MD simulations. A summary of this dissertation is given in Chapter 7.

Some chapters of this dissertation have been published or in preparation for publication. The following list gives the references to the papers that report the results presented in this dissertation.

Chapter 2:

Section 2.1: Z. Lin and L. V. Zhigilei, Time-resolved diffraction profiles and atomic dynamics in short pulse laser induced structural transformations: Molecular dynamic study, *Phys. Rev. B*, **73**, 184113, 2006.

Section 2.2: Z. Lin and L. V. Zhigilei, Time-resolved diffraction profiles and structural dynamics of Ni film under short laser pulse irradiation, *J. Phys.: Conference Series* **59**, 11-15, 2007.

Section 2.3: Z. Lin, L. V. Zhigilei, E. Leveugle and E. M. Bringa, Molecular Dynamic Simulation of Laser-induced Melting of Nanocrystalline Au, manuscript in preparation.

Chapter 3: Z. Lin, L. V. Zhigilei and V. Celli, Electron-phonon coupling and electron heat capacity of metals under conditions of strong electron-phonon nonequilibrium, *Phys. Rev. B*, **77**, 075133, 2008.

Results of the calculations have been made accessible in tabulated form at <http://www.faculty.virginia.edu/CompMat/electron-phonon-coupling/>

Chapter 4:

Section 4.1: Z. Lin and L. V. Zhigilei, Thermal excitation of d band electrons in Au: Implications for laser-induced phase transformations, High-Power Laser Ablation VI, edited by C. R. Phipps, *Proc. SPIE* **6261**, 62610U, 2006.

Section 4.2: Z. Lin and L. V. Zhigilei, Temperature dependences of the electron-phonon coupling, electron heat capacity and thermal conductivity in Ni under femtosecond laser irradiation, *Appl. Surf. Sci.* **253**, 6295-6300, 2007.

Chapter 5:

Z. Lin, R. A. Johnson, and L. V. Zhigilei, Computational study of the generation of crystal defects in a BCC metal target irradiated by short laser pulses. *Phys. Rev. B*, in press, 2008.

Chapter 6:

Z. Lin and L. V. Zhigilei, Generation of crystal defects in short pulse laser interaction with FCC Ni, manuscript in preparation.

- [13] D. S. Ivanov and L. V. Zhigilei, Phys. Rev. Lett. **91**, 105701, 2003.
- [14] E. Leveugle, D. S. Ivanov, and L. V. Zhigilei, Appl. Phys. A **79**, 1643, 2004.
- [15] L. V. Zhigilei, D. S. Ivanov, E. Leveugle, B. Sadigh, and E. M. Bringa, High-Power Laser Ablation V, Proc. SPIE **5448**, 505, 2004.
- [16] Siwick B J, Dwyer J R, Jordan R E and Miller R J D 2003 Science **302**, 1382
- [17] Lindenberg A M et al. 2005 Science **308**, 392
- [18] X. Y. Wang, D. M. Riffe, Y. S. Lee, and M. C. Downer, Phys. Rev. B **50**, 8016 (1994).
- [19] A. N. Smith and P. M. Norris, Proceedings of 11th International Heat Transfer Conference **5**, 241, 1998.

2. Investigation of Short Pulse Laser Induced Structural Transformations in Metals

2.1 Time-resolved diffraction profiles and atomic dynamics in short pulse laser induced structural transformations

2.1.1 Introduction

Short (pico- and femtosecond) pulse laser irradiation has the ability to bring material into a highly non-equilibrium state and provides a unique opportunity to study the material behavior and phase transition dynamics under extreme conditions. The challenge of probing fast structural transformations is being met by active development of a variety of time resolved probe techniques [1-16]. Until recently most of the data on the kinetics of laser-induced phase transformations has been provided by optical probe techniques, e.g. [1-4]. While high temporal resolution is readily achievable in optical pump-probe experiments, the reflectivity measured by optical probes can only reveal changes in the electronic structure of the irradiated surface and provides limited direct information on atomic structural rearrangements.

Recent advances in time-resolved x-ray and electron diffraction techniques open up an exciting opportunity to go beyond the analysis of the characteristic time-scales of laser-induced phase transformations and to directly probe the transient atomic dynamics. For example, observations of the inertial motion of atoms on the optically modified/softened potential energy landscape, reported by Lindenberg et al. [6], provide new insights into the mechanisms of non-thermal melting of covalently bonded materials.

Excitation of large coherent atomic displacements at low laser fluences and disordering/melting at higher fluences has been deduced by Sokolowski-Tinten et al. from analysis of time evolution of the diffraction signals obtained for 50 nm bismuth films irradiated with femtosecond laser pulses [7]. Resolidification process of laser-melted surface region of an InSb target has been studied with nanosecond temporal resolution by Harbst et al. and the velocity of the resolidification front has been measured for different laser fluences [8]. Due to the limited intensity of the available X-ray pulses, the diffraction signals are typically derived from rocking curves, for fixed Bragg angles. The advances in short-pulsed electron sources enable a competitive alternative to X-rays in the exploration of atomic dynamics [9]. High structural sensitivity and sub-picosecond time resolution were recently demonstrated by Siwick et al. in an electron diffraction study of ultrafast solid-to-liquid transition dynamics in 20 nm aluminum films irradiated with 120 fs laser pulses [11]. The diffraction intensity over a range of scattering vectors was measured in this work, allowing for analysis of time evolution of the density correlation function during the melting process and providing information on the atomic rearrangements during the first picoseconds following the optical excitation.

Although time-resolved diffraction experiments provide important atomic-level insights into the fast laser-induced processes, the complexity of the non-equilibrium phase transformations hinders the direct translation of the diffraction profiles to the transient atomic structures. Atomic-level simulations can help in reliable interpretation of experimental observations. Indeed, classical and *ab initio* molecular dynamics (MD) simulations have been used to study the mechanisms and kinetics of laser-induced non-thermal [17,18] and thermal [19-21] melting processes, the evolution of voids in

photomechanical spallation [22], as well as the dynamics of explosive material disintegration and ablation [23,24]. MD simulations provide complete atomic-level information on the mechanisms of laser-induced phase transformations. At the same time, diffraction profiles and density correlation functions can be calculated from atomic configurations predicted in MD simulations, providing a direct connection between the results of MD simulations and time-resolved diffraction experiments.

In this section, we report the results of calculations of diffraction profiles and density correlation functions from transient atomic configurations obtained in MD simulations of short pulse laser melting of 20 nm Au and Al films. Computational model used in MD simulations of laser melting of metal films is briefly described next, in Section 2.1.2. Numerical methods for calculation of the structure function from atomic configurations are discussed in Section 2.1.3. The microscopic picture of the competition between the homogeneous and heterogeneous melting processes obtained in MD simulations is discussed and related to the evolution of the diffraction profiles and density correlation functions in Section 2.1.4. Connections between the characteristic features of the diffraction profiles and the mechanisms of laser melting revealed in the simulations, as well as the implications of the simulation results for interpretation of experimental data are reviewed in Section 2.1.5.

2.1.2 Computational setup for simulations of laser interactions with Au thin films

MD simulations of fast laser-induced structural transformations are performed for thin, 20 nm, freestanding metal films irradiated by a short, 200 fs, laser pulse. This choice of the computational system is defined by the availability of high-quality time-

resolved electron diffraction data obtained in the transmission mode for thin freestanding films [10-16]. Most of the simulations reported in this section are for Au films, with an additional simulation performed for an Al film with irradiation conditions comparable to the ones used in a recent experimental study [11]. The simulations are performed with a hybrid atomistic-continuum model that combines the classical MD method for simulation of non-equilibrium processes of lattice superheating, deformation, and melting with a continuum description of the laser excitation and subsequent relaxation of the conduction band electrons. The model is based on well-known two-temperature model (TTM) [25], which describes the time evolution of the lattice and electron temperatures by two coupled non-linear differential equations. In the combined TTM-MD method, MD substitutes the TTM equation for the lattice temperature. The diffusion equation for the electron temperature is solved by a finite difference method simultaneously with MD integration of the equations of motion of atoms. The electron temperature enters a coupling term that is added to the MD equations of motion to account for the energy exchange between the electrons and the lattice. The cells in the finite difference discretization are related to the corresponding volumes of the MD system and the local lattice temperature is defined for each cell from the average kinetic energy of thermal motion of atoms. A complete description of the combined TTM-MD model is given in Ref. [19].

Irradiation by a laser pulse is represented in the continuum part of the model by a source term with a Gaussian temporal profile and exponential attenuation of laser intensity with depth under the surface (Beer-Lambert law). The electron mean free path in Au is larger than the optical penetration depth and the ballistic energy transport defines

the effective laser energy deposition depth, estimated to be on the order of 100 nm [26]. Since the ballistic range in Au exceeds the thickness of the films considered in this work, 20 nm, the reflection of the ballistic electrons from the back surface of the film results in a uniform distribution of the electronic temperature established on the timescale of electron thermalization. The theoretical prediction of the uniform rise of the electronic temperature for thicknesses smaller than the ballistic range has been confirmed in a series of pump-probe measurements of transient reflectivity performed for Au films of different thicknesses, from 10 nm to 500 nm [27]. The effect of the ballistic energy transport and the finite size of the film are accounted for in the source term describing the laser irradiation [19].

The range of laser fluences used in the simulations for Au films, from 45 J/m² to 180 J/m², is chosen so that only an incomplete heterogeneous melting of the film is observed at the lowest fluence and an ultrafast homogeneous melting of the whole film is observed at the highest fluence. The absorbed laser fluences rather than the incident fluences are given here and are used in the remaining part of the study.

The interatomic interaction in the MD part of the model is described by the embedded atom method (EAM) with the functional form and parameterization suggested in Ref. [28]. The choice of the interatomic potential defines all the thermal and elastic properties of the material. Some of the properties of the EAM Au relevant to the material response to the laser heating are listed in Table 2-1-1, along with experimental data for Au. While there are some quantitative discrepancies between the properties of the model EAM Au and experimental data, the overall agreement is reasonable and we can expect that the model will adequately reproduce the material response to fast laser heating.

Moreover, the knowledge of the thermodynamic parameters of the model material allows us to perform a quantitative analysis and physical interpretation of the simulation results.

The parameters used in the TTM equation for the electron temperature are as follows. For Au [19], the electronic heat capacity is $C_e = \gamma T_e$ with $\gamma = 71 \text{ J m}^{-3} \text{ K}^{-2}$, the electron-phonon coupling constant is $G = 2.1 \times 10^{16} \text{ W m}^{-3} \text{ K}^{-1}$, and the dependence of the electron thermal conductivity on the electron and lattice temperatures is described by an expression suggested in Ref. [32]. For Al, $C_e = \gamma T_e$ with $\gamma = 125 \text{ J m}^{-3} \text{ K}^{-2}$, $G = 3.1 \times 10^{17} \text{ W m}^{-3} \text{ K}^{-1}$ [33], the electron thermal conductivity is $K_e = K_0 T_e / T_l$ with $K_0 = 238 \text{ W m}^{-1} \text{ K}^{-1}$ [34], and the optical penetration depth at 800 nm is 8 nm [12].

Properties	T_m K	ΔV_m $\text{cm}^3 \text{ mol}^{-1}$	ΔS_m $\text{J K}^{-1} \text{ mol}^{-1}$	ΔH_m kJ mol^{-1}	$(dT/dP)_m$ K GPa^{-1}	C_p $\text{J K}^{-1} \text{ mol}^{-1}$	α 10^{-6} K^{-1}
EAM Au	963	0.28	8.7	8.4	32.2	25.9-30.3	10.3-21.4
Experiment	1336 [29]	0.55 [29]	9.6 [29]	12.8 [29]	57.5 [29]	25.4-31.2 [30]	14.2-19.1 [31]

Table 2-1-1. Some of the material parameters determined for the EAM Au material. Values of the equilibrium melting temperature, T_m , volume change, ΔV_m , enthalpy, ΔH_m , and entropy, ΔS_m , of melting are given for zero pressure. The dependence of the equilibrium melting temperature on pressure, $(dT/dP)_m$, is determined from liquid-crystal coexistence simulations and confirmed by the calculations based on the Clapeyron equation, $(dT/dP)_m = \Delta V_m / \Delta S_m$. The value given in the table is calculated for zero pressure. Variations of the coefficient of linear expansion, α , and heat capacity at zero

pressure, C_p , are given for a temperature range from 293 K to 950 K. Experimental values for Au are from Refs. [29,30,31].

The initial MD system in simulations of laser interaction with Au films is an FCC crystal composed of 500,000 atoms with dimensions of $20.46 \times 20.46 \times 20.46$ nm and periodic boundary conditions imposed in the directions parallel to two (001) free surfaces. The periodic boundary conditions simulate the situation in which the laser spot diameter is sufficiently large so that the energy redistribution in the lateral directions, parallel to the free surfaces of the film, can be neglected on the time-scales considered in the simulations. Several simulations are performed for systems with dimensions of $8.18 \times 8.18 \times 20.46$ nm (80,000 atoms), $16.37 \times 16.37 \times 20.46$ nm (320,000 atoms), and $28.64 \times 28.64 \times 20.46$ nm (980,000 atoms) to investigate the effect of the size of the computational cell on the calculated diffraction profiles. In the simulation performed for an Al film, a similar system composed of 500,000 atoms with dimensions of $20.56 \times 20.56 \times 20.56$ nm is used. Before applying laser irradiation, all systems are equilibrated at 300 K and zero pressure.

The identification of liquid and crystal regions in the atomic configurations obtained in the simulations is done with a local order parameter calculated for each atom based on the local structure within the first two neighbor shells [19]. The local order parameter is used to identify the crystal and liquid regions in the transient atomic configurations and to quantitatively describe the kinetics of the melting process.

2.1.3 Numerical methods for calculation of structure function from atomic configurations

In order to calculate diffraction patterns from atomic configurations generated in MD simulations, we consider the scattering of a monochromatic/monoenergetic beam of X-ray photons or electrons on a sample consisting of N atoms. Assuming that only single elastic scattering takes place, the amplitude of the wave scattered by the sample is given by summing the amplitude of scattering from each atom in the configuration [35,36]:

$$\Psi_s(\vec{Q}) = \sum_{i=1}^N f_i \exp(-i\vec{Q} \cdot \vec{r}_i), \quad (2.1.1)$$

where \vec{Q} is the scattering vector, \vec{r}_i is the position of atom i with respect to an arbitrary chosen origin, f_i is the x-ray or electron atomic scattering form factor for the i^{th} atom, and the sum goes over all the atoms. The magnitude of \vec{Q} is given by $Q = 4\pi \sin \theta / \lambda$, where θ is half the angle between the incident and scattered wave vectors, and λ is the wavelength of the incident wave. The scattering form factors f_i are functions of Q with different dependences in X-ray and electron scattering [37]. The intensity of the scattered wave can be found by multiplying the scattered wave function by its complex conjugate:

$$I(\vec{Q}) = \Psi_s(\vec{Q}) \cdot \Psi_s^*(\vec{Q}) = \sum_{j=1}^N \sum_{i=1}^N f_i f_j \exp(-i\vec{Q} \cdot (\vec{r}_i - \vec{r}_j)) \quad (2.1.2)$$

Spherically-averaged powder-diffraction intensity profile can be obtained by integration of Eq. (2.1.2) over all directions of interatomic separation vector $\vec{r}_{ij} = \vec{r}_i - \vec{r}_j$, resulting in the Debye scattering equation [35]:

$$I(Q) = \sum_{j=1}^N \sum_{i=1}^N f_i f_j \frac{\sin(Qr_{ij})}{Qr_{ij}} \quad (2.1.3)$$

By dividing the above equation by $\sum_{i=1}^N f_i^2$ we obtain a function that, following Ref. [38],

we call the structure function:

$$S(Q) = \frac{I(Q)}{\sum_{i=1}^N f_i^2} = 1 + \frac{2}{\sum_{i=1}^N f_i^2} \sum_{j=1}^N \sum_{i<j}^N f_i f_j \frac{\sin(Qr_{ij})}{Qr_{ij}} \quad (2.1.4)$$

This function approaches unity at large Q and is often used to present experimental diffraction results. For monoatomic system the dependence on the atomic form factors can be eliminated and we have

$$S(Q) = 1 + \frac{2}{N} \sum_{j=1}^N \sum_{i<j}^N \frac{\sin(Qr_{ij})}{Qr_{ij}} \quad (2.1.5)$$

The structure function defined by Eq. (2.1.5) can be computed directly from the atomic configurations generated in MD simulations. The calculations, however, involve the summation over all pairs of atoms in the system, leading to the quadratic dependence of the computational cost on the number of atoms and making the calculations prohibitively expensive for large systems [39].

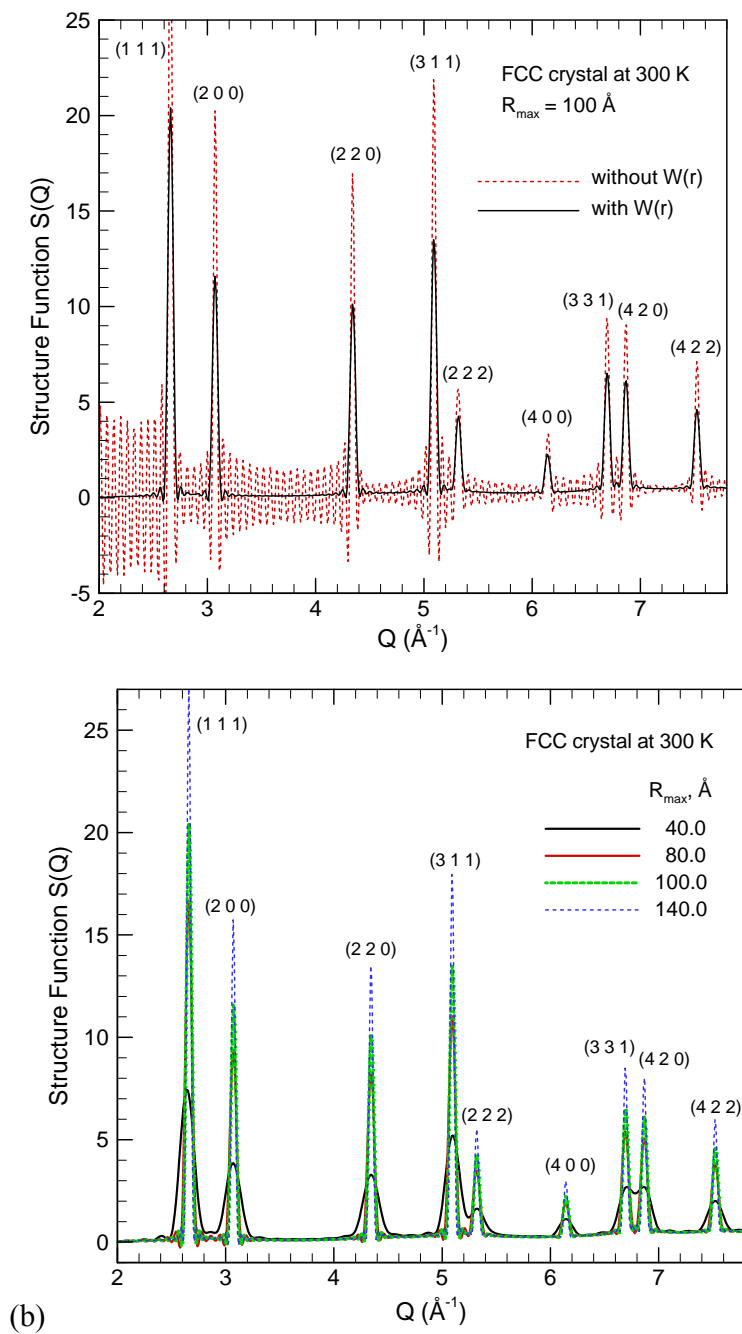


Figure 2-1-1 The effect of the finite size of the MD system on the calculated structure functions. Elimination of spurious ripples induced by the truncation of the pair density function at $R_{\text{max}}=100 \text{ \AA}$ by introduction of the damping function $W(r)$ in Eq. (2.1.8) is illustrated in (a), where the results are shown for $20.46 \times 20.46 \times 20.46 \text{ nm}$ FCC Au system

equilibrated at 300 K. Black and red lines show the results of the calculations performed with and without $W(r)$, respectively. Structure functions calculated using Eq. (2.1.9), with the damping function, for systems of four different sizes in the lateral directions are shown in (b).

An alternative approach to calculation of $S(Q)$ is to substitute the double summation over atomic positions in Eq. (2.1.5) by integration over the pair density function, which is a real space representation of correlations in atomic positions [38],

$$\rho(r) = \frac{1}{4\pi N r^2} \sum_{j=1}^N \sum_{i=1, i \neq j}^N \delta(r - r_{ij}) = \frac{1}{2\pi N r^2} \sum_{j=1}^N \sum_{i < j}^N \delta(r - r_{ij}) \quad (2.1.6)$$

where δ is the Dirac delta function. Although the calculation of the pair density function still involves $N^2/2$ evaluations of interatomic distances r_{ij} , it can be done much more efficiently than the double sum in Eq. (2.1.5) that requires evaluation of \sin function and repetitive calculations for each value of Q . The expression for the structure function, Eq. (2.1.5), can be now reduced to a simple integration, which, in fact, is the Fourier transform of the pair density function:

$$S(Q) = 1 + \int_0^{\infty} 4\pi r^2 \rho(r) \frac{\sin(Qr)}{Qr} dr \quad (2.1.7)$$

In the calculation of the pair density function, the maximum value of r is limited by the size of the MD simulation cell. If the periodic boundary conditions are used to represent a part of a larger/infinite system, the pair density function can only be evaluated up to a maximum value R_{\max} that should not exceed a half of the computational cell. The truncation of the numerical integration in Eq. (2.1.7) at R_{\max} induces spurious ripples with

a period of $\Delta = 2\pi / R_{\max}$ [40]. A number of methods have been proposed to suppress these ripples so that the Fourier ringing dies out more quickly [35,38,39,41,42]. The method that we adopt in this work is to multiply the integrand in Eq. (2.1.7) by a damping function $W(r)$, similar to the Lorch modification function in neutron diffraction experiments [43],

$$W(r) = \frac{\sin\left(\frac{r\Delta}{2}\right)}{\frac{r\Delta}{2}} = \frac{\sin\left(\pi \frac{r}{R_{\max}}\right)}{\pi \frac{r}{R_{\max}}} \quad (2.1.8)$$

Thus the structure function $S(Q)$ can be calculated as

$$S(Q) = 1 + \int_0^{R_{\max}} 4\pi r^2 \rho(r) \frac{\sin(Qr)}{Qr} W(r) dr \quad (2.1.9)$$

The damping function replaces the sharp step function at the cutoff distance R_{\max} by a smoothly decreasing contribution from the density function at large interatomic distances and eventually approaching zero at R_{\max} .

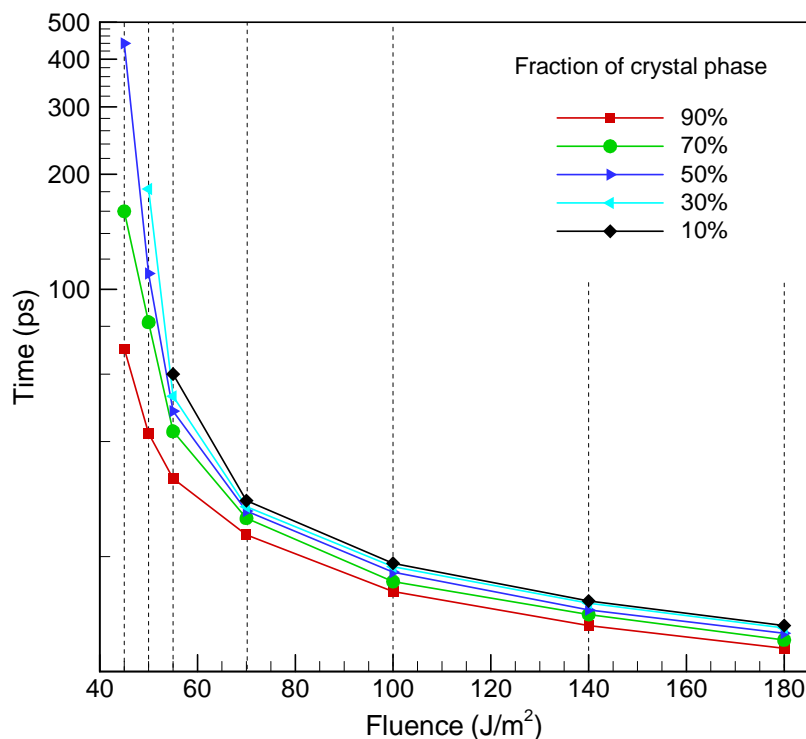
Figure 2-1-1(a) shows structure functions calculated with and without the damping function for an FCC Au system composed of 500,000 atoms ($R_{\max} = 100 \text{ \AA}$) and equilibrated at 300 K. It is apparent that the introduction of the damping function completely eliminates spurious truncation ripples in the structure function. While for the FCC crystallite at 300 K the presence of ripples does not prevent identification of the real structural peaks, Fig. 2-1-1(a), the elimination of ripples is crucial for the analysis of the structural transformations occurring at elevated temperatures, when the real structural peaks can be small and completely obscured by the ripples.

Although application of the damping function eliminates the truncation ripples, the finite size of the MD system and the introduction of the cutoff in the pair density function also affect the real peaks of the structure function. To illustrate the effect of the size of the system on the characteristics of structure function, the results of calculations performed for a 20 nm thick Au film represented by MD computational cells with four different sizes in the directions of periodic boundary conditions, parallel to the surfaces of the film, 8.18, 16.37, 20.46, and 28.64 nm are shown in Fig. 2-1-1(b). The cut-off distances R_{\max} , used in the calculations of the pair density functions are 40 Å, 80 Å, 100 Å, and 140 Å respectively. It can be seen that the failure of including long-range atomic correlations beyond 40 Å results in a significant broadening of all peaks, with some of the peaks starting to merge. As the value of R_{\max} increases to 80 Å, the peaks become sharp and well-defined. Further increase of R_{\max} to 100 Å and to 140 Å results in a much more moderate sharpening of the peaks, with no changes to the peak positions. Analytical calculation of the broadening of the peaks due to the introduction of the damping function with $R_{\max} = 100$ Å predicts a broadening of $\Delta Q = 5.437 / R_{\max} = 0.05437 \text{ Å}^{-1}$ [44]. Since the purpose of the present study is to investigate the evolution of the diffraction pattern during the fast laser heating of the film up to the melting temperature and above, the relatively small finite-size effect is expected to be negligible compared to the changes in the diffraction peaks associated with the temperature rise and structural transformations. Thus, all simulations discussed in the next section are performed for 20.46×20.46×20.46 nm (500,000 atoms) system and all structure functions are calculated with Eq. (2.1.9) and $R_{\max}=100$ Å.

2.1.4 Results and discussion

2.1.4.1 Kinetics and mechanisms of laser melting

The timescales of laser melting predicted in TTM-MD simulations of 20 nm Au films irradiated with 200 fs laser pulses at absorbed fluences ranging from 45 J/m² to 180 J/m² are presented in Fig. 2-1-2. The fraction of the crystal phase is defined by the number of atoms with local crystalline environment, as predicted by the local order parameter [19]. Two distinct regimes can be identified in Fig. 2-1-2, a high-fluence regime when the entire film melts within just several picoseconds, and a low-fluence regime when the melting process slows down and the melting starting time increases sharply with decreasing fluence. Below we briefly discuss the melting mechanisms of Au films in these two regimes.



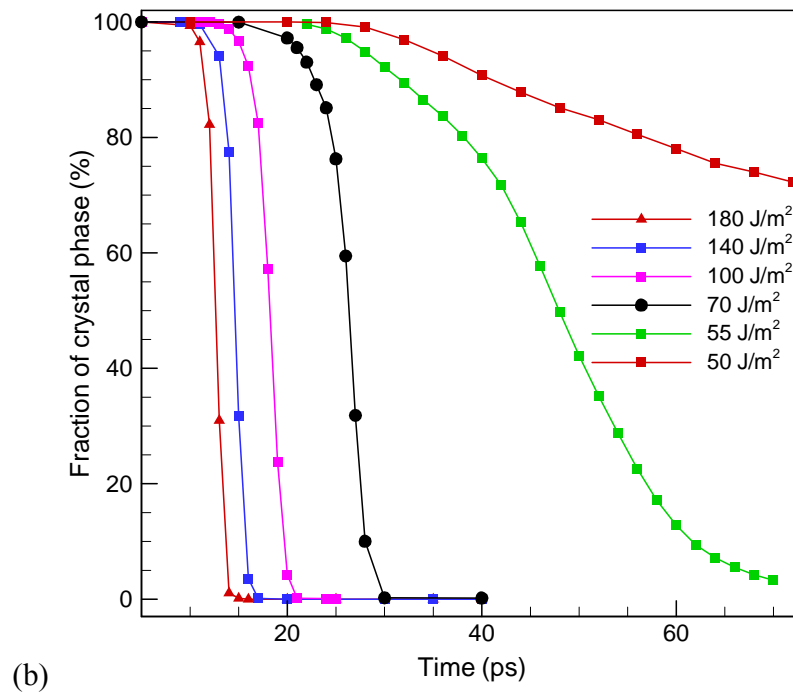
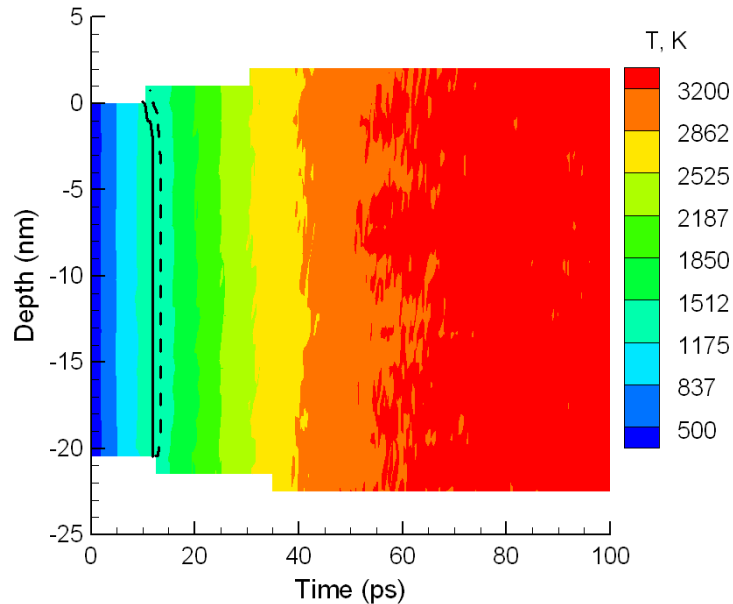


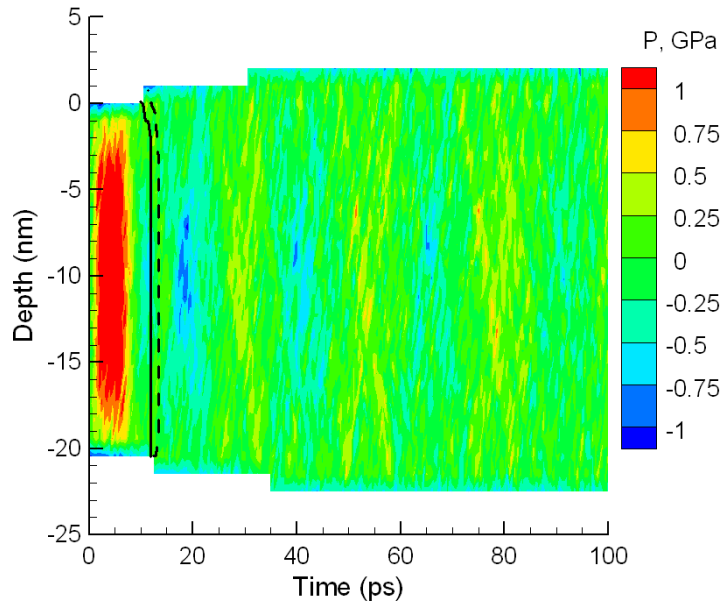
Figure 2-1-2. The timescales of the melting process in a 20 nm Au film irradiated with a 200 fs laser pulse at different absorbed fluences. Semi-logarithmic plots of the time required to melt certain fractions of the film are shown in (a). Each curve corresponds to a particular fraction of the remaining crystal phase as a function of the absorbed fluence. For example, the red curve with squares corresponds to the time after laser excitation when 90% of the atoms in the film belong to the crystal phase. The decrease of the fraction of the crystal phase with time is shown for each simulation in (b). The atoms in the crystal phase are distinguished from the ones in the liquid phase based on the local order parameter [19].

At the highest laser fluence of 180 J/m^2 , melting starts at about 10 ps after the laser pulse and completes by 14 ps. Similarly fast decrease of the fraction of the crystal phase is observed in simulations performed at absorbed fluences of 140 and 100 J/m^2 . The melting mechanism in this high-fluence regime is exemplified here by the results

obtained in a simulation performed at 180 J/m^2 . The temporal and spatial evolution of the lattice temperature and pressure in the irradiated film is shown in the form of contour plots in Fig. 2-1-3. Large mean free path of excited electrons and a weak electron-phonon coupling in Au results in a uniform distribution of the electronic temperature in the film before the electron-lattice thermalization. As a result the whole film is heated up uniformly at a rate on the order of $\sim 10^{14} \text{ K/s}$, Fig. 2-1-3(a). The fastest heating is observed within the first 15 ps of the simulation, whereas complete equilibration between the hot electrons and the lattice takes up to 80 ps. The fast increase of the lattice temperature results in the overheating of the lattice above the limit of its stability, $\sim 1.25T_m$ [19], and leads to the fast homogeneous melting of the whole film within $\sim 3\text{-}4$ ps. The solid and dashed lines in Fig. 2-1-3 mark the beginning (90% of the crystal phase) and the end (10% of the crystal phase) of the melting process and can be related to the corresponding points in Fig. 2-1-2.



(a)

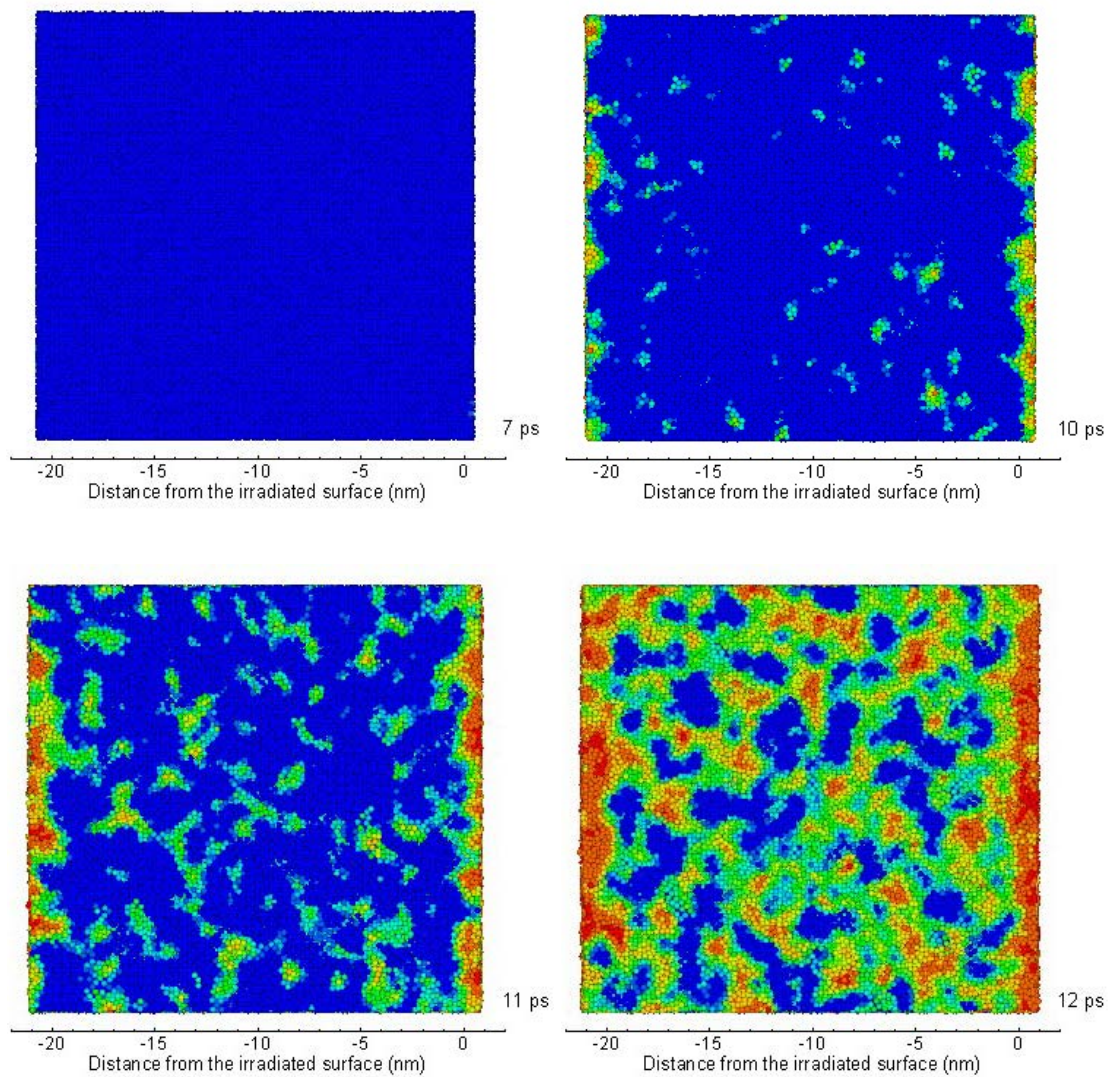


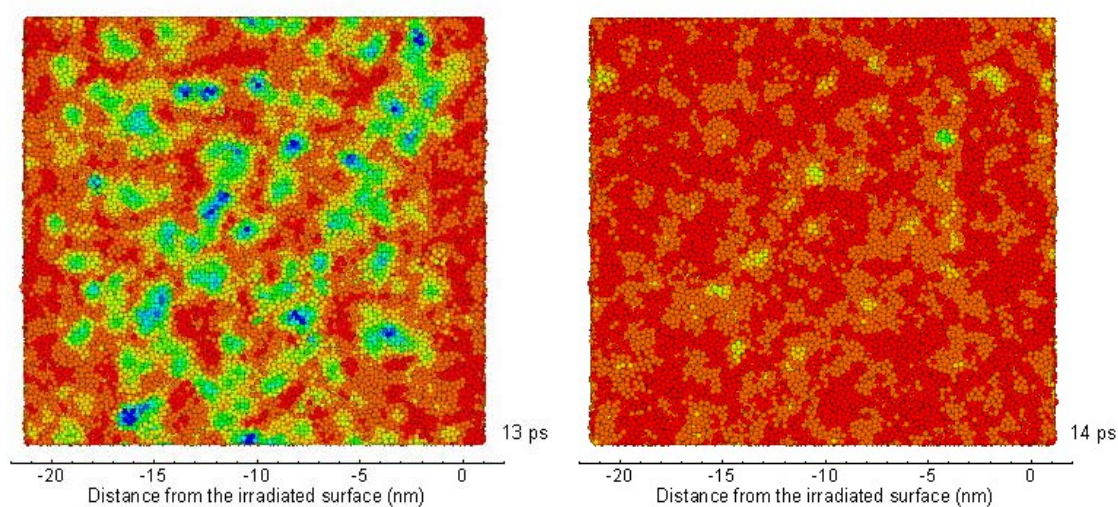
(b)

Figure 2-1-3. Contour plots of the lattice temperature (a) and pressure (b) for a simulation of laser melting of a 20 nm Au film irradiated with a 200 fs laser pulse at an absorbed fluence of 180 J/m^2 . Solid and dashed lines show the beginning and the end of the melting process. Laser pulse is directed along the Y-axes, from the top of the contour plots. The stepwise shape of the contour plot boundaries is related to the discretization of the mesh over which average temperature and pressure values are calculated.

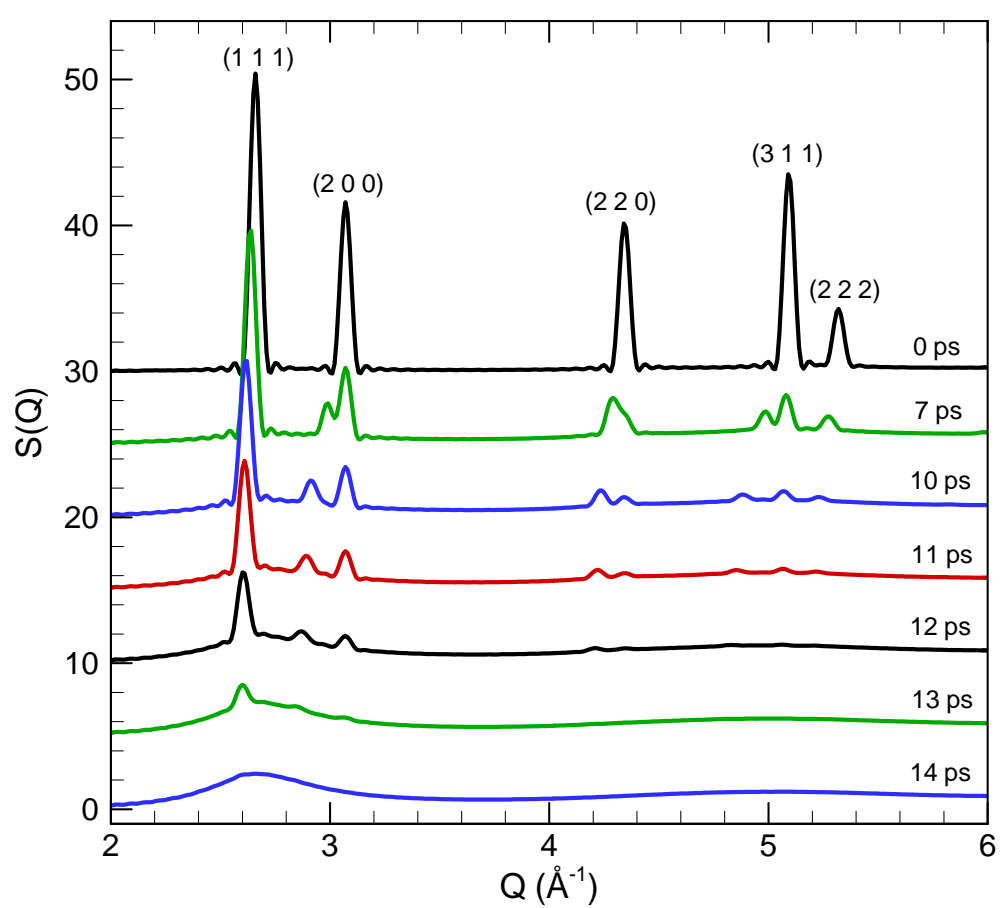
The pressure contour plot in Fig. 2-1-3(b) shows that the fast lattice heating results in the build up of a compressive stresses inside the film within the first ~ 5 ps. The initial compressive pressure drives the expansion of the film. In earlier simulations performed for Ni and thicker Au films [19,20,45] the relaxation of the laser-induced compressive stresses resulted in generation of tensile stresses, followed by pressure oscillations or even disintegration/spallation of the film. For 20 nm freestanding Au film,

however, the time of the mechanical relaxation is on the order of 5 ps (time needed for the two unloading waves to cross a half of the depth of the film), significantly shorter than the time of the lattice heating. As a result, the film expands during the lattice heating and pressure (and film thickness) oscillations can be hardly observed in Fig. 2-1-3(b).





(a)



(b)

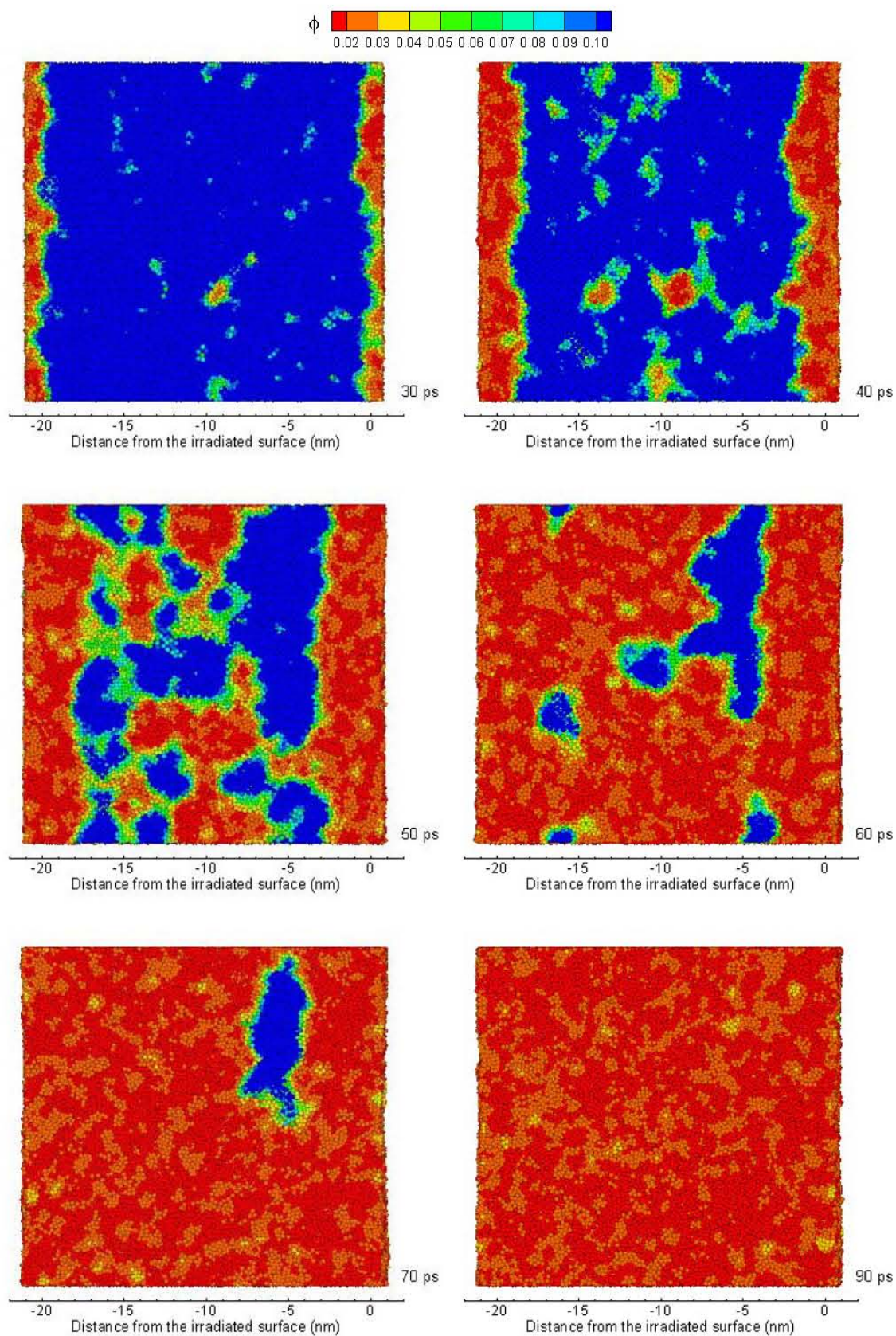
Figure 2-1-4. Snapshots (a) and structure functions (b) of atomic configurations during the melting process in a 20 nm Au film irradiated with a 200 fs laser pulse at an absorbed fluence of 180 J/m^2 . Atoms are colored according to the local order parameter Φ - blue atoms have local crystalline surroundings, red atoms belong to the liquid phase. In (a), the laser pulse is directed from the right to the left sides of the snapshots. In (b), curves are shifted vertically with respect to each other in order to better show the changes in the structure function. Zero time corresponds to a perfect FCC crystal at 300 K just before the laser irradiation.

The atomic-level picture of the homogeneous melting process in the high-energy regime is shown in Fig. 2-1-4(a). The visual analysis of snapshots from the simulation suggests that the growth of the liquid regions appearing at the free surfaces of the film (see a snapshot taken at 10 ps) does not make any significant contribution to the overall melting process. The energy transfer from the hot electrons to the lattice quickly leads to the overheating of the lattice up to the limit of the crystal stability, when a spontaneous nucleation of a large number of small liquid regions occurs throughout the film, leading to the rapid collapse of the crystalline structure from 10 to 14 ps.

Similar melting process, dominated by homogeneous nucleation of liquid regions inside the overheated crystal, is observed for all other fluences in the high-fluence regime, down to 70 J/m^2 . The decrease in fluence shifts the melting process to later time and gradually increases the contribution of the heterogeneous melting that takes place by propagation of two melting fronts from the surfaces of the film. The latter process is reflected in the development of the initial slow shoulders in the melting curves shown in

Fig. 2-1-2(b). The slow components of the melting process are apparent in the curve plotted for 70 J/m^2 , where almost 10% of the film melts due to the propagation of the melting fronts, before the critical superheating is reached and the faster homogeneous melting takes over.

The melting process observed at 55 J/m^2 can be considered to be a transitional one between the high-fluence (homogeneous melting) and low-fluence (heterogeneous melting) regimes. At this fluence both mechanisms of melting contribute approximately equally to the melting process, Fig. 2-1-5(a). During the time from 25 to 40 ps, the propagation of two melting fronts from the surfaces of the film is largely responsible for the increase in the fraction of the liquid phase. After 40 ps, the growth of liquid regions nucleated inside the overheated crystal starts to make a major contribution to the melting process, significantly accelerating the total rate of melting, as reflected in the slope of the melting line in Fig. 2-1-2(b). The melting slows down again at later time due to the lattice temperature decrease. From the time of 70 to 90 ps the last crystalline island slowly melts, Fig. 2-1-5(a), as the temperature of the film is approaching the equilibrium melting temperature.



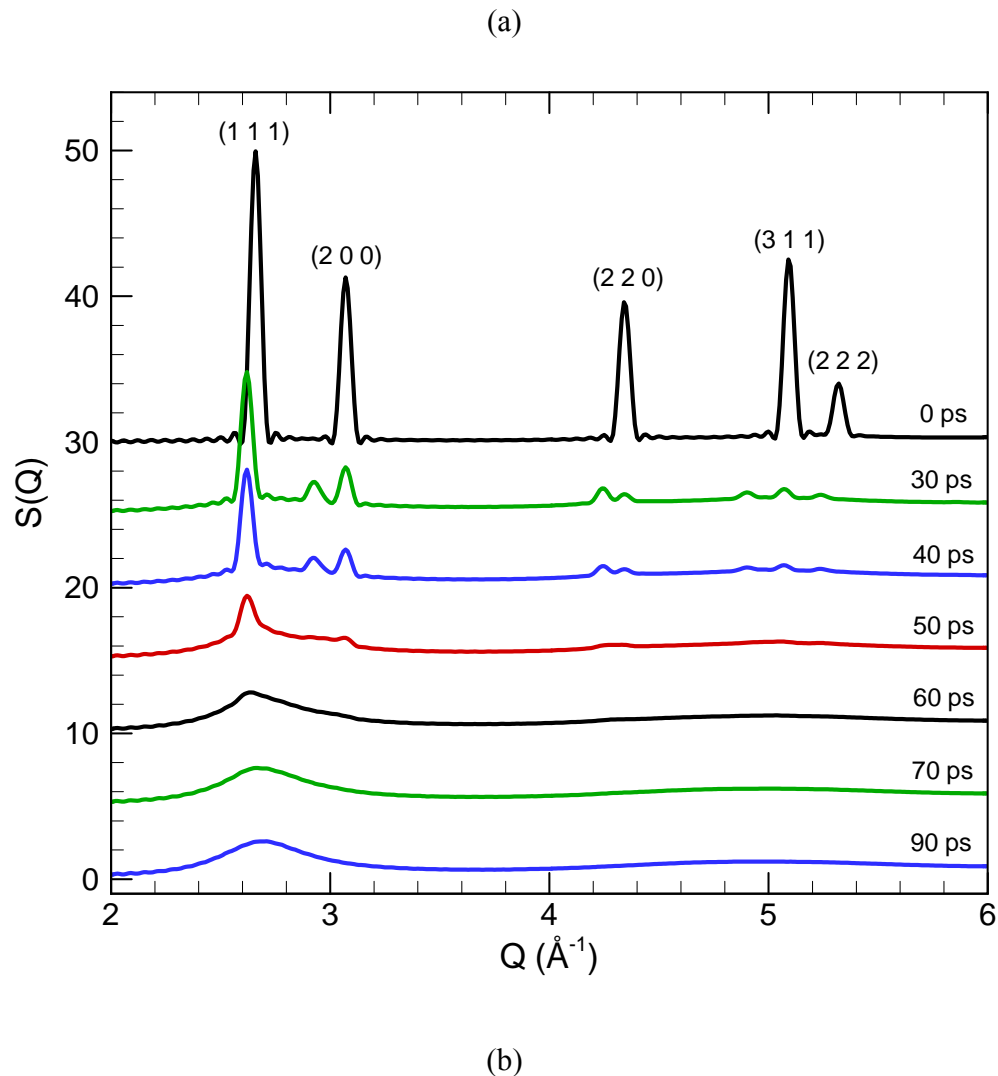
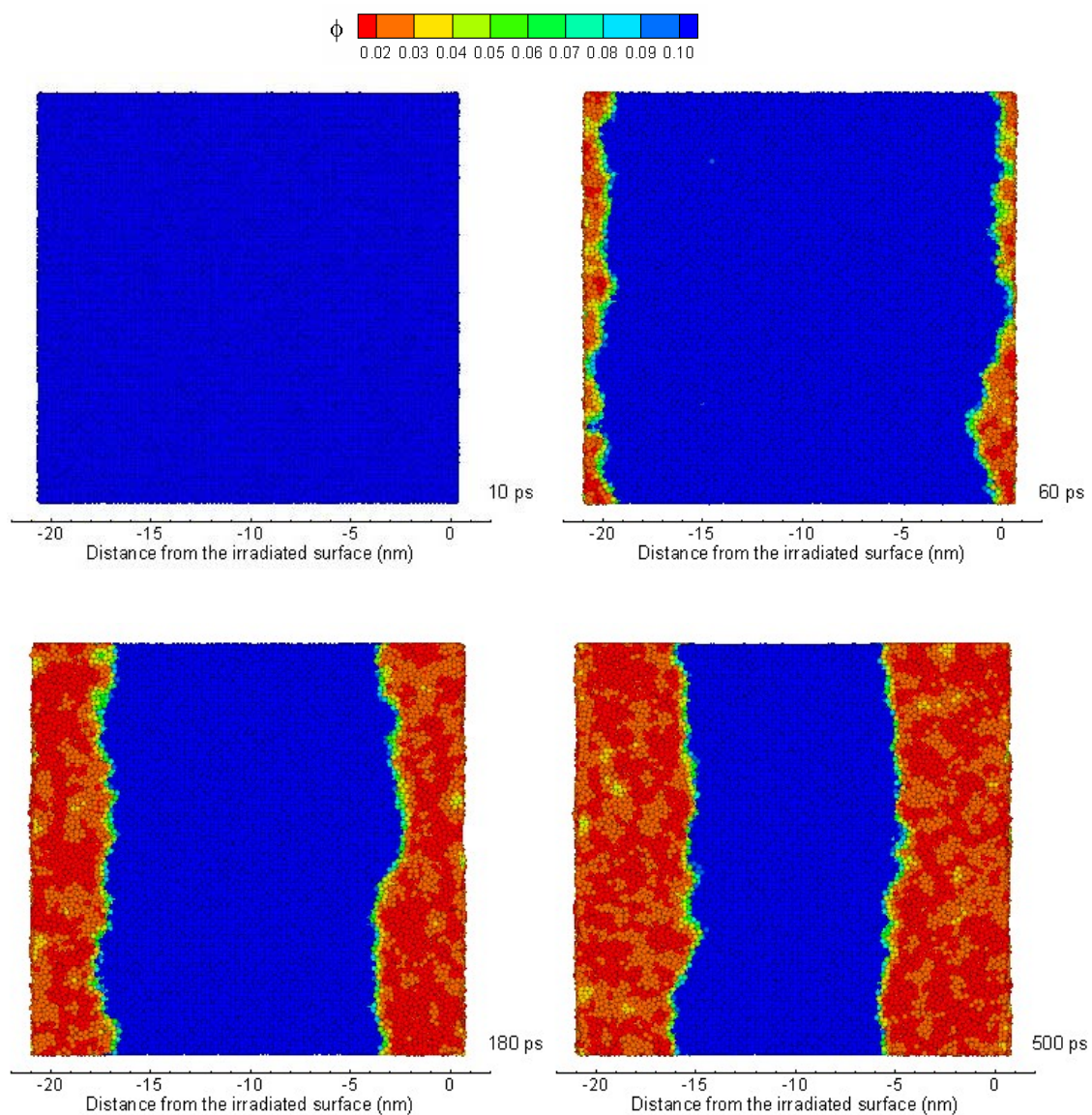


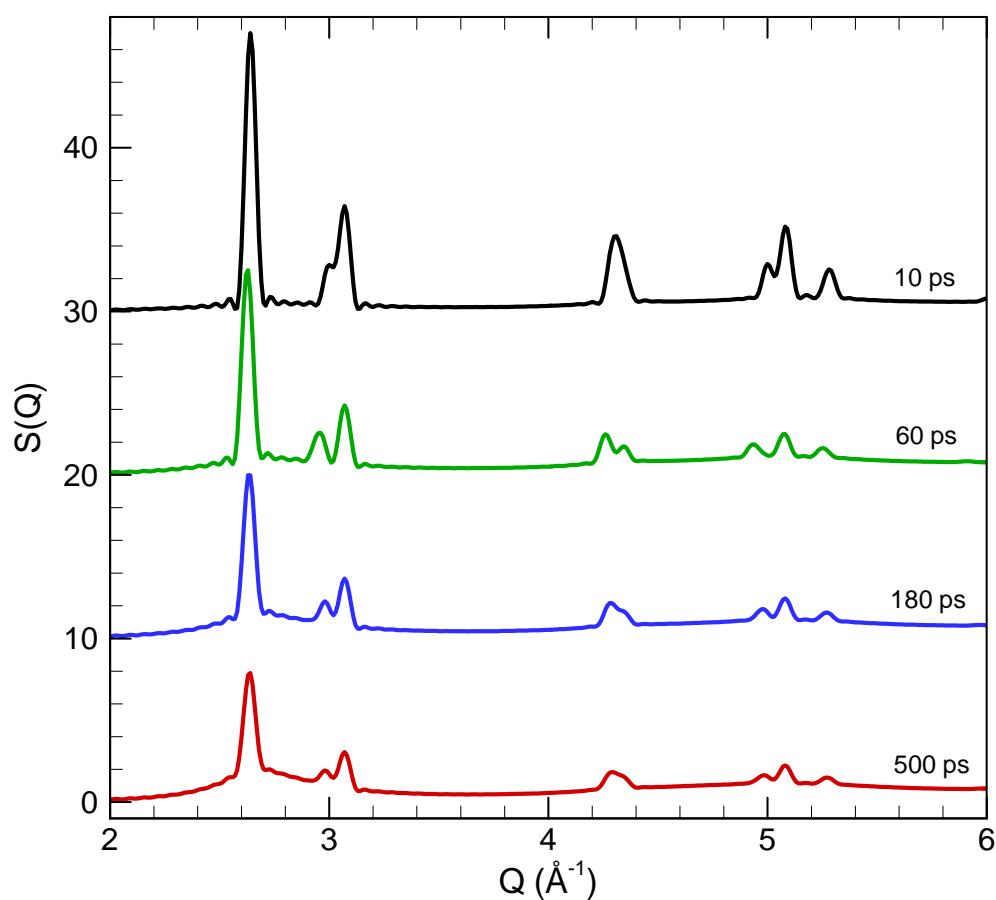
Figure 2-1-5. Snapshots (a) and structure functions (b) of atomic configurations during the melting process in a 20 nm Au film irradiated with a 200 fs laser pulse at an absorbed fluence of 55 J/m^2 . Atoms are colored according to the local order parameter Φ - blue atoms have local crystalline surroundings, red atoms belong to the liquid phase. In (a), the laser pulse is directed from the right to the left sides of the snapshots. In (b), curves are shifted vertically with respect to each other in order to better show the changes in the structure function. Zero time corresponds to a perfect FCC crystal at 300 K just before the laser irradiation.

At laser fluences below 55 J/m^2 , the propagation of the melting fronts from the surfaces of the film dominates the melting process and a significant increase of the melting time is observed in Fig. 2-1-2. Snapshots from a simulation performed at a fluence of 45 J/m^2 illustrate the melting process in this regime, Fig. 2-1-6(a). Two melting fronts propagate from the free surfaces with velocities that decrease down to zero as the melting progresses and the temperature approaches the equilibrium melting temperature. By the end of the simulation (500 ps) the temperature of the film decreases down to the equilibrium melting temperature and the remaining 49% of the film material remains in the crystalline state. Incomplete and purely heterogeneous melting is also observed in the simulations performed at 50 and 51 J/m^2 . Based on the properties of the model EAM Au material we can estimate the critical absorbed fluence, F_m , that would supply enough energy to completely melt the film:

$$F_m = \left(\int_{300}^{T_m} C_l(T) dT + \int_{300}^{T_m} C_e(T) dT + \Delta H_m \right) \times d \quad (2.1.10)$$



(a)



(b)

Figure 2-1-6. Snapshots (a) and structure functions (b) of atomic configurations during the melting process in a 20 nm Au film irradiated with a 200 fs laser pulse at an absorbed fluence of 45 J/m^2 . Atoms are colored according to the local order parameter Φ - blue atoms have local crystalline surroundings, red atoms belong to the liquid phase. In (a), the laser pulse is directed from the right to the left sides of the snapshots. In (b), curves are shifted vertically with respect to each other in order to better show the changes in the structure function.

where d is the thickness of the film, C_l and C_e are the lattice and electron heat capacities and ΔH_m is the heat of melting. Using parameters of EAM Au listed in Table 2-1-1 and electron heat capacity defined in Section 2-1-2 we can estimate $F_m = 53.78 \text{ J/m}^2$, with 36.52 J/m^2 and 0.59 J/m^2 going into heating of the lattice and electrons up to the equilibrium melting temperature T_m and 16.67 J/m^2 required for melting the film at T_m . This estimation is consistent with the results of MD simulation described above.

The relative contribution of the homogeneous and heterogeneous melting mechanisms in the simulations described above is controlled by the temperature dependence of the velocity of the melting fronts propagating from the free surfaces of the film and the lattice heating regime. The rate of the lattice heating is defined by the irradiation parameters (laser fluence and pulse duration) and the strength of the electron-phonon coupling, whereas the temperature dependence of the velocity of the melting front can be described by non-equilibrium kinetic theory [46]. The maximum velocity of the melting front propagation is the velocity at the limit of the crystal stability, above which a massive homogeneous nucleation of liquid regions inside the overheated crystal takes place. While one can safely assume that the maximum velocity of the melting front is ultimately limited by the speed of sound [47], recent MD simulations [19] demonstrate that the real maximum velocity at the limit of crystal stability does not exceed 15% of the speed of sound. Moreover, under conditions of laser melting, the overheating required for the onset of the homogeneous nucleation of liquid regions is significantly reduced by the uniaxial lattice distortions produced as a result of the relaxation of laser-induced thermoelastic stresses [20]. This reduction in the lattice stability explains why the

homogeneous nucleation is observed down to a relatively low fluence of 55 J/m^2 , when the melting process is slow and takes up to 90 ps.

2.1.4.2 *Structure function calculations*

Calculation of the diffraction profiles provides an attractive possibility to directly relate the detailed information on the kinetics and mechanisms of laser-induced structural transformations obtained in MD simulations to the results of time-resolved diffraction experiments [5-8,10-13]. In this Section we present the results on the evolution of the structure function $S(Q)$ in two representative simulations discussed above, a simulation at 180 J/m^2 where a fast homogeneous melting is observed and a simulation at 45 J/m^2 where much slower heterogeneous melting takes place.

The temporal evolution of the diffraction profile is shown for a fluence of 180 J/m^2 in Fig. 2-1-4(b). Although by the time of 7 ps the melting process has barely started and most atoms ($\sim 99\%$) are still identified by the local order parameter as maintaining local crystalline surroundings, the structure function has changed significantly. First, there is a considerable reduction in the heights of all the peaks as compared to the structure function calculated at zero time, before the laser pulse. This reduction can be largely attributed to the fast heating of the crystal from 300 K to 1059 K, Fig. 2-1-3a. Quantitative analysis of peak height reduction due to the increase in the amplitudes of thermal atomic vibrations is given in Section 2.1.4.4. Second, there is a pronounced shift to the left of the (111) diffraction peak and splitting of the (200), (220), and (311) peaks. The appearance of new diffraction peaks may be indicative of solid-solid phase transformations. A detailed structural analysis, however, does not reveal any structural

changes in the film beyond the appearance of a relatively small number of point defects (vacancy-interstitial pairs). Both the shift and the splitting of the peaks are actually related to the uniaxial expansion of the film in response to the laser heating, as explained in Section 2.1.4.3.

Absorbed fluence = 45 J/m²

Time	10 ps	60 ps	180 ps	500 ps
Crystal fraction (%)	100.0	93.1	67.5	49.1

Absorbed fluence = 180 J/m²

Time	11 ps	12 ps	13 ps	14 ps
Crystal fraction (%)	93.1	67.5	15.9	0.3

Table 2-1-2. Fraction of atoms with local crystalline surroundings (local order parameter $\Phi > 0.04$) in a 20 nm Au film irradiated with a 200 fs laser pulse at absorbed fluences of 45 and 180 J/m².

A fast collapse of the crystalline structure from 10 to 14 ps, apparent from the snapshots shown in Fig. 2-1-4(a), is also clearly reflected in the evolution of the structure function. In just 3-4 ps the peaks characteristic of the FCC structure disappear and the structure function takes the shape characteristic of the liquid structure, with only one broad peak that can be identified. The duration of the melting process observed in this simulation is in a good agreement with the one measured in time-resolved electron diffraction experiments performed for 20 nm Al films, 3.5 ps [11]. Some of the differences between the evolution of the diffraction peaks observed in the simulation and

experiment, most notably the absence of peak splitting and shifts in the positions of diffraction peaks in experimental observations, are discussed in Section 2.1.5.

An evolution of the structure function in the low-fluence regime, when the melting process is dominated by the propagation of the melting fronts from the free surfaces of the film, is illustrated in Fig. 2-1-6(b), where the results are shown for an absorbed fluence of 45 J/m^2 . Similarly to the fast homogeneous melting discussed above, laser irradiation leads to the reduction of heights of the peaks and induces a shift of the (111) peak to the left and splitting of other peaks. There are, however, important differences in the evolution of the structure functions in low and high-energy regimes. While the heights of the peaks are decreasing gradually during the melting process, the peaks remain well-defined up to the end of the simulation, when more than 50% of the film is melted. For the same fraction of atoms belonging to the crystalline parts of the system (having crystalline local environment as defined by the local order parameter) the diffraction peaks are more pronounced in the case of heterogeneous melting. For instance, although from Table 2-1-2 we can see that the same number of atoms remain in the crystalline parts of the film at 11 ps after 180 J/m^2 pulse and at 60 ps after 45 J/m^2 pulse, the diffraction peaks are much more clearly defined in the corresponding curve in Fig. 2-1-6(b), as compared to the one in Fig. 2-1-4(b). The same conclusion one can derive from the comparison of structure functions shown for 12 ps in Fig. 2-1-4(b) and 180 ps in Fig. 2-1-6(b).

It is clear from the visual analysis of the snapshots of atomic configurations that the homogeneous nucleation of a large number of liquid regions throughout the film, Fig. 2-1-4(a), is effective in destabilizing the lattice and reducing the long-range order

throughout the film. While most of the atoms still retain their local crystalline surroundings at 11 and 12 ps, the long-range correlations in atomic positions are largely lost and the diffraction peaks are significantly reduced. Similarly, the presence of relatively small crystalline islands observed at 60 and 70 ps in a simulation performed at 55 J/m^2 , Fig. 2-1-5(a), can be hardly identified from the corresponding diffraction patterns, Fig. 2-1-5(b). In the case of heterogeneous melting, the correlations in atomic positions are retained on the scale of the crystalline regions and the diffraction pattern is generated by superposition of the diffraction from the liquid and crystalline parts of the system. In other words, the long-range order is more subtle in homogeneous melting than in heterogeneous melting due to the smaller characteristic length-scales at which the homogeneous phase transformation takes place.

2.1.4.3 *Splitting of the peaks - the uniaxial lattice expansion*

In this section we discuss the splittings of the diffraction peaks that takes place shortly after the laser irradiation, Figs. 2-1-4(b), 2-1-5(b), and 2-1-6(b), and demonstrate that the splitting is a direct consequence of the uniaxial thermoelastic deformation of the film in response to the laser heating.

Laser excitation of the conduction band electrons and following electron-phonon equilibration lead to the fast heating of the lattice, Fig. 2-1-3(a), and generation of thermoelastic stresses, Fig. 2-1-3(b), which drive the expansion of the film. The periodic boundary conditions applied in the directions parallel to the surfaces of the film only allow the expansion of the film to proceed in the direction normal to the surface. These conditions of the lateral confinement are also realized in experiments, where the laser

spot diameter is much larger than the depth of the heated region or thickness of the irradiated film. The simulations are performed for a single-crystalline FCC film with (001) free surfaces. The uniaxial deformation of the FCC lattice along the (001) direction changes the space group symmetry of the lattice as the cubic lattice transforms into tetragonal lattice. Thus, one should expect the occurrence of new diffraction peaks corresponding to the Face Centered Tetragonal (FCT) lattice.

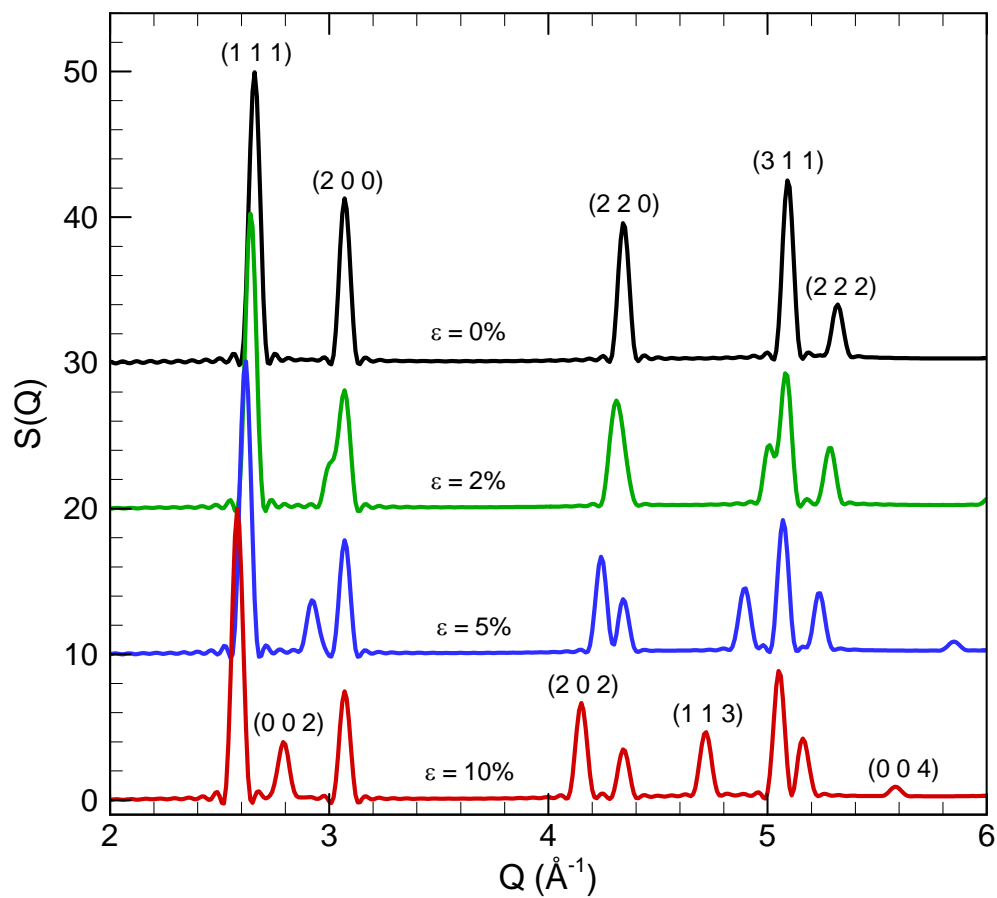


Figure 2-1-7. Structure functions of atomic configurations generated by uniaxial uniform deformation of a 20 nm Au FCC film in the direction normal to the free (001) surfaces. The values of the deformation are indicated in the figure. Temperature of the film is 300 K. Curves are shifted vertically with respect to each other in order to better

show the changes in the structure function. Structure peaks are identified by Miller indices.

In order to investigate the degree to which the lattice expansion alone can explain the splittings observed in the diffraction profiles in Figs. 2-1-4(b), 2-1-5(b), and 2-1-6(b), we calculate structure functions for a series of Au FCC structures uniaxially deformed along (001) direction. The results of the diffraction profile calculations are shown in Fig. 2-1-7. Splittings and shifts of the diffraction peaks, increasing with increasing deformation, are apparent in the Figure. The diffraction peaks from (111) and (311) atomic planes, present in the original FCC structure, shift in the direction of smaller Q . New diffraction peaks with (002), (202), (113), (004) Miller indices appear as the lattice transforms from FCC to FCT.

It should be noted that the appearance of new peaks is not observed in MD simulations of an FCC crystal slowly heated up to the melting temperature under constant hydrostatic pressure conditions (with periodic boundary conditions applied in all directions). In these simulations the effects of an increase in temperature are limited to the decrease of the heights of the peaks due to the atomic thermal vibrations (see Section 2.1.4.4) and shift of the peak positions to smaller values of Q due to the isotropic thermal expansion of the crystal.

By comparing the diffraction profiles obtained for the uniaxially deformed films, Fig. 2-1-7, with the results obtained in the laser melting simulations, Figs. 2-1-4(b), 2-1-5(b), and 2-1-6(b), we can conclude that both the shift and splitting of the peaks can be explained by the uniaxial thermoelastic expansion of the lattice. Using the (002) peak splittings shown in Fig. 2-1-7 as a reference, we can estimate that uniaxial deformations

along the (001) direction of 2.8%, 5.3%, and 6.6% would produce the values of peak shifts and splittings observed in a simulation performed at 180 J/m^2 , Fig. 2-1-4(b), at 7 ps, 10 ps, and 11 ps, respectively. These values calculated from the diffraction spectra are consistent with the ones obtained by directly measuring the thickness of the film in the snapshots of the atomic configurations, Fig. 2-1-4(a), as well as with the distances between the density peaks in the density distribution along the direction normal to the film surfaces. The distances between the density peaks correspond to the spacing between the (001) lattice planes in the expanded film and are directly related to the position of the (002) diffraction peak.

In the case of the absorbed fluence of 45 J/m^2 , Fig. 2-1-6, the splittings of the diffraction peaks at 10 ps, 60 ps, 180 ps, and 500 ps correspond to 2.3%, 3.9%, 3.1%, and 3.1% uniaxial deformations of the lattice. These values are again consistent with inter-plane distances measured in the density distribution along the direction normal to the film surfaces. The direct measurement of deformation based on the thickness of the film is hampered in this case by melting of the surface regions. The diffraction profiles calculated for times of 180 ps and 500 ps show some subtle reverse shifts and decrease in the splittings of the peaks with respect to the shift values observed at 60 ps. These changes may be related to the gradual cooling of the film associated with the melting process, by $\sim 50 \text{ K}$ from 60 ps to 180 ps.

Thus, the results discussed above indicate that, in the fluence range considered in this study, the melting of Au film is preceded by a significant thermoelastic uniaxial lattice expansion, which can be identified from shifts and splittings of the diffraction peaks. It has been shown that the uniaxial expansion and associated anisotropic lattice

distortions can significantly reduce the lattice stability against the initiation of melting and can lead to the homogeneous nucleation of liquid regions at temperatures close to the equilibrium melting temperature [20]. Although the analysis performed in this study is done for a single crystal film oriented perpendicular to [001] direction, quantitative analysis of laser-induced deformations is also possible for polycrystalline samples, as soon as the texture of the sample is known, e.g. [48]. Investigation of the development of thermoelastic deformations in time-resolved X-ray or electron diffraction experiments has a potential for providing important information on the characteristic time-scale of lattice heating and thermoelastic deformation as well as on the role of the uniaxial deformation in laser-induced phase transformations. Indeed, the evolution of the lattice deformation in a Au(111) single crystal following a short pulse laser heating has been measured with ~ 10 ps temporal resolution in X-ray diffraction experiments and related to the kinetics of the lattice temperature evolution in the surface region of the irradiated crystal [49]. Periodic oscillations of the diffraction peak positions have been recently probed with ~ 0.5 ps resolution in electron diffraction experiments and related to the elastic vibrations of a free standing Al film irradiated with a femtosecond laser pulse [15,16]. Similar oscillations of the diffraction peak positions have been observed in simulations of 200 fs pulse laser excitation of a Ni film at low fluences, below the threshold for laser melting [50]. A discussion of the implications of the computational predictions on the shifts and splittings of the diffraction peaks for interpretation of experimental results obtained for polycrystalline targets and a fixed angle of incidence of the probe beam to the target surface is given in Section 2.1.5.

2.1.4.4 Thermal effects

The decrease of the intensity of the diffraction peaks in the irradiated films can result from both structural changes and increasing thermal vibrations of the atoms. The latter contribution, related to the thermal smearing-out of the lattice planes, can be described by the Debye-Waller factor, e^{-2M} , which relates the decrease of the peak intensity to the temperature evolution in the system [35],

$$S(Q, t) - 1 = [S(Q, 0 \text{ ps}) - 1] \frac{\exp[-2M(T(t), Q)]}{\exp[-2M(T(0 \text{ ps}), Q)]} \quad (2.1.11)$$

The temperature dependence of the quantity M in the Debye-Waller factor can be expressed through the mean-square-displacement (MSD), $\langle u^2 \rangle$, of an atom vibrating around its equilibrium lattice position,

$$e^{-2M} = e^{-\frac{16\pi^2 \sin^2 \theta \langle u^2 \rangle}{3\lambda^2}} = e^{-\frac{\langle u^2 \rangle Q^2}{3}} \quad (2.1.12)$$

The MSD can be computed directly from atomic trajectories obtained in constant-volume MD simulations, performed for a range of temperatures corresponding to those measured in the simulations for laser excitation. The results of such calculations can be then used to predict the reduction of the peak heights in the laser excitation simulations due to the increase of the lattice temperature alone.

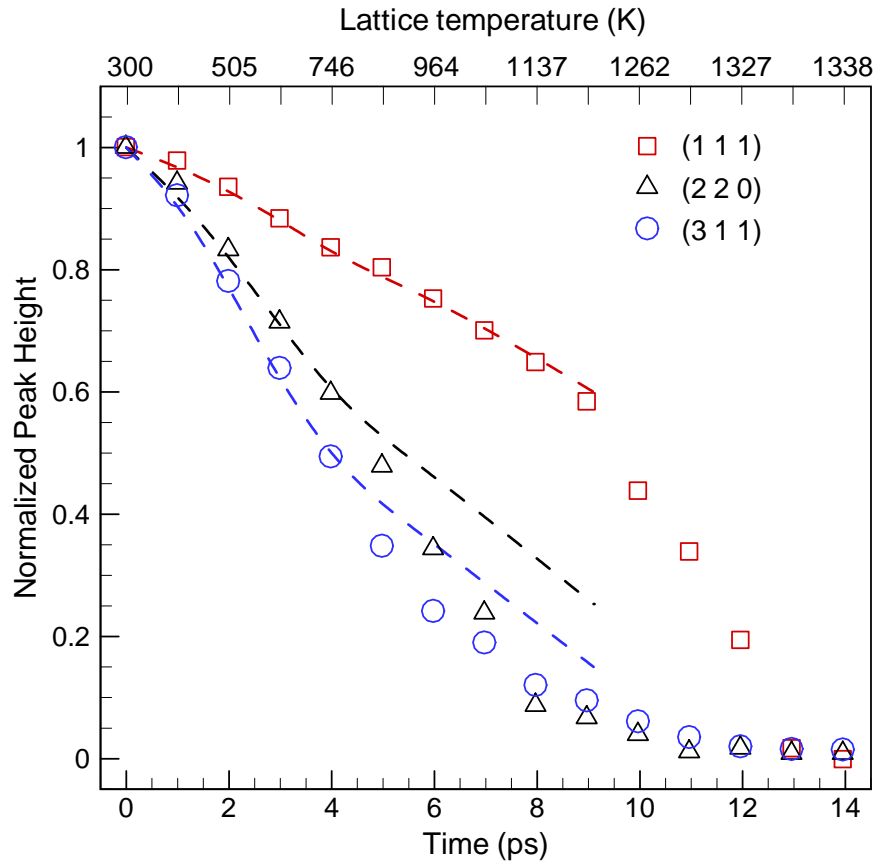


Figure 2-1-8. Normalized height of the (111), (220), (311) peaks as a function of time after irradiation of a 20 nm Au film with a 1 ps laser pulse at an absorbed fluence of 180 J/m². All peak heights are normalized to their values at 0 ps (T=300 K). Dotted lines are calculated through the Debye-Waller factor up to the equilibrium melting temperature of Au. The values of the average temperature of the film at different times after the laser pulse are shown in the additional top x-axis.

The results of the application of this approach to the simulation performed at an absorbed fluence of 180 J/m² are shown in Fig. 2-1-8 for (111), (220) and (311) diffraction peaks. To make the connection between the thermal effects described by Eqs. (2.1.11 and 12) and the laser excitation simulations, we first calculate the average

temperatures of the film at different times. The temperatures are then used to calculate the MSD and corresponding reduction of the peaks from the Debye-Waller factor, Eqs. (2.1.11 and 12). The results of the calculations are shown in Fig. 2-1-8 by dashed lines.

The heights of the peaks in the diffraction spectra calculated for the laser excitation simulation are shown in Fig. 2-1-8 up to 14 ps, whereas the results of the Debye-Waller calculations are shown up to 9 ps, the time when the average temperature of the film reaches $1.25T_m=1203$ K in the simulation of laser melting (above this temperature a fast homogeneous melting takes place within several picoseconds [19-21] and MSD for atomic vibration in a crystal cannot be obtained). There is a good agreement between the normalized peak heights and the Debye-Waller calculations up to ~ 4 ps, when the average lattice temperature is ~ 750 K. This agreement indicates that the observed reduction of the diffraction peaks during the first 4 ps is primarily due to the increased thermal vibration of the atoms. Starting from 5 ps, significant deviations from the Debye-Waller calculations can be observed for (220) and (311) peaks. As shown in Figs. 2-1-2, 3, and 4(a), the melting process starts only at ~ 10 ps in this simulation and the onset of the deviation of the peak intensities from the Debye-Waller calculations can be attributed to the uniaxial film expansion discussed in Section 2.1.4.3. As we can see from Fig. 2-1-3(b), the accumulated compressive pressure increases during the first picoseconds after the laser pulse and drives the expansion of the film. The expansion results in the distortion of the FCC lattice and associated tetragonal splitting of (202)/(022)-(220) and (311)/(131)-(113) peaks. The splitting is apparent in the structure function shown in Fig. 2-1-4(b) for 7 ps, and it starts to contribute to the decrease of the intensity of individual peaks from ~ 4.5 ps. The (111) peak does not split and the data

points are well described by the Debye-Waller calculations up to the onset of melting at about 9 ps, Fig. 2-1-8. During the melting process the (111) peak starts to overlap with a broad first peak characteristic of the liquid structure and the points for the (111) peak plotted in Fig. 2-1-8 for times starting from 10 ps correspond to the heights measured from the background level provided by the broad liquid peak of the structure function, Fig. 2-1-4. A sharp drop of the intensity of the (111) peak is observed during the melting process, from 10 to 14 ps.

Thus, we can conclude that the reduction of the diffraction peaks heights is mainly defined by the increasing lattice temperature (Debye-Waller factor) during the first several picoseconds following the laser excitation, when the film does not have time to expand and is “inertially confined” [22]. As the film expands in response to the laser-induced thermoelastic stresses, the peak splitting due to the uniaxial lattice deformations starts to contribute to the reduction of the peaks. Finally, during the melting process the reduction of the height of the diffraction peaks is dominated by the destruction of the crystal order.

A similar analysis of the effect of the increasing lattice temperature on the diffraction peak intensities measured in the time-resolved electron diffraction study of laser-driven melting of thin Al films is presented in Ref. [12]. The Debye equation and TTM are used in this work to predict the atomic mean square displacements and the temperature evolution, respectively. The conclusions from the analysis of the experimental data are in a good qualitative agreement with the computational results discussed above. The reduction of the diffraction peak heights initially follows the Debye-Waller calculation, with the onset of the deviations attributed to the loss of the

crystalline order. A much shorter, as compared to the simulations, time for the beginning of the melting process, 1.5 ps, can be explained by a much stronger electron-phonon coupling in Al as compared to Au. Indeed, in a simulation performed for an Al film at irradiation conditions comparable to the experimental ones, we obtain an excellent quantitative agreement in both the time of the onset of melting and the duration of the melting process, see Section 2.1.5.

2.1.4.5 Real space correlations

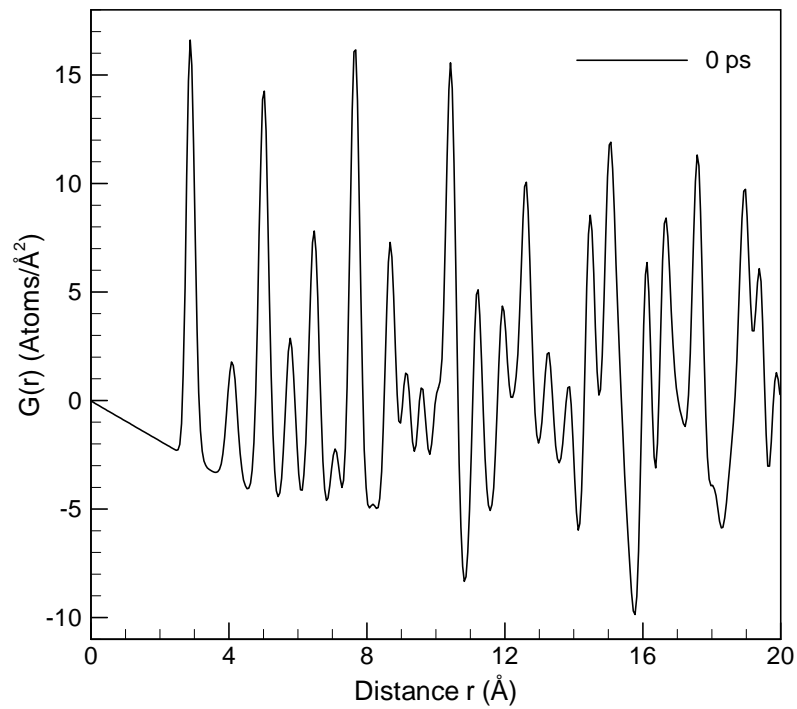
Structural changes during the laser-induced phase transformations can be further investigated by keeping track of the evolution of real-space correlation functions calculated for atomic configurations predicted in MD simulations. In particular, correlations in atomic positions can be expressed in the form of the reduced pair distribution function (PDF), $G(r)$, which describes the deviation of the pair density function $\rho(r)$, defined by Eq. (2.1.6), from the average density ρ_0 ,

$$G(r) = 4\pi r(\rho(r) - \rho_0) \quad (2.1.13)$$

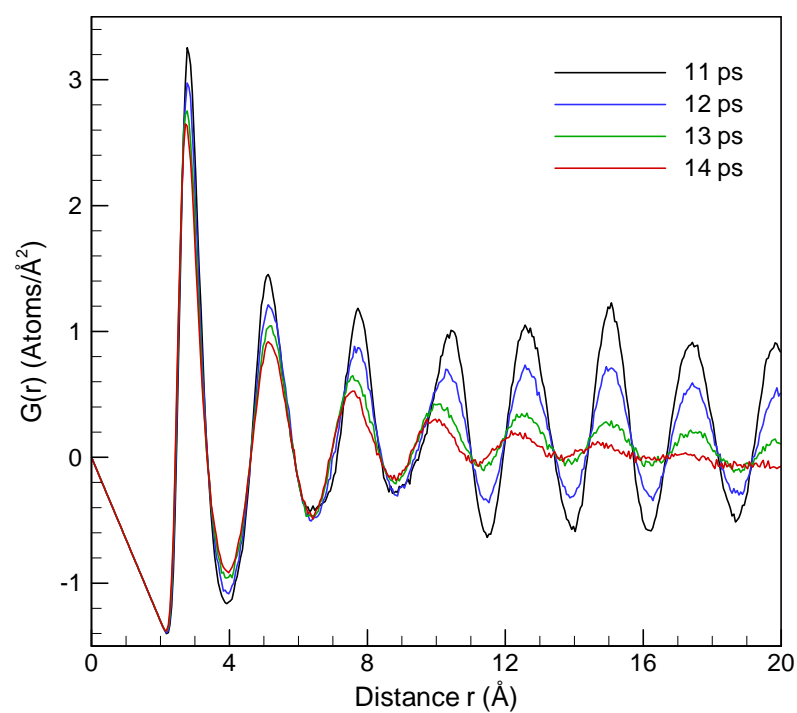
Experimentally, $G(r)$ can be calculated by the sine Fourier transform of the structure function $S(Q)$ and requires the ability to obtain the diffraction intensity of an adequate quality over a broad range of Q . This requirement presents a challenge for ultrafast time-resolved diffraction experiments that are often limited to the analysis of the diffraction signals obtained for fixed Bragg angles. The challenge of performing measurements for a range of scattering vectors can be met by increasing intensity of the X-ray or electron probes and accumulating the diffraction intensity over a large number of pulses

[11,12,14,15]. In simulations, both $\rho(r)$ and $G(r)$ can be calculated directly from atomic configurations, using Eqs. (2.1.6) and (2.1.13).

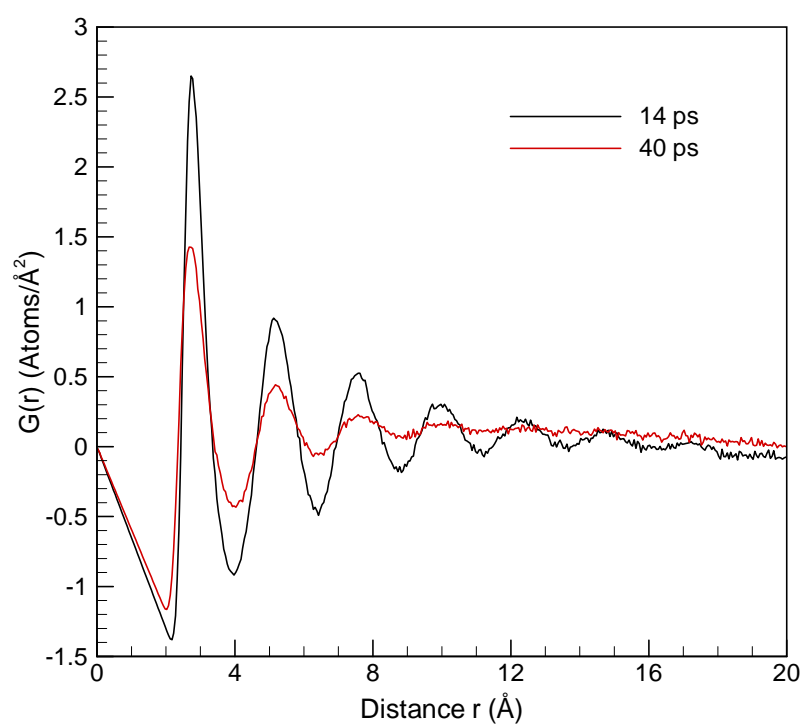
An important advantage of $G(r)$ is that its correlation peaks provide direct information on the structural coherence in the system. In real crystals, $G(r)$ obtained from diffraction experiments oscillate around zero with peak amplitudes gradually decreasing with increasing r due to the crystal imperfections and the finite resolution of Q value in the measurement [38]. For disordered (liquid or amorphous) structures, the amplitude of $G(r)$ oscillations decreases much faster, indicating the absence of the long-range order [51].



(a)



(b)



(c)

Figure 2-1-9. Reduced pair distribution function $G(r)$ computed for atomic configurations obtained in a simulation of a 20 nm Au film irradiated with a 200 fs laser pulse at an absorbed fluence of 180 J/m^2 at times of (a) 0 ps, (b) 11-14 ps, and (c) 14 and 40 ps.

In Fig. 2-1-9, the reduced pair distribution function $G(r)$ is presented for a simulation of a 20 nm Au film irradiated with a 200 fs laser pulse at an absorbed fluence of 180 J/m^2 . Before the laser excitation (0 ps), $G(r)$ exhibits the characteristic features of the FCC crystalline structure. Each peak in $G(r)$ corresponds to a specific interatomic distance between a pair of atoms in a perfect FCC structure. For example, the first peak in $G(r)$ matches the distance between the nearest neighbors (2.89 \AA) in an FCC crystal equilibrated at 300 K. Changes of $G(r)$ during the fast homogeneous melting (see Fig. 2-1-4) are shown in Fig. 2-1-9(b). By comparing $G(r)$ at 0 ps and 11 ps we can see that before the onset of melting the increasing lattice temperature results in a significant broadening of the correlation peaks and reduction of their intensities. Some of the peaks become completely obscured and merge with the neighboring ones, e. g. the peak corresponding to the 2nd neighbor shell cannot be identified in Fig. 2-1-9(b). The seeming “disappearance” of the correlation peaks before the onset of melting, however, does not correspond to any structural changes in the crystal but is just a consequence of the thermal broadening of all peaks, as demonstrated in the analysis presented at the end of this Section. Despite the broadening, the peaks at 11 ps remain well-defined for the range of interatomic distances considered in the calculation, confirming the presence of the long/medium-range crystalline ordering in the atomic configuration. Between the time of 11 ps and 14 ps the peaks in the high r region disappear, reflecting a complete

loss of the long-range order in the solid-to-liquid transition. The remained correlation peaks continue to broaden and diminish between the time of 14 ps and 40 ps, Fig. 2-1-9(c), indicating that there are still some substantial changes in the short/medium-range correlations in atomic positions. This observation suggests that within this period of time the liquid structure created after the collapse of crystalline state is still in a non-equilibrium state and retain some “memory” of the crystalline state [52]. The continuing increase of the lattice temperature (Fig. 2-1-3(a)) facilitates the destruction of the remaining medium-range ordering.

An alternative way of representing real space correlations in atomic positions is provided by the radial distribution function (RDF), $R(r)=4\pi r^2\rho(r)$, from which coordination numbers corresponding to different neighbor shells can be determined by calculating the surface areas under the corresponding correlation peaks. The surface area can be found by the integration of $R(r)$ with the integration limits corresponding to the local minima on the sides of the corresponding peak of RDF. The RDF obtained in a simulation performed for a 20 nm Au film irradiated by a 200 fs laser pulse at 180 J/m^2 is shown for 0 ps, 10 ps, and 20 ps after the laser pulse in Fig. 2-1-10. For 0 ps, the first and second coordination numbers corresponding to the first and second peaks of RDF are calculated to be 11.92 and 5.96. The values are less than the coordination numbers in a perfect FCC lattice, 12 and 6, due to the presence of the two free surfaces in our system, where atoms have a smaller number of neighbors. At 10 ps the first coordination number is determined to be 12.1 ± 0.4 with the error value related to the uncertainty in defining the local minima in Fig. 2-1-10. This result indicates that, in agreement with visual picture of atomic configuration at 10 ps in Fig. 4a, the local crystalline structure at this time is

still preserved and most atoms still maintain 12 nearest neighbors. By the time of 20 ps the first coordination number decreases down to 10.9 ± 0.4 , reflecting the destruction of the crystalline structure that is completed by this time, Fig. 2-1-4a. A similar decrease of the first coordination number from 12 to 10 during the laser-induced melting process has been deduced from time-resolved electron diffraction measurements reported in [11] for a 20 nm Al film.

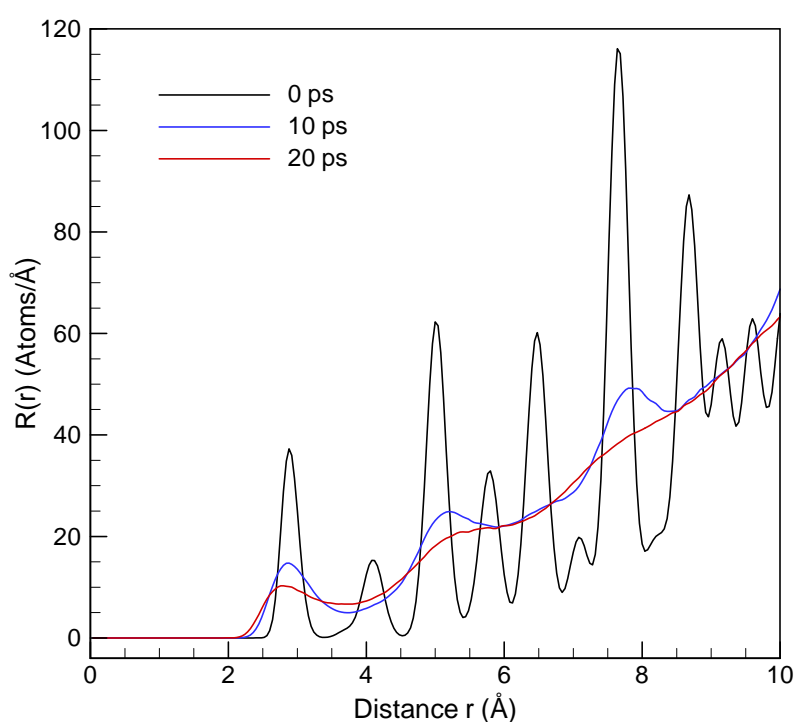
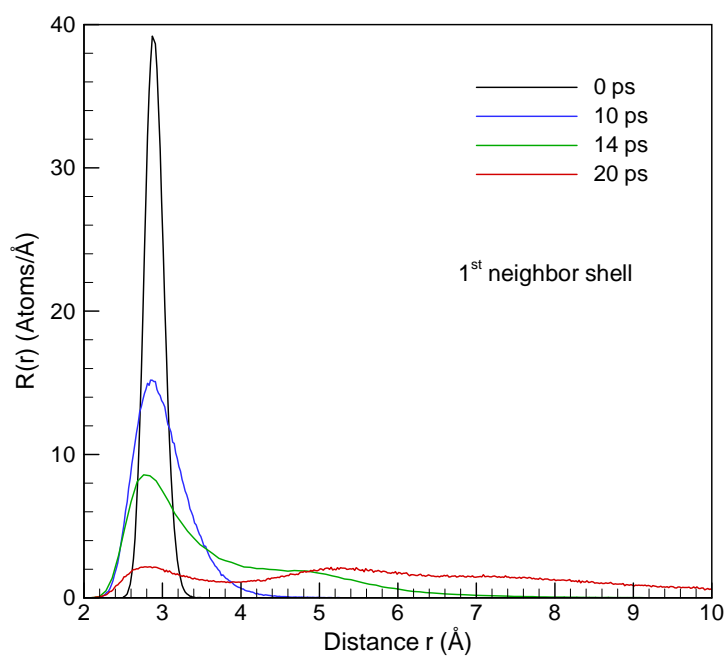
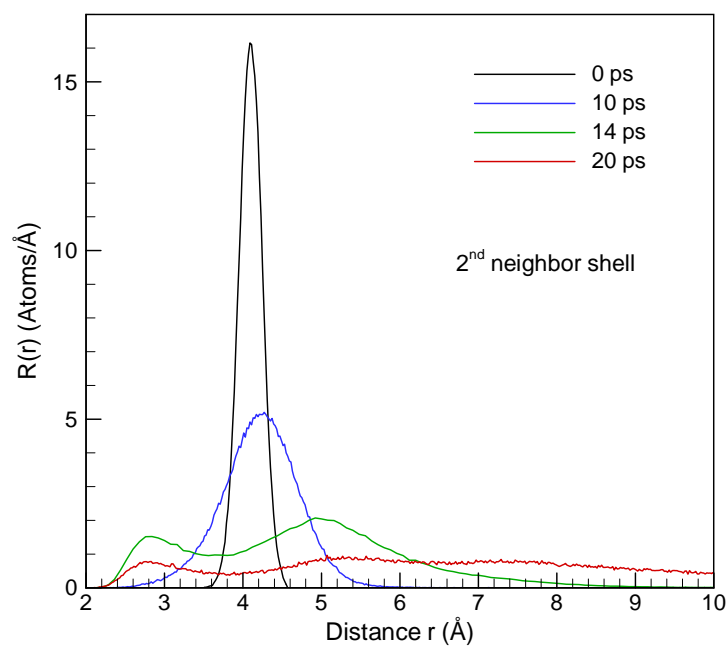


Figure 2-1-10. Radial distribution function $R(r)$ computed for atomic configurations obtained in a simulation of a 20 nm Au film irradiated with a 200 fs laser pulse at an absorbed fluence of 180 J/m^2 at times of 0 ps, 10 ps, and 20 ps. Coordination number N_c for the first coordination shell at $\sim 2.89 \text{ Å}$ can be obtained by integration of $R(r)$ between the two local minima on either side of the first peak.

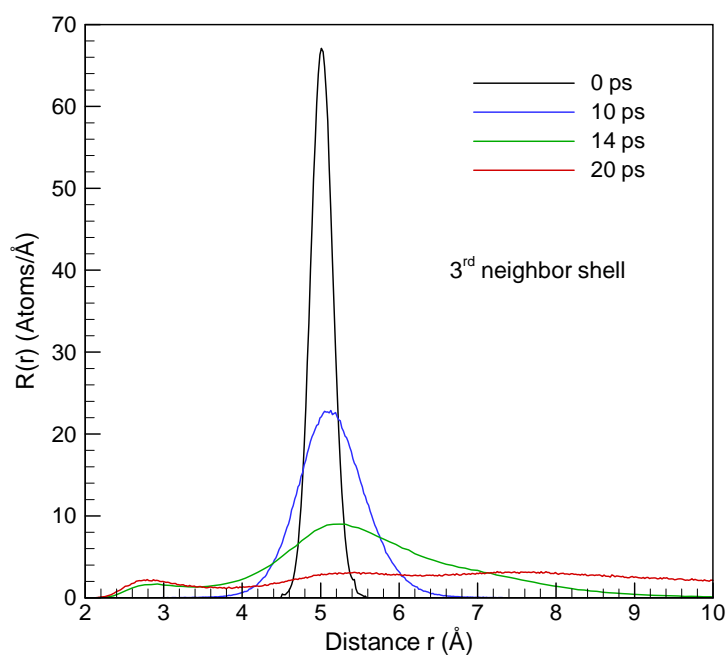
The output of MD simulations contains complete information on the atomic dynamics induced by laser excitation and allows for detailed investigation of the origin of the changes in the correlation functions discussed above and illustrated in Figs. 2-1-9 and 2-1-10. In particular, one question arises as to why the correlation peak corresponding to the second neighbor shell in the FCC structure, Fig. 2-1-9(a), completely disappears even before the onset of the melting process, e.g. plots for 11 ps and 10 ps in Fig. 2-1-9 and Fig. 2-1-10, respectively? To answer this question and to better understand other aspects of the evolution of the correlation functions, we trace the motions of the first-, second- and third-nearest neighbors of each atom in the original FCC lattice. By doing so, we decompose the RDF into separate contributions from the first three original coordination shells. The result of the decomposition, shown in Fig. 2-1-11, indicate that before 10 ps, on average, most atoms in the three coordination shells are still localized around their equilibrium positions. Significant broadening of all the peaks, however, completely obscures the contribution from the peak corresponding to the 2nd neighbor shell, Fig. 2-1-11(d), which shows itself only as a shoulder on the new second peak located at the position corresponding to the 3rd neighbor shell.



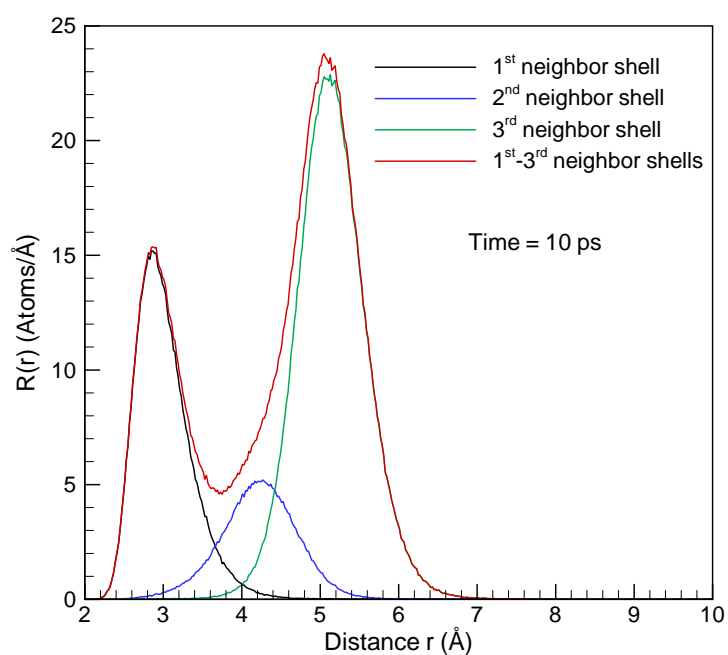
(a)



(b)



(c)



(d)

Figure 2-1-11. Decomposed radial distribution function $R(r)$ of (a) first coordination shell, (b) second coordination shell, (c) third coordination shell computed for atomic configurations obtained in a simulation of a 20 nm Au film irradiated with a 200 fs laser pulse at an absorbed fluence of 180 J/m^2 at times of 0 ps, 10 ps, 14 ps, and 20 ps. The

peaks are calculated for atoms that belong to the corresponding coordination shells at the time of 0 ps. The data of the three coordination shells and their sum at 10 ps are shown in (d).

After the collapse of crystalline order, atoms gain the freedom to diffuse around. For the first nearest neighbor shell, atoms can only move outwards, which leads to the long tail in the original first nearest shell contribution to RDF at 14 ps and 20 ps, Fig. 2-1-11(a). The gradual disappearance of the original peak can be explained by the high mobility of atoms in the liquid state, leading to the loss of the correlation between the positions of the nearest neighbors in the original FCC lattice. Similar gradual disappearance of the peak corresponding to the original third nearest neighbor shell is observed in Fig. 2-1-11(c), with some of the neighbors moving closer to the atoms of origin, others moving further away from them.

The evolution of the peak corresponding to the original second-nearest neighbor shell is rather different from the ones of the first and third peaks, Fig. 2-1-11(b). By the time of 14 ps the second FCC peak completely disappears, splitting its intensity between the two peaks present in the liquid state. The fast disappearance of the second peak, also observed in a recent time-resolved electron diffraction study [11], suggests that the interatomic distance corresponding to the second nearest neighbor shell in the FCC structure is not characteristic of the short-range order in the liquid structure. This interatomic distance appears in the octahedral atomic configuration characteristic of the close-packed crystals but is not typical for tetrahedral clusters responsible for the short-range order in one-component non-crystalline structures [53]. Thus, as soon as material melts, the atoms tend to escape from this interatomic distance – octahedral configurations

disappear and a broad second peak corresponding to the interatomic distances found in clusters with local tetrahedral and icosahedral short-range order [54,55] develops.

2.1.5 Conclusion and connections to experiments

Computational analysis of the structure function and pair distribution function, performed for transient atomic configurations generated in MD simulations of fast laser-induced phase transformations, provides a connection between the atomic-level structural rearrangements and changes in the diffraction profiles. The laser-induced evolution of the diffraction peaks is found to be defined by the combination of the following three factors: (1) increasing amplitude of atomic vibrations associated with the fast temperature rise, (2) peak splitting due to the uniaxial lattice deformations, and (3) destruction of the crystal order in the melting process. The contribution of the increasing thermal atomic vibrations dominates during the first several picoseconds after the laser pulse and can be well described by the Debye-Waller factor. The film expansion in response to the laser-induced thermoelastic stresses results in shifts and splittings of the diffraction peaks, providing an opportunity for experimental probing of the ultrafast deformations. Finally, the onset of the melting process results in further reduction the diffraction peaks due to the destruction of the crystal order.

Two of the three contributions to the reduction of the diffraction peak intensity discussed above have been observed in recent time-resolved electron diffraction experiments [11-13]. For a 20 nm Al film irradiated at an excitation fluence of 700 J/m^2 , the Debye-Waller calculations are found to be in a good agreement with experimental data for the first 1.5 ps, whereas further reduction of the height of the diffraction peaks has been attributed to the ultrafast melting that completes by the time of 3.5 ps after the

laser pulse. No shifts in the positions of the diffraction peaks and no splitting of the peaks have been observed in this study as well as in time-resolved X-ray diffraction investigations of even faster non-thermal melting processes [5,6]. The absence of the shifts and splittings of the diffraction peaks can be related to the condition of the inertial stress confinement [22,56], when the lattice heating and melting are taking place as constant volume processes. In the case of the thermal melting, the time of the lattice heating is defined by the laser pulse duration, τ_p , and the time of the electron-phonon equilibration, τ_{e-ph} , whichever is larger. The condition for the inertial stress confinement can be then formulated as $\max\{\tau_p, \tau_{e-ph}\} \leq \tau_s \sim d/C_s$, where d is the film thickness and C_s is the speed of sound in the film material. Due to the strong electron-phonon coupling in Al, the time of the electron-phonon equilibration (defined by the exponential fit of the time dependence of the energy transferred from the electrons to the lattice) is short, $\tau_{e-ph} \approx 1.5$ ps, and fast homogeneous melting takes place before any significant expansion of the film can take place. Indeed, the results of the simulations of laser melting of a 20 Al nm film performed for experimental conditions reported in [11] show an ultrafast melting process within the first 3-4 ps with no peak shifts and splittings observed in the diffraction spectra, Fig. 2-1-12. The time of the melting onset, 1.5 ps, the duration of melting process, and the evolution of the structure function are all in a very good quantitative agreement with experimental observations. In the case of even more rapid non-thermal melting occurring on a sub-picosecond time scale [5,6] there is no doubt that the destruction of the crystal order takes place before any expansion of the material can take place.

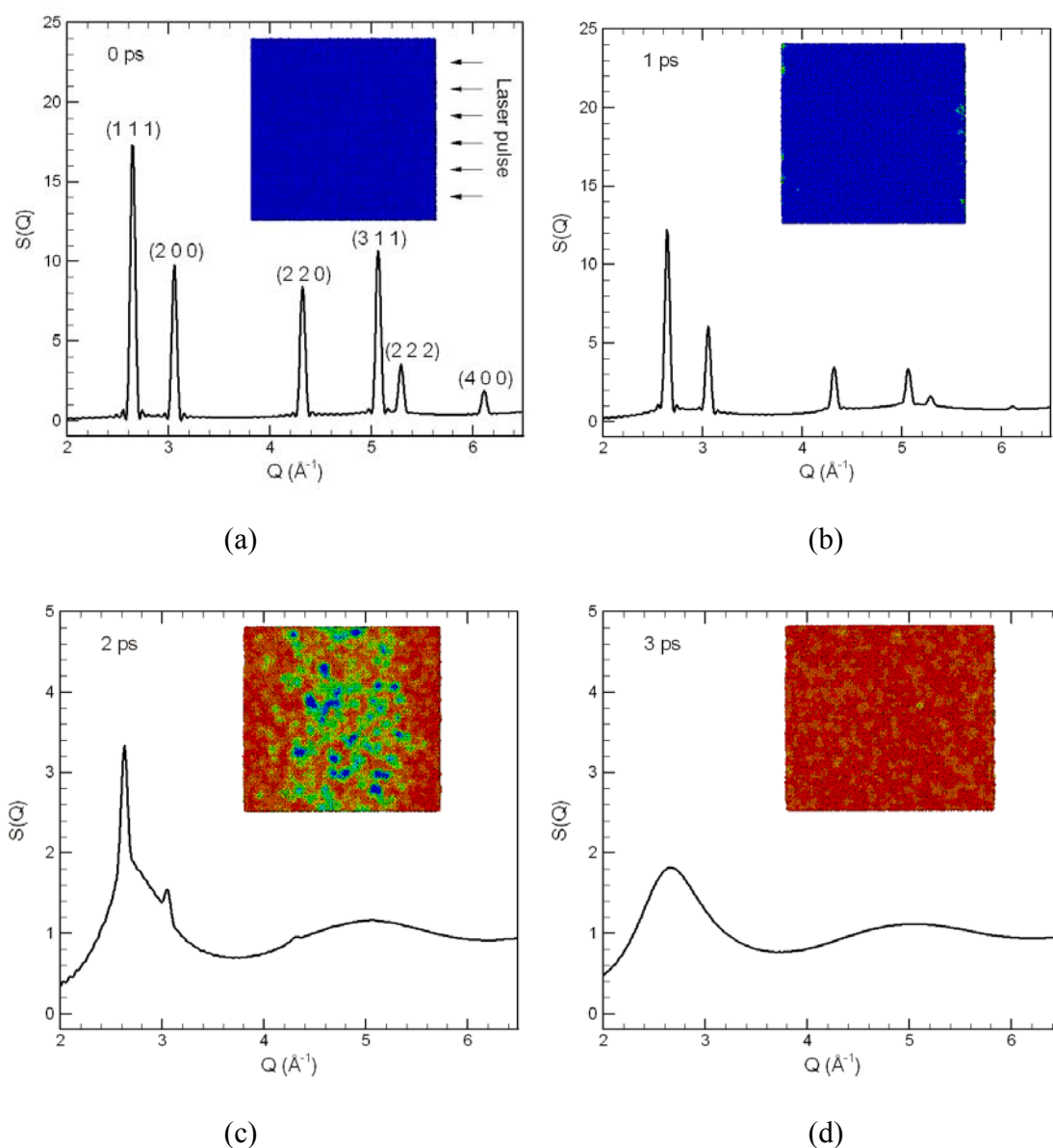


Figure 2-1-12. Structure functions calculated for atomic configurations obtained in a simulation of 20 nm Al film irradiated with 120 fs laser pulse at an absorbed fluence of 84 J/m^2 at times of (a) 0 ps, (b) 1 ps, (c) 2 ps, (d) 3 ps. Insets show the corresponding snapshots of the atomic configurations, with the direction of the laser pulse shown in (a). Atoms are colored according to the local order parameter (blue atoms have local crystalline surroundings; red atoms belong to the liquid phase). The irradiation

conditions are the same as in the experiment reported in Ref. [11] (incident fluence of 700 J/m^2 , reflectivity of 88%).

In the simulations reported in this section for Au films, a weak electron phonon coupling in Au leads to a relatively slow heating of the film, $\tau_{\text{e-ph}} \approx 15 \text{ ps}$, whereas the small thickness of the film allows for a fast relaxation of thermoelastic stresses with $\tau_s \approx 10 \text{ ps}$. Actually, due to the presence of two free surfaces, the relaxation of the initial compressive pressure in a freestanding film takes place at an even shorter time scale of $\sim 5 \text{ ps}$ and is defined by the propagation of the two unloading waves from the free surfaces of the film, Fig. 2-1-3(b). As a result, the uniaxial expansion of the film precedes the onset of the structural transformation, and shifts and splittings of the diffraction peaks are observed in all simulations performed for Au films.

A clear separation of the timescales for lattice heating and melting has been observed in the first time-resolved electron diffraction experiments performed for 20 nm Au films [13]. At an absorbed laser fluence of 119 J/m^2 , well above the threshold for the complete melting of the film, the melting starts at about 7 ps after the laser pulse and is completed in about 3 ps. While the duration of the melting process is in an excellent agreement with the results of our simulations, Fig. 2-1-2, the time of the melting onset is significantly shorter in the experiment as compared to the simulations, 7 ps in experiment vs. 17 ps in a simulation performed for comparable irradiation conditions. This quantitative discrepancy can be attributed to the assumption of the temperature-independent electron-phonon coupling constant used in this work. Indeed, recent calculations accounting for the temperature dependence of the electron-phonon coupling

[57] significantly increase the rate of the lattice heating and show a much better agreement with experimental results.

Note that the structure functions discussed in this section (Figs. 2-1-4-7, 12) are for single crystals and include the information on all the lattice plane systems present in the crystal. In polycrystalline samples different orientations of crystallographic planes will be affected in a different way by the uniaxial expansion of the film and the structure function would exhibit broadening of the peaks instead of the splitting. In experiments performed with a fixed angle of incidence of the probe beam to the target surface, only the lattice planes that have the correct Bragg angle with the probe beam contribute to the measured diffraction spectrum. Splitting of the peaks can only be observed experimentally if probing is done at different incidence angles, so that different orientations of the same system of lattice planes with respect to the direction of the uniaxial thermoelastic lattice expansion is probed. The maximum value of the peak shift is defined in this case not only by the extent of the film expansion but also by the orientation of the corresponding lattice planes with respect to the direction of the film expansion. The peak shift can be rather small if the planes having a small Bragg angle are probed in the transmission mode by an electron beam normal to the surface of the film [15,16]. Nevertheless, for a given direction of the probe beam, analysis of the peak shifts in time-resolved X-ray or electron diffraction experiments can provide valuable information on the characteristic time-scale of the lattice heating and thermoelastic deformation [15,16,49] as well as on the role of the uniaxial deformation in laser-induced phase transformations [20]. A discussion of the simulation results for Ni films, where periodic oscillations of the diffraction peak positions are observed under low-fluence

irradiation conditions (below the threshold for melting) and related to the laser-induced elastic vibrations of the film, is presented elsewhere [50].

The emerging time-resolved electron and X-ray diffraction probe experiments are opening new opportunities for investigation of atomic dynamics in the time and spatial domains accessible for direct atomistic simulations. The results of the simulations provide a direct link between the experimental observations and atomic-level structural changes in the irradiated material and help in interpretation of experimental data. In particular, the observed differences in the evolution of the diffraction profiles in the homogeneous and heterogeneous melting processes can, along with kinetics arguments, be instrumental in distinguishing between the two melting mechanisms. Shift and splitting of the diffraction peaks reflect the uniaxial thermoelastic lattice deformation of the film prior to melting and can be used for experimental probing of the laser-induced ultrafast deformations.

References for Chapter 2.1

- [1] C. Guo, G. Rodriguez, A. Lobad, and A. J. Taylor, Phys. Rev. Lett. **84**, 4493 (2000).
- [2] M. B. Agranat, S. I. Ashitkov, V. E. Fortov, A. V. Kirillin, A. V. Kostanovskii, S. I. Anisimov, and P. S. Kondratenko, Appl. Phys. A: Mater. Sci. Process. **69**, 637 (1999).
- [3] L. Huang, J. P. Callan, E. N. Glezer, and E. Mazur, Phys. Rev. Lett. **80**, 185 (1998).
- [4] O. P. Uteza, E. G. Gamaly, A. V. Rode, M. Samoc, and B. Luther-Davies, Phys.

Rev. B **70**, 054108 (2004).

- [5] A. Rousse, G. Rischel, S. Fourneaux, I. Uschmann, S. Sebban, G. Grillon, Ph. Balcou, E. Förster, J. P. Geindre, P. Audebert, J. C. Gauthier, and D. Hulin, *Nature (London)* **410**, 65 (2001).
- [6] A. M. Lindenberg, J. Larsson, K. Sokolowski-Tinten, K. J. Gaffney, C. Blome, O. Synnergren, J. Sheppard, C. Coleman, A. G. MacPhee, D. Weinstein, D. P. Lowney, T. K. Allison, T. Matthews, R. W. Falcone, A. L. Cavalieri, D. M. Fritz, S. H. Lee, P. H. Bucksbaum, D. A. Reis, J. Rudati, P. H. Fuoss, C. C. Kao, D. P. Siddons, R. Pahl, J. Als-Nielsen, S. Duesterer, R. Ischebeck, H. Schlarb, H. Schulte-Schrepping, Th. Tschentscher, J. Schneider, D. von der Linde, O. Hignette, F. Sette, H. N. Chapman, R. W. Lee, T. N. Hansen, S. Techert, J. S. Wark, M. Bergh, G. Hultdt, D. van der Spoel, N. Timneanu, J. Hajdu, R. A. Akre, E. Bong, P. Krejcik, J. Arthur, S. Brennan, K. Luening, J. B. Hastings, *Science* **308**, 392 (2005).
- [7] K. Sokolowski-Tinten, C. Blome, J. Blums, A. Cavalleri, C. Dietrich, A. Tarasevich, I. Uschmann, E. Förster, M. Kammler, M. Horn-von-Hoegen, and D. von der Linde, *Nature (London)* **422**, 287 (2003).
- [8] M. Harbst, T. N. Hansen, C. Coleman, W. K. Fullagar, P. Jönsson, P. Sondhauss, O. Synnergren, and J. Larsson, *Appl. Phys. A* **81**, 893 (2005).
- [9] W. E. King, G. H. Campbell, A. Frank, B. Reed, J. F. Schmerge, B. J. Siwick, B. C. Stuart, P. M. Weber, *J. Appl. Phys.* **97**, 111101 (2005).
- [10] S. Williamson, G. Mourou, and J. C. M. Li, *Phys. Rev. Lett.* **52**, 2364 (1984).
- [11] B. J. Siwick, J. R. Dwyer, R. E. Jordan, and R. J. D. Miller, *Science* **302**, 1382 (2003).
- [12] B. J. Siwick, J. R. Dwyer, R. E. Jordan, and R. J. D. Miller, *Chem. Phys.* **299**, 285 (2004).
- [13] J. R. Dwyer, C. T. Hebeisen, R. Ernstorfer, M. Harb, V. Deyirmenjian, R. E. Jordan, and R. J. D. Miller, *Philos. Trans. R. Soc. London*, in press (2006).

- [14] J. Cao, Z. Hao, H. Park, C. Tao, D. Kau, and L. Blaszczyk, *Appl. Phys. Lett.* **83**, 1044 (2003).
- [15] H. Park, S. Nie, X. Wang, R. Clinite, and J. Cao, *J. Phys. Chem. B* **109**, 13854 (2005).
- [16] H. Park, X. Wang, S. Nie, R. Clinite and J. Cao, *Solid State Commun.* **136**, 559 (2005).
- [17] H. O. Jeschke, M. E. Garcia, M. Lenzner, J. Bonse, J. Krüger, and W. Kautek, *Appl. Surf. Sci.* **197-198**, 839 (2002).
- [18] P. L. Silvestrelli, A. Alavi, M. Parrinello, and D. Frenkel, *Phys. Rev. B* **56**, 3806 (1997).
- [19] D. S. Ivanov and L. V. Zhigilei, *Phys. Rev. B* **68**, 064114 (2003).
- [20] D. S. Ivanov and L. V. Zhigilei, *Phys. Rev. Lett.* **91**, 105701 (2003).
- [21] L. V. Zhigilei, D. S. Ivanov, E. Leveugle, B. Sadigh, and E. M. Bringa, *Proc. SPIE* **5448**, 505 (2004).
- [22] E. Leveugle, D. S. Ivanov, and L. V. Zhigilei, *Appl. Phys. A* **79**, 1643 (2004).
- [23] L. V. Zhigilei, *Appl. Phys. A* **76**, 339 (2003).
- [24] L. V. Zhigilei, E. Leveugle, B. J. Garrison, Y. G. Yingling, and M. I. Zeifman, *Chem. Rev.* **103**, 321 (2003).
- [25] S. I. Anisimov, B. L. Kapeliovich, and T. L. Perel'man: *Zh. Eksp. Teor. Fiz.* **66**, 776 (1974) [*Sov. Phys. JETP* **39**, 375 (1974)].
- [26] J. Hohlfeld, S.-S. Wellershoff, J. Gudde, U. Conrad, V. Jahnke, and E. Matthias, *Chem. Phys.* **251**, 237 (2000).
- [27] J. Hohlfeld, J. G. Müller, S.-S. Wellershoff, and E. Matthias, *Appl. Phys. A: Mater. Sci. Process.* **64**, 387 (1997).
- [28] X. W. Zhou, H. N. G. Wadley, R. A. Johnson, D. J. Larson, N. Tabat, A. Cerezo, A. K. Petford-Long, G. D. W. Smith, P. H. Clifton, R. L. Martens, and T. F. Kelly, *Acta Mater.* **49**, 4005 (2001).

- [29] Smithell's Metal Reference Book, 6th edition, E. A. Brandes, ed. (London: Butterworths, 1983).
- [30] Y. S. Touloukian, *Thermophysical Properties of Matter, Vol. 4: Specific heat: metallic elements and alloys* (New York: IFI/Plenum, 1970).
- [31] Y. S. Touloukian, *Thermophysical Properties of Matter, Vol. 12: Thermal expansion: metallic elements and alloys* (New York: IFI/Plenum, 1975).
- [32] S. I. Anisimov and B. Rethfeld, *Proc. SPIE* **3093**, 192, 1997.
- [33] B. Rethfeld, A. Kaiser, M. Vicanek, G. Simon, *Phys. Rev. B* **65**, 214303 (2002)
- [34] N. W. Ashcroft and N. D. Mermin, *Solid State Physics* (Holt, Rinehart and Winston, New York, 1976)
- [35] B. E. Warren, *X-Ray Diffraction*, Addison-Wesley, Reading (1969).
- [36] J. M. Cowley, *Electron Diffraction Techniques*, Volume 1, Oxford Science Publications (1992).
- [37] Z. L. Wang, *Elastic and Inelastic Scattering in Electron Diffraction and Imaging* (Plenum Press, New York, 1995).
- [38] T. Egami and S. J. L. Billinge, *Underneath the Bragg Peaks. Structural analysis of complex material*, R. W. Cahn, Edt. (Pergamon Material Series), Elsevier, (2003).
- [39] P. M. Derlet, S. Van Petegem and H. Van Swygenhoven, *Phys. Rev. B* **71**, 024114 (2005).
- [40] R. Lovell, G. R. Mitchell, and A. H. Windle, *Acta Cryst.* **A35**, 598-603 (1979).
- [41] P. F. Peterson, E. S. Bozin, T. Proffen and S. J. L. Billinge, *J. Appl. Crystallogr.* **36**, 53 (2003).
- [42] G. Gutiérrez and B. Johansson, *Phys. Rev. B* **65**, 104202 (2002).
- [43] E. A. Lorch, *J. Phys. C: Solid State Phys.* **2**, 229 (1969).
- [44] K. Laaziri, S. Kycia, S. Roorda, M. Chicoine, J. L. Robertson, J. Wang and S. C. Moss, *Phys. Rev. B* **60**, 13520 (1999).

- [45] L. V. Zhigilei and D. S. Ivanov, Appl. Surf. Sci. **248**, 433 (2005).
- [46] K. A. Jackson, Interface Science **10**, 159 (2002).
- [47] B. Rethfeld, K. Sokolowski-Tinten, D. von der Linde, and S. I. Anisimov, Phys. Rev. B **65**, 092103 (2002).
- [48] T. M. Holden, J. H. Root, R. A. Holt, and M. Hayashi, Physica B **213**, 793 (1995).
- [49] P. Chen, I. V. Tomov, and P. M. Rentzepis, J. Chem. Phys. **104**, 10001 (1996).
- [50] Z. Lin and L. V. Zhigilei, J. Phys.: Conference Series, in press.
- [51] V. Petkov, S. J. L. Billinge, S. D. Shastri, B. Himmel, Phys. Rev. Lett. **85**, 3436 (2000).
- [52] Y. A. Bazin and B. A. Baum, Steel in Translation **26**, 43 (1996).
- [53] V. A. Likhachev, A. I. Mikhailin, and L. V. Zhigilei, Phil. Mag. A **69**, 421 (1994).
- [54] T. Schenk, D. Holland-Moritz, V. Simonet, R. Bellissent, and D. M. Herlach, Phys. Rev. Lett. **89**, 075507 (2002).
- [55] G. X. Li, Y. F. Liang, Z. G. Zhu, and C. S. Liu, J. Phys.: Condens. Matter **15** 2259 (2003).
- [56] G. Paltauf and P.E. Dyer, Chem. Rev. **103**, 487 (2003).
- [57] Z. Lin and L. V. Zhigilei, unpublished results.

2.2 Time-resolved diffraction profiles and structural dynamics of Ni film under short laser pulse irradiation

2.2.1 Introduction

Short (pico- and femtosecond) pulse laser irradiation has the ability to bring material into a highly non-equilibrium state and opens up a unique opportunity to study the transient atomic dynamics under extreme conditions that can hardly be achieved by any other means. Recent advances in time-resolved x-ray and electron diffraction pump-probe techniques provide new means to explore the ultrafast phase transformations, e.g. [1,2]. Atomistic simulations can serve as a bridge between the experimental observations and atomic-level structural changes in the irradiated material [3] and help in interpretation of experimental data. In this section, we report the results of molecular dynamic (MD) simulations of short pulse laser interactions with thin free-standing Ni films. The diffraction profiles are calculated from the transient atomic configurations obtained in the simulations. The evolution of the characteristic features of the diffraction profiles is related to the fast thermoelastic deformation and atomic-level dynamics of structural transformations revealed in the simulations.

2.2.2 Computational model: MD simulation setup and calculation of diffraction profiles

Simulations presented in this section are performed with a hybrid atomistic-continuum model combining classical MD method for simulation of nonequilibrium processes of lattice superheating and fast phase transformations with a continuum description of the laser excitation and subsequent relaxation of the conduction band

electrons [3]. Laser-induced atomic dynamics is investigated for a free-standing 21 nm Ni film irradiated with a 200 fs laser pulse at a range of absorbed fluences, from 100 J/m² to 300 J/m². The initial MD system is an FCC crystal composed of 864,000 Ni atoms with dimensions of 21.19×21.19×21.19 nm and periodic boundary conditions imposed in the directions parallel to two (001) free surfaces. The initial system is equilibrated at 300 K and zero pressure. The embedded-atom method in the functional form and parameterization suggested in Ref. [4] is used to describe the interatomic interaction in the MD part of the model. The properties of the EAM Ni material and the parameters used in the continuum part of the model are given in Ref. [3].

In order to calculate diffraction profiles from atomic configurations generated in MD simulations, we consider elastic scattering of a beam of X-ray photons or electrons on a sample consisting of N atoms. Following the well-known Debye scattering equation [5], one can substitute the summation over atomic pairs by the pair density function $\rho(r)$ and define the structure function $S(Q)$ [6] as

$$S(Q) = 1 + \int_0^{\infty} 4\pi r^2 \rho(r) \frac{\sin(Qr)}{Qr} dr, \quad (2.2.1)$$

where Q is the magnitude of the scattering vector. The pair density function $\rho(r)$ can be calculated from the atomic coordinates obtained in the simulations,

$$\rho(r) = \frac{1}{4\pi N r^2} \sum_{j=1}^N \sum_{i=1, i \neq j}^N \delta(r - r_{ij}), \quad (2.2.2)$$

where r_{ij} is the distance between atoms i and j and δ is the Dirac delta function. In order to reduce spurious ripples from the termination of the pair density function at a finite

distance R_{max} , a damping function $W(r) = \sin(\pi r / R_{max}) / (\pi r / R_{max})$ [7] is used in Equation (2.2.1), resulting in:

$$S(Q) = 1 + \int_0^{R_{max}} 4\pi r^2 \rho(r) \frac{\sin(Qr)}{Qr} W(r) dr, \quad (2.2.3)$$

where R_{max} is chosen to be half of the size of the simulation box. More detailed discussion of the effect of the finite size of the system and the termination ripples is given in Ref. [7].

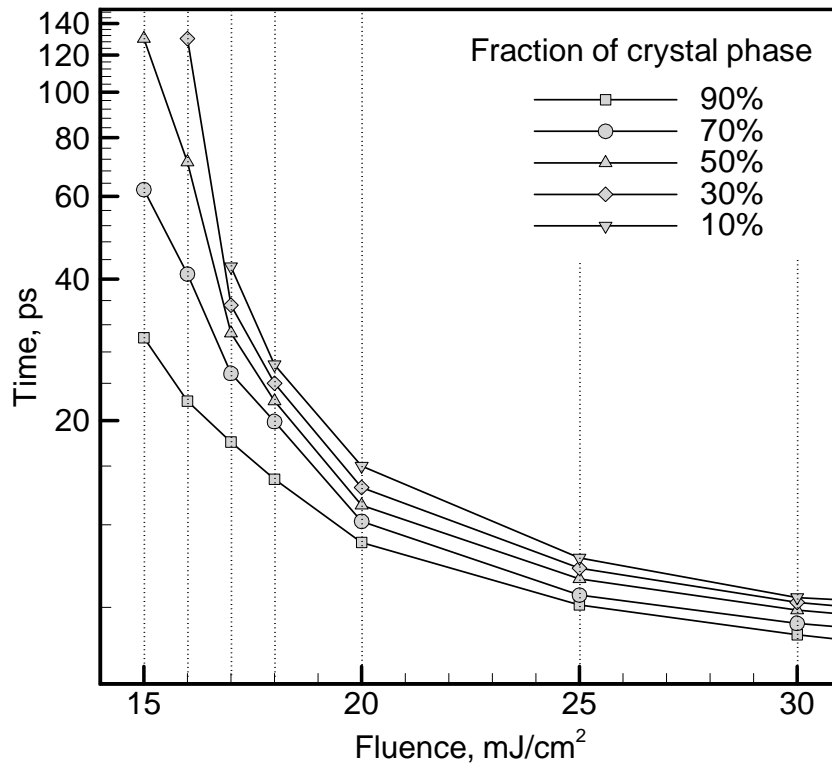


Figure 2-2-1. Semi-log plots showing the timescales of the melting process in a 21 nm Ni film irradiated with a 200 fs laser pulse at different absorbed fluences. Each curve corresponds to a certain fraction of the remaining crystal phase as a function of the absorbed fluence. For example, the curve with squares corresponds to the time after laser excitation when 90% of the atoms in the film belong to the crystal phase for different

laser fluences. The fraction of the crystal phase is determined by the number of atoms with local crystalline environment, as predicted by the local order parameter [3].

2.2.3 Results and discussion

Figure 2-2-1 shows the time evolution of the laser melting process predicted in the simulations of a 21 nm Ni film irradiated with a 200 fs laser pulse at absorbed fluences ranging from 150 J/m² to 300 J/m². Two distinct regimes can be easily identified: a high-fluence regime when the entire film melts within a few picoseconds, and a low-fluence regime when the melting starting time increases sharply with decreasing fluence and the melting process slows down significantly. It is found that in the high-fluence regime, above 200 J/m², homogeneous nucleation of liquid regions is observed throughout the film, whereas in the low-fluence regime, at and below 160 J/m² melting takes place only by propagation of melting fronts from free surfaces. The laser energy absorbed by the film in the low-fluence regime, at and below 160 J/m², is not sufficient for the complete melting the system and a partially melted film equilibrated at the melting temperature is observed at the end of the simulation.

In order to investigate the ultrafast structural transformation during the melting process in the high-fluence regime, we chose the result from the simulation performed at an absorbed fluence of 200 J/m². Figure 2-2-2 shows the results from the calculation of the structure functions at 0 ps, 12 ps, 15 ps and 20 ps after the laser pulse. It can be seen that before the laser excitation, the peaks of the structure function can be easily identified and associated with the Miller indices for FCC structure, Figure 2-2-2(a). By the time of 12 ps, however, the structure function has changed significantly, Figure 2-2-2(b). Although at this time about 77% of atoms still maintain their local crystalline

surroundings, the height of all the peaks have been largely reduced. This reduction can be only partially attributed to the increasing thermal vibrations of the atoms (Debye-Waller effect) [5,7], with an additional contribution coming from the onset of the structural changes (melting). In fact, by the time of 12 ps the energy transfer from the hot electrons to the lattice has lead to the lattice overheating by $\sim 14\%$ above the equilibrium melting temperature of the model Ni material. This overheating, combined with the uniaxial thermoelastic deformation of the film [8], is sufficient to induce the homogeneous nucleation of a large number of liquid regions inside the film, effectively destabilizing the lattice and reducing the long-range order throughout the film, as is apparent from the snapshot shown in Figure 2-2-2(b). The homogeneous nucleation and growth of the liquid regions leads to a fast melting of the entire film within several picoseconds. Although at 15 ps several crystalline regions can be still observed in the snapshot given in Figure 2-2-2(c), the structure function is close to the one at 20 ps, when the loss of crystalline order throughout the film is apparent.

An interesting observation from the analysis of the evolution of the structure function is the appearance of new peaks, such as the one indicated by the arrow in Figure 2-2-2(b). This peak first appears at 4 ps by splitting from the (200) peak and continues shifting to the left at later times. We find that the splitting of the peaks is a direct consequence of the uniaxial thermoelastic deformation of the film in response to the laser heating. Thermoelastic stresses generated by the fast heating of the lattice can only relax by the film expansion in the direction normal to the free surfaces of the film. The uniaxial deformation of the original FCC lattice along the (001) direction changes the space group symmetry of the lattice in a way that the cubic lattice transforms into the

tetragonal one. The new peak could be identified by the Miller indices as (002) that is distinct from the (200)/(020) peak in the Face Centered Tetragonal (FCT) lattice.

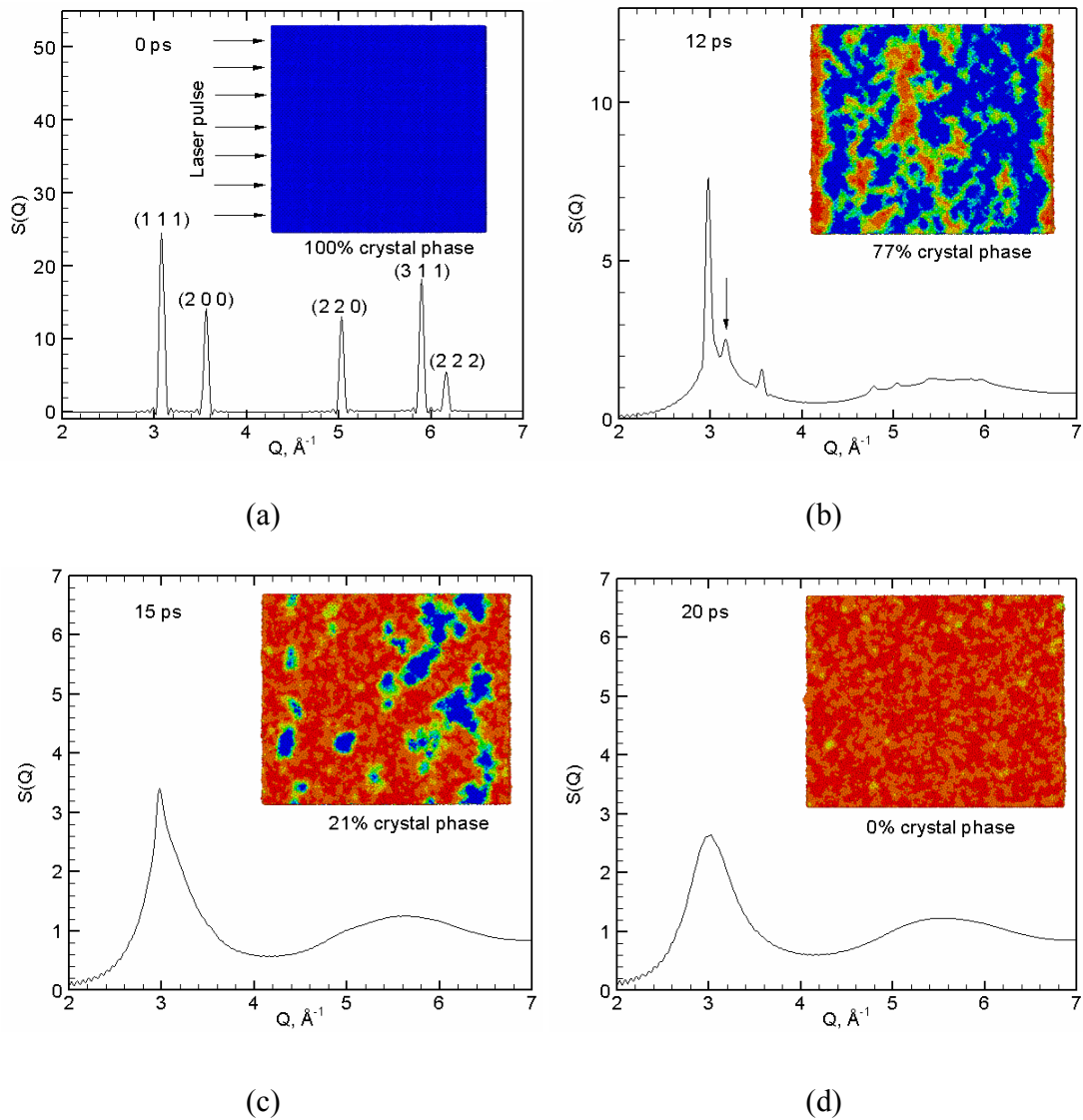


Figure 2-2-2. Structure functions calculated for atomic configurations obtained in a simulation of 21 nm Ni film irradiated with a 200 fs laser pulse at an absorbed fluence of 200 J/m^2 at (a) $t = 0$ ps, (b) $t = 12$ ps, (c) $t = 15$ ps, (d) $t = 20$ ps. Insets show the corresponding snapshots of the atomic configurations, with the direction of the laser

pulse shown in (a). Atoms are colored according to the local order parameter (blue atoms have local crystalline surroundings; red atoms belong to the liquid phase). The arrow in (b) points to the (002) peak that separates from the (200)/(020) peaks in the process of uniaxial expansion of the film in the direction normal to the free surfaces.

To further illustrate the effect of thermoelastic deformation on the structure function we used the results from a simulation performed at an absorbed fluence of 100 J/m^2 , at which no melting is observed. It can be seen that right after laser excitation, both (111) and (002) peaks shift to the left due to the uniaxial expansion of the film and reach the leftmost positions by the time of 8 ps. From the position of (002) peak, one can estimate the lattice deformation along (001) direction at 8 ps to be $\sim 4.5\%$, which is consistent with the direct measurement of the thickness of the film in the atomic-level snapshot. As the relaxation of the initial compressive stresses leads to the uniaxial expansion of the film, tensile stresses are generated in the middle part of the film, pulling the film back and decreasing the deformation of the lattice. As a result, both (111) and (002) peaks shift back to the right from 8 ps to 13 ps. The process repeats itself at later times as the elastic oscillation of the film continue with amplitude gradually decreasing due to the dissipation of the pressure wave trapped inside the film. Similar shifts/oscillations are observed for other peaks of the structure function with the maximum value of the peak displacement defined by the orientation of the corresponding lattice planes with respect to the direction of the film expansion.

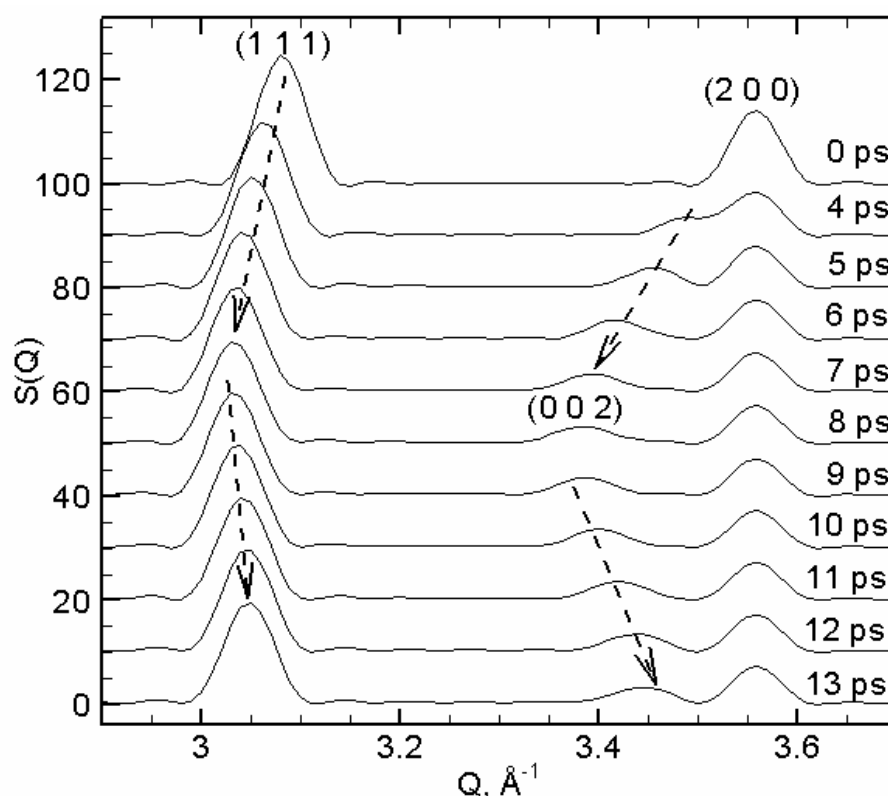


Figure 2-2-3. Structure functions calculated for 21 nm Ni film irradiated with a 200 fs laser pulse at an absorbed fluence of 100 J/m^2 . Curves are shifted with respect to each other in order to better illustrate the shift of the diffraction peaks, indicated by the arrows. Diffraction peaks are identified by the Miller indices as shown in the brackets.

Note that the structure functions plotted in Figures 2-2-2 and 2-2-3 include the information on all the lattice plane systems present in the crystal. In polycrystalline samples different orientations of crystallographic planes will be affected in a different way by the uniaxial expansion of the film and the structure function would exhibit broadening of the peaks instead of the splitting. In experiments performed with a fixed angle of incidence of the probe beam to the target surface, only the lattice planes that have the correct Bragg angle with the probe beam contribute to the measured diffraction

spectrum. Splitting of the peaks can only be observed experimentally if probing is done at different incidence angles, so that different orientations of the same system of lattice planes with respect to the direction of the thermoelastic lattice expansion is probed. Nevertheless, for a given direction of the probe beam, analysis of the peak shifts in time-resolved X-ray or electron diffraction experiments can provide valuable information on the characteristic time-scale of lattice heating and thermoelastic deformation as well as on the role of the uniaxial deformation in laser-induced phase transformations. Indeed, the evolution of the lattice deformation in a Au(111) single crystal following a short pulse laser heating has been measured with ~ 10 ps temporal resolution in X-ray diffraction experiments and related to the kinetics of the lattice temperature evolution in the surface region of the irradiated crystal [9]. Periodic oscillations of the diffraction peak positions have been recently probed with ~ 0.5 ps resolution in electron diffraction experiments performed for a free standing polycrystalline Al film irradiated with a femtosecond laser pulse [10,11]. The oscillations of the diffraction peak positions have the same origin as the ones shown in Figure 2-2-3, albeit the values of the maximum shifts are much smaller since the planes having a small Bragg angle are probed by an electron beam normal to the surface of the film.

2.2.4 Conclusions

The atomic-level dynamics of structural transformations in a thin Ni film irradiated by a short laser pulse are investigated in MD simulations and related to the evolution of the diffraction profiles. Fast disappearance of the diffraction peaks characteristic for the initial crystal structure is observed in the simulations performed at high laser fluences and is related to the homogeneous melting of the film. The melting

process takes only several picoseconds, in agreement with the results of recent time-resolved electron diffraction experiments [1]. Shifts and splittings of the diffraction peaks are found to reflect the transient uniaxial thermoelastic deformation of the film prior to melting, providing an opportunity for probing the ultrafast deformations in experiments [10,11].

References for Chapter 2.2

- [1] Siwick B J, Dwyer J R, Jordan R E and Miller R J D 2003 *Science* **302**, 1382
- [2] Lindenberg A M et al. 2005 *Science* **308**, 392
- [3] Ivanov D S and Zhigilei L V 2003 *Phys. Rev. B* **68**, 064114
- [4] Zhou X W et al 2001 *Acta Mater.* **49**, 4005
- [5] Warren B E 1969 *X-Ray Diffraction* (Reading: Addison-Wesley)
- [6] Egami T and Billinge S J L 2003 *Underneath the Bragg Peaks: Structural analysis of complex materials* (Amsterdam: Elsevier)
- [7] Lin Z and Zhigilei L V 2006 *Phys. Rev. B* **73**, 184113
- [8] Ivanov D S and Zhigilei L V 2003 *Phys. Rev. Lett.* **91**, 105701
- [9] Chen P, Tomov I V and Rentzepis P M 1996 *J. Chem. Phys.* **104**, 10001
- [10] Park H, Nie S, Wang X, Clinite R and Cao J 2005 *J. Phys. Chem. B* **109**, 13854
- [11] Park H, Wang X, Nie S, Clinite R and Cao J 2005 *Solid State Commun.* **136**, 559

2.3 Molecular Dynamic Simulation of Laser-induced Melting of Nanocrystalline Au

2.3.1 Introduction

Ultrafast laser interaction with materials has attracted intensive attention in both theoretical and experimental investigations owing to its importance for understanding the underlying fundamental science as well as its wide industrial applications. The complex character of the pressure and temperature evolution, as well as transient structural dynamics, induced by strong short pulse laser excitation of the target, however, make the investigation of these ultrafast phenomena challenging. While most of the experimental work has been done with polycrystalline, little attention has been given to the presence of grain boundaries in computational studies of laser-materials interactions. In particular, the effect of the existence of grain boundaries on the mechanisms of laser melting remains unclear.

The molecular dynamic (MD) method provides a powerful tool for studying the microstructural changes at the atomic level and can help in a reliable interpretation of the experimental observations. MD method has been widely applied for investigations of the physical properties of nanosized materials at different pressure/temperature conditions. For example, grain growth kinetics has been investigated by Farkas et al. [1] for nanocrystalline Ni. Upon heat treatment, the average grain size of the nanocrystal is shown to linearly increase with time due to a size-dependent mobility of the grain boundaries. Recent MD study of the melting behavior of nanocrystalline Ag in Refs. [2,3]

also suggests that melting of nanocrystals starts from the grain boundaries at a temperature that is below the equilibrium melting temperature of the material.

In this chapter, we present the results of MD simulations of ultrashort pulse laser melting of a thin Au nanocrystalline film. Computational model used in MD simulations of laser melting of metal films is briefly described next, in Section 2.3.2. The microscopic picture of the melting process in nanocrystalline films irradiated by a short laser pulse is discussed and related to the predictions of the classical nucleation theory in Section 2.3.3. A brief summary is given in Section 2.3.4.

2.3.2 Computational setup for simulations of laser interaction with Au nanocrystalline films

MD simulations of short pulse laser interaction with a 20 nm freestanding Au nanocrystalline film are performed with a combined atomistic-continuum model that couples the classical MD method for simulation of non-equilibrium processes of lattice superheating, deformation, and melting, with a continuum-level description of the laser excitation and subsequent relaxation of conduction band electrons. The hybrid model is based on the well-known two-temperature model (TTM) [4] that has been widely used for describing the time evolution of the lattice and electron temperatures in the irradiated target by two coupled non-linear differential equations. In the combined TTM-MD method, Newton's equations of motion from MD substitute the TTM equation for the lattice temperature while the other TTM equation for the electron temperature is numerically solved by a finite difference method simultaneously with MD integration of the equations of motion of atoms. To account for the energy exchange between the

electrons and the lattice systems an energy coupling term is added to the MD equations of motion. A complete description of the combined TTM-MD model is given in Ref. [5].

The initial MD system of a 20 nm nanocrystalline Au film in this study is created by the Voronoi construction method [6,7,8,9]. Briefly, the system is created as follows: first a number of grain centers are generated randomly within the MD cell. The part of space closer to a given grain center than to any other centers is then filled with atoms in a randomly oriented face-centered-cubic (FCC) lattice. In regions close to the grain boundaries it is possible that, after the Voronoi construction, some of the atoms that belong to different grains are too close to each other, leading to unrealistically high configuration energy. Therefore, we remove one atom from each atom pair that has an inter-atomic distance less than 80% of the FCC nearest-neighbor distance. In addition, the system is equilibrated at 300 K for a period of 50 ps in order to relax the structure after the Voronoi construction. The density of the final configuration is ~99.2% of the bulk density of gold. This procedure constructs a system with random grain orientations containing no textures. Effects of texture could be incorporated by introducing preferred grain orientations. The atomic configuration used in this study consists of 31 grains with an average grain diameter of ~8 nm that is calculated by assuming a spherical shape for the grains. The code implementing the generation of nanocrystalline system is created by Dr. Elodie Leveugle (UVa) and Dr. Eduardo Bringa (LLNL) and modified by the author of this dissertation. The inset of Fig. 2-3-1 shows the grain size distribution of the nanocrystalline sample. It is known that for a large number of grains, the Voronoi construction will generate a grain-size distribution close to a log-normal distribution [10]. The total number of Au atoms in the system is ~500, 000. The dimensions of the

computational cell are $20.4 \times 20.4 \times 20.4 \text{ nm}^3$ and the periodic boundary conditions (PBC) are imposed in the directions parallel to two free surfaces. The periodic boundary conditions simulate the condition that the size of the laser spot is sufficiently large so that the energy redistribution in the lateral directions, parallel to the free surfaces of the film, can be neglected on the time-scale considered in the simulations.

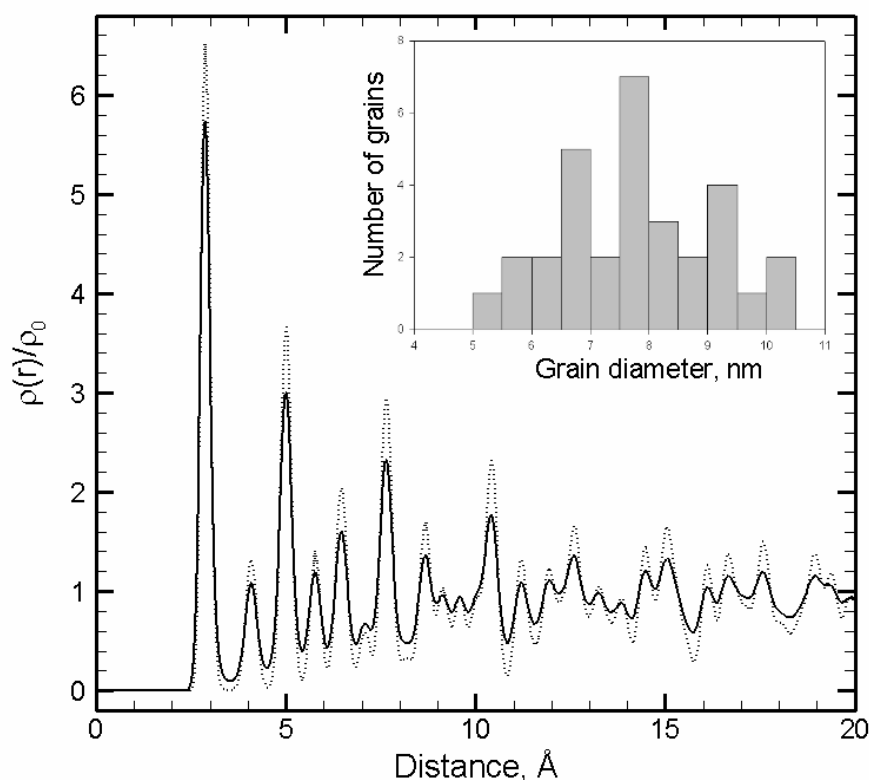


Figure 2-3-1. Comparison of the pair density functions (PDF) of nanocrystalline (solid line) and single crystal (dotted line) Au films with a thickness of ~20 nm equilibrated at 300 K. The values of the PDF are normalized by the average density of the sample. The inset shows the distribution of the grain sizes for the sample with a mean grain diameter of 8 nm.

The pair density function (PDF) of the nanocrystalline Au film at 300 K is shown in Fig. 2-3-1, along with the one for a single crystal Au film. The comparison between the two PDFs suggests that, due to the presence of the grain boundaries, the percentage of atoms with a perfect FCC atomic configuration in the system is reduced, resulting in the decrease in the intensity of all correlation peaks at characteristic interatomic distances that correspond to FCC neighbors. In addition, Fig. 2-3-1 shows an increase of the intensity of PDF for the nanocrystalline film at regions between the peaks, indicating that atoms in the regions of the grain boundaries are not in FCC local structure. It should be noted that there is no change in the widths of the PDF peaks in both PDFs, which are related to the thermal vibration of the atoms, i.e. the Debye-Waller factor at 300 K [11].

The interatomic interaction in the MD part of the model is described by the embedded atom method (EAM) with the functional form and parameterization suggested in Ref. [12]. The EAM potential defines all the thermal and elastic properties of the material. Some of the physical properties of the EAM Au relevant to the material response to the laser heating are shown in Ref. [13], along with corresponding values of experimental data for Au. There are some quantitative deviations of the physical properties of EAM values from the experimental ones. For instance, the melting temperature of EAM Au is found to be 963 K from the solid-liquid coexistence simulation, while the experimental value is 1336 K. However, these deviations should not affect the discussions of the underlying physical mechanisms of the melting process. The parameters of gold used in the TTM equation for the electron temperature are listed as follows. The electronic heat capacity is $C_e = \gamma T_e$ with $\gamma = 71 \text{ Jm}^{-3}\text{K}^{-2}$, the electron-phonon coupling constant which describes the strength of the energy exchange between

the electrons and the lattice, is chosen as $G = 2.1 \times 10^{16} \text{ Wm}^{-3}\text{K}^{-1}$, and the dependence of the electron thermal conductivity on the electron and lattice temperatures is described by an expression suggested in Ref. [14]. It has been shown in Ref. [15] that due to the thermal excitation of 5d band electrons in gold the electron-phonon coupling of gold exhibits a temperature dependent behavior at electron temperatures higher than $\sim 3000 \text{ K}$, while the electron heat capacity could deviate from the commonly used linear dependence on the electron temperature. In addition, the electron-phonon scattering processes at the grain boundaries could differ from those in perfect FCC regions due to the variation of the electronic structure which might leads to a change of the electron-phonon coupling. Experimental measurements of the electron-phonon coupling for Au polycrystalline films give values in a range of $3.6\text{-}5.0 \times 10^{16} \text{ Wm}^{-3}\text{K}^{-1}$ for grain diameters of 27-45 nm [16]. Since the investigation of the electron-phonon coupling at different types of grain boundaries is out of scope of the current study, a constant value, $2.1 \times 10^{16} \text{ Wm}^{-3}\text{K}^{-1}$, from Ref. [17] is chosen for the electron-phonon coupling for Au in this initial study of laser interaction with nanocrystalline Au films.

2.3.3 Results and discussion

A. Mechanisms and Kinetics of Laser-induced Melting

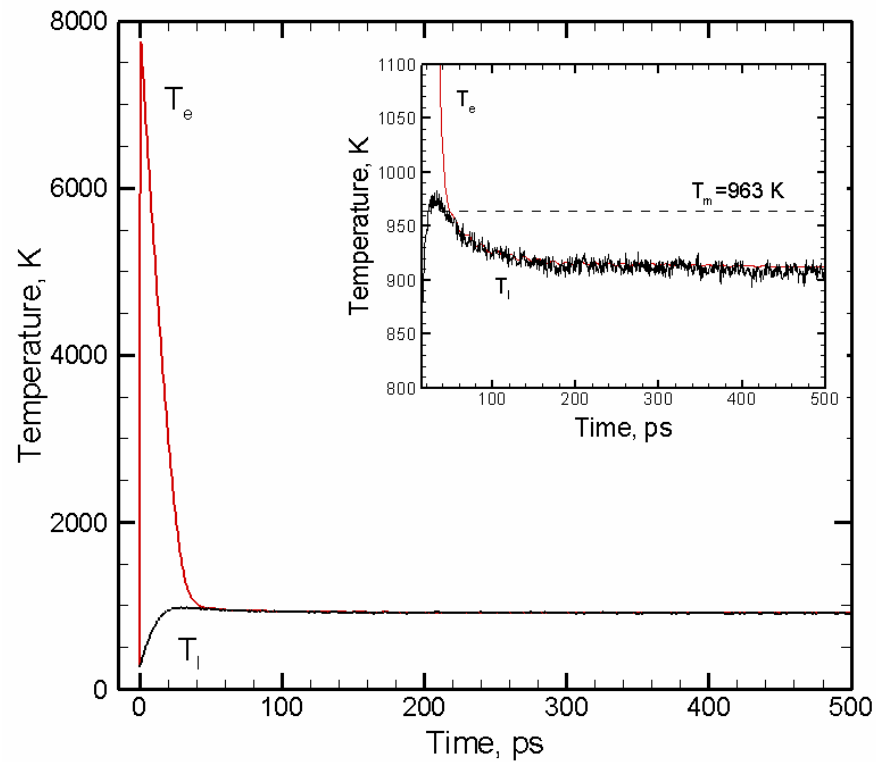
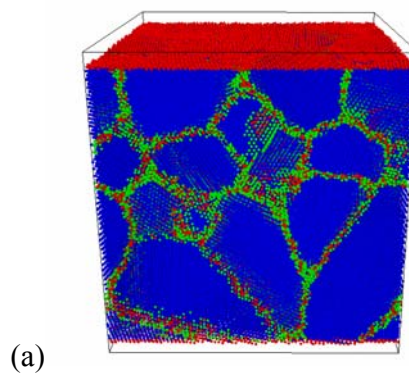


Figure 2-3-2. Temporal evolutions of the electron (red) and lattice (black) temperature, T_e and T_l , obtained in TTM-MD simulations of a nanocrystalline Au film irradiated by a 200 fs laser pulse at an absorbed fluence of 45 J/m^2 . The inset shows the same plot with a closer view of the evolution of the lattice temperature. The dashed line indicates the equilibrium melting temperature of EAM Au, 963 K.

Fig. 2-3-2 shows the temporal evolution of the electron and lattice temperature obtained in a TTM-MD simulation of a nanocrystalline Au film irradiated by a 200 fs laser pulse at an absorbed fluence of 45 J/m^2 . For Au, it is known that the ballistic energy transport defines the effective laser energy deposition depth which is estimated to be on the order of 100 nm [18], which is much larger the thickness of the nanocrystalline Au

film used in this work, ~ 20 nm. The reflection of the ballistic electrons at the back surface of the film should lead to a uniform distribution of the electron temperature throughout the film on the timescale of the electron thermalization. Therefore, the energy transfer from the hot electrons to the lattice results in a uniform heating of the lattice. In Fig. 2-3-2, the electron and lattice temperatures averaged over the film are shown up to 500 ps after the laser irradiation. Due to the small electron heat capacity, the laser irradiation transiently brings the electron temperature up to ~ 8000 K while the lattice temperature remains close to room temperature. The subsequent energy transfer between hot electrons and cold lattice leads to the sharp decrease in the electron temperature and gradual increase of the lattice temperature. The lattice temperature in the film is found to increase from 300 K to the maximum value of ~ 980 K at 30 ps as a result of the energy exchange. At a later time, the melting occurring in the film results in the decrease of the lattice temperature due to the transformation of a part of the thermal energy to the latent heat of melting. The lattice temperature gradually saturates to a value of ~ 913 K, as shown in the inset of Fig. 2-3-2, below the equilibrium melting temperature for EAM Au, 963 K.



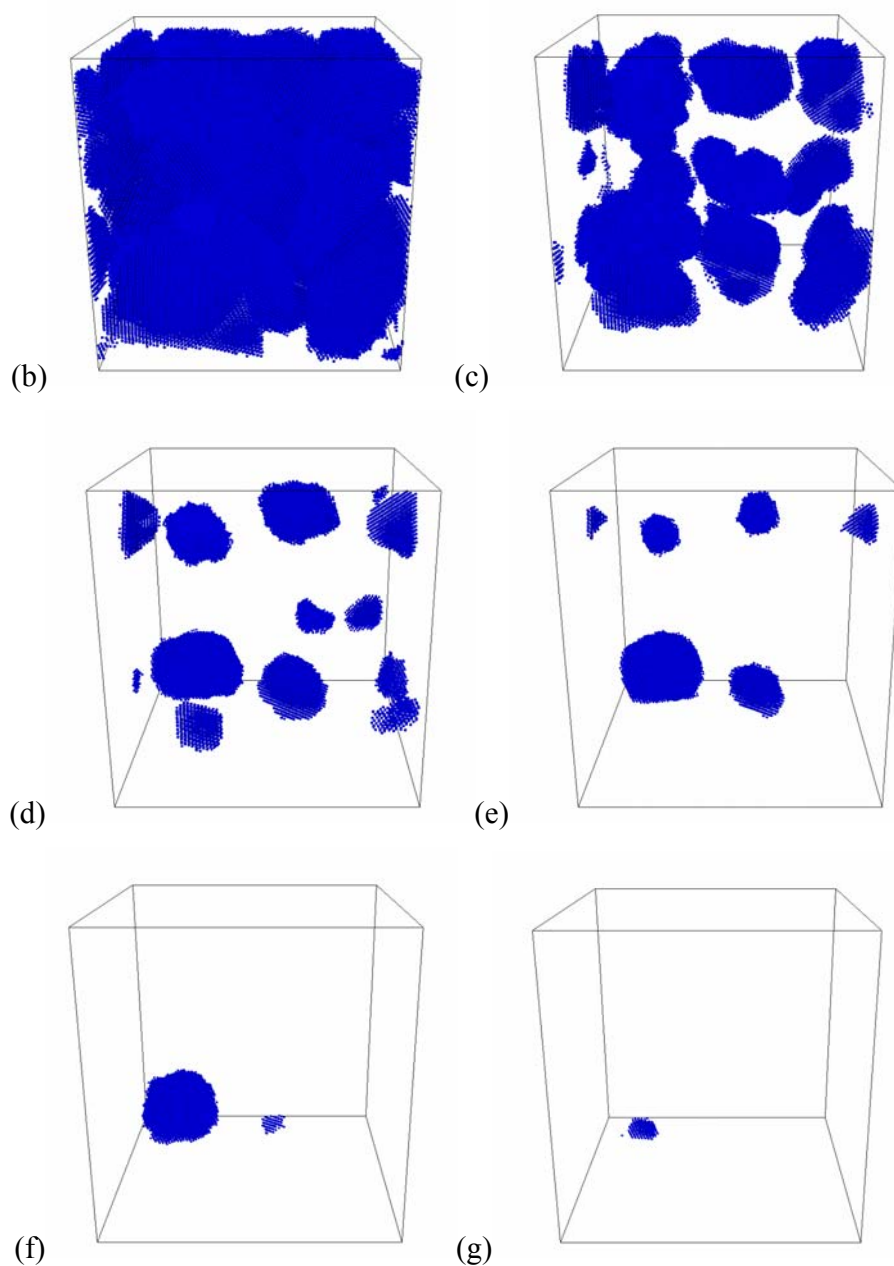


Figure 2-3-3. Snapshots of atomic configurations during the melting process in a 20 nm nanocrystalline Au film irradiated with a 200 fs laser pulse at an absorbed fluence of 45 J /m² shown for times of (a) 0 ps, (b) 20 ps, (c) 50 ps, (d) 100 ps, (e) 150 ps, (f) 200 ps, (g) 500 ps. Atoms are colored by the centrosymmetry parameter. Blue corresponds to solid atoms, red and green correspond to atoms at the surface or the grain boundary. For

clarity, only solid atoms are shown in blue color in (b)-(g) with atoms that belong to the liquid phase blanked. The atomic configurations are quenched, so that the kinetic energy of the system is removed quickly for an easy identification of the local atomic structure.

The snapshots of the atomic configurations during the melting process in the nanocrystalline film are shown in Fig. 2-3-3. The atoms are colored by the centrosymmetry parameter [19]: $\Phi = \sum_{i=1}^6 \left| \vec{R}_i + \vec{R}_{-i} \right|^2$, where \vec{R}_i and \vec{R}_{-i} are the a pair of vectors that connect the atom of interest to its opposite nearest neighbors in the FCC lattice. For FCC lattice, there are six pairs of these nearest neighbors. The value of the centrosymmetry parameter gives a measure of the deviation of the local atomic environment of a particular atom away from the FCC centrosymmetry. For reference, the centrosymmetry parameter is zero for atoms with a perfect FCC surrounding. For liquid atoms, as well as atoms close to grain boundaries, the parameter is well above zero due to the disordered/defected structure. Therefore, we can use this parameter for distinguishing the ordered and disordered/defected regions in the atomic configuration. To avoid the contribution coming from thermal motion of atoms to the values of the centrosymmetry parameter, the atomic configurations obtained from the TTM-MD simulation are quenched for a period of 2 ps to quickly remove the kinetic energy of the system. During these quenching simulations, an atom is allowed to relax only to its local energy minimum, while most of the kinetic energy of the system is removed. The short time of the quenching procedure ensures that the transient structure of the system is captured by the structural analysis based on the centrosymmetry parameter.

The visualization of the atomic configurations obtained in the simulations is shown in Fig. 2-3-3, suggesting that the melting process in the nanocrystalline film is different from the melting in single crystalline films at the same fluence, 45 J/m^2 (see Chapter 2 and Ref. [13]). For the single crystalline film, a partial melting of $\sim 50\%$ of the film proceeds by the propagation of two melting fronts from the free surfaces of the film [13]. As shown in Fig. 2-3-3(e), in the case of nanocrystalline film, small solid clusters still remain close to the free surfaces at $\sim 150 \text{ ps}$, suggesting that the propagation of the melting fronts from two free surfaces contributes little to the overall melting process of the film. This observation indicates that the melting initiated at grain boundaries is responsible for the decrease of the number of solid atoms in the film, shown in Fig. 2-3-4. At 0 ps , the percentage of the atoms in the film that have a local FCC surrounding is $\sim 63\%$, owing to the presence of the grain boundaries and two free surfaces. By $\sim 20 \text{ ps}$ after the laser excitation, this percentage only slightly decreases as the lattice temperature increases up to 943 K . However, as the lattice temperature increase further beyond $\sim 20 \text{ ps}$, the percentage of crystalline atoms in the system decrease drastically from $\sim 60\%$ down to $\sim 20\%$ at 50 ps , and 5% at 100 ps . The rapid decrease in the number of the solid atoms in the film reflects the fast melting process. As shown in the snapshots, after 50 ps the individual nanocrystalline grains, formed as a result of the initial melting of grain boundary regions, continue to shrink. Therefore, the melting process after $\sim 100 \text{ ps}$ could be regarded as melting of these remaining solid clusters surrounded by the liquid. Further discussions of the conditions leading to the melting of small solid clusters in a liquid environment will be provided within the framework of classical nucleation theory (CNT) will be given in the next section.

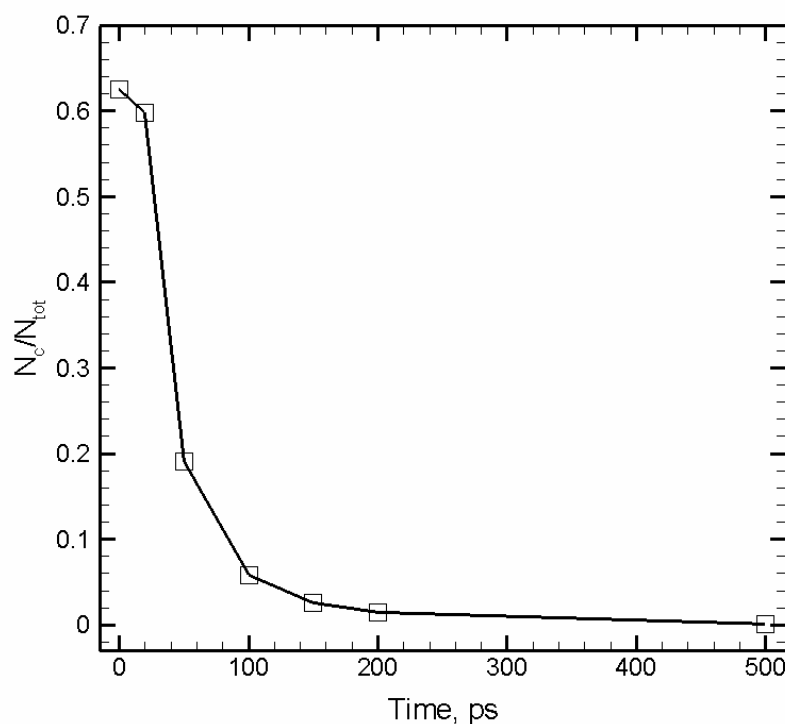
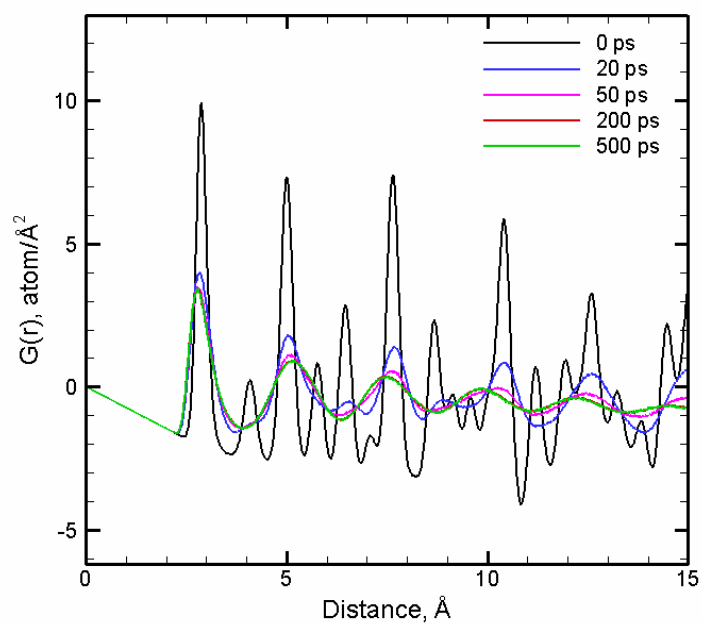


Figure 2-3-4. The time evolution of the number of the FCC atoms in a 20 nm nanocrystalline Au film irradiated with a 200 fs laser pulse at an absorbed fluence of 45 J /m². The solid atoms are identified by the centrosymmetry parameter ($\Phi < 0.01$).

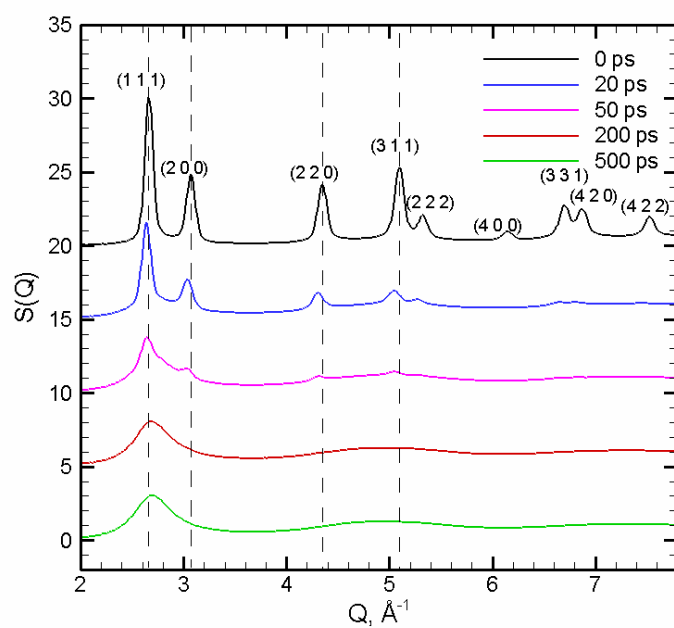
The structural changes in the nanocrystalline film irradiated with an ultrashort laser pulse could be further investigated through examination of the evolution of the real space correlation function, and the structure function calculated directly from the transient atomic configurations generated by MD simulations. The evolution of the reduced pair distribution function $G(r)$ and the corresponding structure function $S(Q)$ during the laser-induced melting process of the nanocrystalline film is shown in Fig. 2-3-5. The well-defined peaks in $G(r)$ at 0 ps reflect the existence of correlations in atomic positions in the nanocrystal extending beyond 15 Å. At 20 ps, some of the correlation peaks become obscure as the peaks are broadened due to the increase of the amplitudes

of the lattice vibrations at high temperature. However, the signature of the long range order could be clearly seen at this timestep, as the structure of the correlation peaks is retained to a large extent. This conclusion is also confirmed by Fig. 2-3-4, where the centrosymmetry parameter identifies ~60% of atoms with a local FCC atomic environment at 20 ps, close to the fraction of FCC atoms obtained at 0 ps. The gradual decrease in the intensity of the correlation peaks at later time reflects the decrease in the over fraction of the FCC atoms and the size of the remaining crystallites as the melting proceeds in the nanocrystalline film. At 500 ps, there are only a few peaks located at short interatomic distances, suggesting that the structure of the system at this time has only short range order, characteristic for a liquid structure. This agrees with the result of the visual analysis of atomic configurations, Fig. 2-3-4, that at 500 ps nearly all atoms are in disordered state.

For single crystalline films under short pulse laser irradiation, it has been shown in Chapter 2 and Ref. [13] that the thermoelastic deformation of the lattice results in the splittings and subsequent shifts of the diffraction peaks. For high fluence regime, where the lattice temperature could be raised well above the equilibrium melting temperature, the shifting of the diffraction peak reflects the maximum uniaxial expansion of the lattice before the initiation of the homogeneous melting throughout the film, leading to the disappearance of the diffraction peaks. For low fluence regime, where no melting is observed in the film [20], it has been shown that the thermoelastic stress induced by the heating of the lattice could create periodic oscillations of the diffraction peaks that correspond to the elastic vibrations of the film.



(a)



(b)

Figure 2-3-5. (a) Reduced pair distribution function $G(r)$ and (b) its corresponding structure function $S(Q)$ computed for atomic configurations obtained in a TTM-MD

simulation of a 20 nm nanocrystalline Au film irradiated with a 200 fs laser pulse at an absorbed fluence of 45 J/m^2 at times of 0, 20, 50, 200 and 500 ps.

The diffraction profiles of the nanocrystalline film, $S(Q)$, are shown in Fig. 2-3-5 (b) for the melting process induced by the laser irradiation. While it is clear that at 20 ps diffraction peak shift to the left that corresponds to the lattice expansion, no splitting of the peaks is observed. This result could be related to the nanocrystalline nature of the sample. As there are many crystalline grains with random crystallographic orientations in the system, the heating of the lattice due to the energy transfer from the hot electrons leads to the uniaxial lattice expansion perpendicular to the free surface. This expansion would affect the lattice spacings in many crystallographic directions, different from the case in the laser melting of single crystalline film where uniaxial expansion along certain crystallographic direction is allowed. As a result, no splitting of the diffraction peaks are observed as the peaks slightly shift, indicating the lattice expansions due to the heating. From Fig. 2-3-5, the structure functions at 200 and 500 ps, show liquid-like profiles despite the fact that there are still a few percent of atoms with local FCC structure.

B. Relation to the Classical Nucleation Theory (CNT)

As shown in the atomic snapshots in section III (A), the initiation of the melting process at the grain boundaries leads to the separations of the remained crystalline domains by liquid regions. Therefore at this stage the melting of the nanocrystalline film proceeds through the dissolution of individual crystalline clusters in the liquid. It has been shown that the melting in the nanocrystalline film following the laser irradiation

continues under conditions where the lattice temperature is well below the equilibrium melting temperature of EAM Au. In order to understand the relationship between the characteristics of the melting processes in the nanocrystalline film and the size of the grains, the classical nucleation theory is applied for investigation of the conditions leading to the melting of a small solid cluster in a liquid environment.

From the classical nucleation theory, it is well known that the change of the Gibbs free energy due to the formation of a small spherical solid cluster of radius r in a undercool liquid is [21]

$$\Delta G_r = -\frac{4}{3}\pi r^3 \Delta G_v + 4\pi r^2 \gamma_{S-L} \quad (2.3.1)$$

where ΔG_v is the Gibbs free energy difference between solid and liquid phases per unit volume at the same temperature, T , and γ_{S-L} is the solid-liquid interfacial free energy. For a small undercooling, $\Delta T = T_m - T$, the difference between the specific heats of the solid and liquid phases can be ignored and ΔG_v can be well approximated as $L_v \Delta T / T_m$, where L_v is the latent heat of fusion per unit volume at the equilibrium melting temperature, T_m .

From the Eq. (2.3.1), it is easy to determine the critical size of the solid cluster for a given undercooling, ΔT

$$r^* = \frac{2\gamma_{S-L}}{\Delta G_v} = \left(\frac{2\gamma_{S-L} T_m}{L_m} \right) \frac{1}{\Delta T} \quad (2.3.2)$$

If $r < r^*$, the solid cluster is thermodynamically unstable and the system will evolve towards the dissolution of the solid in favor of lowering the free energy of the system, whereas if $r > r^*$ the free energy of the system decrease as the size of solid cluster grows. At $r = r^*$, the resulting ΔG_r from Eq. (2.3.1) is zero and the solid cluster is in (unstable) equilibrium with the surrounding liquid. This expression has been widely used in

experimental investigations of solidification processes through homogeneous nucleation in undercool liquids. From the perspective of searching for the condition at which a solid cluster of a particular radius r is in equilibrium with the surrounding liquid, one can directly rewrite Eq. (2.3.2) to obtain the corresponding critical temperature, T_{mc}

$$T_{mc} = T_m \left[1 - \frac{2\gamma_{S-L}}{L_m} \frac{1}{r} \right] \quad (2.3.3)$$

Similar to the discussion of the critical radius, it is apparent that for $T > T_{mc}$, the solid cluster will dissolve into liquid to lower the free energy of the system, whereas for $T < T_{mc}$, solidification of liquid will take place and the size of solid cluster will increase as a result.

As mentioned before, the melting of the nanocrystal after the initial meltdown of the grain boundary regions can be considered as the melting of individual nanosize solid clusters in the liquid. To relate the Eq. (2.3.3) obtained from CNT to the melting behavior of nanocrystalline films induced by laser irradiation, it is necessary to find the solid-liquid interfacial free energy for EAM Au. The solid-liquid interfacial free energy is of fundamental importance for studying the formation of microstructure in the solidification process. We adopt a recently proposed numerical approach called capillary fluctuation method (CFM) to determine the solid-liquid interfacial free energy of EAM Au. Detailed descriptions of this approach could be found in Refs. [22,23,24] and references therein. Briefly the approach is based on the fact that the interfacial stiffness is much more anisotropic than the interfacial free energy. By measuring the height fluctuation spectrum, $h(x)$, of the solid-liquid interface of different crystallographic orientations, the solid-liquid interfacial free energy could be obtained from a simple relation between the interfacial stiffness and the interface fluctuation spectrum. For a

four-fold symmetry (i.e., rotations about the [100] axis) the interfacial free energy could be expressed, to the first order, as [22]

$$\gamma(\theta) = \gamma_0(1 + \varepsilon \cos 4\theta) \quad (2.3.4)$$

where θ is the angle between the [100] direction and the direction normal to the interface that lies in the (001) plane and ε is the characteristic parameter that describes the anisotropy of the interfacial free energy. The interfacial stiffness is

$$\hat{\gamma}(\theta) = \gamma(\theta) + \gamma''(\theta) = \gamma_0(1 - 15\varepsilon \cos 4\theta) \quad (2.3.5)$$

and could be related to the Fourier transform of the height fluctuation spectrum, $A(k)$, through [22]

$$\langle |A(k)|^2 \rangle = \frac{k_B T_m}{(\gamma + \gamma'')k^2} \quad (2.3.6)$$

where $h(x) = \sum_k A(k) \exp(ikx)$, k_B is the Boltzmann constant, and T_m is the equilibrium melting temperature. In order to identify the solid-liquid interfaces for collecting the data of its position, $h(x)$, the local order parameter which characterizes the structural environment of a given atom is obtained for the configuration collected during the simulation. Those atoms that have the local order parameter between 0.05 and 0.1 are identified as atoms of the interface.

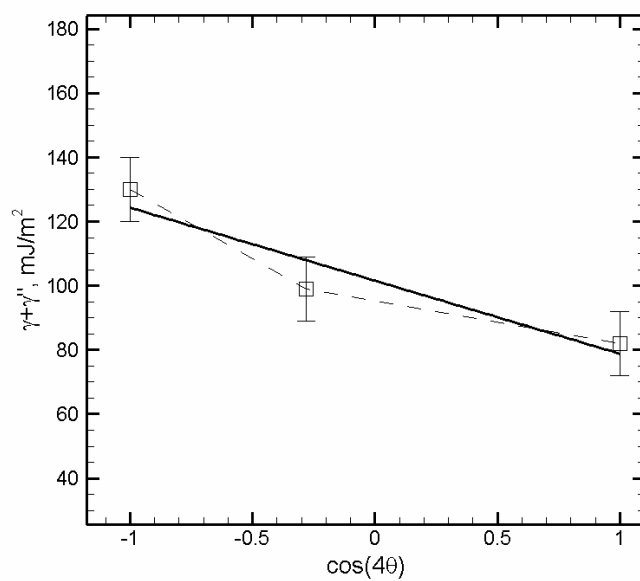
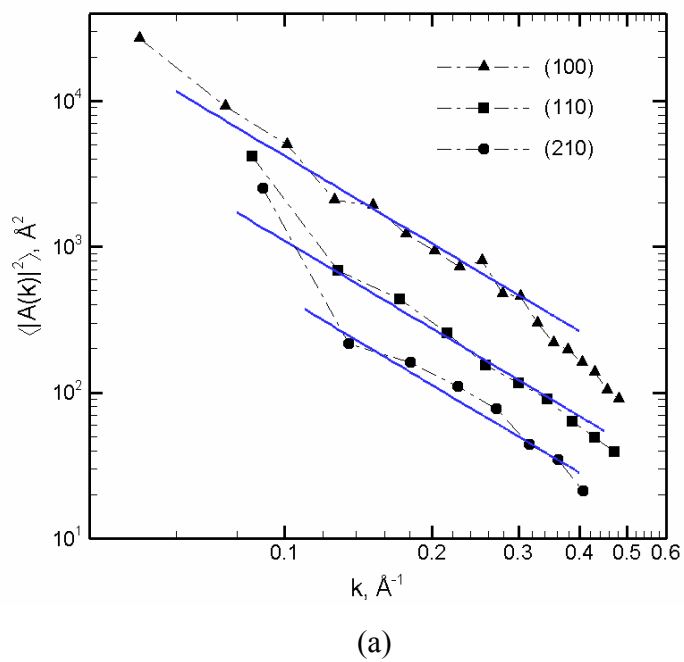


Figure 2-3-6. (a) Fourier spectrum of the interface height fluctuation calculated for different interfaces. Solid lines are fits of the data points to the form given by Eq. (2.3.6).

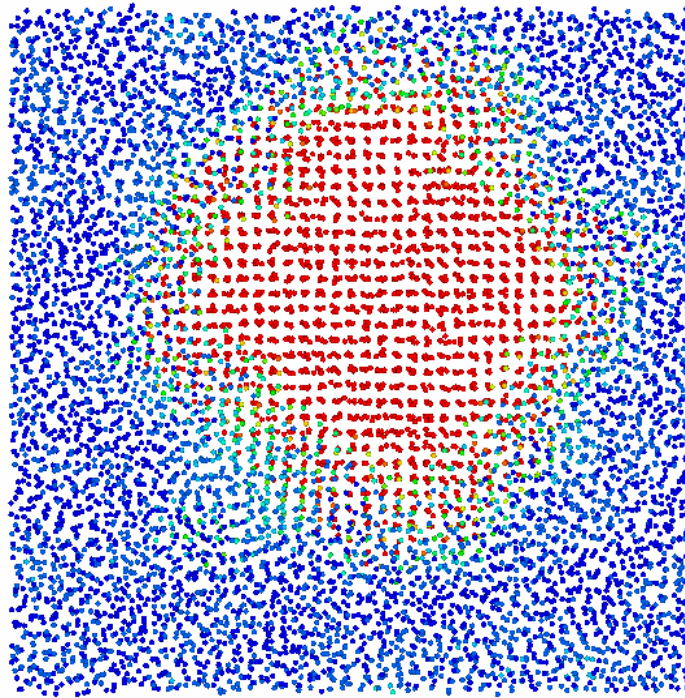
(b) Interfacial stiffness as a function of orientation in $\cos 4\theta$. Solid line is a fit to Eq. (2.3.5).

Fig. 2-3-6(a) shows the Fourier transform of the height fluctuation spectrum for three different interfaces, i.e. (100), (110) and (210). By fitting to Eq. (2.3.6), the values of the interfacial energy for these three interfaces could be obtained. Our calculation shows that the interfacial energies of EAM Au in this work are 0.104 J/m^2 for (100), 0.100 J/m^2 for (110) and 0.102 J/m^2 for (210). These values are smaller than the experimental value of 0.132 J/m^2 estimated from the analysis of the formation of crystal nuclei in supercooling liquid metals by Turnbull [25], and a value of 0.126 J/m^2 predicted for γ_0 with the EAM potential by Voter-Chen for Au [23]. It can be noted that the interfacial energy can be associated with the equilibrium melting temperature of the material through the Turnbull relationship [25], $\gamma = \alpha T_m \Delta S \rho^{2/3}$, where T_m is the equilibrium melting temperature, ΔS is the entropy of fusion, ρ is the solid atomic density and α is the so-called Turnbull coefficient. Therefore, the difference between the interfacial energies determined for both EAM potentials and the experimental value might be attributed to the differences in the equilibrium melting temperature, 963 K for EAM Au in this work and 1120 K for Voter-Chen EAM potential, as compared to the experimental value of 1338 K.

It should be noted that Eq. (2.3.3) assumes a spherical shape for the solid cluster in the liquid environment and does not take into account the difference in the interfacial free energy for different orientations. As shown by the results of the calculation of the solid-liquid free energies with the CFM approach, the difference in the free energies of different interfaces is small, $\gamma_{100} - \gamma_{110} = 0.004 \text{ J/m}^2$. Therefore only γ_0 is used as the

interfacial free energy in Eq. (2.3.3) to calculate the dependence of the critical temperature for the solid cluster in the liquid environment as a function of radius.

An alternative approach to obtain the dependence of the critical temperature on the size of the solid cluster in the liquid is to carry out a series of NPT molecular dynamic simulations (N is the number of atoms in the system, P is pressure and T is temperature) of a solid cluster embedded in an undercool liquid for a wide range of sizes of the solid cluster. By controlling the temperature so that the solid cluster is in equilibrium with the liquid, i.e. the size of the solid cluster remains unchanged, the critical temperature as a function of the size of the solid cluster could be determined. It should be noted that this approach does not require *a priori* knowledge of the solid-liquid interfacial free energy, as well as the theoretical results from CNT, i.e. Eq. (2.3.3).



(a)

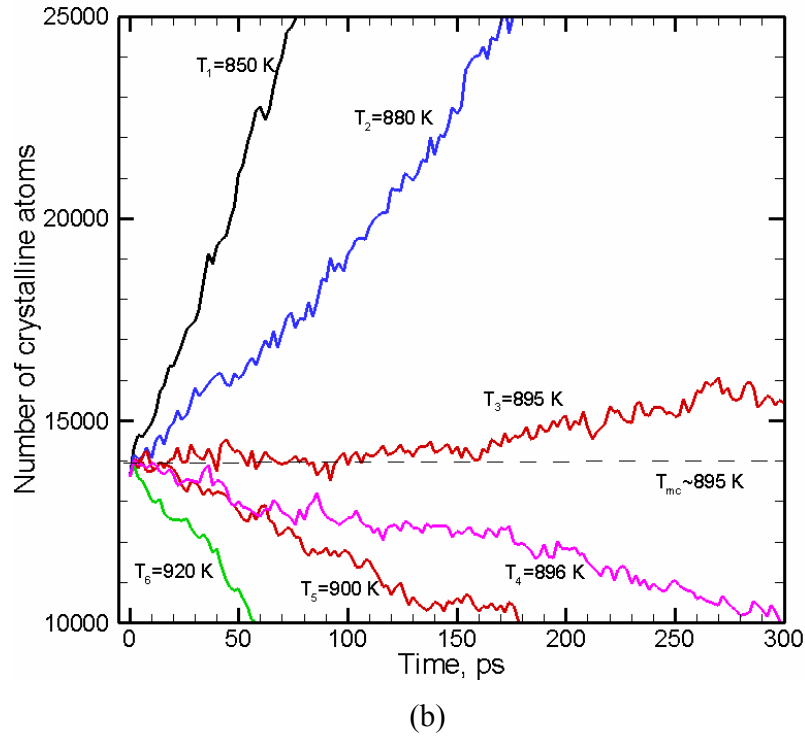


Figure 2-3-7. (a) The cross section snapshot of the atomic configuration of a solid cluster in the liquid. The number of atoms in the solid cluster is identified by the local order parameter to be ~ 14000 . The color corresponds to the local order parameter. (Red is solid; blue is liquid). (b) The time evolution of the number of atoms in the solid cluster at different temperatures. The melting temperature for the size of the solid cluster is estimated to be 895 K.

The initial configuration for the NPT simulations is created as follows. First a spherical region centered at the MD cell is identified. The temperature of the region outside the sphere is increased well above the equilibrium melting temperature to induce melting outside the sphere while keeping the temperature inside below the equilibrium melting temperature so that the sphere is still solid. Once the structure with a solid sphere surrounded by liquid is obtained, the system is equilibrated for 500 ps at the designated temperature. Fig. 2-3-7 (a) gives a typical cross-section view of the atomic

configuration of a solid cluster, which is composed of $N_c \sim 14000$ atoms surrounded by liquid. It can be seen that the solid cluster remains close to a spherical shape with some faceting of the boundary with liquid. According to the local order parameter defined in [19], solid and liquid atoms are colored in red and blue respectively while atoms at the boundary between solid and liquid have intermediate colors. In all of these simulations, zero pressure is maintained while the periodic boundary conditions are imposed in all three directions. For a given size of the solid cluster, the critical temperature, T_{mc} , is determined by varying the temperature in the NPT simulations so that the number of atoms in the cluster remains close to the initial one. It is clear from the previous discussion of the critical temperature in CNT that beyond T_{mc} the number of solid atoms will decrease due to the melting, whereas below T_{mc} it will increase due to the solidification process. Simulation results for several values of temperature with the initial cluster, composed of $N_c \sim 14000$ atoms, are shown in Fig. 2-3-7(b). The number of the atoms in the cluster increases drastically within 100 ps for $T=850$ K and 880 K whereas it decreases for $T=920$ K and 900 K. A trend of gradual decrease is clear for $T=896$ K. However, for $T=895$ K, the number of atoms in the cluster fluctuates around the initial value until ~ 150 ps, and starts to increase slowly at later times. Thus the critical temperature for $N_c \sim 14000$ is determined to be 895 K. Fig. 2-3-8 shows the critical temperature as a function of the cluster size obtained from the results of the NPT simulations under assumption of the spherical shape of the solid cluster. A linear dependence of the critical temperature on the inverse of the cluster radius is clear from Fig. 2-3-8. By fitting the dependence to Eq. (2.3.3), we estimate the value of the solid-liquid interfacial energy of the EAM gold to be 0.119 J/m^2 , in reasonable agreement with

the value from the CFM approach, 0.102 J/m^2 . This approach for obtaining the solid-liquid interfacial energy on the basis of the classical nucleation theory has been recently proposed and used for calculation of the orientationally averaged interfacial energy of a Lennard-Jones potential [26].

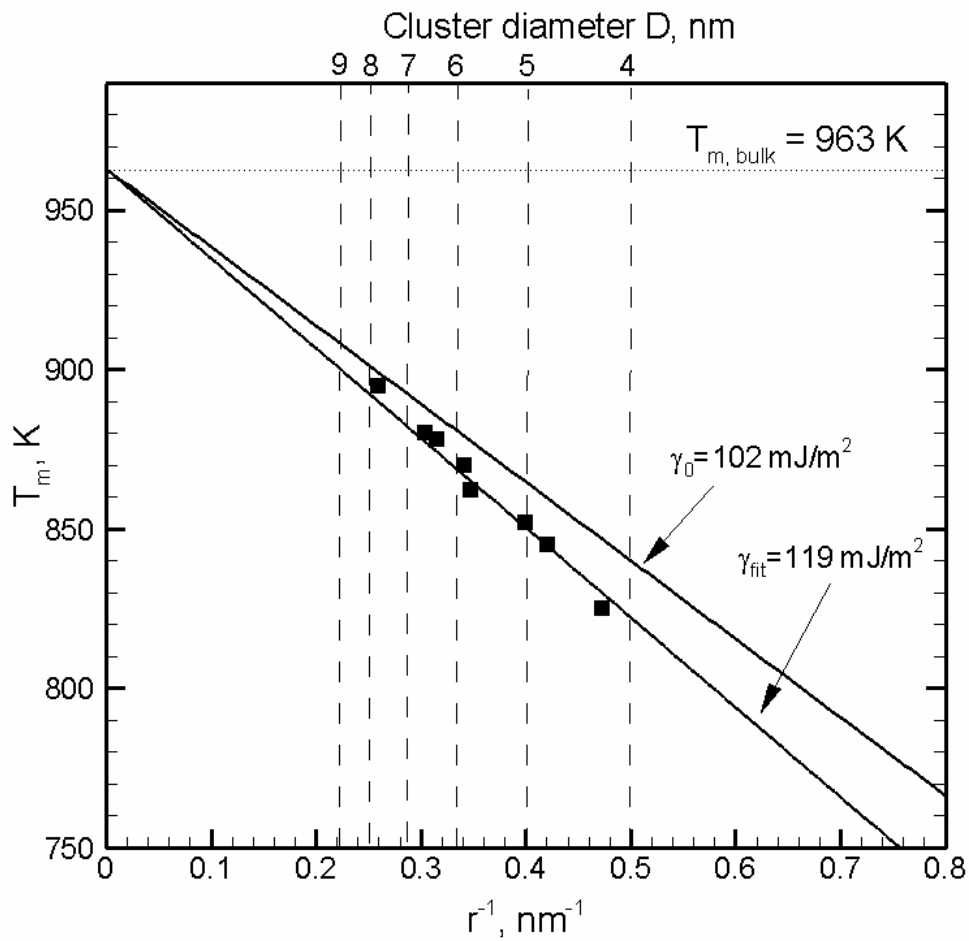


Figure 2-3-8. Dependence of the melting temperature of a solid cluster in a liquid environment on the cluster sizes.

The result of the calculations of the critical temperature of solid clusters in the liquid environment has direct implications for interpretation of the results of the simulations of laser melting of nanocrystalline films, where nanocrystalline grains evolve

into individual solid clusters in the liquid environment. The line predicted by Eq. (2.3.3) using the data from NPT simulations defines the conditions of the stability of solid clusters of a particular size at a give temperature T . For instance, at $T=850$ K, solid clusters with diameter larger than ~ 5 nm are thermodynamically stable and are expected to grow whereas clusters with diameter smaller than ~ 5 nm are unstable and are expected to dissolve. As the small clusters surrounded by the liquid gradually dissolve, the consumption of a part of the thermal energy for the latent heat of melting would lead to the decrease in the temperature of the system. On the other hand, a smaller cluster size implies a lower critical temperature determined by the stability of solid clusters in liquid. The cluster could grow in size if the temperature of the system becomes lower than the critical temperature defined by the size of the cluster, similar to the observation in the NPT simulations shown in Fig. 2-3-7. Therefore the final disappearance of those nanoclusters in the laser-irradiated nanocrystalline film would rely on the stability conditions defined by the critical temperature of solid clusters in equilibrium with liquid and the temperature of the system. For the laser fluence used in this study, the temperature of the film rises up to ~ 1000 K at ~ 25 ps and saturates at ~ 913 K after 100 ps, shown in Fig. 2-3-2,. The critical size of the solid cluster in the equilibrium with the surrounding liquid can be determined directly from Fig. 2-3-8. It can be seen that at ~ 1000 K, larger than the equilibrium melting temperature of EAM gold, 963 K, no solid clusters are thermodynamically stable with the liquid. As a result, these solid clusters shrink due to melting at the boundaries. The temperature at later times saturates at ~ 913 K, which corresponds to a critical size of ~ 9 nm for the solid cluster in equilibrium with the liquid. It is found that at ~ 100 ps the sizes of the remained solid clusters in Fig. 2-3-3

are less than ~ 4 nm. Therefore as shown in the snapshots in Fig. 2-3-3, the small solid clusters after ~ 100 ps are thermodynamically unstable in the liquid environment and gradually dissolve.

2.3.4 Summary

To summarize, the changes in the microstructure of a nanocrystalline Au film irradiated by a short laser pulse are investigated in MD simulations. Effects of the electronic heating and subsequent energy relaxation following the laser excitation are described within the well known two-temperature-model that is realized in a continuum-atomistic computational approach. The inspection of the transient atomic structures generated in the simulation performed with the absorbed fluence of 45 J/m^2 , shows that the melting is initiated at grain boundaries and results in the decomposition of the nanocrystal into individual clusters surrounded by liquid. A complete melting of the nanocrystalline film is achieved at a lattice temperature below the equilibrium melting temperature. In order to explain this behavior, the classical nucleation theory is applied for investigation of the thermodynamic stability of the solid clusters in a liquid surrounding. We find that, due to the contribution of the interfacial energy of grain boundaries to the Gibbs free energy of the system, the individual solid clusters are thermodynamically unstable in a liquid environment at a lattice temperature below the equilibrium melting temperature and gradually dissolve.

References for Chapter 2.3

- [1] D. Farkas, S. Mohanty and J. Monk, Phys. Rev. Lett. **98**, 165502, 2007.
- [2] S. Xiao, W. Hu and J. Yang, J. Phys. Chem. B **109** 20339, 2005.
- [3] S. Xiao and W. Hu, J. Chem. Phys. **125** 014503, 2006.
- [4] S. I. Anisimov, B. L. Kapeliovich, and T. L. Perel'man: Zh. Eksp. Teor. Fiz. **66**, 776, 1974 [Sov. Phys. JETP **39**, 375 (1974)].
- [5] D. S. Ivanov and L. V. Zhigilei, Phys. Rev. B **68**, 064114, 2003.
- [6] A. Okabe, B. Boots, and K. Sugihara, *Spatial Tessellations: Concepts and Applications of Voronoi Diagrams*, Wiley, Chichester, 1992.
- [7] J. Schiotz, T. Vegge, F. D. Di Tolla, K. W. Jacobsen, Phys. Rev. B **60**, 11971, 1999.
- [8] H. Van Swygenhoven, P. M. Derlet, A. G. Frøseth, Nat. Mater. **3**, 399, 2004.
- [9] A. B. Belonoshko, N. V. Skorodumova, S. Davis, A. N. Osipov, A. Rosengren, and B. Johansson, Science **316**, 1603, 2007.
- [10] S. Kumar, S. K. Kurtz, J. R. Banavar, and M. G. Sharma, J. Stat.Phys. **67**, 523, 1992.
- [11] B. E. Warren, X-Ray Diffraction, Addison-Wesley, Reading, MA, 1969.
- [12] X. W. Zhou, H. N. G. Wadley, R. A. Johnson, D. J. Larson, N. Tabat, A. Cerezo, A. K. Petford-Long, G. D. W. Smith, P. H. Clifton, R. L. Martens, and T. F. Kelly, *Acta Mater.* **49**, 4005, 2001.
- [13] Z. Lin and L. V. Zhigilei, Phys. Rev. B **73**, 184113, 2006.
- [14] S. I. Anisimov and B. Rethfeld, Proc. SPIE **3093**, 192, 1997.
- [15] Z. Lin and L. V. Zhigilei, Proc. SPIE **6261**, 62610U, 2006.

- [16] J.L. Hostetler, A.N. Smith, D.M. Czajkowsky and P.M. Norris, Appl. Opt. **38**, 3614, 1999.
- [17] J. Hohlfeld, S.-S. Wellershoff, J. Guddde, U. Conrad, V. Jahnke, and E. Matthias, Chem. Phys. 251, 237, 2000.
- [18] J. Hohlfeld, S.-S. Wellershoff, J. Gudde, U. Conrad, V. Jahnke, and E. Matthias, Chem. Phys. **251**, 237-258, 2000.
- [19] C. Kelchner, S.J. Plimpton and J.C. Hamilton, Phys. Rev. B **58**, 11085, 1998.
- [20] Z. Lin and L. V. Zhigilei, J. Phys.: Conference Series **59**, 11, 2007.
- [21] D. A. Porter and K. E. Easterling, *Phase Transformations in Metals and Alloys*, 2nd ed. (Chapman & Hall, London, 1992).
- [22] J.J. Hoyt, M. Asta, and A. Karma, Phys. Rev. Lett. **86**, 5530, 2001.
- [23] J.J. Hoyt and M. Asta, Phys. Rev. B **65**, 214106, 2002.
- [24] J. R. Morris and X. Song, J. Chem. Phys. **119**, 3920, 2002.
- [25] Turnbull J.Appl.Phys. **21**, 1022, 1950.
- [26] Bai, X. M.; Li, M. J. Chem. Phys. **124**, 124707, 2006.

3. Electron-phonon Coupling and Electron Heat Capacity of Metals under Conditions of Strong Electron-phonon Nonequilibrium

3.1 Introduction

The rapidly growing use of femtosecond lasers in practical applications and fundamental materials research increases the demand for quantitative predictive modeling of the fast and highly nonequilibrium processes induced in the target material by the laser excitation. For metals, theoretical/computational studies of laser interactions have widely employed the two-temperature model (TTM) proposed by Anisimov [1]. The TTM describes the temporal and spatial evolution of the lattice and electron temperatures, T_l and T_e , in the irradiated target by two coupled non-linear differential equations:

$$C_e(T_e) \frac{\partial T_e}{\partial t} = \nabla [K_e(T_e, T_l) \nabla T_e] - G(T_e)(T_e - T_l) + S(\vec{r}, t) \quad (3.1)$$

$$C_l(T_l) \frac{\partial T_l}{\partial t} = \nabla [K_l(T_l) \nabla T_l] + G(T_e)(T_e - T_l) \quad (3.2)$$

where C and K are the heat capacities and thermal conductivities of the electrons and the lattice as denoted by subscripts e and l , $G(T_e)$ is the electron-phonon coupling factor related to the rate of the energy exchange between the electrons and the lattice, and $S(\vec{r}, t)$ is a source term describing the local energy deposition by the laser pulse. The model accounts for the laser excitation of the conduction band electrons and subsequent energy relaxation processes, i.e. the energy transfer from the hot electrons to the lattice vibrations due to the electron-phonon interaction and the electron heat conduction from the irradiated surface to the bulk of the target. In Eq. (3.2), the term describing the lattice

heat conduction is often omitted as it is typically negligible as compared to the electron heat conduction in metals.

The TTM model is also used in investigations of high-energy ion bombardment of metal targets [2,3], with the source term in Eq. (3.1) accounting for the energy transfer from the incident energetic ion to the electronic excitations within the ion track (electronic energy loss by the ion). The TTM equations, typically formulated in this case in cylindrical coordinates, describe the energy transfer from the excited electrons to the lattice, as well as cooling of the thermal spike region, generated by the passage of the incident ion, due to the electronic heat conduction.

Some of the effects and physical processes that are not described by the original TTM can still be included within the general TTM framework. In particular, recent developments include incorporation, through the parameters of TTM, of the description of the surface/grain boundary scattering [4,5] and the energy transfer by ballistic electrons [6,7], combination of TTM with thermoelasticity equations [8], as well as an extension of TTM to include a description of the transient nonthermal electron dynamics during and immediately after the femtosecond laser excitation [9]. Moreover, investigations of the microscopic mechanisms of laser-induced phase transformations and changes in the microstructure of the target material have been enabled by the development of hybrid models that combine the classical molecular dynamics (MD) method with TTM [10,11,12,13,14,15,16,17].

A key issue in the application of the models based on TTM for quantitative description of the kinetics of the energy redistribution in the irradiated target is the choice of adequate temperature dependent thermophysical properties of the target material

included in the TTM equation for the electron temperature, Eq. (3.1), namely, the electron-phonon coupling factor, the electron heat capacity, and the heat conductivity. Due to the small heat capacity of the electrons in metals and the finite time needed for the electron-phonon equilibration, irradiation by a short laser pulse can transiently bring the target material to a state of strong electron-lattice nonequilibrium, in which the electron temperature can rise up to tens of thousand Kelvins, comparable to the Fermi energy, while the lattice still remains cold. At such high electron temperatures, the thermophysical properties of the material can be affected by the thermal excitation of the lower band electrons, which, in turn, can be very sensitive to the details of the spectrum of electron excitations specific for each metal. Indeed, it has been shown for Au, that in the range of electron temperatures typically realized in femtosecond laser material processing applications, thermal excitation of d band electrons, located ~ 2 eV below the Fermi level, can lead to a significant (up to an order of magnitude) increase in the electron-phonon coupling factor and positive deviations of the electron heat capacity from the commonly used linear dependence on the electron temperature [18,19,20]. On the other hand, in Ni and Pt, where the Fermi level cuts through the high density of electron states d band, the same effect of the thermal excitation of d band electrons results in the decrease in the strength of the electron-phonon coupling [21] and negative deviations of the electron heat capacity from the linear temperature dependence [21,22]. Thus, the approximations of a linear temperature dependence of the electron heat capacity and a temperature independent electron-phonon coupling factor, used in most of the current TTM calculations, are inappropriate for the quantitative description of

material response to a strong ultrafast laser excitation and should be reconsidered based on the analysis of the electronic structure of a given material.

In this chapter, we report the results of a systematic analysis of the connections between the electron density of states (DOS) in the target material and the electron temperature dependence of the electron-phonon coupling and the electron heat capacity. Calculations are performed for eight representative metals (aluminum, copper, silver, gold, nickel, platinum, tungsten, and titanium). The chapter is organized as follows. In the next section, the theoretical background and computational methods used in the calculations of the electron heat capacity and the electron-phonon coupling are described. In Section 3.3, the results of the calculations of the temperature dependent thermophysical properties of the eight metals are presented, compared to the predictions of the free electron gas (FEG) model, and related to the available experimental data obtained at different levels of laser excitation. A brief summary of the results and a discussion of the implications for realistic modeling of femtosecond pulse laser processing are given in Section 3.4.

3.2 Theory and computational methods

The effect of the thermal excitation of electrons on the electron heat capacity and electron-phonon coupling in metals is determined by the details of the electron DOS, which defines the spectrum of electron excitations and corresponding contributions to the thermophysical properties. Thus, in this section, the method used in the calculations of the electron DOS is described first, followed by the theoretical analysis of the temperature dependence of the electronic heat capacity and electron-phonon coupling. A

brief discussion of the electron thermal conductivity is also given for completeness, although more detailed analysis of the electron temperature dependence of this parameter will be addressed in future work.

	Al	Ag	Cu	Au	Ni	Pt	W	Ti
	$3s^2 3p^1$	$4d^{10} 5s^1$	$3d^{10} 4s^1$	$5d^{10} 6s^1$	$3d^8 4s^2$	$5d^9 6s^1$	$5d^4 6s^2$	$3d^2 4s^2$
a_0	4.05	4.16	3.635	4.175	3.53	3.92	3.175	2.886 [*]
λ	0.45 ^a 0.44 ^b 0.38 ^f	0.12 ^d	0.13 ^d 0.14 ^b	0.17 ^a 0.15 ^d	0.084 ^e	0.66 ^d	0.28 ^{c,f}	0.38 ^{c,f}
θ_D	428	225	343	165	450	240	400	420
$\lambda\theta_D^2/2$	304.8 298.1 257.4	22.5	56.6 60.1	17.1 15.1	62.9	140.6	165.7	247.9
$\lambda\langle\omega^2\rangle$	185.9 ^g	22.5	29 \pm 4 ^c	23 \pm 4 ^c	49.5 ^g	142.5 ^g	112 \pm 15 ^c	350 \pm 30 ^c

^{*} $c/a = 1.63$

^a Reference 49.

^b Reference 50.

^c Reference 58.

^d Reference 55.

^e Reference 51.

^f Reference 43.

^g Obtained from experimental values of G_0 (see the text in Section 3.3).

Table 3.1. The valence electrons treated in VASP calculations, the equilibrium lattice constant at $T_l = 0$ K used in VASP calculations a_0 (Å), the electron-phonon coupling

constant λ , the Debye temperature θ_D (K) [47], the value of $\lambda\langle\omega^2\rangle$ estimated using the approximation $\langle\omega^2\rangle \sim \theta_D^2/2$ (meV²), and the value of $\lambda\langle\omega^2\rangle$ (meV²) used in Eq. (3.8) for calculation of the temperature dependence of the electron-phonon coupling factor.

3.2.1 Electronic structure calculations

The electron DOS of the eight metals discussed in this study are obtained from the electronic structure calculations performed within the density functional theory, using the Vienna Ab-initio Simulation Package (VASP) [23]. The projector augmented wave potential [24] is used in these calculations and the exchange correlation term is accounted for within the generalized gradient approximation. Only valence electrons are explicitly treated in the calculations, while the more tightly bound electrons are represented as core electrons. The integration over the Brillouin zone is performed using a mesh of 31×31×31 points equally spaced in the reciprocal space [25,26]. The equilibrium lattice constants and valence electrons treated for each metal are given in Table 3.1.

3.2.2 Electron heat capacity $C_e(T_e)$

The electron heat capacity can be calculated by taking the derivative of the total electron energy density with respect to the electron temperature [27]:

$$C_e(T_e) = \int_{-\infty}^{\infty} \frac{\partial f(\varepsilon, \mu, T_e)}{\partial T_e} g(\varepsilon) \varepsilon d\varepsilon \quad (3.3)$$

where $g(\varepsilon)$ is the electron DOS at the energy level ε , μ is the chemical potential at T_e , and $f(\varepsilon, \mu, T_e)$ is the Fermi distribution function, defined as $f(\varepsilon, \mu, T_e) = \{\exp[(\varepsilon - \mu)/k_B T_e] + 1\}^{-1}$. At low electron temperatures, the Sommerfeld expansion of the electronic free energy is commonly used, giving a linear temperature

dependence of the electron heat capacity: $C_e(T_e) = \gamma T_e$, where γ is the electron heat capacity constant, $\gamma = \pi^2 k_B^2 g(\varepsilon_F)/3$, defined by the value of the electron DOS at the Fermi level, $g(\varepsilon_F)$. Within the free electron gas model [27], γ can be further associated with the free electron number density n_e and the Fermi energy ε_F , $\gamma = \pi^2 n_e k_B^2 / 2\varepsilon_F$.

At high electron temperatures, however, the Sommerfeld expansion is not valid and the electron heat capacity should be calculated directly from Eq. (3.3), using the full spectrum of the density of states and $\partial f / \partial T_e$. The evaluation of $\partial f / \partial T_e$ requires the knowledge of the chemical potential as a function of the electron temperature, $\mu(T_e)$. From the conservation of the total number of electrons, the chemical potential can be obtained by setting the result of the integration of the product of the electron DOS and the Fermi distribution function at T_e over all energy levels to be equal to the total number of electrons N_e [27],

$$N_e = \int_{-\infty}^{\infty} f(\varepsilon, \mu(T_e), T_e) g(\varepsilon) d\varepsilon \quad (3.4)$$

The chemical potential, obtained with Eq. (3.4) for different electron temperatures, can then be used in Eq. (3.3) to predict the temperature dependence of the electron heat capacity. The results of the calculations of $\mu(T_e)$ and $C_e(T_e)$ are presented for eight different metals and compared with the predictions of the free electron gas model in Section 3.3.

3.2.3 Electron thermal conductivity

The electron thermal conductivity is related to the electron heat capacity through the Drude model relationship, $K_e(T_e, T_l) = v^2 C_e(T_e) \tau_e(T_e, T_l) / 3$ [27], where $\tau_e(T_e, T_l)$ is the total electron scattering time and v^2 is the mean square velocity of the electrons contributing to the electron heat conductivity. At low electron temperatures v^2 can be approximated as the Fermi velocity squared, v_F^2 . The total electron scattering rate is given by the sum of the electron-electron scattering rate, $1/\tau_{e-e} = AT_e^2$, and the electron-phonon scattering rate, $1/\tau_{e-ph} = BT_l$: $1/\tau_e = 1/\tau_{e-e} + 1/\tau_{e-ph} = AT_e^2 + BT_l$, where A and B are typically assumed to be constants [18,28]. The electron-electron and electron-phonon scattering rates, however, might be sensitive to the spectrum of states available for the scattering processes [27] and the temperature dependences of the scattering rates given above might undergo some modifications at high electron temperatures. Thus, in addition to the deviations of the electron heat capacity from the linear temperature dependence, the electron thermal conductivity described by the Drude model relationship might be affected by the modification of the temperature dependences of the electron-phonon and electron-electron scattering rates.

3.2.4 Electron-phonon coupling factor $G(T_e)$

The electron-phonon coupling was first analyzed within the free electron gas model by Kaganov *et al.* [29]. It was suggested that the electron-lattice energy exchange rate could be expressed in terms of the electron relaxation time at T_e and T_l . At lattice and electron temperatures much higher than the Debye temperature and $T_e \gg T_l$, the rate of energy transfer from the electrons to the lattice per unit volume can then be expressed as [1,29]

$$\partial E_e / \partial t = G(T_l - T_e), \quad G = \frac{\pi^2}{6} \frac{m_e C_s^2 n_e}{\tau(T_e) T_e}, \quad (3.5)$$

where m_e is the effective electron mass, C_s is the speed of sound, n_e is the number density of the electrons, and $\tau(T_e)$ is the electron relaxation time defined as the electron-phonon scattering time, τ_{e-ph} , and evaluated under the assumption that the lattice temperature is equal to the electron temperature [29]. The electron-phonon scattering is proportional to the inverse of the lattice temperature and, under the condition of $T_e = T_l$, $\tau(T_e) \sim 1/T_e$, leading to a constant value of the coupling factor given by Kaganov's expression [1].

Although a constant value for the electron-phonon coupling factor is used in most of current computational and theoretical investigations of short-pulse laser interactions with metals, there is growing experimental evidence suggesting that the applicability of the constant electron-phonon coupling may be limited to low laser intensities (low electronic temperatures) [18,30,31,32]. For example, the coupling constant has been used as a fitting parameter to obtain an agreement between the calculated and experimental values of the ablation threshold in Au [33], whereas empirical or semi-empirical $G(T_e)$ dependences have been introduced to provide a good description of experimental electron photoemission data [34] and ablation rates [35,36]. Moreover, the measurements of the electron-phonon coupling constants reported in literature exhibit a broad variation, e.g. from 3.6×10^{17} to $10.5 \times 10^{17} \text{ Wm}^{-3}\text{K}^{-1}$ for Ni [37,38,39], that may be, in addition to the differences in the measurement techniques, related to the different levels of laser excitation used in the experiments.

Several approaches have been proposed in order to account for the temperature dependence of the electron-phonon coupling factor. Based on the Kaganov's expression

for the electron-phonon energy exchange rate, Eq. (3.6), Chen *et al.* [35] introduced a model in which both electron-electron and electron-phonon scattering rates are included in the evaluation of the electron relaxation time, $\tau(T_e)$ in Eq. (3.5). The electron-electron scattering, indeed, starts to significantly contribute to the total electron scattering rate at high electron temperatures, above ~ 1 eV. While this contribution directly affects the electron transport properties (thermal and electrical conductivities), the relevance of the electron-electron scattering to the electron-phonon coupling factor is questionable. Similarly, the evaluation of the electron relaxation time $\tau(T_e)$ based on the temperature dependence of the electrical or thermal conductivity [2,40] includes the contribution of electron-electron scattering and is applicable for the calculation of the electron-phonon coupling only at low electron temperatures.

At high electron temperatures, the thermal excitation of the electrons located below the Fermi level starts to contribute to the rate of the electron-phonon energy exchange and a quantitative analysis of the electron-phonon coupling should go beyond the free electron gas model and should include the consideration of the electron DOS. A general description of the electron-phonon energy exchange involving arbitrary electron DOS was developed by Allen [41] based on the rate equations for the electron-phonon collisions that characterize the phonon emission and absorption processes. Following Allen's analysis, the rate of the energy exchange between the electrons and the lattice within one unit cell can be expressed as

$$\left. \frac{\partial E_e}{\partial t} \right|_{ep} = \frac{4\pi}{\hbar} \sum_{k,k'} \hbar \omega_Q |M_{kk'}|^2 S(k,k') \delta(\varepsilon_k - \varepsilon_{k'} + \hbar \omega_Q) \quad (3.6)$$

where k and Q denote the electron and phonon quantum numbers, respectively. $M_{kk'}$ is the electron-phonon scattering matrix element that defines the probability of scattering of an electron from the initial state k with energy ε_k to the final state k' with energy $\varepsilon_{k'}$ by a phonon of energy $\hbar\omega_Q$ [42]. $S(k, k') = (f_k - f_{k'})n_Q - f_{k'}(1 - f_k)$ is the so-called thermal factor, expressing the phonon absorption and emission processes in the electron-phonon scattering in terms of the electron and phonon occupation numbers, f_k and n_Q , respectively (see also the Appendix). Assuming that phonons and electrons can be characterized by distinct electron and lattice temperatures, the occupation numbers can be described by Fermi-Dirac and Bose-Einstein distribution functions respectively: $f(\varepsilon) = 1/[1 + \exp((\varepsilon - \mu)/k_B T_e)]$ and $n(\hbar\Omega, T_l) = 1/[\exp(\hbar\Omega/k_B T_l) - 1]$. Near room temperature only electron states around the Fermi energy contribute to the scattering processes and Eq. (3.6) can be rewritten in terms of the Eliashberg spectral function for electron-phonon coupling, $\alpha^2 F(\Omega)$, commonly used in the superconductivity theory [41]:

$$\left. \frac{\partial E_e}{\partial t} \right|_{ep} = 2\pi g(\varepsilon_F) \int_0^\infty \alpha^2 F(\Omega) (\hbar\Omega)^2 [n(\hbar\Omega, T_l) - n(\hbar\Omega, T_e)] d\Omega \quad (3.7)$$

Allen further suggested a Taylor expansion of Eq. (3.7) in terms of $\hbar\Omega/k_B T_e$ and $\hbar\Omega/k_B T_l$ under conditions of $\hbar\Omega \ll k_B T_e$ and $\hbar\Omega \ll k_B T_l$, leading to $\partial E_e / \partial t|_{ep} \approx G_0 (T_l - T_e)$, where G_0 is the electron-phonon coupling constant: $G_0 = \pi \hbar k_B \lambda \langle \omega^2 \rangle g(\varepsilon_F)$. In this expression, $\langle \omega^2 \rangle$ is the second moment of the phonon spectrum defined by McMillan [43], and λ is the electron-phonon mass

enhancement parameter [44] defined as the first reciprocal moment of the spectral

$$\text{function, } \alpha^2 F(\Omega): \lambda \langle \omega^2 \rangle = 2 \int_0^\infty d\Omega \Omega \alpha^2 F(\Omega).$$

For high electron temperatures, it is necessary to take into account the scattering processes of electrons away from the Fermi surface, i.e. the electron energy dependence of the electron-phonon spectral function, $\alpha^2 F(\varepsilon, \varepsilon', \Omega)$. Wang *et al.* [18] proposed an approximation of the spectral function based on the assumption that $|M_{kk'}|^2$, when summed over scattering angles, is independent of the electron states, which leads to $\alpha^2 F(\varepsilon, \varepsilon', \Omega) = [g(\varepsilon)g(\varepsilon')/g^2(\varepsilon_F)]\alpha^2 F(\varepsilon_F, \varepsilon_F, \Omega)$. A simple expression for the temperature dependent electron-phonon coupling factor can then be obtained:

$$G(T_e) = \frac{\pi \hbar k_B \lambda \langle \omega^2 \rangle}{g(\varepsilon_F)} \int_{-\infty}^{\infty} g^2(\varepsilon) \left(-\frac{\partial f}{\partial \varepsilon}\right) d\varepsilon \quad (3.8)$$

The derivation of Eq. (3.8) and the related assumptions are discussed in more detail in the Appendix. It is easy to verify that at very low electron temperatures, $-\partial f / \partial \varepsilon$ reduces to a delta function centered on the Fermi level at 0 K, and Eq. (3.8) reduces to a constant value, recovering the expression for G_0 shown by Allen and given above in this section. At elevated electron temperatures, however, the value of $-\partial f / \partial \varepsilon$ at ε away from ε_F can no longer be neglected, leading to a temperature dependent electron-phonon coupling, $G(T_e)$, as described by Eq. (3.8).

It should be noted that the assumption of the effective independence of the magnitude of the scattering matrix element on the electron states, adopted by Wang *et al.*, is commonly used for estimation of the phonon-induced contribution to the excited

electron decay rate, where the electron-phonon scattering matrix is assumed to be constant and the spectral function, therefore, could be computed from the phonon density of states, given the fact that the electron scatterings take place close to the Fermi surface [45]. This assumption needs further verification when relative contributions from p/s- and d-bands different bands undergo significant changes with electron temperature. Another assumption implied in the theoretical approach presented above, as well as in other investigations [18,19,41], is the neglect of the umklapp process [27] in the electron-phonon scattering. Since the temperature dependence of the electron-phonon coupling in this work is determined based on the experimental value of either $\lambda\langle\omega^2\rangle$ or the electron-phonon coupling constant near the room temperature (see the discussion in Section 3 and Table I), the contribution from the umklapp scattering to the room temperature value of the electron-phonon coupling is implicitly taken into account. Furthermore, it has been shown recently by Petrov [46] that the effect of the umklapp process on the temperature dependence of the electron-phonon coupling in aluminum is relatively weak for temperatures exceeding the Debye temperature.

3.3 Results

In this section, the temperature dependence of the electron heat capacity and the electron-phonon coupling is investigated for eight representative metals in the range of electron temperatures, typically realized in the ultrafast laser processing applications. The results are grouped according to the characteristics of the electron structure of the metals, namely (1) aluminum and the free electron gas model; (2) noble metals: silver, copper and gold; (3) transition metals with almost filled d band: nickel and platinum; (4)

transition metals with less than half filled d band: tungsten and titanium. All calculations are performed based on the theoretical background presented in Section 2, with the electron DOS obtained from the VASP calculations.

3.3.1 Aluminum and the free electron gas model

The results of the calculations of the electron temperature dependence of the thermophysical properties of aluminum, a metal that has a free electron-like electronic structure, are discussed first and related to the predictions of the free electron gas model. The electron DOS obtained for aluminum in electronic structure calculations performed with VASP at $T_e=0$ K is shown in Fig. 3-1 (a), along with the DOS for the free electron gas model obtained by fitting the parabolic band dependence of $\epsilon^{1/2}$ to the DOS of aluminum and assuming that the total number of free electrons is 3. While the DOS of aluminum follows the general trend predicted by the free electron gas model, it also exhibits some detailed structure superimposed on the fitted $\epsilon^{1/2}$ curve. The deviations of the DOS determined for Al in VASP calculations from the free electron gas model DOS result in a slight divergence between the chemical potentials calculated with Eq. (3.4) using the two DOS, Fig. 3-1(b). Nevertheless, the overall quantitative agreement in the temperature dependences of the chemical potentials predicted with Al and the free electron gas model DOS is very good.

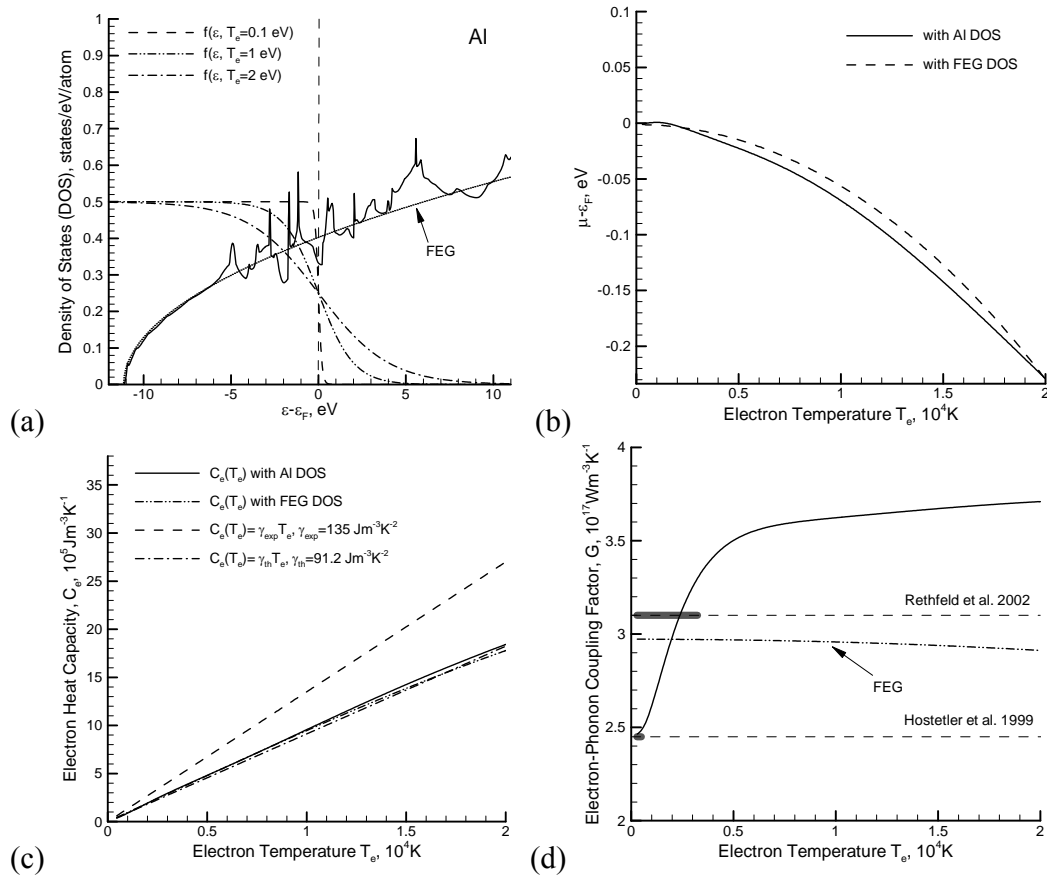


Figure 3-1. (a) The electron DOS of aluminum obtained in the electronic structure calculation performed with VASP (solid line), the DOS for the free electron gas (FEG) model obtained by fitting $\epsilon^{1/2}$ dependence of to the DOS of aluminum and assuming that the total number of free electrons is 3 (dotted line), and the Fermi distribution function shown for three different values of the electron temperature (dashed and dash-dotted lines). The Fermi distributions are shown centered at the Fermi level at zero temperature. (b,c,d) Electron temperature dependence of thermophysical properties of aluminum: (b) the chemical potential, (c) the electron heat capacity, and (d) the electron-phonon coupling factor. Solid lines show the results of the calculations performed with DOS obtained from VASP. Dashed lines in (c) and (d) show the commonly used approximations of the thermophysical material properties based on experimental

measurements. The ranges of the electron temperature variation in the experiments/calculations used in the measurements of the electron-phonon coupling are shown by bold segments in (d). Dash-dotted lines in (c) and (d) show the predictions of the FEG model. Data presented in this figure is accessible in tabulated form from [53].

Similar to the chemical potential, the temperature dependence of the electron heat capacity calculated for Al DOS almost coincides with the one calculated for the free electron gas model DOS, Fig. 3-1(c). Moreover, the results of both calculations obtained with Eq. (3) can be well described by the linear dependence, $C_e = \gamma T_e$, with the theoretical value of the coefficient γ calculated within the free electron gas model using the number density of ‘free’ electrons in aluminum ($3s^2 3p^1$), $n_e = 3.0 \text{ atom}^{-1}$, as $\gamma_{th} = \pi^2 n_e k_B^2 / 2 \mathcal{E}_F = 91.2 \text{ Jm}^{-3}\text{K}^{-2}$, as shown in Fig. 3-1(c). Note that the experimental value of the electron heat capacity coefficient given in Ref. [47], $\gamma_{exp} = 135 \text{ Jm}^{-3}\text{K}^{-2}$, is ~48% higher than the theoretical value, $\gamma_{th} = 91.2 \text{ Jm}^{-3}\text{K}^{-2}$. This difference in γ can be explained by the fact that the experimental value of γ_{exp} is measured at very low temperatures ranging from 0.1 to 4.0 K [48], where one needs to consider an additional contribution to the electron heat capacity from the electron-phonon interaction, i.e. $C_e = \gamma_{th}(1 + \lambda)T_e$ [44]. Taking into account that, for aluminum, $\lambda \sim 0.42$ (Table 3.1), the agreement between the theoretical calculations of the electron heat capacity and the low-temperature experimental data is very good.

The calculation of the electron temperature dependence of the electron-phonon coupling is based on Eq. (3.8) and, apart from the electron DOS, requires the knowledge

of $\lambda\langle\omega^2\rangle$ material parameter. In the absence of experimental measurements of $\lambda\langle\omega^2\rangle$ for aluminum, a quantitative estimation can be obtained using the reported calculated and experimental values of λ ranging from 0.38 to 0.45 [43,49,50] and the approximation for $\langle\omega^2\rangle\sim\theta_D^2/2$ [43,51], yielding the range of values for $\lambda\langle\omega^2\rangle$ from 257.4 to 304.8 meV², as shown in Table 3.1. An alternative approach is to choose $\lambda\langle\omega^2\rangle$ based on the results of experimental measurements of electron-phonon coupling. Using the value of the electron-phonon coupling constant measured for Al in thermoreflectance pump-probe experiments [52], 2.45×10^{17} Wm⁻³K⁻¹, as $G(T_e=300\text{ K})$ in Eq. (3.8) yields $\lambda\langle\omega^2\rangle = 185.9$ meV². In this work, the latter value of $\lambda\langle\omega^2\rangle$ is adopted in the calculations of the temperature dependent electron-phonon coupling factor for aluminum.

Fig. 3-1(d) shows the electron-phonon coupling factor, $G(T_e)$, for aluminum, together with the result obtained with the free electron gas model DOS. The temperature dependence obtained with the aluminum DOS exhibits a sharp increase for electron temperatures up to 5000 K, followed by a slower increase and saturation at higher temperatures. The increase of the strength of the electron-phonon coupling with electron temperature can be interpreted based on analysis of the DOS for aluminum in the region around the Fermi energy affected by thermal excitations ($\sim k_B T_e$), Fig. 3-1(a). In contrast to the free electron gas model DOS, where the density of the states increases monotonically with energy, the value of the aluminum DOS at the Fermi level is smaller than that below the Fermi level. As a result, for aluminum, more excited electrons participate in the electron-phonon scattering processes at higher electron temperatures, leading to an increase of the rate of energy exchange between the electrons and the lattice. Note that the enhancement in the strength of the electron-phonon coupling observed for

aluminum is relatively small, as compared to other metals considered in this study (Sections 3.2-3.4), and reaches ~40% of the room temperature value as the electron temperature increases up to 1×10^4 K.

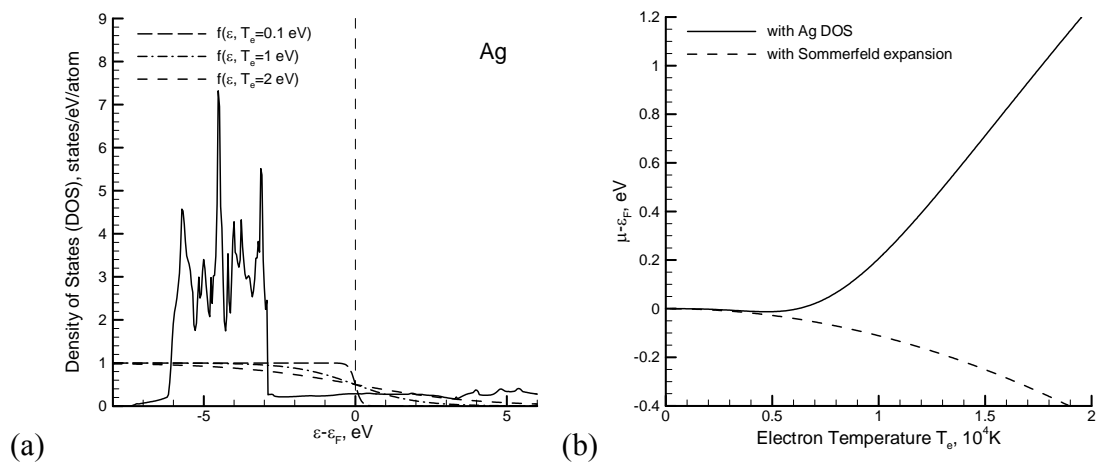
Contrary to the results for aluminum, the electron-phonon coupling calculated for the free electron gas model DOS slightly decreases with temperature, showing a very weak temperature dependence, Fig. 3-1(d). The difference in the low-temperature values of the electron-phonon coupling between the results obtained for aluminum and the free electron gas model DOS is related to the difference in the values of the two DOS at the Fermi level at 0 K, as can be seen from Fig. 3-1 (a).

Relating the temperature dependence of the electron-phonon coupling predicted for aluminum in this work to the literature values of the electron-phonon coupling constant, one should take into account that the dependence shown in Fig. 3-1(d) is based on fitting the room temperature value of $G(T_e)$ to $G_0 = 2.45 \times 10^{17} \text{ Wm}^{-3}\text{K}^{-1}$ measured in thermoreflectance pump-probe experiments performed under conditions when the estimated rise of the electron temperature does not exceed 170 K [52]. A somewhat higher value of $3.1 \times 10^{17} \text{ Wm}^{-3}\text{K}^{-1}$, obtained in a theoretical analysis of the kinetics of electron-phonon equilibration under conditions of laser excitation leading to $T_e^{max} \sim 3200$ K [54], is consistent with the predicted temperature dependence.

3.3.2 Silver, copper and gold

The electron DOS calculated with VASP for three noble metals, silver, copper and gold, Figs. 2-4(a), exhibit similar characteristics of the electron band structure. The common feature of the three DOS is the presence of prominent regions of high density of

states, associated with the d bands located $\sim 2\text{-}3$ eV below the Fermi level. The mere visual analysis of the DOS together with the Fermi distribution functions, shown in Figs. 2-4(a) for three electron temperatures, suggests that at low electron temperatures, $T_e \sim 0.1$ eV ($\sim 10^3$ K), the region of the electron DOS affected by thermal excitations ($\sim k_B T_e$) is similar to the one of the free electron gas model, with only s electrons being excited. At higher electron temperatures, $T_e \sim 1$ eV ($\sim 10^4$ K), a significant number of d band electrons can be excited and can make a substantial contribution to the thermophysical properties of the material. Indeed, at electron temperatures below ~ 5000 K for silver and ~ 3000 K for copper and gold, the calculated chemical potentials, Figs. 2-4(b), follow the dependence predicted from the Sommerfeld expansion of the electron free energy in the free electron gas model with one free electron per atom. At higher electron temperatures, however, the thermal excitation of electrons from the high density of states edge of the d band to the lower density of states s band results in the increase of the chemical potential and large deviations from the prediction of the free electron gas model.



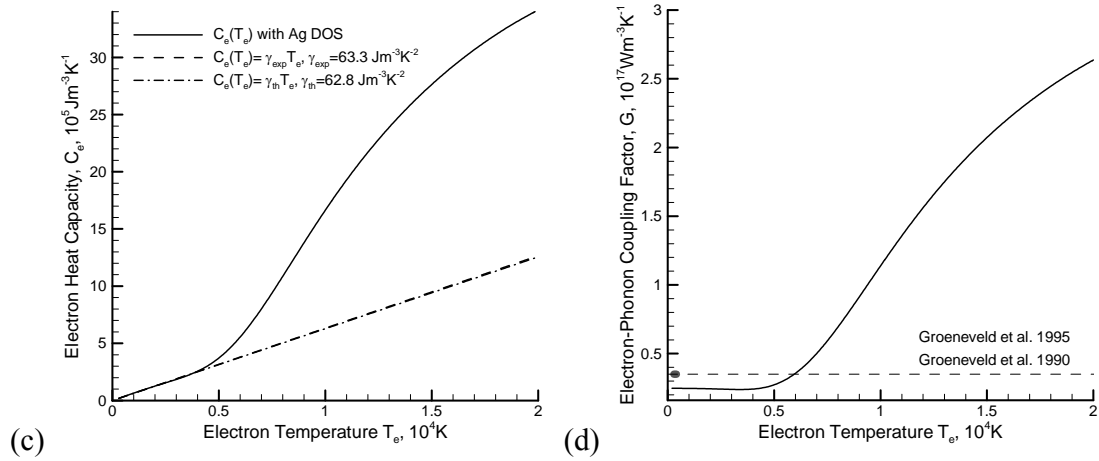


Figure 3-2. (a) The electron DOS of silver obtained in the electronic structure calculation performed with VASP (solid line) and the Fermi distribution function shown for three different values of the electron temperature (dashed and dash-dotted lines). The Fermi distributions are shown centered at the Fermi level at zero temperature. (b,c,d) Electron temperature dependence of thermophysical properties of silver: (b) the chemical potential, (c) the electron heat capacity, and (d) the electron-phonon coupling factor. Solid lines show the results of the calculations performed with DOS obtained from VASP. Dashed lines in (c) and (d) show the commonly used approximations of the thermophysical material properties based on experimental measurements. The ranges of the electron temperature variation in the experiments used in the measurements of the electron-phonon coupling are shown by bold segments in (d). Dash-dotted line in (c) shows the predictions of the free electron gas model. Data presented in this figure is accessible in tabulated form from [53].

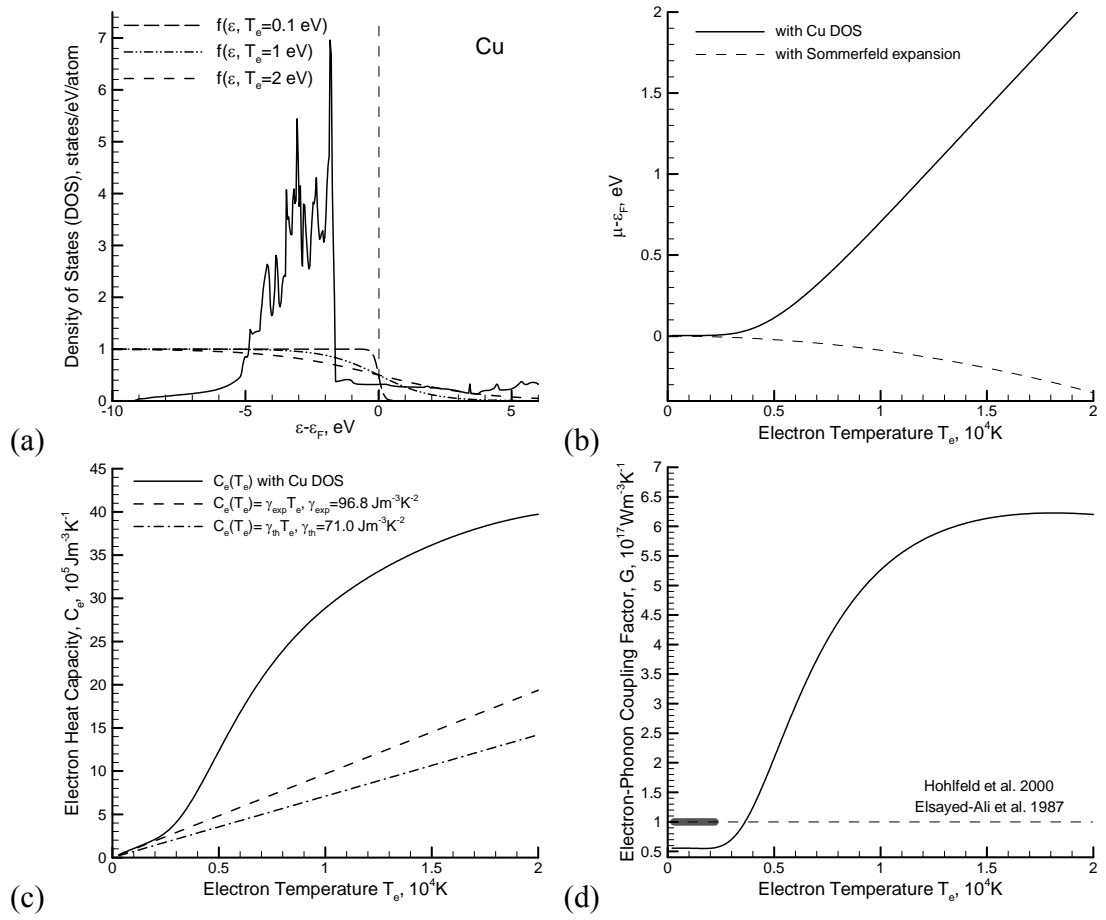
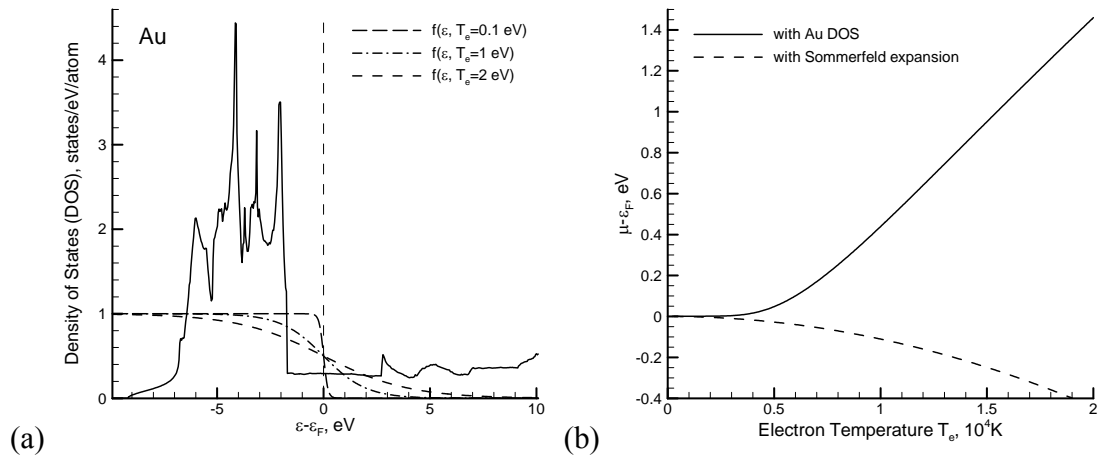


Figure 3-3. Same as Fig. 3-2 but for copper.



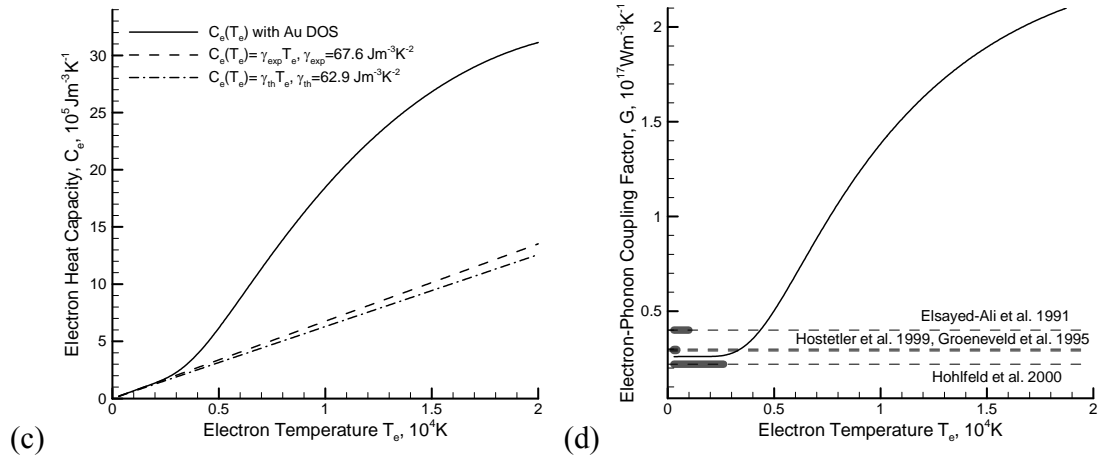


Figure 3-4. Same as Fig. 3-2 but for gold.

The results on the electron temperature dependence of the electron heat capacity, $C_e(T_e)$, obtained by incorporating the results for the chemical potential into Eq. (3.3), are shown for the three noble metals in Figs. 3-2, 3-3 and 3-4(c). For comparison, the linear dependences, $C_e(T_e) = \gamma T_e$, are plotted for both the low-temperature experimental values of the electron heat capacity coefficient, γ_{exp} ($63.3 \text{ Jm}^{-3} \text{ K}^{-2}$ for Ag, $96.8 \text{ Jm}^{-3} \text{ K}^{-2}$ for Cu, and $67.6 \text{ Jm}^{-3} \text{ K}^{-2}$ for Au [47]), and the theoretical value, calculated as $\gamma_{\text{th}} = \pi^2 n_e k_B^2 / 2 \varepsilon_F$ using the number density of s electrons in these noble metals, i.e. $n_e = 1.0 \text{ atom}^{-1}$ ($62.8 \text{ Jm}^{-3} \text{ K}^{-2}$ for Ag, $71.0 \text{ Jm}^{-3} \text{ K}^{-2}$ for Cu, and $62.9 \text{ Jm}^{-3} \text{ K}^{-2}$ for Au). A better, as compared to Al, agreement between the experimental and theoretical values of the heat capacity coefficients can be attributed to the lower values of the electron-phonon coupling constant, λ , and Debye temperature, θ_D , listed in Table 3.1 [44].

At low electron temperatures, below a few thousand Kelvins, the $C_e(T_e)$ dependences predicted by Eq. (3.3) follow closely the linear dependences plotted with experimental values of the heat capacity coefficients. However, as the electron

temperature becomes sufficiently high for thermal excitation of a significant number of d electrons, positive deviations from the linear temperature dependences are observed for all three noble metals. The deviations start at ~ 3000 K in Cu and Au, where the high-energy edge of the d-band is located ~ 2 eV below the Fermi energy, and at a higher temperature of ~ 5000 K in Ag, where the d-band is located deeper, ~ 3 eV below the Fermi level. The large deviations of the electron heat capacity from the linear dependence at electron temperatures that are readily achieved in laser material processing applications suggest that the application of the commonly used linear approximation $C_e(T_e) = \gamma T_e$ can result in a significant overestimation of the transient values of the electron temperature during the time of the electron-lattice nonequilibrium. The linear approximation is, therefore, inappropriate for quantitative modeling of the laser-induced processes in noble metals under conditions when the electron temperature exceeds several thousand Kelvins.

The effect of the thermal excitation of d band electrons, discussed above for electron heat capacity, has also strong implications for the temperature dependence of the electron-phonon coupling, $G(T_e)$. The results of the calculations of $G(T_e)$, performed with Eq. (3.8) for the three noble metals, are shown in Figs. 3-2 and 4(d). The common feature of the three dependences is a nearly constant strength of the electron-phonon coupling up to the temperatures of ~ 3000 K for Cu and Au and ~ 5000 K for Ag, and a significant strengthening of the electron-phonon coupling at higher temperatures, when a large number of d electrons are thermally excited and make contribution to the electron-phonon energy exchange. The rate and the degree of the increase of $G(T_e)$ with respect to the low-temperature levels, however, are different for the three metals and are defined by

the detailed structure of the DOS, particularly by the location, the width, and the shape of the d band. The d bands in Cu and Au are located at approximately the same depth under the Fermi level, but the width of the d band in Cu, ~ 3.5 eV, is much smaller than the one in Au, ~ 6 eV, Figs. 3-3 and 4(a). This difference in the width of the d band is reflected in a higher density of states at the high-energy edge of the d band in Cu as compared to Au. As a result, for the same electron temperature, the thermal excitation of d band electrons in Cu leads to a more significant increase in the electron-phonon coupling factor as compared to Au, e.g. at $T_e = 10^4$ K the electron-phonon coupling factor exceeds the room temperature value by a factor of 9.5 in Cu, Fig. 3-3(d), compared to 5.8 in Au, Fig. 3-4(d). The widths of the d bands in Ag and Cu are similar, but the separation of the d band from the Fermi level is larger in Ag, Figs. 3-2 and 3(a). As a result, at the same electron temperature of 10^4 K, the electron-phonon coupling in Cu exceeds its room temperature value by a factor of 9.5, as compared to 4.6 in Ag. Moreover, $G(T_e)$ saturates at $T_e \geq 1.5 \times 10^4$ K in Cu, but continues a sharp rise at and above this temperature in Ag, Figs. 3-2 and 3(d).

While the temperature dependences of the electron-phonon coupling calculated with Eq. (3.8) are defined mainly by the characteristics of the electron DOS, the low-temperature levels in these calculations are preset by the choice of the value of $\lambda \langle \omega^2 \rangle$. For Ag, the calculations are performed with a value of $\lambda \langle \omega^2 \rangle$ obtained using the approximation of $\langle \omega^2 \rangle \sim \theta_D^2/2$ and λ evaluated from the experimental electrical resistivity data [55], as shown in Table 3.1. This estimation of $\lambda \langle \omega^2 \rangle$ gives a relatively good agreement of the room temperature values of the electron-phonon coupling factor predicted by Eq. (3.8), $G(300\text{ K}) = 2.5 \times 10^{16} \text{ Wm}^{-3}\text{K}^{-1}$, with the experimental value of the

electron-phonon coupling constant, $3.5 \times 10^{16} \text{ Wm}^{-3}\text{K}^{-1}$, measured in femtosecond optical transient-reflection experiments performed at low laser excitations, when the increase of the electron temperature does not exceed 90 K [56,57].

For Cu and Au, the values of $\lambda \langle \omega^2 \rangle$ obtained in pump-probe reflectivity measurements, performed with laser excitations at which the electron temperature does not exceed 1000 K [58], are used in the calculations, Table 3.1. The levels of the low-temperature plateaus in the dependences $G(T_e)$ calculated for Cu and Au are in a good agreement with the values of the electron phonon coupling constants measured in pump-probe experiments, $3.5\text{-}4.0 \times 10^{16} \text{ Wm}^{-3}\text{K}^{-1}$ [59], $3.0 \times 10^{16} \text{ Wm}^{-3}\text{K}^{-1}$ [56], $2.9 \times 10^{16} \text{ Wm}^{-3}\text{K}^{-1}$ [52], $2.2 \times 10^{16} \text{ Wm}^{-3}\text{K}^{-1}$ [6] for Au, and $10^{17} \text{ Wm}^{-3}\text{K}^{-1}$ [6,60] for Cu. Note that all of these experiments are performed at relatively low laser excitations, when the variation of the electron temperature is limited to the range of temperatures up to ~ 3000 K, that corresponds to nearly constant values of the electron-phonon coupling factor, Fig. 3-3-4 (d).

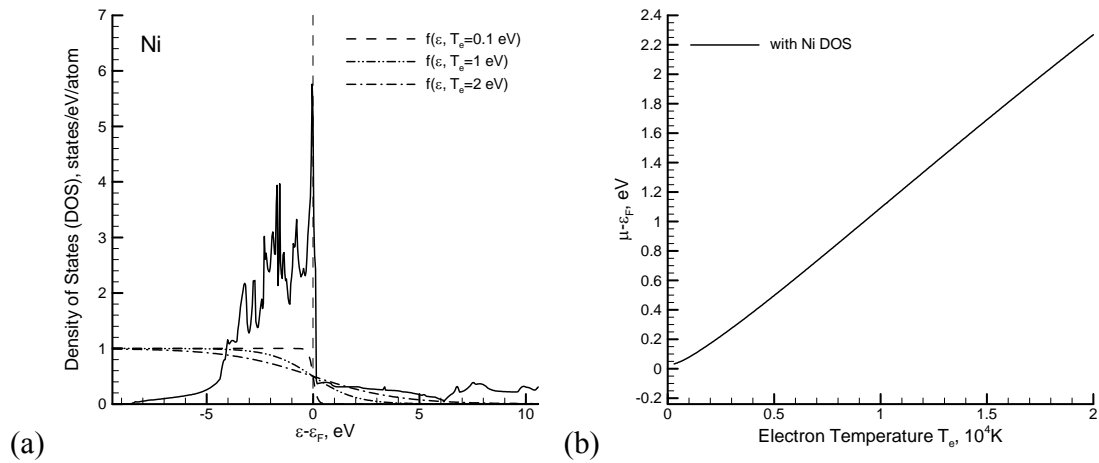
At higher laser fluences, typical for laser processing applications, the temperature dependence of the electron-phonon coupling starts to play an important role in defining the characteristics of the material response to the laser excitation. The enhancement of the electron-phonon coupling at high electron temperatures implies a faster energy transfer from the hot electrons to the lattice, generation of stronger thermoelastic stresses, reduction of the threshold fluences for the onset of laser melting and ablation, as well as changes in the timescales of the laser induced phase transformations. In particular, the results of recent TTM-MD simulations of femtosecond laser melting of 20 nm Au films [20] demonstrate that the time of the melting onset, measured in time-resolved electron

diffraction experiments [31,61], can only be reproduced with a model accounting for the temperature dependence of the electron-phonon coupling. A simulation performed with a constant electron-phonon coupling and a linear temperature dependence of the electron heat capacity is found to overpredict the time of the beginning of the melting process by a factor of 2. Similarly, an introduction of the temperature dependent electron-phonon coupling is found to be necessary in order to reconcile the calculated and experimental values of the ablation threshold and the fluence dependence of the ablation depth in Au films irradiated by 500 fs laser pulses [33,35], as well as to provide a good computational description of electron photoemission data [18,34,30].

In this study, no attempt has been made to account for the modifications in the electron DOS due to the changes of the electronic structure at elevated electron temperatures. Recent electronic structure calculations performed for Au and Al at an electronic temperature of 6 eV [62] predict that the reduced screening due to the thermal excitation of d band electrons results in a significant width compression and shift to lower energies of the d band in Au, whereas the Al electron DOS at 6 eV remains the same as the one at 0 K. Although the modifications of the electron DOS of Au at high electron temperatures would not affect the essential physics responsible for the temperature dependence of the electron heat capacity and electron-phonon coupling, they may introduce some quantitative corrections to these dependences and should be taken into account in a more detailed analysis of the material response to the extreme levels of laser excitation. In the range of electron temperatures considered in this work ($T_e \leq 2$ eV), however, the effect of the modification of the electron DOS on the calculated thermophysical properties is expected to be relatively small.

3.3.3 Nickel and platinum

In transition metals with almost full d-bands, such as Ni and Pt, the Fermi level cuts through the high energy edge of the d bands, Figs. 3-5-6(a), leading to a very high density of electron states at the Fermi level. The d band electrons at the energy levels around the Fermi energy can be easily excited even at low electron temperatures, shifting the Fermi level (chemical potential) to higher energies, Figs. 3-5 and 6(b), and altering the electron heat capacity and the electron-phonon coupling in a way very different from what is discussed above for the free electron gas model, Al, and noble metals. Indeed, the excitation of electrons from the high density of states d-band to the much lower density of states s band, Figs. 3-5 and 6(a), and the shift of the chemical potential to higher energies, away from the high density of states edge of the d band, Figs. 5-6(b), result in strong negative deviations of the heat capacity from the linear dependences, $C_e(T_e) = \gamma T_e$, shown in Figs. 3-5 and 6(c) for low-temperature experimental values of the coefficient γ ($1077.4 \text{ Jm}^{-3}\text{K}^{-2}$ for Ni and $748.1 \text{ Jm}^{-3}\text{K}^{-2}$ for Pt [47]).



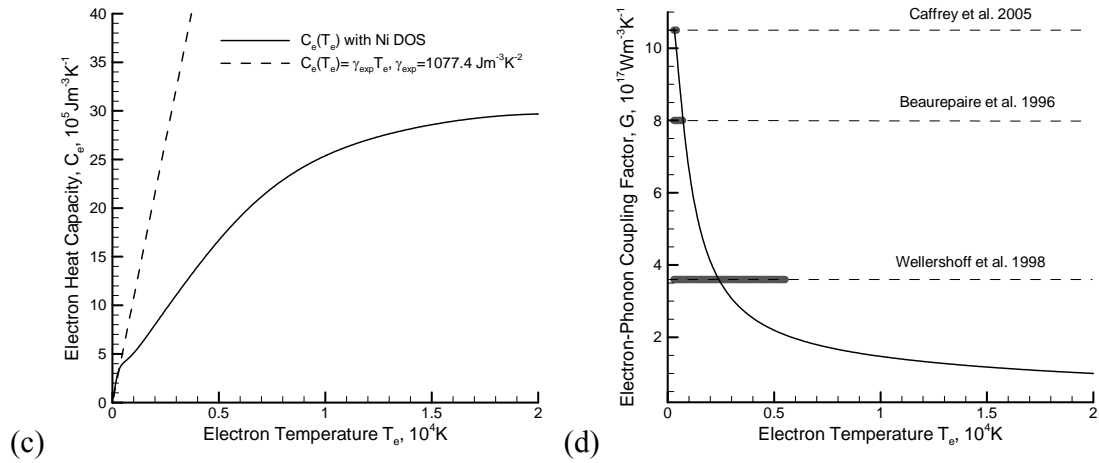


Figure 3-5. Same as Fig. 2 but for nickel.

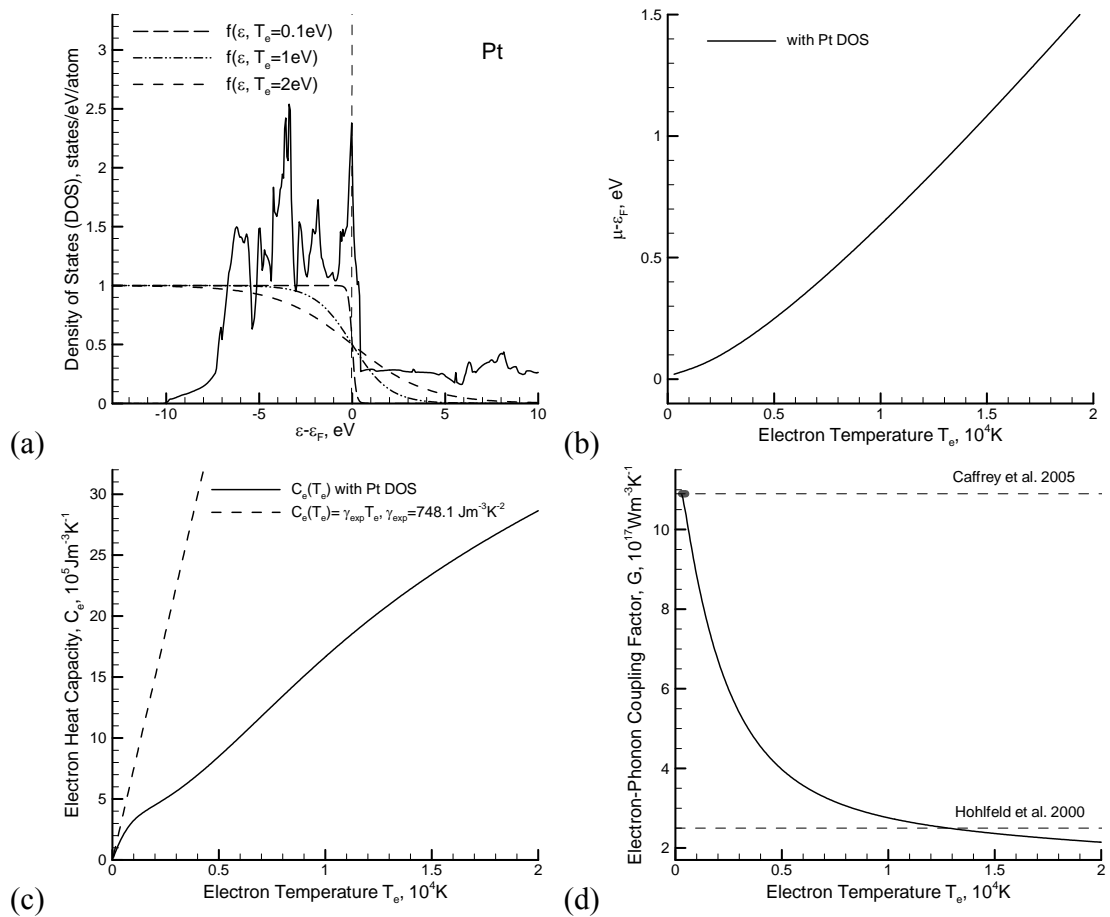


Figure 3-6. Same as Fig. 3-2 but for platinum. The range of the electron temperature variation in the experiment used in the measurement of the electron-phonon coupling of Pt by Hohlfeld et al. is not given in Ref. [6] and, therefore, is not shown in (d).

The trend of the negative deviation of the electron heat capacity from the linear dependence agrees with experimental results reported in Ref. [63] for Ni and Pt, where the electronic heat capacity was obtained by subtracting the lattice heat capacity (assumed to follow the Dulong-Petit law at high temperatures), from the total heat capacity measured in experiments for temperatures up to 1600 K. The results of the calculations of the electron heat capacity of Pt, shown in Fig. 3-5(c), are also consistent with earlier calculations reported in Ref. [22].

The temperature dependences of the electron-phonon coupling are shown for Ni and Pt in Figs. 3-5 and 6(d). The values of $\lambda\langle\omega^2\rangle$, used in the calculations, are based on the values of the electron-phonon coupling constants measured in pump-probe reflectivity experiments, $10.5\times 10^{17} \text{ Wm}^{-3}\text{K}^{-1}$ for Ni and $10.9\times 10^{17} \text{ Wm}^{-3}\text{K}^{-1}$ for Pt [37]. Since the experiments were performed under low-excitation conditions, when the transient increase of the electron temperature above the room temperature did not exceed 100 K for Ni and 150 K for Pt, the measured coupling constants are taken here as the room temperature values and are used in Eq. (3.8) to obtain $\lambda\langle\omega^2\rangle$ listed in Table 1. These values of $\lambda\langle\omega^2\rangle$ are relatively close to the estimations based on experimental measurements of λ and the approximation for $\langle\omega^2\rangle\sim\theta_D^2/2$, see Table 3.1.

The temperature dependences of the electron-phonon coupling predicted for Ni and Pt are similar and are characterized by a steep decrease as temperature increases up to $3\text{-}5 \times 10^3$ K, followed by a slower decrease with further temperature rise. This temperature dependence can be explained based on the analysis of the electron DOS of the two transition metals, Figs. 3-5 and 6(a). Thermal excitation of d band electrons leads to the shift of the chemical potential to higher energies and away from the high density of states edge of the d-band, Figs. 3-5 and 6(b). This shift reduces the contribution of the d band electrons to the electron-phonon coupling, with the reduction being particularly sharp as the temperature increases up to several thousand Kelvin, leading to the separation of the Fermi level from the edge of the d band. In particular, as the electron temperature increases up to 5000 K, the electron-phonon coupling drops, with respect to the room temperature values, by a factor of 4.8 for Ni and 2.8 for Pt. Further slower decrease of the electron-phonon coupling is defined by the balance between the increased probability of the thermal excitations from deeper energy levels and the continuing shift of the chemical potential to higher energies.

The reduction in the strength of the electron-phonon coupling with increasing electron temperature is consistent with the relative values of the electron-phonon coupling constants obtained in experiments performed at different levels of laser excitation. In particular, for Ni, the highest value of the electron-phonon constant, $10.5 \times 10^{17} \text{ Wm}^{-3}\text{K}^{-1}$, is measured in transient thermoreflectance experiments [37], where the maximum electron temperature increase does not exceed 100 K. A somewhat smaller value of $8 \times 10^{17} \text{ Wm}^{-3}\text{K}^{-1}$ is deduced from pump-probe transmission experiments [38], where the electron temperature goes up to 700 K. Finally, the smallest value of the

coupling constant, $3.6 \times 10^{17} \text{ Wm}^{-3}\text{K}^{-1}$, is obtained by fitting the predictions of the TTM calculations to the threshold fluences for the onset of surface melting [39]. The electron temperature in the latter case reaches several thousands of Kelvin and the reported value of the effective electron-phonon coupling “constant” is consistent with the temperature dependence shown in Fig. 3-5(d).

Large negative deviations of the electron heat capacity from the linear temperature dependence suggest that the commonly used linear temperature dependence may result in a significant underestimation of the transient values of the electron temperature during the time of the electron-phonon nonequilibrium in Ni and Pt targets. The fast drop of the strength of the electron-phonon coupling with increasing electron temperature, on the other hand, can slow down the electron-lattice energy equilibration and reduce the localization of the deposited laser energy in the surface region of the irradiated target. Incorporation of the new temperature dependences into TTM or TTM-MD models may improve the reliability of the models in quantitative analysis of practically important characteristics in laser processing applications. In particular, preliminary TTM calculations incorporating the new temperature dependence of the thermophysical parameters in Ni [21], predict the threshold laser fluences for surface melting in films of different thicknesses that are closer to the experimentally measured values as compared to the results obtained with commonly used approximations of the thermophysical parameters.

3.3.4 Tungsten and titanium

The last two metals considered in this study are W and Ti, transition metals with BCC and hcp crystal structures, respectively. The characteristic feature of the electron

DOS of these metals is a wide (~ 10 eV) less than half filled d band with relatively small values of density-of-states at the Fermi level, located within a local dip in the DOS, Figs. 3-7 and 8(a). The complex structure of the DOS results in a complex and, in some cases, non-monotonic temperature dependences of the thermophysical parameters of these metals.

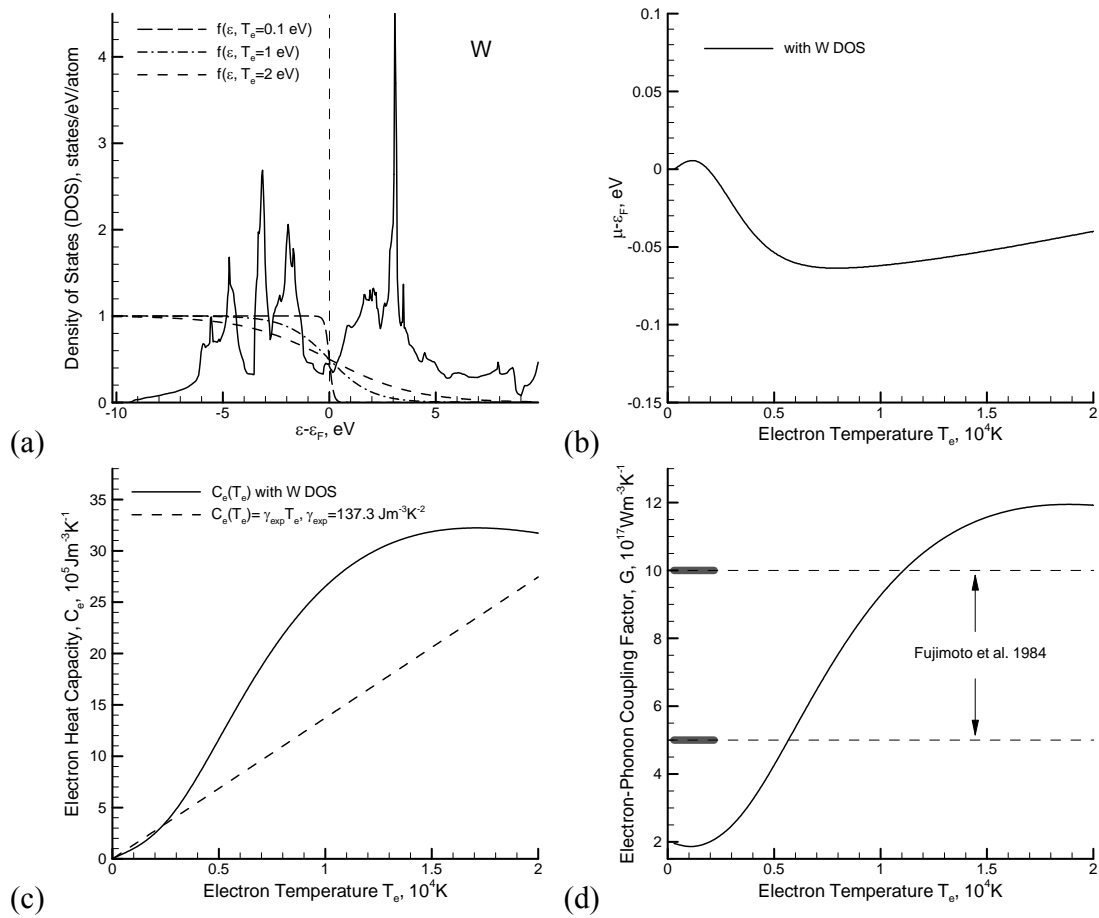


Figure 3-7. Same as Fig. 3-2 but for tungsten.

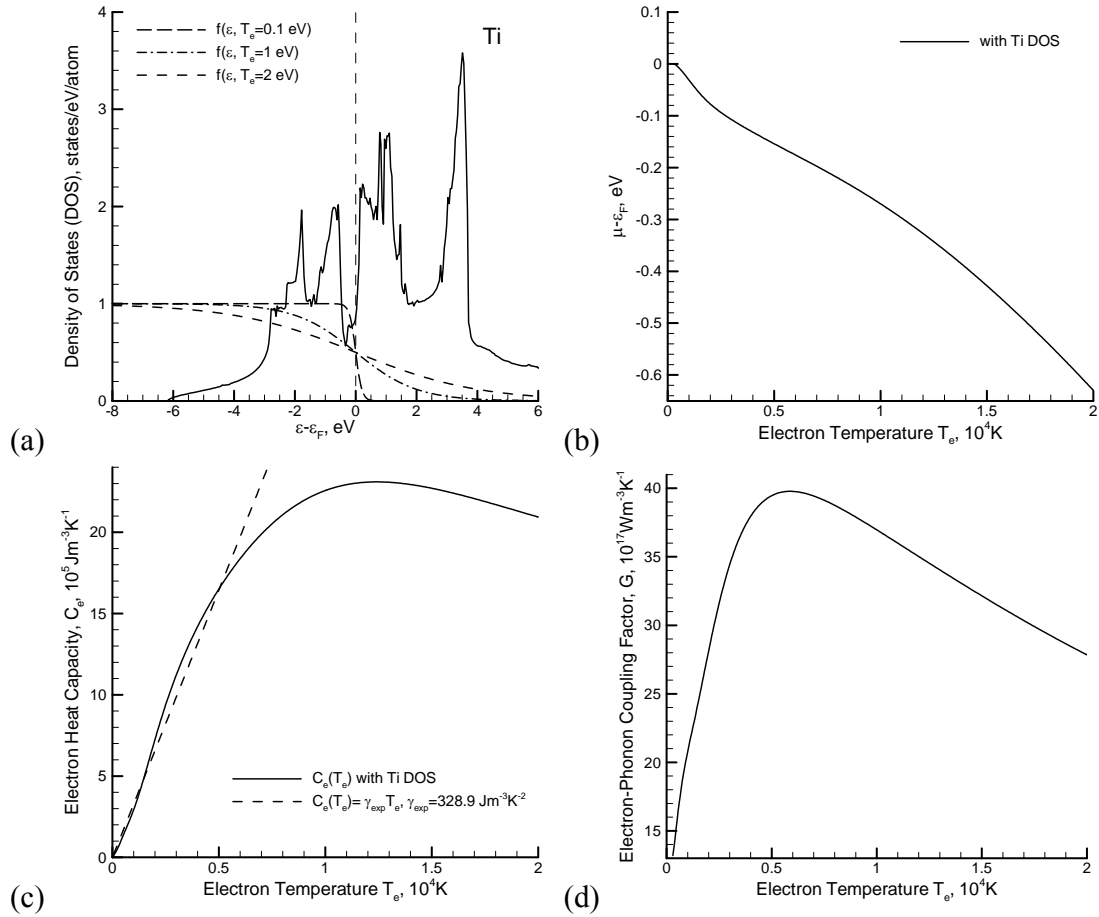


Figure 3-8. Same as Fig. 3-2 but for titanium.

In tungsten, the region of thermal excitations ($\sim k_B T_e$) at low temperatures, below $\sim 3000 \text{ K}$, has nearly the same density of states residing on both sides of the Fermi level, Fig. 3-7(a), resulting in relatively small variations of the chemical potential, Fig. 3-7(b), and the temperature dependence of the electron heat capacity following the linear dependence characteristic of the free electron gas model. At electron temperatures exceeding 3000 K , the temperature dependence of the electron heat capacity exhibits positive deviations from the linear dependence, Fig. 3-7(c), similar to the ones predicted for noble metals, Figs. 3-2, 3 and 4(c). The split from the linear dependence in W,

however, is not as drastic as in the case of the noble metals, with the maximum deviation observed at a temperature of 1.1×10^4 K, when the heat capacity exceeds the value predicted by the linear dependence by a factor of 1.9. At higher temperatures, the electron heat capacity saturates and even starts to decrease at $T_e \geq 1.7 \times 10^4$ K.

The comparison of the DOS of noble metals, Fig. 3-2, 3 and 4 (a), and tungsten, Fig. 3-7(a), reveals that the high density of states peaks of the d band in W are closer to the Fermi level, which, unlike in the case of the noble metals, does not shift to higher energies with increasing electron temperature, compare Figs. 3-2, 3 and 4(b) and 3-7(b). Furthermore, the number of occupied d states in W is much smaller due to fewer 5d electrons in W as compared to the number of d electrons in the noble metals. As a result, the effective contribution of the presence of high density of d states on both sides of the Fermi level to the electron heat capacity of W diminishes at temperatures exceeding $\sim 1 \times 10^4$ K.

The characteristic features of the electron DOS of W discussed above also affect the temperature dependence of the electron-phonon coupling, Fig. 3-7(d). While a significant increase of the strength of the electron-phonon coupling is ensured by the high values of the density of states on both sides from the Fermi level, the coupling tends to saturate at $T_e \geq 1.5 \times 10^4$ K. This behavior can be related to the results obtained for Cu, whose d band is relatively close to the Fermi level and narrow in width, Fig. 3-3(d). Although, due to the larger number of d electrons, the increase in the electron-phonon coupling above the room temperature value is larger in Cu (11-fold increase in Cu vs. 6-fold increase in W at $T_e = 2 \times 10^4$ K), the overall shapes of the temperature dependences are similar for the two metals. Similar temperature dependences of the electron heat

capacity and the electron-phonon coupling are also predicted for molybdenum [53], that has the characteristics of the electron DOS similar to tungsten.

The predicted temperature dependence of the electron-phonon coupling for W can be related to the results of pump-probe photoemission measurements, suggesting that the value of the electron-phonon coupling constant is within the range of $5\text{--}10 \times 10^{17} \text{ Wm}^{-3}\text{K}^{-1}$ [64]. Although these values are within the range of variation of the electron-phonon coupling, predicted in this work, Fig. 3-7(d), the electron temperature variations estimated for the laser excitations used in the pump-probe experiments are within several thousand Kelvins, where the coupling strength exhibits relatively weak temperature dependence. The low-temperature value of $\lambda \langle \omega^2 \rangle$, obtained in pump-probe reflectivity measurements [58] and used in the calculation of the temperature dependence shown in Fig. 3-7(d), yields a value of the coupling constant, $2 \times 10^{17} \text{ Wm}^{-3}\text{K}^{-1}$, that is outside the range suggested in Ref. [64]. This discrepancy in the reported experimental values suggests that additional accurate measurements of the electron-phonon coupling at low excitation levels are needed to verify the position of the low temperature level of the coupling strength in the dependence shown in Fig. 3-7(d).

A distinct characteristic of the electron DOS of titanium is the presence of a high density of available d states right above the Fermi level, Fig. 3-8(a). Thermal excitation of d electrons to the higher density of states energy region leads to a shift of the chemical potential to lower energies. The electron heat capacity, however, follows the linear dependence up to $\sim 6000 \text{ K}$ and exhibits a sharp turn from an almost linear increase to a decrease after reaching its maximum value at $\sim 1.2 \times 10^4 \text{ K}$. Similarly, the electron-phonon coupling is showing a non-monotonic temperature dependence, with a strong

enhancement of the coupling strength at $T_e \leq 5000$ K, followed by a decrease at $T_e \geq 6000$ K.

An interpretation of the temperature dependences predicted for Ti can be provided based on the analysis of the contributions from the two high density of states regions present on both sides of the Fermi level, similar to the case of W discussed above. At quantitative level, however, the transitions from the increase to the saturation and the decrease of both the electron heat capacity and the electron-phonon coupling takes place within a much narrower electron temperature range in Ti, as compared to W. The differences in temperature sensitivity of the thermophysical parameters of the two metals can be explained by the quantitative differences in their electron DOS. In particular, a smaller number of d electrons, a smaller width of the occupied part of the d-band, and a large gap between two high-density peaks at ~ 1 eV and ~ 3.5 eV above the Fermi level are the factors that contribute to the higher temperature sensitivity of the electron heat capacity and the electron-phonon coupling in Ti, as compared to W.

For the electron-phonon coupling in titanium, a high value of $10^{19} \text{ Wm}^{-3}\text{K}^{-1}$ have been estimated from fitting the sputtering yields measured in heavy ion bombardment of Ti targets to the predictions of the inelastic thermal spike model [3,65]. This value is more than twice larger than the maximum value obtained in the present calculations, Fig. 8(d). Given the uncertainty with respect to an adequate representation of the sputtering mechanisms by the inelastic thermal spike model, however, the accuracy of the evaluation of the coupling constant in sputtering experiments is limited and the predicted value can be considered only as a rough estimate. The temperature dependence, shown in Fig. 3-8(d), is based on the value of $\lambda\langle\omega^2\rangle$, obtained in pump-probe reflectivity

experiments [58] and corresponding to the room temperature electron-phonon coupling factor of $1.3 \times 10^{18} \text{ Wm}^{-3}\text{K}^{-1}$. While the low-temperature value of the electron-phonon coupling factor may require further verification in accurate pump-probe experiments, it is apparent, from the results of the calculations presented in this work, that the strong temperature dependences of the electron-phonon coupling and the electron heat capacity are the direct consequences of the characteristics of the electron DOS and should be taken into account in interpretation of experimental data obtained under conditions when the transient values of the electron temperature undergo significant variations.

3.4 Summary

The connections between the electron DOS and the electron temperature dependences of the electron-phonon coupling and the electron heat capacity are investigated for eight representative metals (aluminum, copper, silver, gold, nickel, platinum, tungsten, and titanium). The electron DOS used in the calculations of the thermophysical properties are obtained from ab initio electronic structure calculations performed within the density functional theory. The results of the calculations suggest that the effect of the thermal excitation of electrons on the thermophysical properties is sensitive to the structure of the electron DOS and can lead to large variations of the properties under conditions of electron-phonon non-equilibrium generated in the material by short pulse laser irradiation.

For Al, the free electron gas model provides a good description of the temperature dependence of the electron heat capacity, but fails to predict a relatively moderate (~40%) increase in the strength of the electron-phonon coupling with increasing electron

temperature. In noble metals (Au, Cu, Ag), the electron heat capacity and the electron-phonon coupling factor are strongly enhanced by the thermal excitation of d band electrons at electron temperatures exceeding several thousand Kelvins. In Ni and Pt, on the other hand, the location of the Fermi level at the high density of states edge of the d band results in the opposite trend, when the thermal excitation of d band electrons leads to a drastic decrease in the electron-phonon coupling factor and large negative deviations of the electron heat capacity from the linear dependence on the electron temperature. For W and Ti, the location of the Fermi level in the middle of partially filled d band, in a local dip in the electron DOS, results in complex non-monotonic dependences of the thermophysical parameters on the electron temperature.

Thus, depending on the electronic structure of a metal, the electron heat capacity and the electron-phonon coupling factor can increase, decrease, or exhibit non-monotonic changes in response to the increase of the electron temperature. The range of electron temperatures considered in this work, up to 2×10^4 K is typical for the electron temperature variations in ultrafast laser material processing applications. The strong deviations of the thermophysical parameters from the commonly used approximations of a constant electron-phonon coupling and a linear dependence of the electron heat capacity, revealed in this work, have important implications for quantitative computational analysis of ultrafast processes associated with laser interaction with metals. A number of practically important characteristics of the laser-material interaction, such as the threshold fluences for the onset of melting and ablation, the strength of the laser-induced stress wave, the emission of electrons from the irradiated surface, and the depth of the melting and/or heat-affected zone, can all be significantly altered by the transient changes

of the thermophysical parameters of the material occurring during the time of electron-phonon equilibration.

3.5 Appendix

For the completeness of the discussion of the electron-phonon coupling, presented in Section 3.2.4, the derivation of the equation for the temperature dependence of the electron-phonon coupling, Eq. (3.8), not explicitly shown by Wang *et al.* in Ref. [18], is given in this Appendix. The approximations used in the derivation are discussed, and the results obtained with the approximate Eq. (3.8) are compared with predictions of the full integration treatment of the energy exchange rate between the electrons and the phonons.

The expression for the electron-phonon energy exchange rate in Eq. (3.6) can be rewritten as:

$$\left. \frac{\partial E_e}{\partial t} \right|_{ep} = 2\pi g(\varepsilon_F) \int_0^\infty d\Omega \hbar \Omega \int_{-\infty}^\infty d\varepsilon \int_{-\infty}^\infty d\varepsilon' \alpha^2 F(\varepsilon, \varepsilon', \Omega) S(\varepsilon, \varepsilon') \delta(\varepsilon - \varepsilon' + \hbar \Omega) \quad (3.9)$$

where $S(\varepsilon, \varepsilon') = [f(\varepsilon) - f(\varepsilon')]n(\hbar\Omega, T_l) - f(\varepsilon')[1 - f(\varepsilon)]$, and $f(\varepsilon)$ and $n(\hbar\Omega, T_l)$ denote the Fermi-Dirac and Bose-Einstein distribution functions, respectively:

$f(\varepsilon) = 1/[1 + \exp((\varepsilon - \mu)/k_B T_e)]$ and $n(\hbar\Omega, T_l) = 1/[\exp(\hbar\Omega/k_B T_l) - 1]$. It is convenient to rewrite the thermal factor as

$$\begin{aligned} S(\varepsilon, \varepsilon') &= [f(\varepsilon) - f(\varepsilon')] \left\{ n(\hbar\Omega, T_l) - \frac{f(\varepsilon')[1 - f(\varepsilon)]}{f(\varepsilon) - f(\varepsilon')} \right\} = \\ &= [f(\varepsilon) - f(\varepsilon')] [n(\hbar\Omega, T_l) - n(\varepsilon' - \varepsilon, T_e)] \end{aligned} \quad (3.10)$$

From the conservation of the total energy in the electro-phonon scattering processes, i.e. $\varepsilon' = \varepsilon + \hbar\Omega$, one can simplify Eq. (3.9) by eliminating the integration over ε' . Further,

under the experimental conditions characteristic of laser processing, the high-temperature approximations ($\hbar\Omega \ll k_B T_e$, $\hbar\Omega \ll k_B T_l$) of the Bose-Einstein distribution functions present in Eq. (3.10) can be used. Then, Eq. (3.9) takes the following form:

$$\left. \frac{\partial E_e}{\partial t} \right|_{ep} = 2\pi g(\varepsilon_F) k_B (T_l - T_e) \int_0^\infty d\Omega \int_{-\infty}^\infty d\varepsilon \alpha^2 F(\varepsilon, \varepsilon + \hbar\Omega, \Omega) [f(\varepsilon) - f(\varepsilon + \hbar\Omega)] \quad (3.11)$$

Using the assumption that $|M_{kk'}|^2$, when averaged over scattering angles, is independent of the electron states, the electron-phonon spectral function can be approximated as [18], $\alpha^2 F(\varepsilon, \varepsilon + \hbar\Omega, \Omega) = [g(\varepsilon)g(\varepsilon + \hbar\Omega)/g^2(\varepsilon_F)]\alpha^2 F(\varepsilon_F, \varepsilon_F, \Omega)$. This approximation provides a simple description of the electron energy dependence of the Eliashberg spectral function based on the electron DOS. More sophisticated representations of the spectral function for different excited electron transitions, such as *ab initio* calculations using the linear-response approach [66], have a potential for more accurate description of the temperature dependence of the electron-phonon coupling without making the assumption of the independence of the electron-phonon scattering matrix elements on the electron states. A more detailed consideration of the spectral function may introduce additional corrections to the temperature dependence of the electron-phonon coupling predicted in this work.

The approximate expression of the electron-phonon spectral function discussed above can be further simplified by assuming that $g(\varepsilon + \hbar\Omega) \sim g(\varepsilon)$, since ε varies in a much wider range (on the order of eVs) than $\hbar\Omega$ (~ 50 meVs, defined by the Debye frequency). Then, Eq. (3.11) can be re-written as

$$\left. \frac{\partial E_e}{\partial t} \right|_{ep} = 2\pi\hbar g(\varepsilon_F) k_B (T_l - T_e) \int_0^\infty d\Omega \alpha^2 F(\Omega) \Omega \int_{-\infty}^\infty d\varepsilon \frac{g(\varepsilon)^2}{g(\varepsilon_F)^2} \left(-\frac{\partial f}{\partial \varepsilon} \right) \quad (3.12)$$

Expressing the integral over phonon frequencies through $\lambda \langle \omega^2 \rangle$, defined in Section 3.2.4, and introducing the temperature dependent electron-phonon coupling factor through $\partial E_e / \partial t|_{ep} = G(T_e)(T_l - T_e)$, one can arrive to the expression for $G(T_e)$ given by Eq. (3.8).

Alternatively, one can obtain $G(T_e)$ without making an assumption of $g(\varepsilon + \hbar\Omega) \sim g(\varepsilon)$, as well as without using the high-temperature approximations of the Bose-Einstein distribution functions in the derivation of Eq. (3.12). This can be done by a straightforward numerical calculation of the rate of the electron-phonon energy exchange $\partial E_e / \partial t$ directly from Eq. (3.9), while retaining the description of the electron energy dependence of the electron-phonon spectral function based on the electron DOS.

The temperature dependent electron-phonon coupling can then be directly related to the rate of the energy exchange between the electrons and the lattice:

$$G(T_e) = \frac{2\pi\hbar g(\varepsilon_F)}{T_l - T_e} \int_0^\infty d\Omega \alpha^2 F(\Omega) \Omega \int_{-\infty}^\infty d\varepsilon \frac{g(\varepsilon)g(\varepsilon + \hbar\Omega)}{g(\varepsilon_F)^2} S(\varepsilon, \varepsilon + \hbar\Omega) \quad (3.13)$$

In order to evaluate the assumptions made in the derivation of Eq. (3.8), the temperature dependence of the electron-phonon coupling is calculated for aluminum at $T_l = 300$ K with both theoretical approaches, i.e. Eq. (3.8) and Eq. (3.13). The spectral function $\alpha^2 F(\Omega)$ obtained in *ab initio* linear-response calculations for aluminum [50] is used in Eq. (3.13), and the electron DOS of the free electron gas model and aluminum are used in both calculations. The comparison of the results obtained with the two approaches, shown in Fig. 3-9, suggests that the approximation of $g(\varepsilon + \hbar\Omega) \sim g(\varepsilon)$ has

negligible effect on the temperature dependence of the calculated coupling factor, whereas the increasing deviation between the predictions of the two methods at low T_e can be related to the high-temperature approximations of the Bose-Einstein distribution functions used in the derivation of Eq. (3.8). Additional calculations of $G(T_e)$ for other metals performed with Eq. (3.13) also show similarly small deviations from the results obtained with Eq. (3.8).

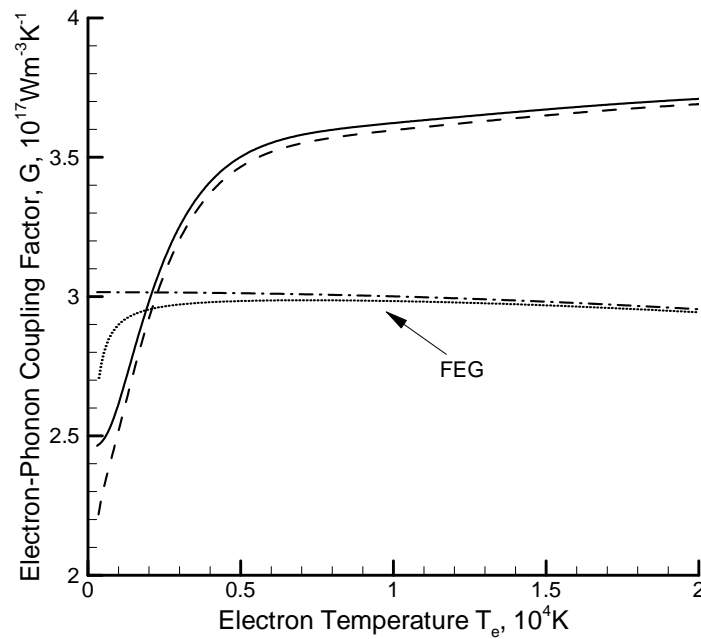


Figure 3-9. Temperature dependence of the electron-phonon coupling factor calculated with aluminum (solid and dashed lines) and the free electron gas model (dash-dotted and dotted lines) electron DOS using Eq. (3.8) (solid and dash-dotted lines) and Eq. (3.13) (dashed and dotted lines). The results obtained with Eq. (3.13) are normalized so that $\lambda\langle\omega^2\rangle$ calculated from $\alpha^2F(\Omega)$ has the same value as the one used in Eq. (3.8), i.e. 185.9 meV² shown for aluminum in Table 3.1.

References for Chapter 3

- [1] S. I. Anisimov, B. L. Kapeliovich, and T. L. Perel'man, Zh. Eksp. Teor. Fiz. **66**, 776 (1974) [Sov. Phys. JETP **39**, 375 (1974)].
- [2] Z. G. Wang, Ch. Dufour, E. Paumier, and M. Toulemonde, J. Phys.: Condens. Matter **6**, 6733 (1994).
- [3] M. Toulemonde, W. Assmann, C. Trautmann, F. Grüner, H. D. Mieskes, H. Kucal, and Z.G. Wang, Nucl. Instr. Meth. **212**, 346 (2003).
- [4] T. Q. Qiu and C. L. Tien, J. Heat Transfer **115**, 842 (1993).
- [5] P. E. Hopkins and P. M. Norris, Appl. Surf. Sci. **253**, 6289 (2007).
- [6] J. Hohlfeld, S.-S. Wellershoff, J. Güdde, U. Conrad, V. Jähnke, and E. Matthias, Chem. Phys. **251**, 237 (2000).
- [7] J. K. Chen and J. E. Beraun, Numer. Heat Transfer, Part A **40**, 1 (2001).
- [8] J. K. Chen, J. E. Beraun, L. E. Grimes, and D. Y. Tzou, Int. J. Solids Struct. **39**, 3199 (2002).
- [9] E. Carpenne, Phys. Rev. B **74**, 024301 (2006).
- [10] H. Hakkinen and U. Landman, Phys. Rev. Lett. **71**, 1023 (1993).
- [11] C. Schäfer, H. M. Urbassek, and L. V. Zhigilei, Phys. Rev. B **66**, 115404 (2002).
- [12] D. S. Ivanov and L. V. Zhigilei, Phys. Rev. B, **68**, 064114 (2003).
- [13] E. Leveugle, D. S. Ivanov, and L. V. Zhigilei, Appl. Phys. A **79**, 1643 (2004).
- [14] Z. Lin and L. V. Zhigilei, Phys. Rev. B **73**, 184113 (2006).
- [15] C. Cheng and X. Xu, Phys. Rev. B **72**, 165415 (2005).
- [16] F. Gao, D. J. Bacon, P. E. J. Flewitt, and T. A. Lewis, Modelling Simul. Mater. Sci. Eng. **6**, 543 (1998).
- [17] D. M. Duffy and A. M. Rutherford, J. Phys: Cond. Matt. **19**, 016207 (2007).

- [18] X. Y. Wang, D. M. Riffe, Y. S. Lee, and M. C. Downer, Phys. Rev. B **50**, 8016 (1994).
- [19] A. N. Smith and P. M. Norris, Proceedings of 11th International Heat Transfer Conference **5**, 241, 1998.
- [20] Z. Lin and L. V. Zhigilei, Proc. SPIE **6261**, 62610U (2006).
- [21] Z. Lin and L. V. Zhigilei, Appl. Surf. Sci. **253**, 6295 (2007).
- [22] T. Tsuchiya and K. Kawamura, Phys. Rev. B **66**, 094115 (2002).
- [23] G. Kresse and J. Hafner, Phys. Rev. B **47**, 558 (1993); *ibid.* **49**, 14251 (1994).
- [24] G. Kresse and D. Joubert, Phys. Rev. B **59**, 1758 (1999).
- [25] H. J. Monkhorst and J. D. Pack, Phys. Rev. B **13**, 5188 (1976).
- [26] A. E. Mattsson, P. A. Schultz, M. P. Desjarlais, T. R. Mattsson, and K. Leung, Modelling Simul. Mater. Sci. Eng. **13**, R1 (2005).
- [27] N. W. Ashcroft and N. D. Mermin, *Solid State Physics* (Holt, Rinehart and Winston, New York, 1976).
- [28] M. Kaveh and N. Wiser, Adv. Phys. **33**, 257 (1984).
- [29] M. I. Kaganov, I. M. Lifshitz, and L. V. Tanatarov, Zh. Eksp. Teor. Fiz. **31**, 232 (1956) [*Sov. Phys. JETP* **4**, 173 (1957)].
- [30] W. S. Fann, R. Storz, H. W. K. Tom, and J. Bokor, Phys. Rev. Lett. **68**, 2834 (1992).
- [31] J. R. Dwyer, R. E. Jordan, C. T. Hebeisen, M. Harb, R. Ernstorfer, T. Dartigalongue, and R. J. D. Miller, J. Modern Opt. **54**, 905 (2007).
- [32] O. P. Uteza, E. G. Gamaly, A. V. Rode, M. Samoc, and B. Luther-Davies, Phys. Rev. B **70**, 054108 (2004).
- [33] J. K. Chen and J. E. Beraun, J. Opt. A: Pure Appl. Opt. **5**, 168 (2003).
- [34] J. P. Girardeau-Montaut and C. Girardeau-Montaut, Phys. Rev. B **51**, 13560 (1995).

- [35] J. K. Chen, W. P. Latham, and J. E. Beraun, *J. Laser Applications*, **17**, 63 (2005).
- [36] B. H. Christensen, K. Vestentoft, and P. Balling, *Appl. Surf. Sci.* **253**, 6347 (2007).
- [37] A. P. Caffrey, P. E. Hopkins, J. M. Klopff, and P. M. Norris, *Microscale Thermophys. Eng.* **9**, 365 (2005).
- [38] E. Beaupaire, J.-C. Merle, A. Daunois, and J.-Y. Bigot, *Phys. Rev. Lett.* **76**, 4250 (1996).
- [39] S.-S. Wellershoff, J. Güdde, J. Hohlfeld, J. G. Müller, and E. Matthias, *Proc. SPIE* **3343**, 378 (1998).
- [40] D. Y. Tzou, *Macro- to Microscale Heat Transfer: The Lagging Behavior* (Washington, DC: Taylor & Francis, 1997).
- [41] P. B. Allen, *Phys. Rev. Lett.* **59**, 1460 (1987).
- [42] J. M. Ziman, *Electrons and Phonons* (Oxford Univ. Press London, 1960).
- [43] W. L. McMillan, *Phys. Rev.* **167**, 331 (1968).
- [44] G. Grimvall, *The Electron-Phonon Interaction in Metals*, Selected Topics in Solid State Physics; E. Wohlfarth, Ed.; (North-Holland: New York, 1981).
- [45] E. V. Chulkov, A. G. Borisov, J. P. Gauyacq, D. Sánchez-Portal, V. M. Silkin, V. P. Zhukov, and P. M. Echenique, *Chem. Rev.* **106**, 4160 (2006) and references therein.
- [46] Yu. V. Petrov, *Laser Part. Beams* **23**, 283 (2005).
- [47] *American Institute of Physics Handbook*, 3rd edition (McGraw-Hill, New York, 1972).
- [48] N.E. Phillips, *Phys. Rev.* **114**, 676 (1959).
- [49] R. Bauer, A. Schmid, P. Pavone, and D. Strauch, *Phys. Rev. B* **57**, 11276 (1998).
- [50] S. Y. Savrasov and D. Y. Savrasov, *Phys. Rev. B* **54**, 16487 (1996).

- [51] D. A. Papaconstantopoulos, L. L. Boyer, B. M. Klein, A. R. Williams, V. L. Morruzzi, and J. F. Janak, *Phys. Rev. B* **15**, 4221 (1977).
- [52] J. L. Hostetler, A. N. Smith, D. M. Czajkowsky, and P. M. Norris, *Appl. Opt.* **38**, 3614 (1999).
- [53] Electron temperature dependences of thermophysical properties of metals discussed in this study are accessible in tabulated form from <http://www.faculty.virginia.edu/CompMat/electron-phonon-coupling/>
- [54] B. Rethfeld, A. Kaiser, M. Vicanek, and G. Simon, *Phys. Rev. B* **65**, 214303 (2002).
- [55] P. B. Allen, *Phys. Rev.* **36**, 2920 (1987).
- [56] R. H. M. Groeneveld, R. Sprik, and A. Lagendijk, *Phys. Rev. B* **51** 11433 (1995).
- [57] R. H. M. Groeneveld, R. Sprik, and A. Lagendijk, *Phys. Rev. Lett.* **64** 784 (1990).
- [58] S. D. Brorson, A. Kazeroonian, J. S. Moodera, D. W. Face, T. K. Cheng, E. P. Ippen, M. S. Dresselhaus, and G. Dresselhaus, *Phys. Rev. Lett.* **64**, 2172 (1990).
- [59] H. E. Elsayed-Ali, T. Juhasz, G. O. Smith, and W. E. Bron, *Phys. Rev. B* **43**, 4488 (1991).
- [60] H. E. Elsayed-Ali, T. B. Norris, M. A. Pessot, and G. A. Mourou, *Phys. Rev. Lett.* **58**, 1212 (1987).
- [61] J. R. Dwyer, C. T. Hebeisen, R. Ernstorfer, M. Harb, V. Deyirmenjian, R. E. Jordan, and R. J. D. Miller, *Phil. Trans. R. Soc. A* **364**, 741 (2006).
- [62] V. Recoules, J. Cl  rouin, G. Z  rah, P.M. Anglade, and S. Mazevet, *Phys. Rev. Lett.* **96**, 055503 (2006).
- [63] G. K. White, *Aust. J. Phys.* **46**, 707 (1993).
- [64] J. G. Fujimoto, J. M. Liu, E. P. Ippen, and N. Bloembergen, *Phys. Rev. Lett.* **53**, 1837 (1984).
- [65] Ch. Dufour, E. Paumier, and M. Toulemonde, *Nucl. Instr. Meth. B* **122**, 445 (1997).

- [66] I. Y. Sklyadneva, A. Leonardo, P. M. Echenique, S. V. Eremeev, and E. V. Chulkov, *J. Phys.: Condens. Matter* **18**, 7923 (2006).

4. Practical Implication of Thermal Excitation of Electrons in Short Pulse Laser Interaction with Metals

4.1 Thermal excitation of d band electrons in Au: implications for laser-induced phase transformations

4.1.1 Introduction

Irradiation of a solid target with an intense ultrashort (femtosecond) laser pulse has the ability to bring material to a state of strong electron-lattice nonequilibrium and trigger a cascade of coupled transient processes that include electron-phonon thermalization, nonequilibrium energy transport, as well as structural/phase transformations occurring under extreme and dynamic pressure-temperature conditions. The transient and highly nonequilibrium character of laser-induced processes makes the quantitative theoretical/computational description of the laser-materials interactions challenging. For metals, computational modeling of ultrashort-pulse laser interactions is commonly based on the two-temperature model (TTM) [1], which describes the time evolution of the lattice and electron temperatures, T_l and T_e , by two coupled non-linear differential equations:

$$C_e(T_e) \frac{\partial T_e}{\partial t} = \nabla [K_e(T_e, T_l) \nabla T_e] - G(T_e)(T_e - T_l) + S(\vec{r}, t) \quad (4.1.1)$$

$$C_l(T_l) \frac{\partial T_l}{\partial t} = G(T_e)(T_e - T_l) \quad (4.1.2)$$

where C and K are the heat capacities and thermal conductivities of the electrons and the lattice as denoted by subscripts e and l , $G(T_e)$ is the electron-phonon coupling factor related to the rate of the energy exchange between the electrons and the lattice, and $S(\vec{r}, t)$

is a source term describing the local energy deposition by the laser pulse. The model accounts for the laser excitation of the conduction band electrons, energy transfer to the atomic vibrations due to the electron–phonon coupling, and the electronic heat diffusion from the irradiated surface to the bulk of the target.

Despite numerous successful applications of TTM, the inherent limitation of the model is its inability to adequately describe the kinetics of phase transformations and changes in the microstructure occurring under highly nonequilibrium conditions induced in the target material by short pulse laser irradiation. In order to overcome this limitation we have recently developed a combined atomistic-continuum model that incorporates the classical molecular dynamics (MD) method into the general framework of the TTM model [2]. In the combined TTM-MD model, MD substitutes the TTM equation for the lattice temperature in the region of irradiated target affected by laser-induced structural transformations. The diffusion equation for the electron temperature is solved simultaneously with MD integration of the equations of motion of atoms and an additional coupling term is added to the conventional MD equations of motion in order to account for the energy exchange between the electrons and the lattice [2]. First applications of the combined TTM-MD model have provided insights into the microscopic mechanisms of laser melting and photomechanical damage in metal films and bulk targets [3,4,5,6]. Moreover, the important role of non-thermal channels of laser energy redistribution (energy transfer to the energy of collective atomic motions associated with the relaxation of laser-induced stresses and the energy of quasi-static anisotropic stresses), not accounted for in the conventional TTM model, has been revealed in TTM-MD modeling [7].

An important aspect in the application of the TTM or TTM-MD models for quantitative descriptions of the material response to the ultrashort pulse laser irradiation is the choice of adequate temperature dependent thermo-physical properties of the target material. Due to the small heat capacity of the electrons, laser excitation can transiently bring the electron temperature to very high values, comparable to the Fermi temperature. At such high electron temperatures, the temperature dependent thermophysical properties of the system can be directly affected by the thermal excitation of the lower band electrons in noble and transition metals [8,9]. A detailed analysis of the connections between the electron density of states (DOS) in the target material and the temperature dependence of the electron-phonon coupling, electron heat capacity and thermal conductivity are needed for a realistic description of laser-material interactions.

In this chapter, the effects of the electron DOS on thermophysical material properties are illustrated for femtosecond laser interactions with Au films. In the next section, the temperature dependences of the electron heat capacity and the electron-phonon coupling factor are analyzed based on the electronic structure calculations performed within the density functional theory. The results of the analysis of the thermophysical properties of Au at high electron temperatures are incorporated into TTM-MD model and applied for simulations of laser melting of thin Au films. The results of the simulations are presented and related to the experimental data obtained for a similar system in recent time-resolved electron diffraction experiments in Section 4.1.3. A brief summary of the results is given in Section 4.1.4.

4.1.2 The effect of DOS and thermal excitation of electrons on thermophysical properties

The effect of the thermal excitation of 5d band electrons in Au on the thermophysical properties of the material irradiated by an intense laser pulse is discussed in this section. In particular, the temperature dependences of the electron heat capacity $C_e(T_e)$ and the electron-phonon coupling factor $G(T_e)$ are analyzed in a broad range of the electron temperatures based on the electron DOS obtained from *ab initio* electronic structure calculations. The results of the calculations are compared with the predictions of the free electron gas model.

4.1.2.1 Electron DOS, chemical potential, and electron heat capacity

The electron heat capacity can be calculated by taking the derivative of the total electronic energy density with respect to the electron temperature [10]:

$$C_e(T_e) = \left(\frac{\partial u}{\partial T_e} \right)_V = \int_{-\infty}^{\infty} (\varepsilon - \varepsilon_F) \frac{\partial f(\varepsilon, \mu, T_e)}{\partial T_e} g(\varepsilon) d\varepsilon \quad (4.1.3)$$

where μ is the chemical potential at T_e , ε_F is the Fermi energy, $g(\varepsilon)$ is the electron DOS at the energy level ε , and $f(\varepsilon, \mu, T_e)$ is the Fermi distribution function defined as $f(\varepsilon, \mu, T_e) = \{\exp[(\varepsilon - \mu)/k_B T_e] + 1\}^{-1}$. When the electron temperature is much smaller than the Fermi temperature ($T_F = 64\,200$ K for Au [27]), only electrons at around the Fermi surface are excited and the electron heat capacity is known to be a linear function of the electron temperature, $C_e(T_e) = \gamma T_e$, where γ is the electron heat capacity constant defined, within the free electron gas model, by the free electron density n_e and the Fermi energy ε_F , $\gamma = \pi^2 n_e k_B^2 / 2\varepsilon_F$. In particular, using the values of the free electron density and the Fermi energy from Ref. [27], the electron heat capacity constant for Au can be calculated to be $\gamma = 62.7 \text{ J m}^{-3} \text{ K}^{-2}$. At high electron temperatures, however, lower band electrons

could be excited to the conduction band, resulting in deviations from the linear temperature dependence of the electron heat capacity.

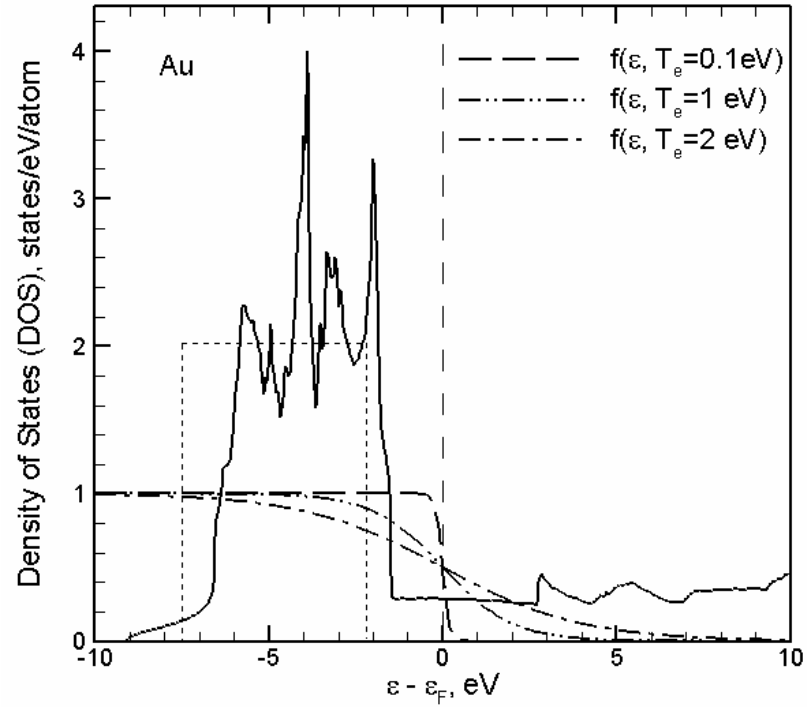


Figure 4-1-1. Electron DOS obtained in electron structure calculations performed with VASP (solid line) and a square function approximation for the 5d band in Au used in Ref. [19] (dashed line). The Fermi distribution functions are also shown for three different values of the electron temperature.

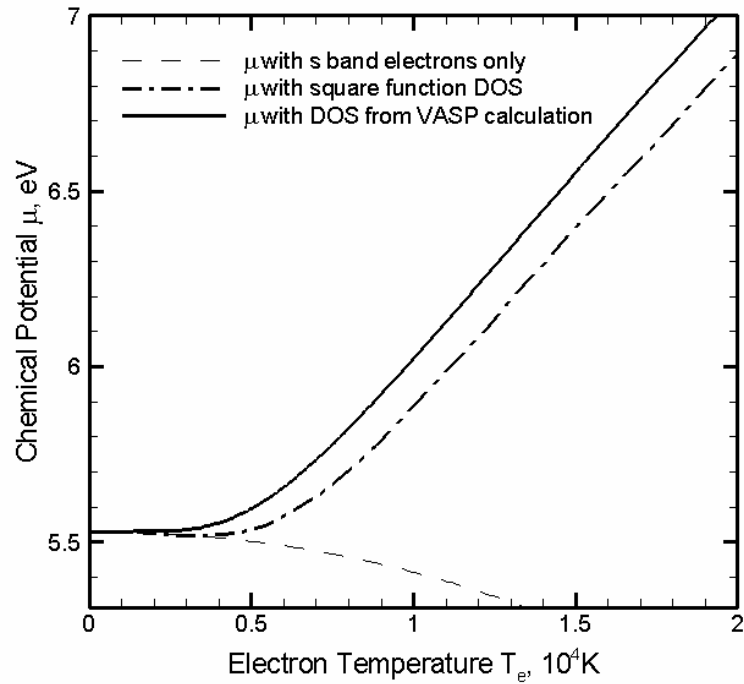


Figure 4-1-2. Chemical potential of Au as a function of the electron temperature calculated using three different approximations of DOS for Au: DOS obtained with VASP (solid line), square function approximation for the 5d band (dash-dotted line), and neglecting the contribution of the d electrons (dashed line).

Both theoretical calculations [11,12,13] and X-ray photoemission spectroscopy experiments [14] have shown that the d band in Au, located relatively close to the Fermi level, has a rather complicated structure. In the analysis of the temperature dependence of the thermophysical properties of Au performed in [19], a square function centered at 4.8 eV below the Fermi energy with a width of 5.2 eV was used as an approximation of the d band. In order to understand to what degree the fine structure of the electron DOS would affect the temperature dependent thermophysical properties in Au, we perform the electronic structure calculation using the *Vienna Ab-initio Simulation Package* (VASP)

[15] and obtain the electron DOS for Au at $T_e=0$ K, shown in Fig. 4-1-1. The calculation is done for the equilibrium lattice parameter, 4.166 Å, using the Vanderbilt ultrasoft pseudopotential (US) [16] where the exchange correlation term is treated within the generalized gradient approximation (GGA). It can be seen from Fig. 4-1-1 that, although the square function describes the presence of high density of states associated with d band electrons, accounting for the detailed structure of the d band, especially on the high energy side close to the Fermi level, can introduce significant corrections to the calculated number of thermally excited electrons.

From examination of the electron DOS together with the Fermi distribution functions at various electron temperatures, it is clear that for electron temperatures less than 0.1 eV ($\sim 10^3$ K) only electrons around the Fermi level are excited, while at $T_e \sim 1$ eV ($\sim 10^4$ K) or higher, the number of excited d band electrons can be significant and should be taken into account.

In order to calculate the electron heat capacity from Eq. (4.1.3), it is necessary to evaluate the expression for $\partial f / \partial T_e$, which requires the determination of the chemical potential $\mu(T_e)$. From the conservation of the total number of electrons, one can obtain the chemical potential by setting the result of the integration of the product of DOS and the Fermi distribution function at T_e over all energy levels to be equal to the total number of electrons N_e [27],

$$N_e = \int_{-\infty}^{\infty} f(\varepsilon, \mu(T_e), T_e) g(\varepsilon) d\varepsilon \quad (4.1.4)$$

The chemical potential obtained from Eq. (4.1.4) as a function of the electron temperature using three different approximations of DOS for Au is shown in Fig. 4-1-2. It

is easy to verify that with only s electrons taken into account, the chemical potential obeys the expression derived from the Sommerfeld expansion in the free electron gas model [27],

$$\mu(T_e) = \varepsilon_F \left[1 - \frac{\pi^2}{12} \left(\frac{k_B T_e}{\varepsilon_F} \right)^2 \right] \quad (4.1.5)$$

It is clear from Fig. 4-1-2 that in both calculations accounting for the presence of d band electrons, the chemical potentials agree well with the free electron gas model, Eq. (4.1.5), for T_e less than ~ 3000 K. However, as discussed above for Fig. 4-1-1, as T_e is increasing, the number of excited d band electrons becomes significant and the chemical potential starts to deviate from Eq. (4.1.5). In the case of the DOS calculated from VASP, the sharp increase of the number of states at energies that are higher than the high-energy edge of the square function, $\varepsilon = -2.2$ eV, and the contribution of d band states at around the Fermi level, Fig. 4-1-1 and Ref. [17], result in the higher values of the chemical potential as compared to the ones obtained with the square function approximation of the d band [19].

In Fig. 4-1-3 the temperature dependences of the electron heat capacity, calculated from Eq. (4.1.3), are shown for three approximations of DOS discussed above and used in the calculation of the chemical potential in Fig. 4-1-2. The difference in the temperature dependences of the predicted electron heat capacity can be understood from the fact that at a sufficiently high temperature significant excitation occurs from the d band in Au, which contains a large number of electron states. Calculations performed with the square function approximation of the d band give a similar temperature

dependence for the electron heat capacity but underestimate the values of the heat capacity due to lack of a complete description of the d band.

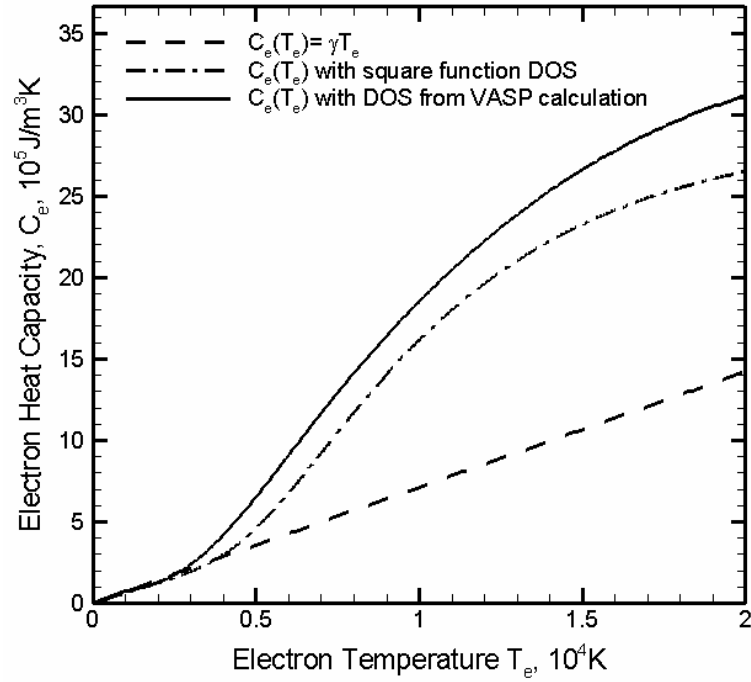


Figure 4-1-3. Electron heat capacity of Au as a function of the electron temperature calculated using $C_e = \gamma T_e$ with $\gamma = 71 \text{ Jm}^{-3}\text{K}^{-2}$ [18] and with the same two approximations of DOS for Au as in Fig. 2.

Large deviations of the electron heat capacity from the linear dependence at electron temperatures that can be readily achieved by ultrashort laser pulses suggest that the application of commonly used linear approximation $C_e(T_e) = \gamma T_e$ could result in a significant overestimation of the transient values of the electron temperature during the time of the electron-lattice nonequilibrium.

The electron thermal conductivity is also affected by the thermal excitation of lower band electrons as it is related to the electron heat capacity through the Drude model relationship, $\kappa(T_e, T_l) = v_F^2 C_e(T_e) \tau_e(T_e, T_l) / 3$ [27], where v_F is the Fermi velocity and $\tau_e(T_e, T_l)$ is the total electron scattering time with other electrons and the lattice. The total electron scattering time is defined by the electron-electron scattering time, τ_{e-e} , and the electron-phonon scattering time, τ_{e-ph} , and can be evaluated from the sum of the scattering rates, $1/\tau_e = 1/\tau_{e-e} + 1/\tau_{e-ph} = AT_e^2 + BT_l$, where A and B are constants [18,27]. The deviation of the electron heat capacity from the linear temperature dependence, Fig. 4-1-3, would also result in a faster electronic heat transfer during the initial stage of the electron-phonon nonequilibrium. In the example problem considered in Section 4.1.3 (laser interaction with 20 nm free standing Au film), however, a uniform distribution of the electron temperature is established in the film on the timescale of the electron-phonon thermalization and the electron thermal conductivity does not play a role in this case.

4.1.2.2 Temperature dependence of the electron-phonon coupling factor

While the electron-phonon coupling has been under active investigations in the field of superconductivity for several decades, it has also attracted a renewed interest with the fast growth of femtosecond laser applications, in which the rate of the energy transport between hot electrons and the lattice has direct implications on laser induced processes. Theoretical investigations have been focused on describing the energy exchange through electron-phonon collision equations that characterize the phonon emission and absorption processes. The electron-phonon energy exchange within the free electron gas model was first addressed by Kaganov *et al.* [19]. It was found that the

energy exchange rate could be expressed in terms of the electron relaxation time at T_e and T_l . At lattice and electron temperatures much higher than the Debye temperature and $T_e \gg T_l$, the rate of the energy transfer from the electrons to the lattice per unit volume is

$$\partial E_e / \partial t = G(T_l - T_e), \quad G = \frac{\pi^2}{6} \frac{m_e C_s^2 n_0}{\tau(T_e) T_e}, \quad (4.1.6)$$

where m_e is the effective electron mass, C_s is the speed of sound, n_0 is the number density of the electrons, and $\tau(T_e)$ is the electron relaxation time defined as the electron-phonon scattering time and evaluated under the assumption that the lattice temperature is equal to the electron temperature [29]. The electron-phonon scattering is proportional to the inverse of the phonon temperature and, under the condition of $T_e = T_l$, $\tau(T_e) \sim 1/T_e$, leading to a constant value of the coupling factor given by the Kaganov's expression [1].

While a constant value for the electron-phonon coupling factor is used in most of current computational and theoretical studies of short-pulse laser interactions with metals, there is growing experimental evidence suggesting that the applicability of the constant electron-phonon coupling may be limited to low laser intensities (low electronic temperatures). For example, the coupling constant is used as a fitting parameter in Ref. [20] to obtain an agreement between the calculated and experimental values of the ablation threshold in Au, whereas an empirical $G(T_e)$ dependence is introduced in Ref. [21] to provide a good description of electron photoemission data.

Several approaches have been proposed in order to account for the temperature dependence of the electron-phonon coupling factor. Based on the Kaganov's expression for the electron-phonon energy exchange rate, Eq. (4.1.6), Chen *et al.* [22] introduced a phenomenological model in which both electron-electron and electron-phonon scattering

rates are included in the evaluation of the electron relaxation time, $\tau(T_e)$ in Eq. (4.1.6). The electron-electron scattering, indeed, starts to significantly contribute to the total electron scattering rate at high electron temperatures, above ~ 1 eV. While this contribution directly affects the electron transport properties (thermal and electrical conductivities), the relevance of the electron-electron scattering to the electron-phonon coupling factor is questionable. Similarly, the evaluation of the electron relaxation time $\tau(T_e)$ based on the temperature dependence of the electrical or thermal conductivity [1,23,24] includes the contribution of electron-electron scattering and is inappropriate for the calculation of the electron-phonon coupling at high electron temperatures.

As discussed above, in Section 4.1.2.1, in the high electron temperature regime, a quantitative analysis of the electron relaxation dynamics in metals with low-lying d bands should go beyond the free electron model and should include the consideration of the electron DOS effects. Thus, the discussion provided in Section 4.1.2.1 for the electron heat capacity and chemical potential should be extended to the electron-phonon coupling. A general description of the electron-phonon energy exchange involving arbitrary electron DOS was developed by Allen [25] based on the electron-phonon collisions equations. The rate of the energy exchange between the electrons and the lattice can be then expressed as

$$\left[\frac{\partial E_e}{\partial t} \right]_{ep} = \frac{4\pi}{\hbar N_c} \sum_{k,k'} \hbar \omega_Q |M_{kk'}|^2 S(k,k') \delta(\varepsilon_k - \varepsilon_{k'} + \hbar \omega_Q) \quad (4.1.7)$$

where $M_{kk'}$ is the electron-phonon scattering matrix element [26], N_c is the number of unit cells in the sample, k and Q denote the electron and phonon quantum numbers, respectively. $S(k,k') = (F_k - F_{k'})N_Q - F_{k'}(1 - F_k)$ is the so-called thermal factor that

characterizes the phonon absorption and emission processes in the electron-phonon scattering, where F_k and N_Q are the Fermi-Dirac and Bose-Einstein distribution functions, respectively. Assuming that near room temperature only electron states around the Fermi energy contribute to the scattering processes, Eq. (4.1.7) can be rewritten in terms of the “electron-phonon spectral function” $\alpha F^2(\Omega)$ from the superconductivity theory [41]:

$$\left[\frac{\partial E_e}{\partial t} \right]_{ep} = 2\pi N_c g(\varepsilon_F) \int_0^\infty \alpha F^2(\Omega) (\hbar\Omega)^2 [N(\Omega, T_l) - N(\Omega, T_e)] d\Omega \quad (4.1.8)$$

By defining $\partial E_e / \partial t = G_e(T_e)(T_l - T_e)$ and making a Taylor expansion of Eq. (4.1.8) in terms of $\hbar\Omega / k_B T_e$ and $\hbar\Omega / k_B T_l$, one could obtain the electron-phonon coupling constant: $G_0 = \pi \hbar k_B \lambda \langle \omega^2 \rangle g(\varepsilon_F)$, where λ is the electron-phonon coupling constant used in the superconductivity theory and $\langle \omega^2 \rangle$ is the second moment of the phonon spectrum defined by McMillan [27]. For Au, with the value $\lambda \langle \omega^2 \rangle = 23 \pm 4 \text{ meV}^2$ measured in Ref. [28] and DOS shown in Fig. 4-1-1, we can determine the room temperature electron-phonon coupling constant, $G_0 = 2.5 \times 10^{16} \text{ Wm}^{-3}\text{K}^{-1}$, which is consistent with the one obtained from reflectivity experiments: $G = (2.2 \pm 0.3) \times 10^{16} \text{ Wm}^{-3}\text{K}^{-1}$ at low electron temperatures (a few thousand K) [18].

For high T_e situations, it is necessary to take into account the electron energy dependence of the electron-phonon spectral function, i. e. $\alpha F^2(\varepsilon, \varepsilon', \Omega)$. In order to explicitly account for the d band electrons in Au, Wang *et al.* [18] proposed an approximation of the spectral function based on the assumption that the magnitude of $M_{kk'}$ is independent of the electron states, which leads to: $\alpha F^2(\varepsilon, \varepsilon', \Omega) = [g(\varepsilon)g(\varepsilon') / g^2(\varepsilon_F)] \alpha F^2(\varepsilon_F, \varepsilon_F, \Omega)$. An expression for the temperature

dependent electron-phonon coupling factor could be then obtained using the approach discussed in Ref. [41]:

$$G(T_e) = \frac{\pi \hbar k_B \lambda \langle \omega^2 \rangle}{g(\varepsilon_F)} \int g^2(\varepsilon) \left(-\frac{\partial f}{\partial \varepsilon} \right) d\varepsilon \quad (4.1.9)$$

It is easy to verify that at low electron temperatures, $-\partial f / \partial \varepsilon$ reduces to a delta function and Eq. (4.1.9) gives a constant value, recovering the expression G_0 given by Allen, whereas at high electron temperatures, $-\partial f / \partial \varepsilon$ for ε away from ε_F can no longer be neglected, leading to a temperature dependence of the electron-phonon coupling factor.

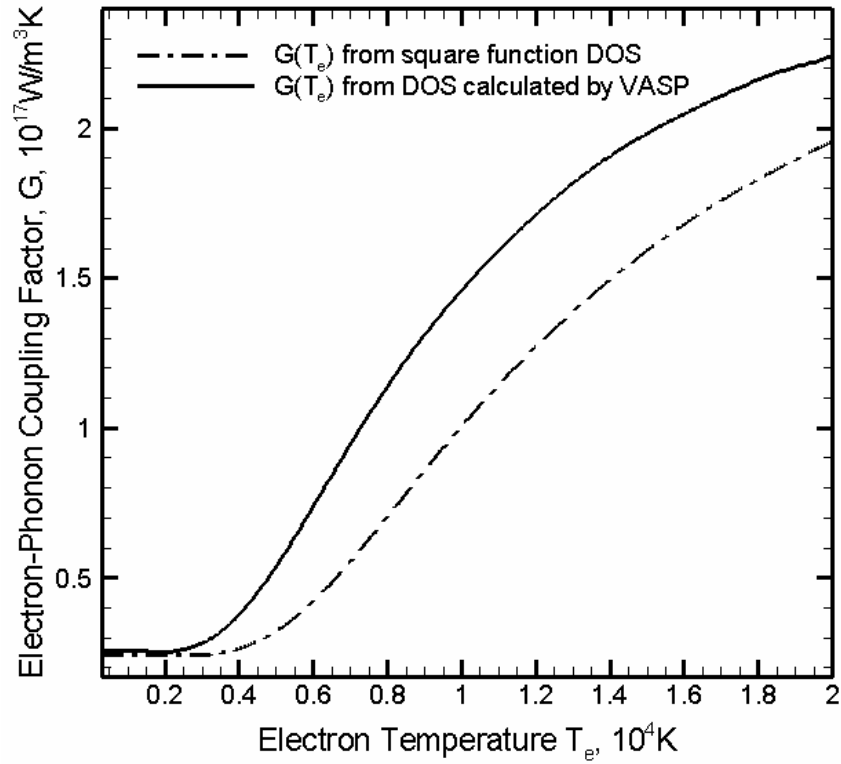


Figure 4-1-4. Electron-phonon coupling factor as a function of the electron temperature calculated for DOS obtained with VASP (solid line) and square function approximation for the 5d band (dash-dotted line).

The results for $G(T_e)$ in Au obtained with Eq. (4.1.9) using two different descriptions of the d band electrons discussed in Section 4.1.2.1, are shown in Fig. 4-1-4. In both cases the electron-phonon coupling factor remains approximately constant at T_e below ~ 3000 K. This observation is consistent with the results shown in Figs. 4-1-2 and 4-1-3 for the electron heat capacity and chemical potential, where the contribution from the thermal excitation of the d band electrons also becomes significant only when T_e becomes larger than ~ 3000 K. This fact also implies that at low excitation levels, where the electron temperature only reaches several thousand K, the assumption of the constant electron-phonon coupling factor provides a very good description of the rate of the electron-lattice energy exchange. However, as the electron temperature increases above ~ 3000 K, the value for the electron-phonon coupling factor with the full description of the electron DOS starts to significantly deviate from the constant value. The electron-phonon factor calculated with the full description of DOS exceeds the room temperature value by a factor of 5.8 at $T_e = 1 \times 10^4$ K and by a factor of 8.9 at $T_e = 2 \times 10^4$ K. As apparent from Fig. 4, the detailed description of electron DOS obtained in the electronic structure calculation gives a consistently higher value of the electron-phonon coupling than the one using the square function approximation for d band electrons.

A significant increase in the electron-phonon coupling in the range of electron temperatures typically realized in femtosecond laser material processing applications may lead to important practical implications. The faster energy transfer from the hot electrons to the lattice can result in the thermal energy confinement in a smaller surface region of the irradiated target, generation of stronger thermoelastic stresses, reduction of the

threshold fluences for the onset of laser melting and ablation, and changes in the timescales of the laser induced phase transformations. Some of the implications of the temperature dependence of the thermophysical parameters discussed in this section are illustrated in the TTM-MD simulations presented in Section 4.1.3.

4.1.3 TTM-MD Simulations of laser melting of a thin Au film

In order to test the effect of the modified temperature dependence of the electron heat capacity and the electron-phonon coupling factor discussed above on the material response to the ultrashort pulse laser irradiation, we incorporated the results illustrated in Figs. 4-1-3 and 4-1-4 into the TTM-MD computational model [2] and performed simulations of laser melting of a 20 nm freestanding Au film. The conditions of the simulations are chosen to be similar to the ones realized in recent time-resolved electron diffraction experiments performed in the transmission mode for thin freestanding films [29]. The results of the simulations obtained with and without taking into account the DOS effects are related to the experimental observations.

4.1.3.1 *Computational model*

Simulations of laser melting of a 20 nm freestanding Au film irradiated by a 200 fs laser pulse at an absorbed fluence of 92.5 J/m^2 are performed with a combined TTM–MD model described in details elsewhere [2]. Briefly, the model is based on the TTM equations in which the classical MD method substitutes the TTM equation for the lattice temperature, Eq. (4.1.2). The equation for the electron temperature, Eq. (4.1.1), is solved by a finite difference method simultaneously with the MD integration of equations of motion of atoms. The electron temperature enters a coupling term that is added to the

MD equations of motion to account for the energy exchange between the electrons and the lattice. The cells in the finite difference discretization are related to the corresponding volumes of the MD system and the local lattice temperature is defined for each cell from the average kinetic energy of the thermal motion of atoms.

Irradiation by a laser pulse is represented in the continuum part of the model by a source term with a Gaussian temporal profile. The electron mean free path in Au is larger than the optical penetration depth and the ballistic energy transport defines the effective laser energy deposition depth, estimated to be on the order of 100 nm [18]. This depth of effective electronic excitation exceeds the thickness of the Au film considered in this work, 20 nm. The reflection of the ballistic electrons from the back surface of the film results in a uniform distribution of the electronic temperature established on the timescale of the electron thermalization. The effect of the ballistic energy transport and the finite size of the film are accounted for in the source term describing the laser irradiation [2].

The initial MD computational cell is an FCC crystal, consisting of 80,000 atoms with dimensions of $8.18 \times 8.18 \times 20.46$ nm and periodic boundary conditions imposed in the directions parallel to two (001) free surfaces. The periodic boundary conditions simulate the situation in which the laser spot diameter is sufficiently large so that the energy redistribution in the lateral directions, parallel to the free surfaces of the film, can be neglected on the time-scales considered in the simulations. An additional simulation with a larger, $20.46 \times 20.46 \times 20.46$ nm, MD computational cell consisting of 500,000 atoms is also performed to provide a better visual picture of the melting process. The interatomic interaction in the MD part of the model is described by the embedded atom

method (EAM) [30]. The choice of the interatomic potential defines all the thermal and elastic properties of the material. Thermodynamic properties of the EAM Au relevant to the laser heating and melting processes are given in Ref. [4]. Before applying laser irradiation, all systems are equilibrated at 300 K and zero pressure.

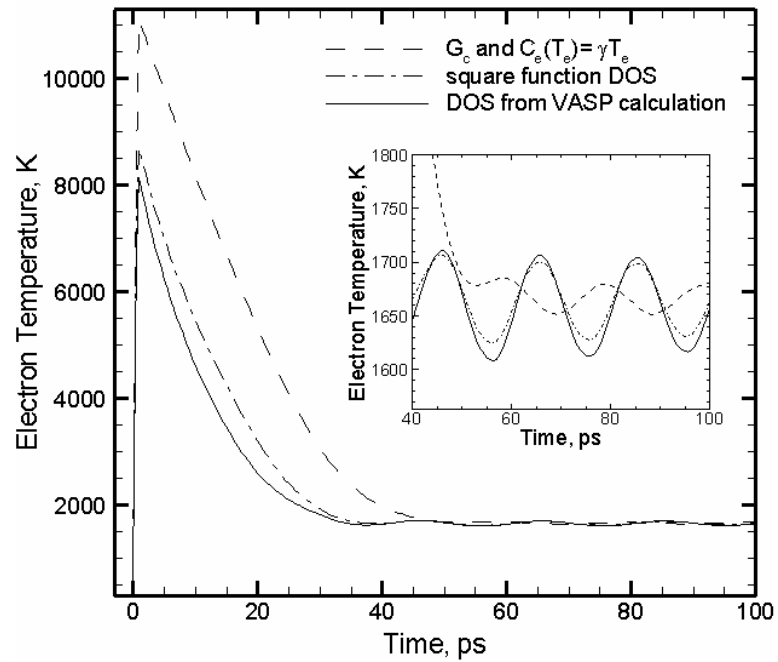
To illustrate the practical implications of effect of the electron DOS on the thermophysical parameters of the material discussed in Section 4.1.2, the TTM-MD simulations were performed for three sets of parameters of the TTM equation for the electron temperature. One simulation was performed for the parameters that correspond to the free electron gas model with only s band electrons taken into account. In this case the linear temperature dependence of the electronic heat capacity, $C_e = \gamma T_e$ with $\gamma = 71 \text{ Jm}^{-3}\text{K}^{-2}$ (Fig. 4-1-3), and a constant electron-phonon coupling constant taken as the room temperature value calculated from the Allen's expression (Eq. 4.1.8), $G_c = 2.5 \times 10^{16} \text{ Wm}^{-3}\text{K}^{-1}$ are used. In two other simulations, the temperature dependences of the electron heat capacity and the electron-phonon coupling factor accounting for thermal excitations of the d band electrons and calculated with the square function approximation for the d band in one case and with the detailed DOS obtained with VASP in another case (Figs. 4-1-3 and 4-1-4) are used.

4.1.3.2 *Transient evolution of electron and lattice temperatures*

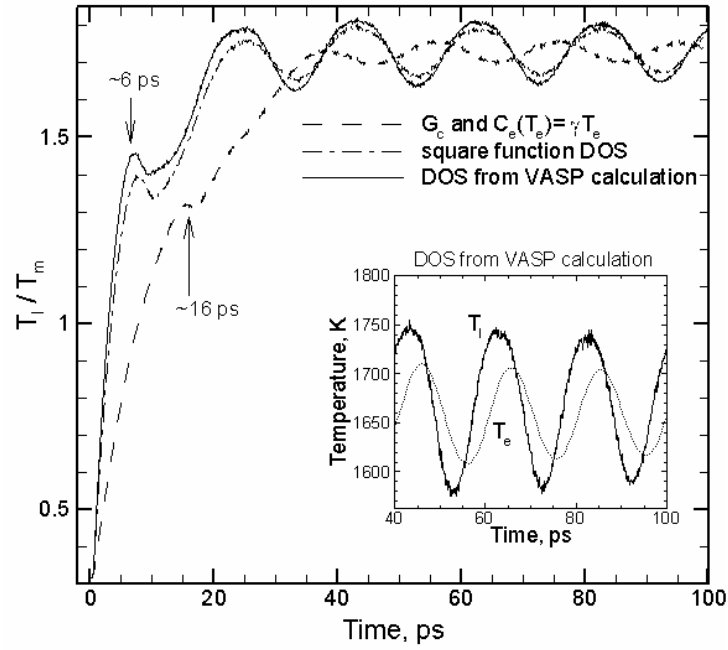
The evolution of the lattice and electron temperatures, predicted in TTM-MD simulations, is shown for three different treatments of the electron DOS for Au in Fig. 4-1-5. The maximum electron temperature achieved by the end of the laser pulse is significantly, by ~35%, overestimated in the model where the conventional linear

dependence of the heat capacity on electron temperature is used. As discussed in Section 4.1.2.1 and illustrated in Fig. 4-1-3, the contribution of the 5d band electrons to the electron heat capacity becomes significant at high electron temperatures and results in smaller values of the electron temperature during the time of the initial electron-lattice equilibration, Fig. 4-1-5a.

The rate of the initial increase of the lattice temperature, shown in Fig. 4-1-5b, is also significantly affected by the choice of the approximation used in the model. In the simulations that account for the temperature dependence of the electron-phonon coupling (Fig. 4-1-4), the lattice temperature rise is much faster, the time when the onset of the fast homogeneous melting of the film is observed shifts from ~ 16 ps to ~ 6 ps, and the time of the saturation of the lattice temperature decreases from ~ 35 ps to ~ 20 ps.



(a)



(b)

Figure 4-1-5. Evolution of the electron (a) and lattice (b) temperatures in 20 nm Au film irradiated with a 200 fs laser pulse at an absorbed fluence of 92.5 J/m^2 . The lattice temperature in (b) is normalized to the equilibrium melting temperature of EAM Au. The temperatures are averaged over the thickness of the film. The arrows show the time of the onset of melting. The parameters used in the simulations are calculated using three different approximations of DOS for Au: DOS obtained with VASP (solid line), square function approximation for the 5d band (dash-dotted line), and neglecting the contribution of the d electrons (dashed line), as shown in Figs. 4-1-3 and 4-1-4.

While the evolution of the electron and lattice temperatures reflects the rate of the energy exchange between the electrons and the lattice, the electron energy profiles shown in Fig. 4-1-6 provide more direct information on the electron-phonon energy transfer rate and the time of the electron-lattice equilibration. It is apparent from Fig. 4-1-6 that the

energy transfer is much faster when the thermal excitation of the d band electrons is taken into account and the temperature dependent electron-phonon coupling factor is used in the TTM-MD simulations. Based on the electron energy plots, the electron-phonon equilibration time can be estimated to be 33 ps, 35 ps, and 50 ps for the three plots shown in Fig. 4-1-6.

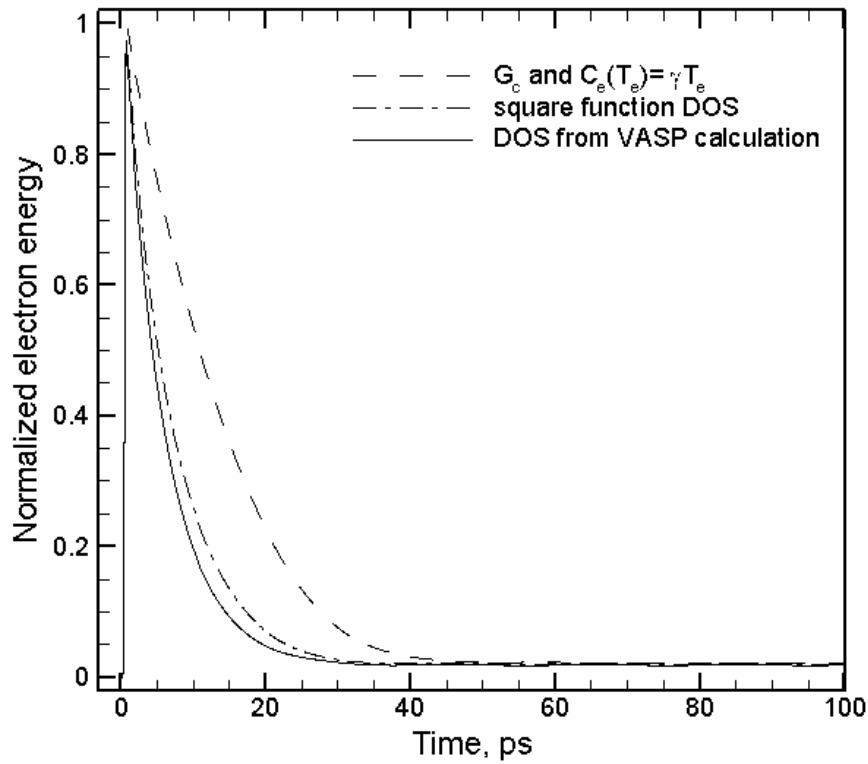
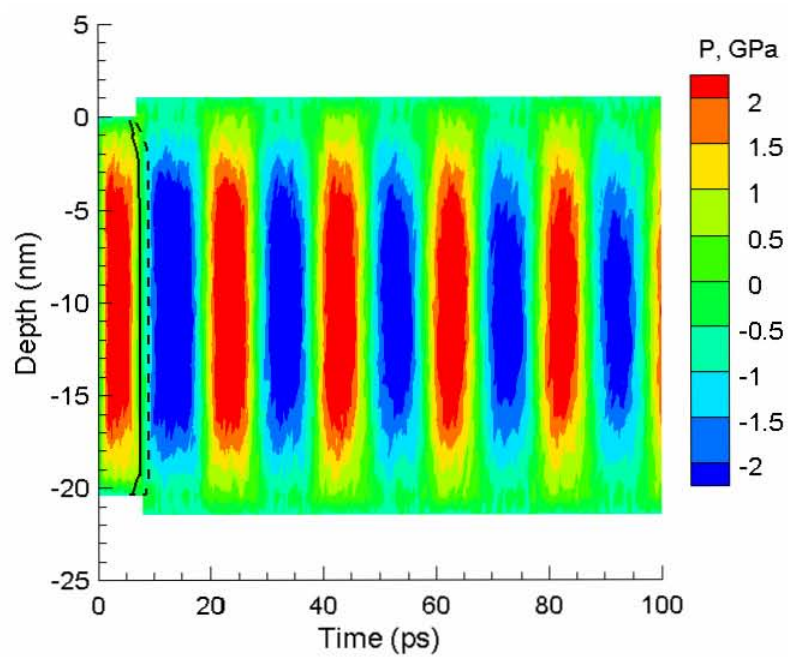


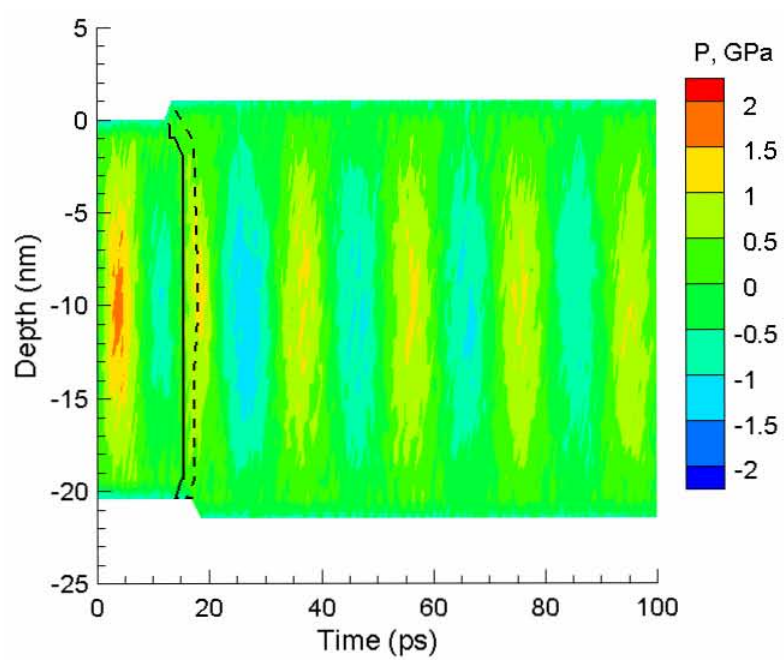
Figure 4-1-6. Evolution of the electron energy in the same three simulations illustrated in Fig. 4-1-5. The electron energies are normalized to the total laser energy absorbed by the film, $E_{\text{tot}} = F_{\text{abs}} S$, where S is the surface area of the TTM-MD computational cell, and F_{abs} is the absorbed laser fluence.

Although the initial electron-phonon equilibration of the deposited laser energy is completed by 33-50 ps after the laser pulse, the insets in Fig. 4-1-5 show long-term

oscillations of the lattice and electron temperatures. The oscillations are stronger in the simulations where d band electrons are taken into account and a temperature dependent electron phonon coupling factor is used. The temperature oscillations can be related to the relaxation of the laser-induced thermoelastic stresses. The pressure contour plot in Fig. 4-1-7 shows that the fast lattice heating results in the build up of a compressive stresses inside the film within the first ~ 5 ps. For a 20 nm freestanding Au film, 5 ps corresponds to the time of the mechanical relaxation, i. e. the time needed for two unloading waves to cross a half of the depth of the film. During the first several picoseconds the lattice heating takes place under conditions of the inertial stress confinement [5], leading to the buildup of compressive stresses in the central part of the film, Fig. 4-1-7. The initial compressive pressure drives the expansion of the film, with tensile stresses concentrating in the central part of the film. The following gradually dissipating oscillations of the film continue beyond the time of the simulation. The oscillation of the lattice and electron temperatures shown in the insets in Fig. 4-1-5, are directly related to the pressure oscillations in Fig. 4-1-7. Compression leads to the increase of the lattice temperature whereas expansion corresponds to cooling. The electronic temperature lags behind the lattice temperature oscillations, inset in Fig. 4-1-5b, with the delay defined by the strength of the electron-phonon coupling. Quantitative thermodynamic analysis performed in Refs. [2,3] confirms that the temperature variations with pressure can be attributed to the adiabatic/isentropic expansion of the film.



(a)



(b)

Figure 4-1-7. Contour plots showing the spatial and temporal evolution of pressure in simulations of laser melting of a 20 nm Au film irradiated with a 200 fs laser pulse at an absorbed fluence of 92.5 J/m^2 . The simulations are performed with two sets of parameters: (a) $C_e(T_e)$ and $G(T_e)$ calculated with DOS from VASP and shown by solid lines in Figs. 3 and 4; (b) $C_e = \gamma T_e$ with $\gamma = 71 \text{ Jm}^{-3}\text{K}^{-2}$ and $G_c = 2.5 \times 10^{16} \text{ Wm}^{-3}\text{K}^{-1}$. Solid and dashed lines show the beginning (90% of the crystal phase, as defined by the local order parameter [2]) and the end (10% of the crystal phase) of the melting process. Laser pulse is directed along the vertical axes, from the top of the contour plots. The stepwise shape of the contour plot boundaries is related to the discretization of the mesh over which the average temperature and pressure values are calculated.

As discussed above, the characteristic time of the mechanical relaxation of the film is $\sim 5 \text{ ps}$ and, therefore, the amount of energy transferred from the hot electrons to the lattice during this time defines the magnitude of the initial compressive pressure and the amplitude of the pressure oscillations. The fraction of the laser energy transferred from the electrons to the lattice during the first 5 ps can be obtained from the electron energy plots shown in Fig. 4-1-6 and is 54% in the simulation performed with parameters that account for the DOS effects and 23% in the simulation performed with a constant electron-phonon coupling factor and a linear temperature dependence of the electron heat capacity. As a result, in the former simulation the fast transfer of more than a half of the deposited laser energy to the thermal energy of atomic motions during the first 5 ps takes place under conditions of the inertial stress confinement and leads to the buildup of strong compressive stresses, Fig. 4-1-7a, whereas in the latter simulation the film expands

during the lattice heating, the initial pressure is weak and the oscillations can be hardly observed in Fig. 4-1-7b.

The difference in the pressure oscillations in Fig. 4-1-7 is reflected in the difference in the temperature oscillations in Fig. 4-1-5, where much weaker temperature oscillations are observed in the simulation performed with parameters that do not account for the effect of the d band electrons. Note that at lower laser fluences, below the threshold for laser melting, the laser-induced elastic oscillations of the film would result in periodic oscillations of the diffraction peak positions – the effect that has been recently predicted in simulations [31] and observed in time-resolved electron diffraction experiments [32].

4.1.3.3 *Ultrafast melting process*

The atomic-level picture of the melting process predicted in a TTM-MD simulation using $C_e(T_e)$ and $G(T_e)$ calculated with DOS from VASP is presented in Fig. 4-1-8. The visual analysis of the snapshots taken during the melting process shows that at ~6 ps the growth of liquid regions first occurs at two free surfaces of the film, where the kinetic energy barrier is absent for liquid nucleation. However, due to the fast rate of the lattice heating, the propagation of melting fronts from the free surfaces of the film does not make any significant contribution to the overall melting process. By the time of 6 ps, the lattice temperature exceeds the overheating that corresponds to the limit of the crystal stability of the EAM Au, $\alpha=T/T_m \sim 1.25$ [2], leading to a spontaneous homogeneous nucleation of a large number of small liquid regions throughout the film and a rapid collapse of the crystalline structure within the subsequent 3-4 ps.

As discussed in Refs. [2,4], the relative contribution of the homogeneous and heterogeneous melting mechanisms in laser melting is controlled by the rate of the lattice heating and the temperature dependent velocity of the propagation of the melting fronts from the free surfaces of the film. The value of laser fluence used in the simulations presented in this study significantly, by $\sim 75\%$, exceeds the fluence needed for the complete melting of a 20 nm Au film [4]. At this level of laser excitation, the fast homogeneous melting within 3-4 ps, similar to the one illustrated in Fig. 4-1-8, is also observed in the simulation performed with a smaller constant value of the electron-phonon coupling factor. A large difference between the simulations performed with and without taking into account the effect of the thermal excitation of d band electrons, however, is found in the time of the onset of the melting process.

The difference in the time of the beginning of the melting process is apparent from Figs. 4-1-5b and 4-1-7, where the onsets of melting are marked by arrows and solid lines, respectively. A more clear representation of the timescales of the melting process is given in Fig. 4-1-9, where the evolution of the fraction of the crystal phase is shown for simulations performed with two sets of $C_e(T_e)$ and $G(T_e)$ parameters. In the case of constant G and γ , the melting starts at ~ 13 ps, the fraction of atoms in the liquid phase reaches 10% by 15 ps, 90% by 18 ps, and the crystalline regions completely disappear by 19 ps. In the simulation performed with $C_e(T_e)$ and $G(T_e)$ predicted using the electron DOS obtained in electronic structure calculation, the melting starts at ~ 6 ps, the fraction of atoms in the liquid phase reaches 10% by 7 ps, 90% by 9 ps, and the crystalline regions completely disappear by 10 ps.

The large difference in the starting time of the melting process observed between the two simulations discussed above provides a good opportunity for experimental verification of theoretical models discussed in Section 4.1.3. In particular, the results of the simulations discussed in this section can be directly related to recent time-resolved electron diffraction measurements performed for a 20 nm Au film irradiated by a 200 fs laser pulse at an absorbed laser fluence of 119 J/m² [29]. In order to quantitatively relate the simulation conditions to the experimental ones, we use the same overheating parameter $\alpha = T/T_m = 1.9$ as in the experiment. The overheating parameter is defined as a ratio of the maximum achievable lattice temperature (obtained under the assumption that no melting occurs) to the equilibrium melting temperature, T_m [33]. Using the thermodynamic parameters of the EAM Au material [4], the value of the absorbed fluence corresponding to $\alpha = 1.9$ is found to be 92.5 J/m² [34]. The experimental results show the presence of the long-range correlations in the diffraction profiles up to ~ 7 ps and the fast disappearance of the diffraction peaks corresponding to the crystal ordering during the time between 7 ps and 10 ps [29]. These experimental observations are in excellent agreement with the simulation results accounting for the thermal excitation of d band electrons. We can conclude, therefore, that the commonly used approximations of the constant electron-phonon coupling factor and the linear temperature dependence of the electron heat capacity are not appropriate for a realistic description of ultrashort pulse laser-material interactions in the high-fluence regime, where electron DOS effects start to play an important role in defining the timescales and other parameters of laser-induced processes.

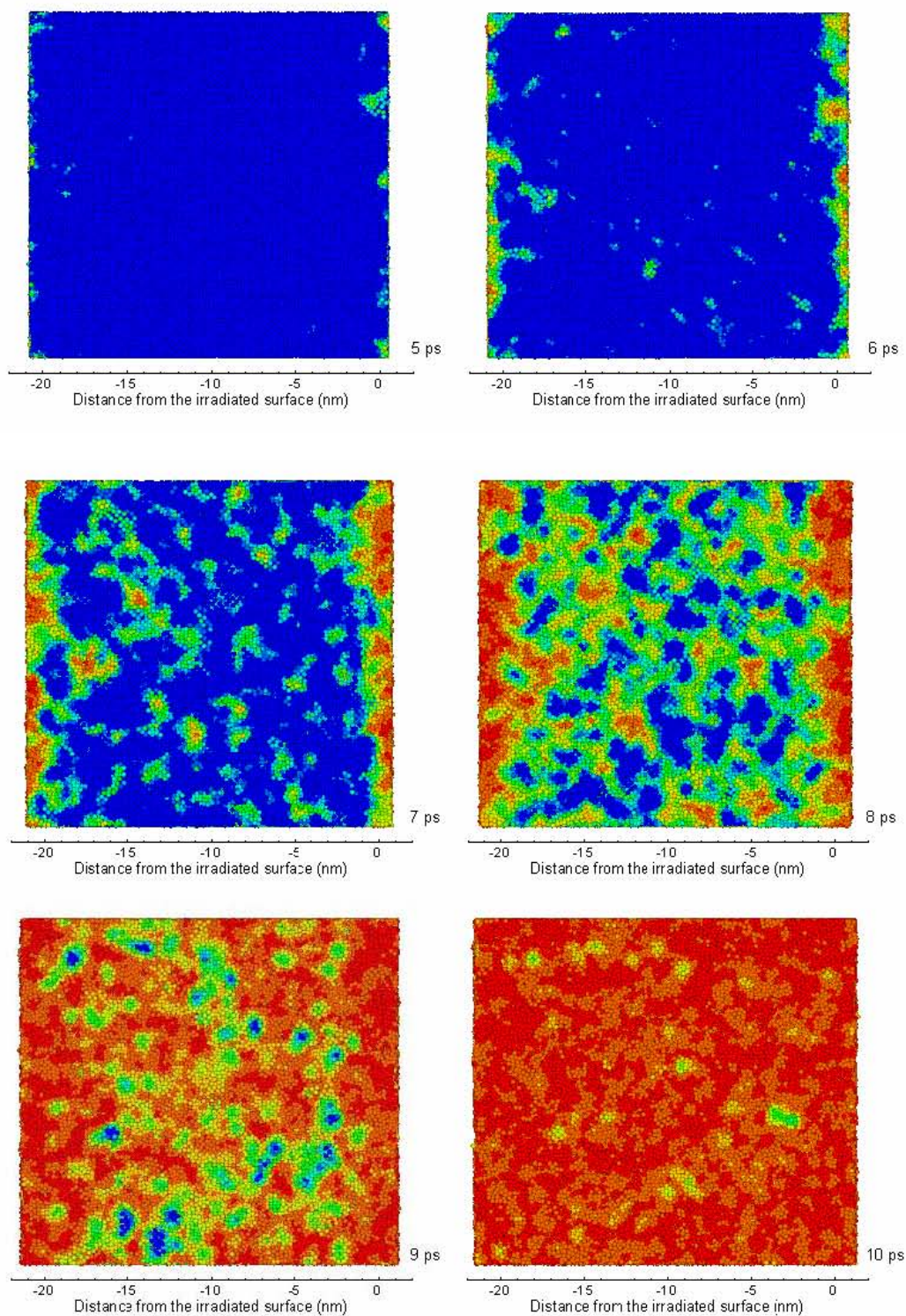


Figure 4-1-8. Snapshots of atomic configurations during the melting process in a 20 nm Au film irradiated with a 200 fs laser pulse at an absorbed fluence of 92.5 J/m^2 . Atoms

are colored according to the local order parameter - blue atoms have local crystalline surroundings, red atoms belong to the liquid phase. The laser pulse is directed from the right to the left sides of the snapshots. The simulation is performed with $C_e(T_e)$ and $G(T_e)$ calculated with DOS from VASP.

In this study no attempt has been made to account for the change in the electron DOS due to the modification of the electronic structure at high electron temperatures. The modifications of the electron structure would not affect the essential physics responsible for the change of the electron heat capacity and electron-phonon coupling caused by the thermal excitation of lower band electrons. Moreover, in the irradiation regime considered in this work the effect of the variations of the electron DOS on the calculated physical properties is small. Recent investigation of the modification of the electronic structure at much higher electron temperatures (~ 6 eV) [35] shows that the d band shifts towards lower energies while the width of the d band decreases. As a result, the contribution from the thermal excitation of d band electrons to the electron heat capacity and the electron-phonon coupling factor can be expected to be reduced at these extreme electron temperatures. In the case of transition metals, such as Ni or Pt, due to the unfilled d states in the electronic configurations, the Fermi level cuts through the d band [27]. Thus, the effect of the thermal excitation of electrons at high electron temperatures could affect the electron heat capacity and electron-phonon coupling in a very different way as compared to what is discussed in Section 4.1.3 for Au. In particular, the electron heat capacity would be smaller than the values given by the linear dependence on the electron temperature, as shown for Pt in Ref. [12], while the thermal

excitation of electrons may lead to the decrease of the electron-phonon coupling with increasing electron temperature [36].

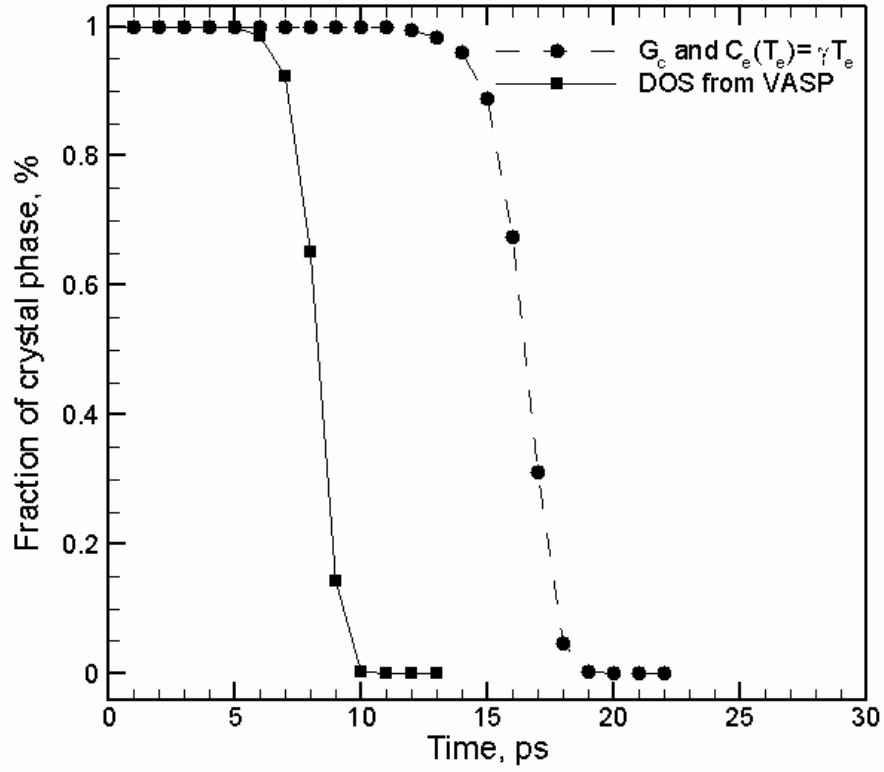


Figure 4-1-9. The evolution of the fraction of the crystal phase as a function of time in simulations performed with two sets of parameters: (Solid line) $C_e(T_e)$ and $G(T_e)$ calculated with DOS from VASP; (Dashed line) $C_e = \gamma T_e$ with $\gamma = 71 \text{ J m}^{-3} \text{ K}^{-2}$ and $G_c = 2.5 \times 10^{16} \text{ W m}^{-3} \text{ K}^{-1}$. The atoms in the crystal phase are distinguished from the ones in the liquid phase based on the local order parameter.

4.1.4 Summary

The temperature dependences of the electron-phonon coupling factor and the electron heat capacity are investigated for Au based on the electronic structure calculation performed within the density functional theory. Thermal excitation of d band electrons leads to a significant (up to an order of magnitude) increase in the electron-phonon coupling factor and makes a considerable contribution to the electron heat capacity in the range of electron temperatures typically realized in femtosecond laser material processing applications. The results of the analysis of the thermophysical properties of Au at high electron temperatures are incorporated into TTM-MD model and applied for simulations of laser melting of thin Au films. The increase in the strength of the electron-phonon coupling at high electron temperatures leads to a faster lattice heating, generation of stronger thermoelastic stresses and a higher amplitude of long-term oscillations of the film thickness, as well as significant changes in the time of the onset of the melting process. The latter can be directly related to the results of recent time-resolved electron diffraction experiments. The experimental time of the melting onset and the duration of the melting process are in excellent agreement with the results of the simulations in which the thermal excitation of d band electrons is accounted for. A simulation performed with commonly used approximations of a constant electron-phonon coupling factor and a linear temperature dependence of the electron heat capacity, on the other hand, is found to significantly (by a factor of 2) overpredict the time of the beginning of the melting process, supporting the importance of the electron DOS effects and thermal excitation of lower band electrons for realistic modeling of femtosecond pulse laser processing.

References for Chapter 4.1

- [1] S. I. Anisimov, B. L. Kapeliovich, and T. L. Perel'man, Sov. Phys. JETP **39**, 375-377, 1974.
- [2] D. S. Ivanov and L. V. Zhigilei, Phys. Rev. B **68**, 064114, 2003.
- [3] D. S. Ivanov and L. V. Zhigilei, Phys. Rev. Lett. **91**, 105701, 2003.
- [4] Z. Lin and L. V. Zhigilei, Phys. Rev. B **73**, in press.
- [5] E. Leveugle, D. S. Ivanov, and L. V. Zhigilei, Appl. Phys. A **79**, 1643, 2004.
- [6] L. V. Zhigilei, D. S. Ivanov, E. Leveugle, B. Sadigh, and E. M. Bringa, High-Power Laser Ablation V, Proc. SPIE **5448**, 505, 2004.
- [7] L. V. Zhigilei and D. S. Ivanov, Appl. Surf. Sci. **248**, 433, 2005.
- [8] X. Y. Wang, D. M. Riffe, Y. S. Lee, and M. C. Downe, Phys. Rev. B **50**, 8016, 1994.
- [9] A. N. Smith and P. M. Norris, Proceedings of 11th International Heat Transfer Conference **5**, 241, 1998.
- [10] N. W. Ashcroft and N. D. Mermin, Solid State Physics (Holt, Rinehart and Winston, New York, 1976).
- [11] K. M. Ho and K. P. Bohnen, Phys. Rev. Lett. **59**, 1833, 1987.
- [12] T. Tsuchiya and K. Kawamura, Phys. Rev. B **66**, 094115, 2002.
- [13] F. Kirchhoff, M. J. Mehl, N. I. Papanicolaou, D. A. Papaconstantopoulos, and F.S.Khan, Phys. Rev. B **63**, 195101, 2001.

- [14] G. K. Wertheim and D. N. E. Buchanan, Phys. Rev. B **33**, 914, 1986.
- [15] G. Kresse and J. Hafner, Phys. Rev. B **47**, 558, 1993.
- [16] D. Vanderbilt, Phys. Rev. B **41**, 7892, 1990.
- [17] F. Ladstädter, U. Hohenester, P. Puschnig, and C. Ambrosch-Draxl, Phys. Rev. B **70**, 235125, 2004.
- [18] J. Hohlfeld, S.-S. Wellershoff, J. Gudde, U. Conrad, V. Jahnke, and E. Matthias, Chem. Phys. **251**, 237-258, 2000.
- [19] M. I. Kaganov, I. M. Lifshitz, and L. V. Tanatarov, Sov. Phys. JETP **4**, 173, 1957.
- [20] J. K. Chen and J. E. Beraun, J. Opt. A: Pure Appl. Opt. **5**, 168, 2003.
- [21] J. P. Girardeau-Montaut and C. Girardeau-Montaut, Phys. Rev. B **51**, 13560, 1995.
- [22] J. K. Chen, W. P. Latham and J. E. Beraun, J. Laser Applications, **17**, 63, 2005.
- [23] D. Y. Tzou, Macro- to Microscale Heat Transfer: The Lagging Behavior (Washington, DC: Taylor & Francis, 1997).
- [24] Z. G. Wang, Ch. Dufour, E. Paumier, and M. Toulemonde, J. Phys.: Condens. Matter **6**, 6733, 1994.
- [25] P. B. Allen, Phys. Rev. Lett. **59**, 1460, 1987.
- [26] J. M. Ziman, Electrons and Phonons (Oxford Univ. Press London, 1960).
- [27] W. L. McMillan, Phys. Rev. **167**, 331, 1968.
- [28] S. D. Brorson, A. Kaeroonian, J. S. Moodera, D. W. Face, T. K. Cheng, E. P. Ippen, M. S. Dresselhaus and G. Dresselhaus, Phys. Rev. Lett. **64**, 2172, 1990.

- [29] J. R. Dwyer, C. T. Hebeisen, R. Ernstorfer, M. Harb, V. Deyirmenjian, R. E. Jordan and R. J. D. Miller, *Phil. Trans. R. Soc. A* **364**, 741, 2006.
- [30] X. W. Zhou, H. N. G. Wadley, R. A. Johnson, D. J. Larson, N. Tabat, A. Cerezo, A. K. Petford-Long, G. D. W. Smith, P. H. Clifton, R. L. Martens, and T. F. Kelly, *Acta Mater.* **49**, 4005, 2001.
- [31] Z. Lin and L. V. Zhigilei, *J. Phys.: Conference Series*, in press.
- [32] H. Park, X. Wang, S. Nie, R. Clinite, and J. Cao, *Phys. Rev. B* **72**, 100301(R), 2005.
- [33] B. Rethfeld, K. Sokolowski-Tinten, D. von der Linde, and S. I. Anisimov, *Phys. Rev. B* **65**, 092103, 2002.
- [34] In simulations, the calculation of the overheating parameter $\alpha=1.9$ is done with a temperature dependent lattice heat capacity determined for the EAM Au material [4], whereas in Ref. [29] a constant heat capacity is assumed. Using an experimental temperature dependent heat capacity for Au [28], a smaller overheating factor of 1.7 can be obtained for the absorbed laser fluence of 119 J/m² used in the experiment [29]. Nevertheless, this discrepancy does not affect the physical interpretations and conclusions derived from the comparison of the simulations and experiments presented in this study. In the simulation performed at a lower overheating of 1.7 with $C_e(T_e)$ and $G(T_e)$ calculated with DOS from VASP, the timescale of the melting process is very similar to the one at $\alpha=1.9$: the melting starts at ~ 8 ps, the fraction of atoms in the liquid phase reaches 10% by 10 ps, 90% by 14 ps, and the crystalline regions completely disappear by ~ 15 ps.

- [35] V. Recoules, J. Cl  rouin, G. Z  rah, P. M. Anglade, and S. Mazevet, *Phys. Rev. Lett.* **96**, 055503, 2006.
- [36] Z. Lin and L. V. Zhigilei, unpublished.

4.2 Temperature dependences of the electron-phonon coupling, electron heat capacity and thermal conductivity in Ni under femtosecond laser irradiation

4.2.1 Introduction

The fast growth of femtosecond laser applications has increased the demand for realistic computational description of highly nonequilibrium processes induced in a target material by the fast laser energy deposition. The time evolution of the electron and lattice temperatures in a metal target irradiated by a femtosecond laser pulse is commonly described by the two-temperature model (TTM) [1], that accounts for the laser energy absorption by the conduction band electrons, energy transfer from hot electrons to the atomic vibrations due to the electron–phonon coupling, and the electronic heat diffusion from the irradiated surface to the bulk of the target.

The accuracy of a quantitative description of the kinetics of energy redistribution in the irradiated target in a big part relies on the appropriate choice of the temperature dependent thermophysical properties of the target material included in the TTM equations, namely, the electron-phonon coupling factor, the electron heat capacity, and the heat conductivity. Due to the small electron heat capacity of the electrons, the electron temperature in the surface region of the irradiated target can be transiently brought to very high values, comparable to the Fermi temperature. At such high electron temperatures, T_e , the temperature dependent thermophysical properties of noble [2,3,4] and transition metals [5] can be directly affected by the thermal excitation of the lower band electrons.

The effect of the thermal excitation of electrons on the thermophysical properties is sensitive to the details of the electronic structure of the target material. In particular, in

Au the d band lies ~ 2 eV below the Fermi level and at T_e below ~ 3000 K (~ 0.25 eV) the d band electrons do not contribute to the electron-phonon coupling and the electron heat capacity, whereas at $\sim 10^4$ K (~ 1 eV) thermal excitation of d band electrons results in a significant increase of both the electron-phonon coupling factor and the electron heat capacity (e.g. the electron-phonon coupling factor exceeds the room temperature value by a factor of 8.9 at $T_e = 2 \times 10^4$ K [4]). On the other hand, in transition metals, such as Ni or Pt, the Fermi level cuts through the d band, resulting in a very high density of electron states at the Fermi level. In this case, the thermal excitation of electrons from high-density of states d band to the low density of states s band can have the opposite effect on the electron heat capacity and electron-phonon coupling as compared to noble metals. In particular, the electron heat capacity of Pt has been shown to become smaller than the value given by the linear dependence on the electron temperature predicted by the Sömmersfeld expansion for the electronic free energy [5]. Therefore, a detailed analysis of the connections between the electron density of states (DOS) in the target material and the temperature dependence of the thermophysical material properties is needed for a realistic description of laser-material interactions.

In this section, we investigate the effect of the thermal excitation of the d band electrons on the thermophysical properties of Ni. In the next section, the connections between the electron DOS of Ni and the temperature dependence of the electron-phonon coupling, electron heat capacity and thermal conductivity are analyzed. The qualitative differences between the temperature dependences obtained for Ni and earlier predictions for Au [4] are related to the differences in the electron DOS of the two metals. In Section 4.2.3, practical implications of the thermal excitation of the d band electrons are

investigated by performing a series of TTM simulations with the modified temperature-dependent thermophysical properties. The evolution of the kinetics of the electron-phonon equilibration, the electron and lattice temperatures, and the fluence thresholds for surface melting are investigated for Ni films at various thickness and bulk targets. A brief summary of the results is given in Section 4.2.4.

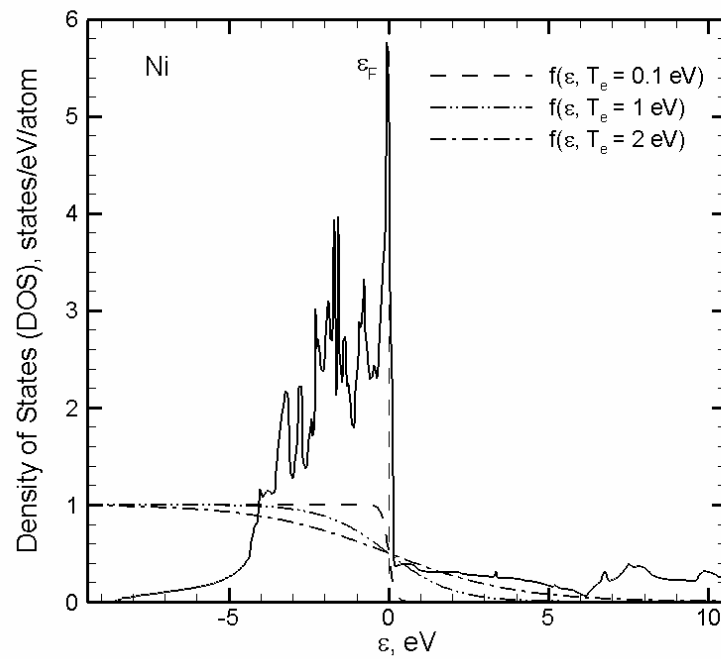


Figure 4-2-1. Electron DOS of Ni obtained in electron structure calculations performed with VASP (solid line). The Fermi distribution functions are also shown for three different values of the electron temperature. The energy is shown with respect to the Fermi level at zero temperature, ε_F .

4.2.2 The effect of thermal excitation of electrons on thermophysical properties of Ni

The effect of the thermal excitation of electrons on thermophysical properties of Ni is investigated here based on the electron DOS obtained from the electronic structure

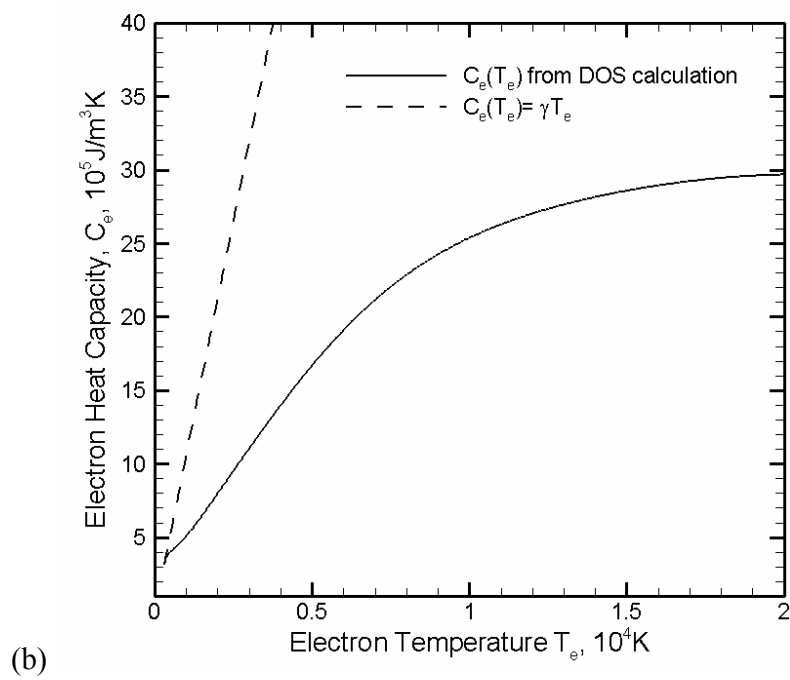
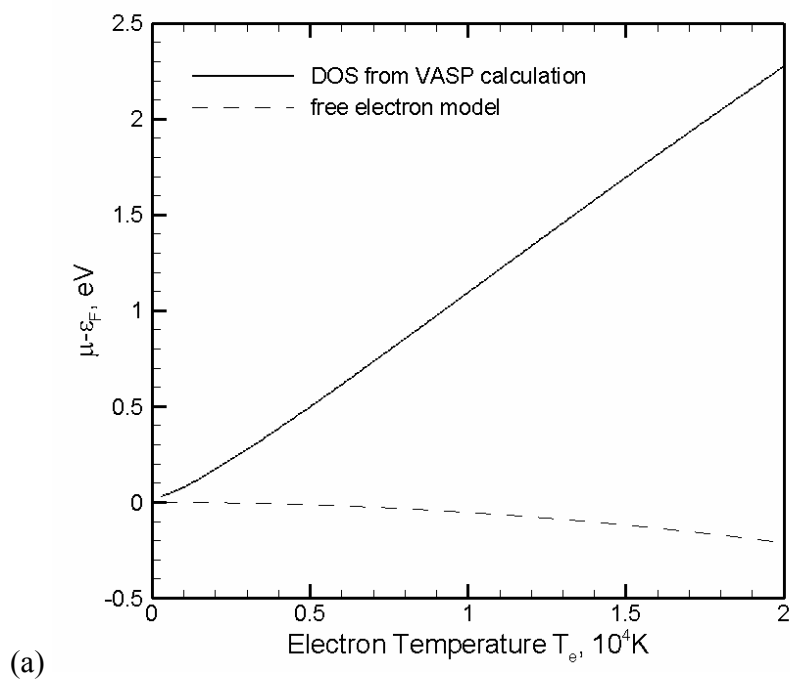
calculation performed within the density functional theory using the Vienna Ab-initio Simulation Package (VASP) [6]. The Projector Augmented Wave (PAW) potential [7] is used in the calculation, where the exchange correlation term is treated within the Generalized Gradient Approximation (GGA). The calculations are done for nonmagnetic Ni at the equilibrium lattice constant of 3.53 Å. The electron DOS for Ni obtained from VASP at $T_e=0$ K is shown in Fig. 4-2-1, together with the Fermi distribution function plotted at three different values of the electron temperature.

The electron heat capacity dependence on the electron temperature can be expressed as [8]:

$$C_e(T_e) = \int_{-\infty}^{\infty} (\varepsilon - \varepsilon_F) \frac{\partial f(\varepsilon, \mu, T_e)}{\partial T_e} g(\varepsilon) d\varepsilon \quad (4.2.1)$$

where $g(\varepsilon)$ is the electron DOS at the energy level ε , μ is the chemical potential at T_e , and $f(\varepsilon, \mu, T_e)$ is the Fermi distribution function, defined as $f(\varepsilon, \mu, T_e) = \{\exp[(\varepsilon - \mu)/k_B T_e] + 1\}^{-1}$.

The determination of the chemical potential μ , required in Eq. (4.2.1), is done through setting the result of the integration of the product of DOS and the Fermi distribution function at T_e over all energy levels to be equal to the total number of electrons. It can be seen from Figs. 4-2-1 and 4-2-2(a) that as the electron temperature increases, the excitation from high density of states below ε_F to the states above ε_F increases, leading to the increase in the chemical potential, whereas the chemical potential of the free electron model, calculated from the Sömmersfeld expansion at low temperatures [27], decreases.



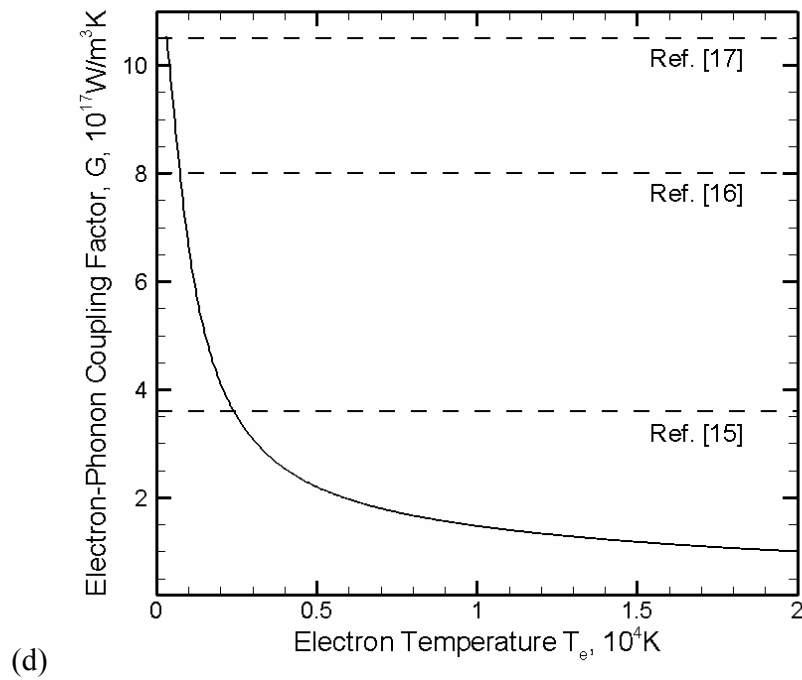
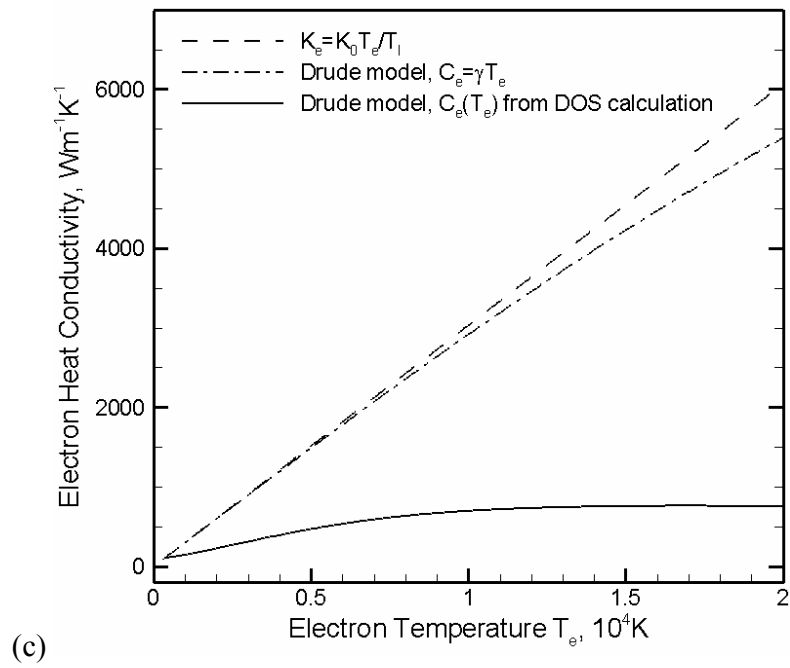


Figure 4-2-2. Electron temperature dependences of thermophysical properties of Ni. Solid lines show the results of the calculations performed with DOS obtained from VASP.

Dashed lines show the commonly used approximations of the thermophysical material properties. Chemical potential is shown in (a) electron heat capacity in (b), electron thermal conductivity in (c), and electron-phonon coupling factor in (d). Data presented in this figure is accessible in tabulated form from [11].

In Fig. 4-2-2(b), the temperature dependence of the electron heat capacity, calculated from Eq. (4.2.1) with the DOS determined from VASP calculations, is shown together with the commonly used linear approximation, $C_e(T_e) = \gamma T_e$, obtained from Sömmersfeld expansion with $\gamma = 1065 \text{ Jm}^{-3}\text{K}^{-2}$ measured at low temperatures [9]. The heat capacity calculated with the realistic DOS is lower than the one predicted by the linear dependence, $C_e(T_e) = \gamma T_e$, at all temperatures and exhibits a steadily increasing deviation from the linear dependence. This deviation can be explained by analyzing the characteristics of the Ni DOS shown in Fig. 4-2-1. The high density of electron states at the Fermi level ensures that the 3d band electrons can be easily excited to the 4s band. The 4s band has a much smaller density of states as compared to the density of states at the Fermi level, leading to the negative deviation of the heat capacity from the linear dependence, which is obtained from the Sömmersfeld expansion at a low electron temperature. This behavior of the heat capacity is similar to the one reported for Pt [5], which has the electron DOS similar to Ni, but different from Au, where the thermal excitation from the low-laying d band results in the positive deviation of the heat capacity from the linear dependence at sufficiently high electron temperatures [4,5]. The trend of the negative deviation of the electron heat capacity from the linear dependence shown in Fig.4.2.2 (b) agrees with the results reported for Ni in Ref. [10], where the electronic heat

capacity was obtained by subtracting the lattice heat capacity (assumed to follow the Dulong-Petit law at high temperatures), from the total heat capacity measured in experiments for temperatures up to 1600 K.

The electron thermal conductivity is directly affected by the thermal excitation of d band electrons as it is related to the electron heat capacity through the Drude model relationship, $\kappa(T_e, T_l) = v_F^2 C_e(T_e) \tau_e(T_e, T_l) / 3$ [27], where v_F is the Fermi velocity and $\tau_e(T_e, T_l)$ is the total electron scattering time. The total electron scattering time is defined by the electron-electron scattering time, τ_{e-e} , and the electron-phonon scattering time, τ_{e-ph} , and can be evaluated from the sum of the scattering rates, $1/\tau_e = 1/\tau_{e-e} + 1/\tau_{e-ph} = AT_e^2 + BT_l$, where $A = 1.4 \times 10^6 \text{ K}^{-2}\text{s}^{-1}$ and $B = 1.624 \times 10^{13} \text{ K}^{-1}\text{s}^{-1}$ for Ni [12]. Fig. 4-2-2(c) shows the electron thermal conductivity calculated with three different approximations, namely, a linear dependence on the electron temperature neglecting the contribution from the electron-electron scattering, $K_e = K_0 T_e / T_l$ with $K_0 = 91 \text{ Wm}^{-1}\text{K}^{-1}$ [9], Drude model with $C_e(T_e) = \gamma T_e$, and Drude model with $C_e(T_e)$ evaluated from Eq. (4.2.1) using the DOS calculated with VASP. It is clear from Fig. 4.2.2(c) that the deviation of the heat capacity from the linear dependence, Fig. 4.2.2(b), will also result in slower electron heat conduction, especially at the early stage of the electron-phonon equilibration, when the electron temperature is close to its maximum.

In the analysis of the electron temperature dependence of the electron-phonon coupling factor we follow the approach suggested in Refs. [18, 13] and applied earlier for the analysis of the temperature dependence of the electron-phonon coupling in Au [18, 19, 4]. Within this approach, the electron-phonon coupling factor accounting for the

thermal excitation of electrons from the energy levels located below the Fermi level can be expressed as [18]:

$$G(T_e) = \frac{\pi \hbar k_B \lambda \langle \omega^2 \rangle}{g(\varepsilon_F)} \int g^2(\varepsilon) \left(-\frac{\partial f}{\partial \varepsilon} \right) d\varepsilon \quad (4.2.2)$$

where λ is the electron-phonon coupling constant used in the superconductivity theory and $\langle \omega^2 \rangle$ is the second moment of the phonon spectrum defined by McMillan [14]. At low electron temperatures, $-\partial f / \partial \varepsilon$ reduces to a delta function and Eq. (4.2.2) yields the expression proposed by Allen: $G_0 = \pi \hbar k_B \lambda \langle \omega^2 \rangle g(\varepsilon_F)$ [13], featuring a constant value. Using $\lambda=0.084$ for Ni [15] and an approximation for $\langle \omega^2 \rangle = 1/2\theta_D^2$ [14,15], where $\theta_D=450$ K is the Debye temperature for Ni [9], one can estimate the coupling constant for Ni to be $G_0=18 \times 10^{17} \text{ Wm}^{-3}\text{K}^{-1}$. It should be noted that literature values of the electron-phonon coupling constant for Ni vary in a range from 3.6 to $10.5 \times 10^{17} \text{ Wm}^{-3}\text{K}^{-1}$ [16,17,18]. As the verification of the value of $\lambda \langle \omega^2 \rangle$ for nonmagnetic Ni is beyond the scope of this study, and considering that in Ref. [18] the electron-phonon coupling constant of $10.5 \times 10^{17} \text{ Wm}^{-3}\text{K}^{-1}$ is measured in pump-probe reflectivity experiments at relatively low electron temperatures (the transient increase of the electron temperature above the room temperature does not exceed 150 K), we set the coupling factor in Eq. (4.2.2) to be equal to $10.5 \times 10^{17} \text{ Wm}^{-3}\text{K}^{-1}$ at $T_e=300$ K and obtain $\lambda \langle \omega^2 \rangle = 49.5 \text{ meV}^2$. This value of $\lambda \langle \omega^2 \rangle$ is then used in Eq. (4.2.2) to calculate the temperature dependence of the electron-phonon coupling factor in a broad range of temperatures, shown in Fig. 4-2-2(d).

As shown in Fig. 4-2-2(d), the electron-phonon coupling factor decreases monotonically as the electron temperature increases. The decrease is particularly sharp as the temperature increases up to $3\text{--}4\times 10^3$ K and becomes less steep at higher temperatures. As the chemical potential shifts to higher energies, Fig. 4-2-2(a), the contribution of the d band electrons to the electron-phonon coupling decreases. As a result, the electron-phonon coupling factor decreases with respect to its room temperature value by a factor of 4.8 at $T_e = 0.5\times 10^4$ K, by a factor of 7.1 at $T_e = 1\times 10^4$ K, and by a factor of 10.5 at $T_e = 2\times 10^4$ K. The decrease in the strength of the electron-phonon coupling with increasing electronic temperature is consistent with the relative values evaluated in experiments performed at different levels of laser excitation. The highest value of the electron-phonon constant, 10.5×10^{17} Wm⁻³K⁻¹, is obtained from transient thermoreflectance measurements [18], where the maximum electron temperature increase does not exceed 150 K. Somewhat smaller value of 8×10^{17} Wm⁻³K⁻¹ is deduced from pump-probe transmission experiments [17], where the electron temperature increases up to 700 K. Finally, the smallest value of the coupling constant, 3.6×10^{17} Wm⁻³K⁻¹, is obtained by fitting the predictions of the TTM calculations to the threshold fluences for the onset of surface melting [39]. The electron temperature in this case reaches several thousands of Kelvin and the reported value of the effective electron-phonon coupling “constant” is consistent with the temperature dependence shown in Fig. 4-2-2(d).

The trend of the temperature dependence of the electron-phonon coupling predicted for Ni in Fig.4-2-2 (d) is in apparent contrast with the result predicted for Au [4], where the d band lies ~ 2 eV below the Fermi level and, at sufficiently high temperatures, the thermal excitation of d band electrons results in a significant increase of

the electron-phonon coupling factor with respect to its room temperature value (by a factor of 5.8 at $T_e = 1 \times 10^4$ K and by a factor of 8.9 at $T_e = 2 \times 10^4$ K). Thus, the neglect of the effect of the thermal excitation of electrons on thermophysical properties of the target material and, in particular, the assumption of a temperature-independent electron-phonon coupling factor, can result, depending on the characteristics of the electron DOS, in either significant overestimation (e.g. Ni) or underestimation (e.g. Au) of the rate of the electron-phonon energy transfer during the time of the electron-phonon equilibration following short pulse laser irradiation.

The theoretical approach used in this work and other studies [18,19,4] for the calculation of the temperature dependent electron-phonon coupling does not explicitly take into account the umklapp electron-phonon scattering processes [27]. As shown recently by Petrov [19], the umklapp processes make a large contribution to the theoretically predicted values of the electron phonon coupling. The effect of the umklapp processes on the electron temperature dependence of the electron-phonon coupling, however, is relatively weak for temperatures exceeding the Debye temperature. Since the temperature dependence of the electron-phonon coupling for Ni, shown in Fig. 4-2-2(d), is obtained based on the experimental value for the electron-phonon coupling near the room temperature, the contribution from the umklapp processes to the room temperature value of the electron-phonon coupling is implicitly taken into account. As for the temperature dependence of the electron-phonon coupling, the contribution of the umklapp processes [46] is negligible as compared to the contribution from the thermal excitation of d band electrons revealed in this work.

4.2.3 TTM results and discussion

Significant deviations of the thermophysical properties of Ni from the commonly used approximations, observed in a range of electron temperatures readily accessible in femtosecond laser material processing applications, may have important practical implications. In order to investigate to what degree the changes in the transient material properties predicted in the previous section would affect the material response to short pulse laser irradiation, we incorporate the new temperature dependences into TTM model and perform simulations of laser heating and melting of Ni thin films and bulk targets.

Two series of TTM simulations are performed for the same irradiation conditions. In the first series, the commonly used approximations of $C_e = \gamma T_e$ with $\gamma = 1065 \text{ Jm}^{-3}\text{K}^{-2}$, $G = 3.6 \times 10^{17} \text{ Wm}^{-3}\text{K}^{-1}$, and $K_e = K_0 T_e / T_l$ with $K_0 = 91 \text{ Wm}^{-1}\text{K}^{-1}$ [9,12,39,20] are used. The value of the coupling constant is used to allow for the comparison with earlier simulations and experiments performed for surface melting of Ni films of different thickness [39,20]. In the second series of simulations, the new thermophysical parameters, discussed in Section 4.2.2, illustrated in Fig. 4-2-2, and given in tabulated form at [11] are used. In both series of TTM simulations the experimental values of the melting temperature and the latent heat of melting are used, 1728 K and $2.45 \times 10^9 \text{ Jm}^{-3}$ [21]. The lattice heat capacity, C_l , is obtained by subtracting the electronic contribution from the room temperature value of the total heat capacity, $C_l = C_{total}(300 \text{ K}) - C_e(T_e = 300 \text{ K}) = 3.68 \times 10^6 \text{ Jm}^{-3}\text{K}^{-2}$, with $C_{total}(300 \text{ K}) = 4 \times 10^6 \text{ Jm}^{-3}\text{K}^{-2}$ [21]. The lattice heat capacity is assumed to be constant as the lattice temperature in the TTM calculations reported in this work is either close or higher than the Debye temperature of Ni, 450 K.

4.2.3.1 *Transient evolution of the electron and lattice temperatures*

The evolution of the electron and lattice temperatures at the surface of a bulk Ni target irradiated with a 200 fs laser pulse at an absorbed fluence of 250 J/m^2 is shown in Fig. 4-2-3 for the two sets of thermophysical parameters discussed above. Following the laser irradiation, the maximum electron temperature achieved by the end of the laser pulse is significantly, by 45%, higher in the model that takes into account the DOS effects on the thermophysical parameters of the material. The observation of the higher maximum electron temperature is directly related to a much weaker increase of the heat capacity with electron temperature as compared to the commonly used linear dependence, Fig. 4-2-2(b).

The evolution of the lattice temperature in the irradiated target is also affected by the choice of the parameters used in the simulations. Despite the weakening of the electron-phonon coupling at high electron temperatures, Fig. 4-2-2(d), the time required for the equilibration between the electron and lattice is close in both simulations, $\sim 10 \text{ ps}$, whereas the maximum lattice temperature achieved at the surface increases by $\sim 13\%$, from 1430 K to 1620 K, when the modified thermophysical parameters are used. The similarity of the rates of the electron-phonon relaxation can be explained by the larger difference between the lattice and electron temperatures created by the laser excitation predicted with the new set of parameters, Fig. 4-2-3, which balances the effect of the weaker coupling at high electron temperatures.

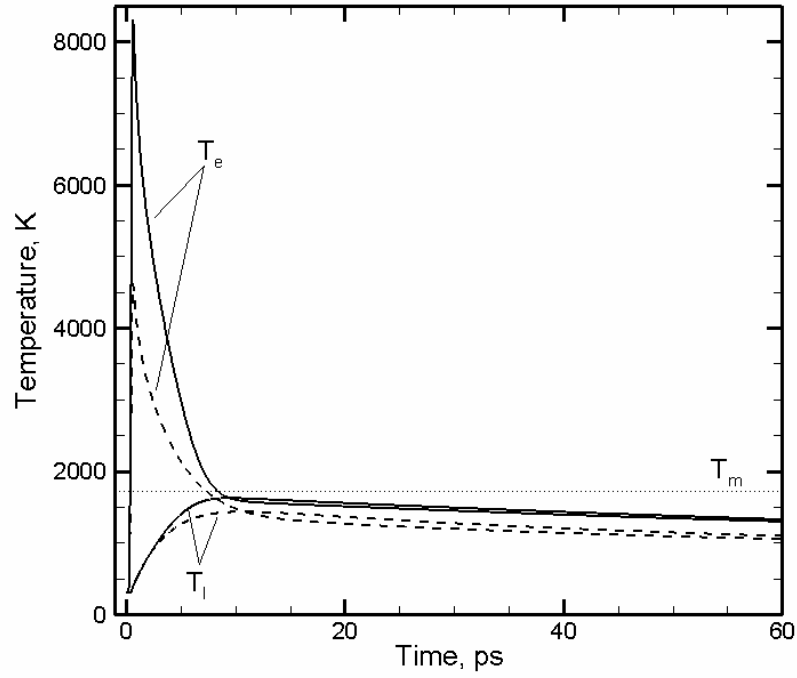


Figure 4-2-3. Evolution of the electron and lattice temperatures at the surface of a bulk Ni target irradiated with a 200 fs laser pulse at an absorbed fluence of 250 J/m^2 predicted in TTM simulations performed with thermophysical parameters calculated with DOS obtained from VASP (solid lines) and the commonly used approximations described in the text (dashed lines). The temperature dependences of thermophysical parameters used in the TTM simulations are shown in Fig. 4-2-2.

4.2.3.2 Fluence threshold for surface melting

To study the effect of changes in the temperature dependence of thermophysical parameters on the thresholds for the onset of surface melting, we perform a series of TTM calculations for Ni films of various thicknesses irradiated with a 200 fs laser pulse. The threshold for surface melting is defined as the fluence at which the lattice

temperature at the surface reaches the melting temperature, 1728 K. As shown in Fig. 4-2-4, the experimental threshold fluences [39] and the results obtained in both series of simulations follow the same general trend: linear increase of the threshold fluence with film thickness up to the thickness that corresponds to the diffusive penetration depth of the excited electrons during the time of the electron-phonon equilibration, L_c [39,20], and saturation of the threshold fluence at higher fluences. In a film thinner than L_c , nearly uniform temperature distribution is established by the time of the electron-phonon equilibration and the threshold fluence for melting is defined by the energy density needed to homogeneously heat the film up to the melting temperature. For films thicker than L_c , the electron-phonon equilibration takes place within the electron diffusion length of L_c from the irradiated surface and the threshold fluence for melting becomes independent of thickness. As can be seen from Fig. 4, the values of L_c at the threshold for surface melting are similar, ~ 50 nm, in the two series of TTM simulations, as well as in the experiment.

The saturation threshold fluence at large film thicknesses obtained in the TTM simulations performed with the commonly used parameters, 325 J/m^2 , is significantly higher than the experimental value, 220 J/m^2 [39], whereas the value predicted in TTM simulations performed with the new thermophysical parameters, 270 J/m^2 , is in a better agreement with the experimental data, Fig. 4-2-4. As the experimental values are obtained by conversion of multi-shot data to single-shot threshold fluences, further accurate single-shot experimental measurements, along with further improvements of the computational model, might be needed to clarify the remaining discrepancy between the experimental and computational values of the laser melting threshold fluences.

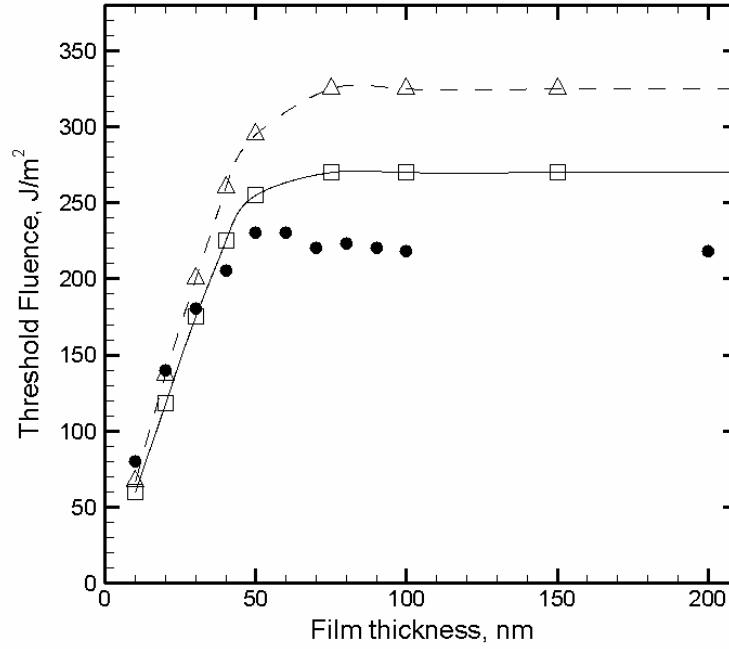


Figure 4-2-4. Threshold fluence for surface melting as a function of film thickness obtained in TTM simulations performed with thermophysical parameters calculated with DOS obtained from VASP (solid lines) and the commonly used approximations described in the text (dashed lines). Experimental data for the melting thresholds from Ref. [39] is shown by filled circles.

4.2.4 Summary

The electron temperature dependences of the electron-phonon coupling factor, electron heat capacity, and thermal conductivity are investigated for Ni based on the electron DOS obtained from ab initio electronic structure calculations. Due to the presence of large density of states around the Fermi level, thermal excitation of d band electrons leads to a significant decrease in the electron-phonon coupling factor and large negative deviations of the electron heat capacity and the electron thermal conductivity

from commonly used linear dependences on the electron temperature. These large deviations of the thermophysical parameters away from the low temperature values/dependences are predicted for electron temperatures that are realized in ultrashort laser material processing applications and, therefore, can have important practical implications. In particular, TTM simulations performed with the new set of thermophysical parameters predict higher maximum lattice and electron temperatures achieved at the surface, as well as 17% decrease in the saturation threshold fluence for surface melting of film thicker than 50 nm, as compared to the results obtained using a constant electron-phonon coupling factor and linear temperature dependences of the electron heat capacity and electron thermal conductivity. The new calculated values of the threshold fluences for surface melting are in a better agreement with the results of experimental measurements.

References for Chapter 4.2

- [1] S. I. Anisimov, B. L. Kapeliovich, T. L. Perel'man, Sov. Phys. JETP 39 (1974) 375.
- [2] X. Y. Wang, D.M . Riffe, Y. S. Lee, M. C. Downe, Phys. Rev. B 50 (1994) 8016.
- [3] A. N. Smith, P. M. Norris, Proceedings of 11th International Heat Transfer Conference 5 (1998) 241.
- [4] Z. Lin, L. V. Zhigilei, Proc. SPIE 6261 (2006) 62610U.
- [5] T. Tsuchiya, K. Kawamura, Phys. Rev. B 66 (2002) 094115.
- [6] G. Kresse, J. Hafner, Phys. Rev. B 47 (1993) 558; *ibid.* 49 (1994) 14 251.
- [7] G. Kresse, D. Joubert, Phys. Rev. 59 (1999) 1758.
- [8] N. W. Ashcroft and N. D. Mermin, Solid State Physics (Holt, Rinehart and Winston, New York, 1976).
- [9] American Institute of Physics Handbook, 3rd edition (McGraw-Hill, New York, 1982).
- [10] G. K. White, Aust. J. Phys. 46 (1993) 707.
- [11] Electron temperature dependences of thermophysical properties of Ni and several other metals are accessible in tabulated form from
<http://www.faculty.virginia.edu/CompMat/electron-phonon-coupling/>
- [12] D. S. Ivanov, L. V. Zhigilei, Phys. Rev. B 68 (2003) 064114.
- [13] P. B. Allen, Phys. Rev. Lett. 59 (1987) 1460.
- [14] W. L. McMillan, Phys.Rev.167 (1968) 331.
- [15] D. A. Papaconstantopoulos, L. L. Boyer, B. M. Klein, A. R. Williams, V. L. Moruzzi, J. F. Janak, Phys. Rev. B 15 (1977) 4221.
- [16] S.-S. Wellershoff, J. Gdde, J. Hohlfeld, J. G. Mller, E. Matthias, Proc. SPIE 3343 (1998) 378.

- [17] E. Beaupaire, J.-C. Merle, A. Daunois, J.-Y. Bigot, *Phys. Rev. Lett.* 76 (1996) 4250.
- [18] A. P. Caffrey, P. E. Hopkins, J. M. Klopf, P. M. Norris, *Microscale Thermophys. Eng.* 9 (2005) 365.
- [19] Yu. V. Petrov, *Laser Part. Beams* 23 (2005) 283.
- [20] D. S. Ivanov, L. V. Zhigilei, *Appl. Phys. A: Mater. Sci. Process.* 79 (2004) 977.
- [21] *CRC Handbook of Chemistry and Physics*, 72nd edition, ed. by D.R. Lide, (CRC Press, Boca Raton, FL 1991).

5. Generation of Crystal Defects in a BCC Metal Target Irradiated by Short Laser Pulses

5.1 Introduction

Surface modification by laser irradiation is in the core of many modern processing and fabrication techniques, including laser surface alloying, annealing, and hardening, e.g. [1,2,3,4]. The improvement of surface properties is achieved by structural and compositional modification of a surface layer through the formation of metastable phases, grain refinement, generation/annealing of crystal defects, and redistribution of the alloying elements. Recent progress in the development of accessible sources of short (pico- and femtosecond) laser pulses opens up new possibilities for surface modification with high accuracy and spatial resolution. The shallow depths of the laser energy deposition and steep temperature gradients, typically produced by the short pulse laser irradiation, can result in the confinement of the laser-induced structural modifications within a surface layer as small as tens to hundreds of nanometers, e.g. [5,6,7,8]. The small size of the laser-modified zone makes characterization of laser-induced structural changes challenging and, at the same time, increases the importance of understanding of the nucleation, mobility, interactions and stability of individual crystal defects and their ensembles.

With a quickly expanding range of time- and length-scales accessible for molecular dynamics (MD) simulations (systems containing $\sim 10^6$ - 10^7 atoms, with sizes on the order 100s of nm can be simulated for nanoseconds [9,10]), the atomistic computer modeling has a good potential of revealing the mechanisms of laser-induced phase and structural transformations. Indeed, MD simulations have been successfully applied for

investigation of the microscopic mechanisms of laser melting [11 , 12 , 13], photomechanical spallation [14,15], and ablation [10,16,17,18,19,20] of metal targets. A detailed analysis of the crystal defects introduced by short pulse irradiation, however, have not been performed in MD simulations so far and the question on the atomic-level mechanisms responsible for the generation and evolution of defect configurations in laser materials processing remains largely unexplored.

In this chapter, we present the results of MD simulations of short pulse laser interaction with a body centered cubic (BCC) metal, Cr. The laser fluences used in the simulations are chosen to be close to the threshold for the onset of surface melting and the main focus of the study is on the detailed analysis of the crystal defects generated in the surface region of the irradiated bulk target. A long term evolution of sub-surface defect configurations is studied and implications for practical applications of non-ablative laser surface modification are discussed. A brief description of the computational model used in the simulations is given below, in Section 5.2. A new parameterization of a computationally efficient embedded atom method (EAM) potential for Cr, as well as the physical properties of the model Cr material predicted by the potential are presented in Section 5.3. The results of the simulations of a transient surface melting and generation of crystal defects in the surface region of a Cr target irradiated by a femtosecond laser pulse are presented in Section 5.4 and summarized in Section 5.5.

5.2 TTM-MD model for laser interactions with a Cr target

The simulations of short pulse laser irradiation of a bulk Cr target are performed with a computational model that combines the classical MD method with a continuum

description of the laser excitation and subsequent relaxation of the conduction band electrons [11]. The model is based on well-known two-temperature model (TTM) [21], which describes the time evolution of the lattice and electron temperatures by two coupled nonlinear differential equations. In the combined model, the MD method substitutes the TTM equation for the lattice temperature in the surface region of the target, where the laser-induced structural transformations are expected to take place. The diffusion equation for the electron temperature is solved by a finite difference method simultaneously with MD integration of the equations of motion of atoms. The electron temperature enters a coupling term that is added to the MD equations of motion to account for the energy exchange between the electrons and the lattice. The cells in the finite-difference discretization are related to the corresponding volumes of the MD system and the local lattice temperature is defined for each cell from the average kinetic energy of thermal motion of atoms.

The hybrid atomistic-continuum model, briefly discussed above, combines the advantages of TTM and MD methods. TTM provides an adequate description of the laser energy deposition into the electronic system, energy exchange between the electrons and phonons, and fast electron heat conduction in metals, whereas the MD representation of the surface region of the target enables atomic-level investigations of laser-induced structural and phase transformations. A complete description of the TTM-MD model is given elsewhere [11]. Below we provide the details of the computational setup designed for the simulation of laser interaction with a bulk Cr target.

The MD part of the TTM-MD model represents the top 100 nm surface region of the Cr target and is composed of 630 000 atoms initially arranged in a BCC crystallite

with dimensions of $8 \text{ nm} \times 8 \text{ nm} \times 100 \text{ nm}$. Periodic boundary conditions are imposed in the directions parallel to the (100) free surface of the target. At the bottom of the MD computational cell, a dynamic non-reflecting boundary condition [22,23] is applied to account for the propagation of the laser-induced pressure wave from the surface region of the target represented by the MD method to the continuum part of the model. The energy carried away by the pressure wave is monitored, allowing for control over the total energy conservation in the combined model. In the continuum part of the model, beyond the MD region, the electron heat conduction and the energy exchange between the electrons and the lattice are described by the conventional TTM. The size of the continuum (TTM) region is chosen to be 500 nm, so that no significant changes in the electron and lattice temperatures are observed at the bottom of the continuum region during the time of the simulations.

The thermal and elastic properties of the target material, such as the lattice heat capacity, elastic moduli, coefficient of thermal expansion, melting temperature, volume and entropy of melting and vaporization, etc., are all defined by the interatomic interaction potential, described in this work by EAM in the form described in the next section. The parameters used for Cr in the TTM equation for the electron temperature are as follows. The electronic heat capacity is $C_e = \gamma T_e$ with $\gamma = 194 \text{ Jm}^{-3}\text{K}^{-2}$ [24], the electron-phonon coupling constant is $G = 4.2 \times 10^{17} \text{ Wm}^{-3}\text{K}^{-1}$ [25], and the dependence of the electron thermal conductivity on the electron and lattice temperatures is described as $K_e = K_0 T_e / T_l$ with $K_0 = 94 \text{ Wm}^{-1}\text{K}^{-1}$ [24]. Irradiation by a 200 fs laser pulse is represented through a source term with a Gaussian temporal profile and exponential attenuation of laser intensity with depth under the surface (Beer-Lambert law) added to

the TTM equation for the electron temperature. An optical penetration depth of 8.9 nm at a laser wavelength of 400 nm [26] is assumed in the simulations and the absorbed laser fluence rather than the incident fluence is used in the discussion of the simulation results. Before applying laser irradiation, the whole computational system is equilibrated at 300 K.

5.3 EAM interatomic potential for Cr

Several potentials based on the modified embedded atom method (MEAM) [27,28,29] have been suggested for BCC transition metals. The parameterizations of MEAM include Cr, which features a negative Cauchy pressure at low temperatures. Consideration of the angular dependence in the interatomic interactions, however, complicates the implementation of MEAM potentials and makes large-scale MD simulations computationally expensive. In this section we present a new formulation of the Johnson's EAM potential [30,31] for Cr that provides an attractive alternative to MEAM. With a simple analytical functional form and absence of explicit angular terms, the potential is easy to implement and computationally efficient, making it appropriate for MD simulations that involve large numbers of atoms. Below, the EAM potential and the parameterization for Cr are described. Some of the physical properties of the model EAM Cr material are calculated and related to the experimental data and the predictions of density functional theory (DFT) calculations.

In the EAM formalism, the total potential energy of a system of N atoms is defined as

$$E_{pot} = \sum_{i=1}^N E_i = \frac{1}{2} \sum_{i=1}^N \sum_{\substack{j=1 \\ j \neq i}}^N \phi_{ij}(r_{ij}) + \sum_{i=1}^N F_i(\rho_i), \quad (5.1)$$

were E_i is the potential energy of an atom i , $\phi(r_{ij})$ is the pair energy term defined as a function of the interatomic distance r_{ij} between atoms i and j , and $F_i(\rho_i)$ is the many-body embedding energy term defined as a function of the local electron density, ρ_i , at the position of atom i . The local electron density is calculated as a linear sum of the partial electron density contributions from the neighboring atoms,

$$\rho_i = \sum_{\substack{j=1 \\ j \neq i}}^N f_j(r_{ij}), \quad (5.2)$$

where $f_j(r_{ij})$ is the contribution from atom j to the electron density at the site of the atom i .

The functional form of the EAM Cr is similar to the one suggested in Ref. [31].

The pair energy term is defined as

$$\phi(r) = \frac{A \exp[-\alpha(\frac{r}{r_e} - 1)]}{1 + (\frac{r}{r_e} - \kappa)^{20}} - \frac{B \exp[-\beta(\frac{r}{r_e} - 1)]}{1 + (\frac{r}{r_e} + \lambda)^{20}}, \quad (5.3)$$

the electron density function is

$$f(r) = \frac{f_e \exp[-\beta(\frac{r}{r_e} - 1)]}{1 + (\frac{r}{r_e} - \lambda)^{20}}, \quad (5.4)$$

and the embedding energy function is represented by three equations defining the function in different electron energy ranges and having matching values and slopes at the two junctions,

$$\begin{aligned}
 F(\rho) &= \sum_{i=0}^3 F_i \left(\frac{\rho}{\rho_{in}} - 1 \right)^i, \quad \rho < 0.85\rho_e, \\
 F(\rho) &= \sum_{i=0}^3 F_{mi} \left(\frac{\rho}{\rho_e} - 1 \right)^i, \quad 0.85\rho_e < \rho < 1.15\rho_e, \\
 F(\rho) &= F_n \left(1 - \eta \cdot \ln \left(\frac{\rho}{\rho_s} \right) \right) \left(\frac{\rho}{\rho_s} \right)^\eta, \quad \rho > 1.15\rho_e.
 \end{aligned} \tag{5.5}$$

$r_e, \text{\AA}$	$f_e, \text{eV/\AA}$	$\rho_e, \text{eV/\AA}$	$\rho_s, \text{eV/\AA}$	κ
2.493879	1.793835	17.641302	19.60545	0.18533
λ	A, eV	B, eV	α	β
0.277995	1.551848	1.827556	8.604593	7.170494
F_0, eV	F_1, eV	F_2, eV	F_3, eV	η
-2.022754	0.039608	-0.183611	-2.245972	0.456
F_{m0}, eV	F_{m1}, eV	F_{m2}, eV	F_{m3}, eV	F_n, eV
-2.02	0	-0.056517	0.439144	-2.020038

Table 5-1. Parameters of the EAM potential for Cr.

Properties	T_m K	ΔH_m kJ mol ⁻¹	$\Delta V_m/V_{\text{solid}}$ %	C_p J K ⁻¹ mol ⁻¹	α 10 ⁻⁶ K ⁻¹	E_v^m eV
EAM Cr	2381	22.6	7.0	26.3	8.2	0.81
Experiment	2180	21.0	N/A	24.0-32.0	6.5-12.0	0.95

MEAM Cr [27]	2050	18.8	4.4	26.8	9.0	0.70
-----------------	------	------	-----	------	-----	------

Table 5-2. Some of the material properties determined for the EAM Cr material. Values of the equilibrium melting temperature, T_m , enthalpy of melting, ΔH_m , and volume change on melting, $\Delta V_m/V_{\text{solid}}$, are given for zero pressure. The coefficient of linear expansion, α , and heat capacity at zero pressure, C_p , predicted with EAM Cr and MEAM Cr [27] potentials are given for 300 K. Variations of the experimental coefficient of linear expansion and heat capacity are given for zero pressure and a temperature range from 300 K to 1000 K. The experimental values are from Ref. [32] for T_m and ΔH_m , from Ref. [33] for C_p , from Ref. [34] for α , and from Ref. [35] for vacancy migration energy, E_v^m .

The parameters of the potential for Cr are given in Table 5-1. They are obtained by fitting to the experimental equilibrium lattice constant of 2.88 Å [24], the cohesive energy of 4.10 eV [24], the vacancy formation energy of 2.08 eV [35], the bulk modulus $B = (C_{11} + 2C_{12})/3$ of 194.8 GPa [36], the Voigt average shear modulus $G = (3C_{44} + 2C')/5$ of 123 GPa [36], and the anisotropy ratio C_{44}/C' of 0.68 [36], where C_{44} and $C' = (C_{11} - C_{12})/2$ are the two shear moduli of the cubic crystal. There is no explicit cutoff distance in the potential functions, but the pair potential and the electron density function are vanishing beyond the third neighbor shell in the Cr BCC structure (the contribution from the fourth neighbors to the interaction energy is two orders of magnitude smaller than that from the third neighbors).

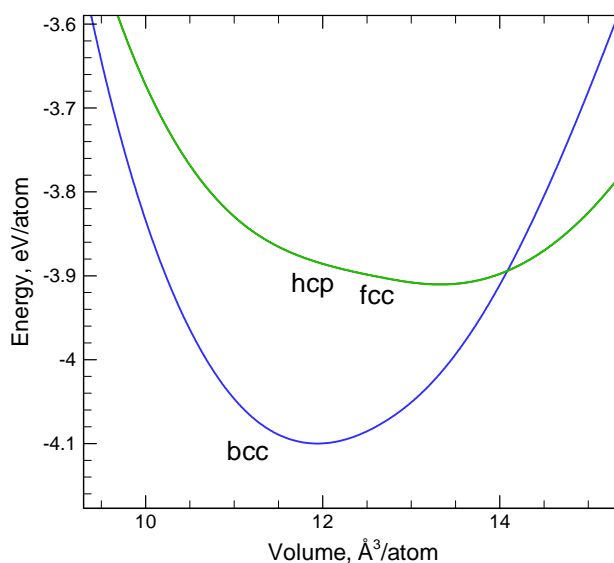


Figure 5-1. Total energy at zero temperature as a function of atomic volume predicted by the EAM Cr potential for BCC, FCC, and hcp crystal structures. The energy difference between the FCC and hcp structures is so small that the plots for these two structures cannot be visually distinguished.

The energies of BCC, FCC and hcp crystal structures calculated with the EAM Cr potential are shown in Fig. 5-1 as functions of atomic volume. The BCC lattice remains the lowest energy structure for large variations around the equilibrium volume, up to more than 15 % expansion and even larger compression. The short-range of the interactions contributing to the EAM Cr potential and the similarity of the local atomic structure results in a very small energy difference between the two close-packed structures.

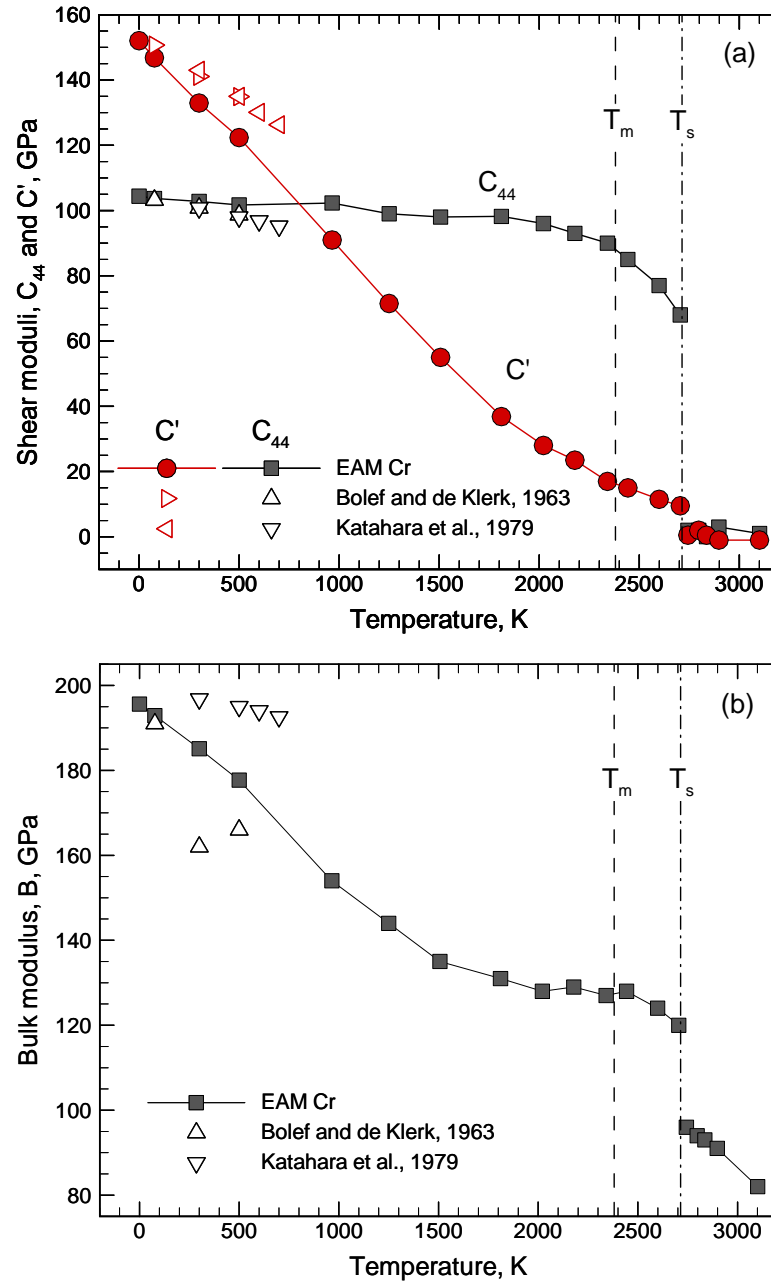


Figure 5-2. Temperature dependences of (a) two shear moduli, C_{44} and C' , and (b) bulk modulus B calculated with the EAM Cr potential, along with experimental data from Refs. [36,41]. The vertical dashed and solid lines are marking the equilibrium melting temperature T_m and the maximum superheating temperature T_s calculated for EAM Cr.

The temperature dependences of the elastic constants are calculated for the EAM Cr using the statistical fluctuation method suggested in Ref. [37] and widely used to obtain finite temperature values of elastic constants in MD simulations performed with many-body potentials, e.g. [38,39,40]. The calculations of the elastic constants for EAM Cr are performed with a MD cell containing 2000 atoms arranged in a BCC structure and periodic boundary conditions applied in all directions. After equilibration of the system at a given temperature and constant zero pressure, a constant energy and constant volume simulation is carried out and the elastic constants are calculated using the statistical fluctuation method. The convergence of the calculations is ensured by collecting statistics over sufficiently long MD trajectories, 200 ps. Results of the calculations of the temperature dependences of the two shear moduli, C_{44} and C' , and the bulk modulus are shown and compared with experimental values in Fig. 5-2. While there are no experimental measurements reported for elastic constants above 700 K, a reasonable agreement between the values and trends in the temperature dependences predicted with the EAM Cr potential and experimental data is found up to 700 K [36,41]. The EAM Cr potential also correctly reproduces the negative sign of the Cauchy pressure $CP = B - \frac{5}{3}G = C_{12} - C_{44}$, which is determined to be -10.2 GPa at 0 K and -6.3 GPa at 300 K.

Some other properties of the EAM Cr material, relevant to the laser heating/melting simulations presented in this study, are listed in Table 5-2, along with experimental data for Cr and the predictions of the MEAM potential [27]. A series of constant temperature and constant zero pressure simulations are performed to determine the temperature dependence of volume and internal energy of the model material, with

the values of heat capacity and coefficient of thermal expansion calculated from slopes of these dependences [11]. The equilibrium melting temperature, $T_m = 2381 \pm 3$ K (with the error of 3 K corresponding to 95% confidence interval), is determined from a liquid-crystal coexistence simulation performed at zero pressure for a system consisting of 4000 atoms ($3.0 \times 3.0 \times 5.8$ nm), with liquid-crystal interface oriented along (100) plane of the BCC crystal. The method used to calculate the vacancy migration energy is described in Section 5.4.4. The predicted thermophysical properties show a good agreement with experimental data. In particular, the equilibrium melting temperature and the enthalpy of melting of the EAM Cr material are within 10% of the experimental values.

The steady decrease of the shear modulus C' with increasing temperature and the fast drop of C_{44} at temperatures exceeding the equilibrium melting temperature, Fig. 5-2a, can be related to the interpretation of the homogeneous melting at the limit of lattice superheating in terms of the elastic shear instability facilitated by the diminishing shear moduli [42,43,44,45]. The temperature that corresponds to the superheating limit of the EAM Cr has been determined to be 2714 K, $\sim 14\%$ above the equilibrium melting temperature. The limit of superheating is defined as the maximum temperature at which no melting is observed within 300 ps in simulation of slow incremental heating performed at zero pressure. The value of the maximum superheating is smaller than typical values reported for close-packed metals (19-30%) [46] but is in agreement with the value of 13% determined for BCC EAM vanadium [44]. While the shear moduli are not vanishing as the temperature approaches the limit of superheating ($C' = 9.5$ GPa and $C_{44} = 64$ GPa, at 2714 K), the value of C' is small enough to allow for the local destabilization of the lattice and the onset of homogeneous melting. This mechanism of

local “mechanical” melting has been suggested based on the results of recent MD simulations [45,49]. The generation of vacancy-interstitial pairs and the interactions among the point defects are likely to facilitate the generation of the lattice instabilities [44,47,48]. Moreover, it has been shown in Ref. [45] that the generation of vacancy-interstitial pairs makes positive contributions to the values of the elastic moduli, suggesting that the change in slope of the temperature dependence of C' and B at high temperatures can be, at least partially, attributed to the rapid increase in the density of the point defects generated at temperatures approaching and exceeding the equilibrium melting temperature.

5.4 TTM-MD simulations: Results and discussion

In this section, the conditions leading to the transient and permanent structural changes in a surface region of a Cr target irradiated by a femtosecond laser pulse are discussed based on the results of two large-scale TTM-MD simulations. The results from a simulation performed at an absorbed laser fluence of 638 J/m^2 , just above the threshold for surface melting, are presented first, followed by a brief discussion of the second simulation performed at a lower absorbed fluence of 425 J/m^2 , when no permanent structural changes are observed in the target at the end of the simulation.

5.4.1 Laser-induced stresses, surface melting

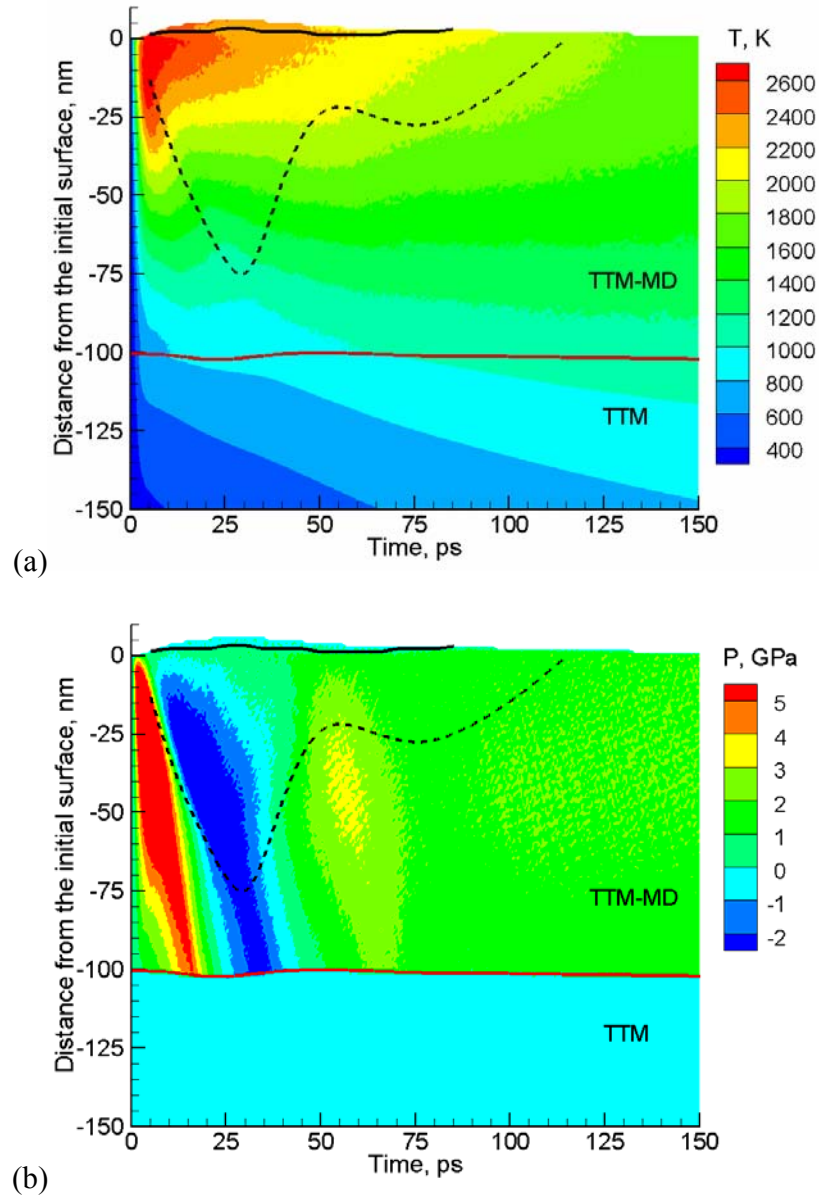


Figure 5-3. Contour plots of the spatial and temporal evolution of (a) temperature and (b) pressure in a TTM-MD simulation of a bulk Cr target irradiated with a 200 fs laser pulse at an absorbed fluence of 638 J/m^2 . The laser pulse is directed along the Y axes, from the top of the contour plots. The red solid line separates the continuum (TTM) and atomistic (TTM-MD) parts of the computational system. The black dashed line marks the depth of

the region where stacking faults are observed. The black solid line separates the transiently melted surface region from the crystalline bulk of the target.

The temporal and spatial evolution of the lattice temperature [49] and pressure in the surface region of a bulk Cr target irradiated by a 200 fs pulse at an absorbed fluence of 638 J/m^2 is shown in the form of contour plots in Fig. 5-3. The low electronic heat capacity of Cr results in a sharp spike of the electron temperature and a strong electron temperature gradient established in the surface region of the irradiated target immediately after the laser energy deposition. This, in turn, provides the conditions for the fast spread of the laser energy absorbed within the optical penetration depth throughout a deeper surface region of the target during the first 2-3 ps after the pulse. At the same time, the electron-phonon coupling leads to the energy transfer from the hot electrons to the lattice vibrations, as reflected by the initial lattice temperature increase throughout the 150 nm surface region of the target shown in Fig. 5-3a. The lattice temperature at the surface of the target, shown in Fig. 5-4, exceeds the equilibrium melting temperature of the model EAM Cr material, 2381 K, by the time of 3 ps and reaches its maximum level of 2650 K by the time of 5 ps. The initial lattice heating turns into cooling when the electron temperature drops below the lattice temperature due to the fast electron heat conduction to the bulk of the target.

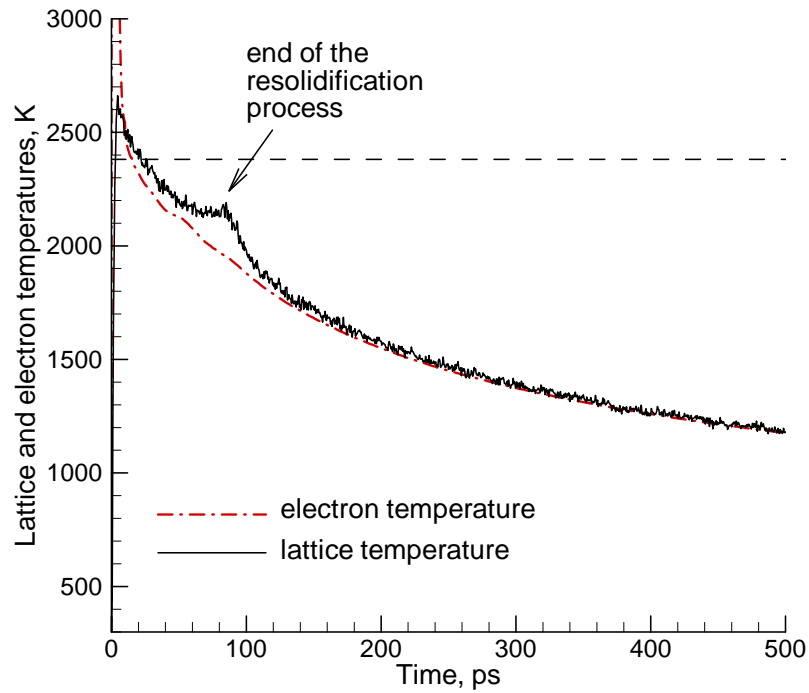


Figure 5-4. Time dependence of the electron temperature (dash-dotted red line) and lattice (solid black line) temperatures of the top 1 nm surface layer of a bulk Cr target irradiated with a 200 fs laser pulse at an absorbed fluence of 638 J/m^2 , as predicted in a TTM-MD simulation. The horizontal dashed line shows the equilibrium melting temperature of the model EAM Cr material, 2381 K. The lattice temperature is calculated from the average kinetic energy of atoms in the top layer of the sample and the statistical fluctuations of the temperature value are related to the finite number of atoms used in the calculation (1 nm of the original film consists of 6244 atoms).

The level of overheating (maximum of $1.11 T_m$ at the surface) is not sufficient to trigger the homogeneous nucleation of liquid regions in the overheated part of the target [11,12,13] and the melting proceeds by the propagation of the melting front from the surface. The melting front reaches a depth of $\sim 3 \text{ nm}$ by the time of 22 ps, when the

surface lattice temperature drops below the equilibrium melting temperature and the melting turns into resolidification. The release of the latent heat of melting upon the epitaxial crystallization of the surface region partially offsets the cooling due to the electron heat conduction, leading to the increasing split of the electron and lattice temperatures, Fig. 5-4. In particular, the release of the latent heat of melting at the crystal-liquid interface stabilizes the lattice temperature of the top 1 nm surface layer at 2140 K from 60 to 80 ps, when the resolidification front approaches the surface. Similarly to the observation in an earlier investigation of surface melting and resolidification [50], the time when the resolidification front reaches the surface of the target, 85 ps, is signified by a spike of the lattice temperature of the top surface layer up to 2190 K.

The split between the electron and the lattice temperatures, Fig. 5-4, is reflecting the fast rates of the electron cooling due to the steep temperature gradient and the lattice heating due to the release of the latent heat of melting in the resolidification process, as well as the finite time needed for the electron-phonon equilibration. A reverse effect, when the lattice temperature drops significantly below the electron temperature, has been observed for the melting process, where the velocity of the melting front is found to be strongly affected by the local electron-phonon non-equilibrium [51]. The split between the electron and lattice temperatures is larger for metals with weaker electron-phonon coupling.

The fast temperature increase, occurring under conditions of the inertial stress confinement [14], leads to the compressive pressure buildup in the surface region of the irradiated target, Fig. 5-3b. The compressive stresses increase during the time of the

lattice heating and reach a maximum value of ~ 11 GPa at a depth of 16 nm by the time of 3 ps after the laser excitation. The compressive stresses relax by driving a compressive stress wave deeper into the bulk of the target and inducing an unloading tensile wave that follows the compressive component, Fig. 5-3b. The pressure-transmitting heat-conductive boundary condition, applied at the depth of 100 nm, ensures that both the compressive and tensile components of the pressure wave propagate without any noticeable reflection from the boundary separating the TTM-MD and TTM parts of the model (Fig. 5-3b), whereas the temperature field exhibits a seamless transition at the boundary (Fig. 5-3a).

In addition to the strong pressure wave propagating to the bulk of the target, the laser heating generates an elevated level of the compressive stresses in the surface region of the target. The quasi-static compressive stresses of ~ 1.5 -2 GPa, observed in Fig. 5-3b long after the relaxation of the initial transient stresses, are related to the confinement of the heated crystalline material in the lateral directions [14]. For a typical laser spot diameter of ~ 100 μm , the fast relaxation of the laser-induced thermoelastic stresses can only proceed in the direction normal to the surface. These conditions of lateral confinement are correctly reproduced by the periodic boundary conditions applied in the directions parallel to the surface. The uniaxial expansion of the crystalline part of the target results in anisotropic lattice deformations and corresponding anisotropic stresses that remain in the crystalline part of the target as long as the temperature gradients persist in the irradiated target. The value of pressure, shown in Fig. 5-3b, is defined as negative one third of the first invariant of the stress tensor, $P = -(\sigma_{xx} + \sigma_{yy} + \sigma_{zz})/3$, and contains different contributions from different diagonal components of the stress tensor. For

example, the quasi-static compressive pressure of 1.88 GP measured at a depth of 50 nm at 150 ps contains contributions from $\sigma_{xx} = \sigma_{yy} = -2.91$ GPa and $\sigma_{zz} = 0.18$ GPa. The temperature at this depth and time is 1518 K, the lattice parameter in lateral (x and y) directions is fixed at its room temperature value of 0.288 nm, whereas the lattice parameter in z direction is 0.298 nm. In the thin transiently melted surface layer the stresses remain isotropic and zero pressure quickly establishes, Fig. 5-3b.

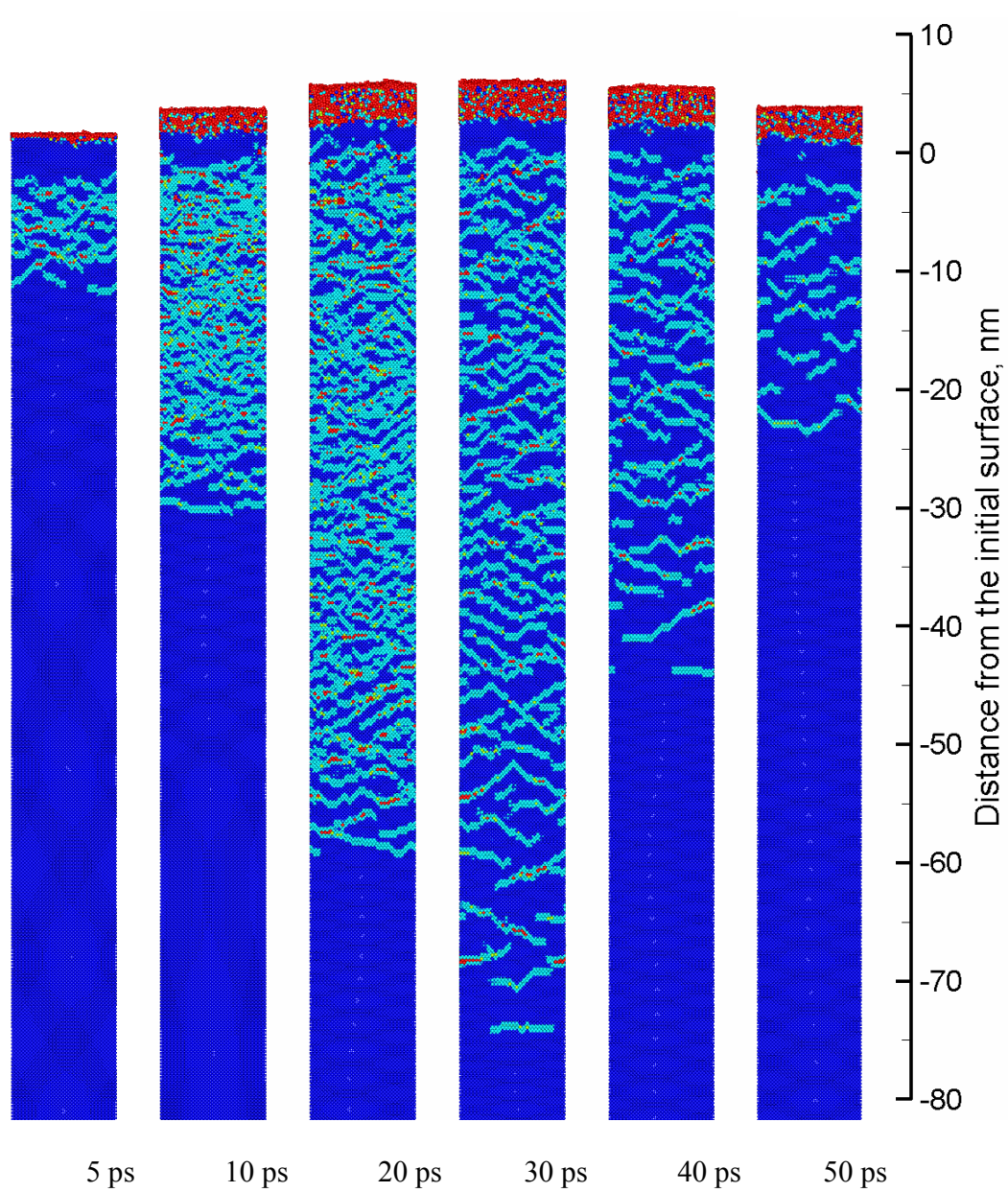
5.4.2 Transient generation of stacking faults

A visual inspection of the snapshots of atomic configurations taken at different times of the simulation can serve as a starting point in the analysis of the laser-induced structural changes in the target. In order to reduce the thermal noise in atomic positions and energies, each configuration is quenched for 2 ps using a velocity dampening technique, where the velocity of each individual atom is set to zero at the time when the kinetic energy of the atom maximizes. The fast quenching does not introduces any structural changes to the atomic configurations but makes the visual analysis more straightforward. In the snapshots shown in Fig. 5-5, the atoms are colored according to their potential energies, from dark blue used for atoms with energies characteristic of the original BCC structure, to light blue, green and red corresponding to increasingly higher potential energies. In this coloring scheme, the transient melting of the surface region discussed above and shown by a black line in Fig. 5-3 shows up as a red layer that disappears (reduces to a plane composed of atoms located at the surface of the recrystallized target) by the time of 90 ps.

A prominent feature of the snapshots shown in Fig. 5-5 is the appearance, expansion (up to 30 ps), retraction, and disappearance (by 110 ps) of a complex pattern of

stripes composed of atoms with elevated potential energy. A detailed analysis of the atomic configurations indicates that most of the atoms with elevated potential energy belong to pairs of atomic planes with crystallographic orientations of $(0\bar{1}1)$, (011) , $(10\bar{1})$, (101) . These pairs of atomic planes correspond to the stacking faults outlining the regions of the crystal shifted with respect to each other by a displacement vector $a/8\langle 110 \rangle$, where a is the lattice constant. An example of the atomic configurations that includes stacking faults along the (101) plane is shown in Fig. 5-6a. Four consecutive (101) planes are shown in this figure, with a lower right part of the crystal displaced down by a vector $a/8[10\bar{1}]$ along (101) planes with respect to the surrounding lattice. The areas of stacking fault are the areas where two atomic planes are displaced with respect to each other, e.g. planes II and III in Fig. 5-6a.

The stacking fault discussed above and illustrated in Fig. 5-6a has been analyzed based on the hard sphere model [52], where shifts of parts of a crystal along $\{110\}$ planes by displacement vectors $a/8\langle 110 \rangle$ bring atoms to local energy minima, as schematically illustrated in Fig. 5-6b. Analysis of the stability of this intrinsic stacking fault predicted by the hard sphere model, however, has revealed that it is unstable if an interatomic potential appropriate for BCC crystals is used in the calculations [53,54]. It has been also suggested [54] that an expansion of the crystal may reduce the interatomic interactions beyond the first nearest neighbors and stabilize the stacking faults.



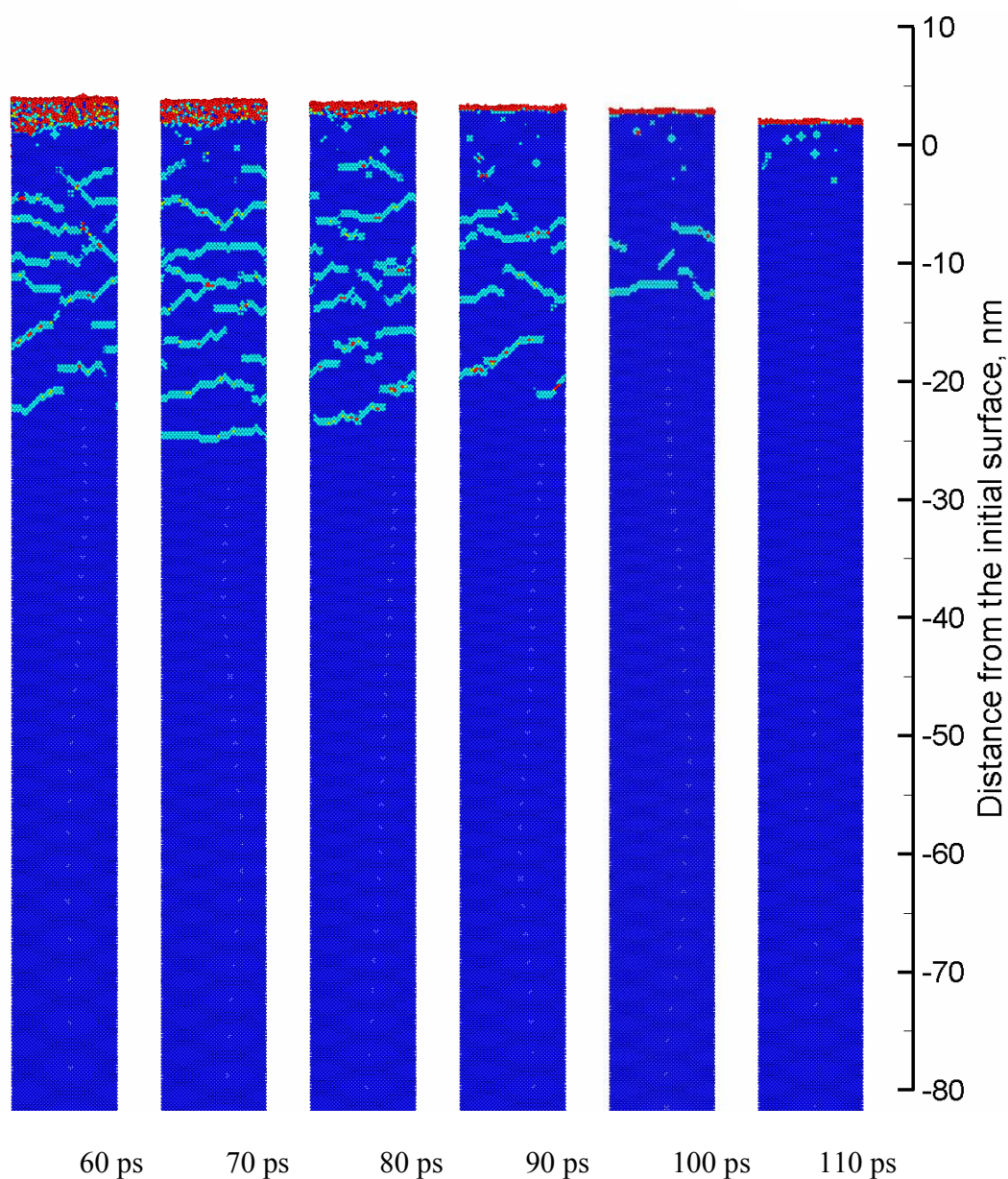
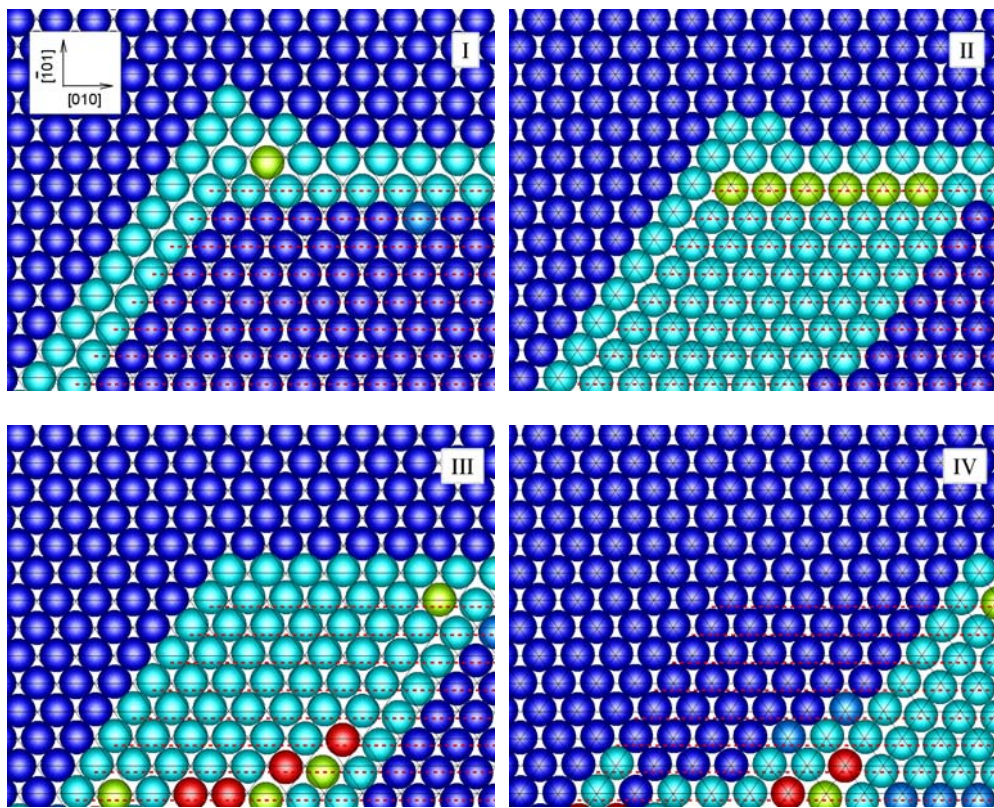


Figure 5-5. Snapshots of atomic configurations obtained in a TTM-MD simulation of a bulk Cr target irradiated with a 200 fs laser pulse at an absorbed fluence of 638 J/m^2 . The snapshots are taken along the [010] view direction. The configurations are quenched to 0 K in order to reduce thermal noise in atomic positions and energies. Atoms are colored according to their potential energies, from dark blue color corresponding to the energies below -3.99 eV to red color corresponding to the energies above -3.9 eV. This coloring

scheme shows the atoms that belong to the original BCC structure in dark blue, the melted surface region in red, and the crystal defects in light blue, green, and red. Enlarged views of the surface parts of these snapshots with low energy BCC atoms blanked are shown in Fig. 5-8.



(a)

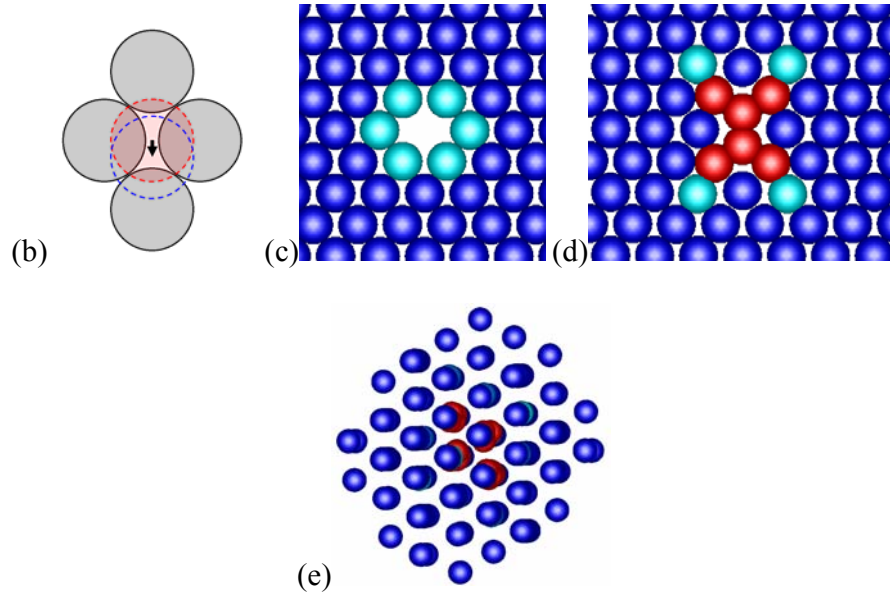


Figure 5-6. Close up on the atomic arrangements that correspond to the crystal defects observed in the TTM-MD simulation and identified in Fig. 5-8. A region marked by “A” in a snapshot shown for 100 ps in Fig. 5-8 is illustrated in (a), where four consecutive (101) planes are shown. This region includes a part (lower right) of the crystal displaced down by a vector $a/8[10\bar{1}]$ along a (101) plane with respect to the original crystal structure. The displacement leads to the formation of the stacking fault that shows up in the figure as a pairs of atomic planes (e.g. II and III) with elevated potential energy. The red dashed lines mark the displaced rows of atoms in plane (II). This type of displacement results in the formation of stacking faults along $\{110\}$ planes as illustrated by an atomic arrangement in (b), where the displacement of a top atom (dashed circles) is shown by an arrow with respect to four atoms in the underlying (101) plane (solid circle). Atomic configurations that correspond to the defects marked by “B”, “C”, and “D” in a snapshot shown for 450 ps in Fig. 5-8 are illustrated in (c) - a vacancy, (d) - an interstitial in a $\langle 110 \rangle$ -dumbbell configuration, and (e) - a cluster of four interstitials arranged in a $\langle 111 \rangle$ -crowdion configuration, respectively. A single (101) plane is shown in (c) and (d),

and all atoms in the vicinity of the four $\langle 111 \rangle$ -crowdion interstitial cluster that have potential energy higher than -4.09 eV are shown in (e), where the view direction is slightly tilted with respect to the $[\bar{1}11]$ direction. Atoms are colored according to their potential energies, from dark blue color corresponding to the energies below -3.99 eV (these atoms are blanked in Fig. 5-8) to red color corresponding to the energies above -3.9 eV. The cohesive energy of the EAM Cr BCC crystal is 4.10 eV.

To provide a background for quantitative interpretation of the laser-induced generation of the stacking faults, we perform calculation of the generalized stacking fault energy for the EAM Cr potential. The generalized stacking fault energy is calculated in a simulation performed with a computational cell consisting of 4394 atoms. Following the approach discussed in Ref. [53], the stacking fault is created by dividing the system into two parts by a (101) plane and shifting one part with respect to another in the $[\bar{1}01]$ direction in small increments. After each incremental displacement, the atoms are allowed to relax in the direction perpendicular to the (101) slip plane using the energy minimization method. After the relaxation, the generalized stacking fault energy is obtained by dividing the energy difference between the displaced system and the perfect lattice by the area of the slip plane. In order to investigate the effect of the laser-induced uniaxial expansion of the lattice on the generalized stacking fault energy, a similar set of simulations is performed for the lattice expanded in [001] direction. In these simulations the displacement vector that defines the generalized stacking fault is $\bar{u} = X \times [\bar{1}, 0, 1 + \alpha]$, where α is the uniaxial strain applied to the BCC lattice in the [001] direction and X is the ratio of the generalized stacking fault vector \bar{u} to the magnitude of vector $[\bar{1}, 0, 1 + \alpha]$.

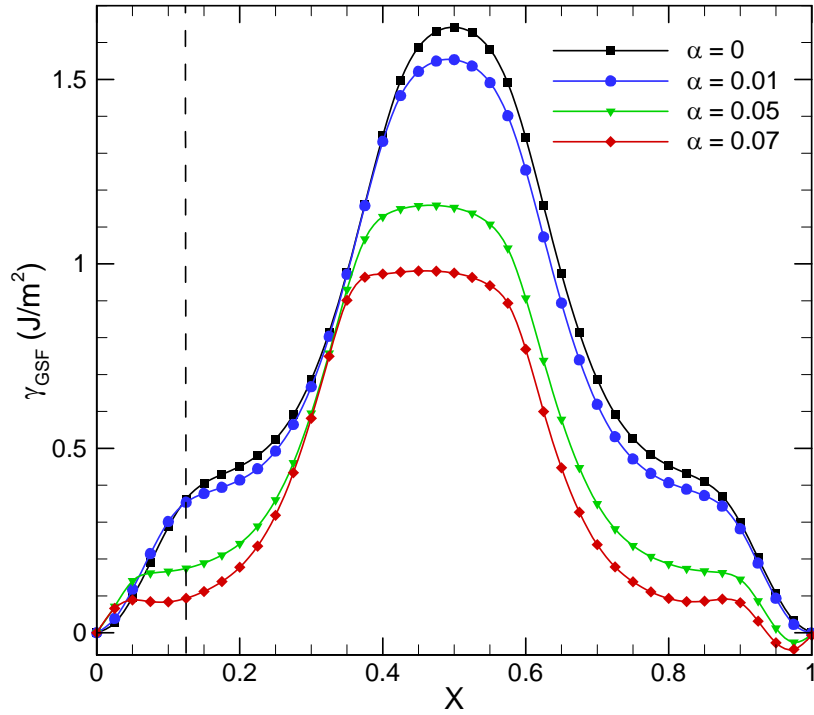


Figure 5-7. Generalized stacking fault energy, γ_{GSF} , for the (101) slip plane in BCC EAM Cr as a function of the magnitude of the fault vector, $\vec{u} = X \times [\bar{1}, 0, 1 + \alpha]$. The GSF curves are calculated for different values of the uniaxial strain, α , applied to the BCC lattice in the [001] direction. The dashed line corresponds the stacking fault at $X = 1/8$, predicted with the hard sphere model.

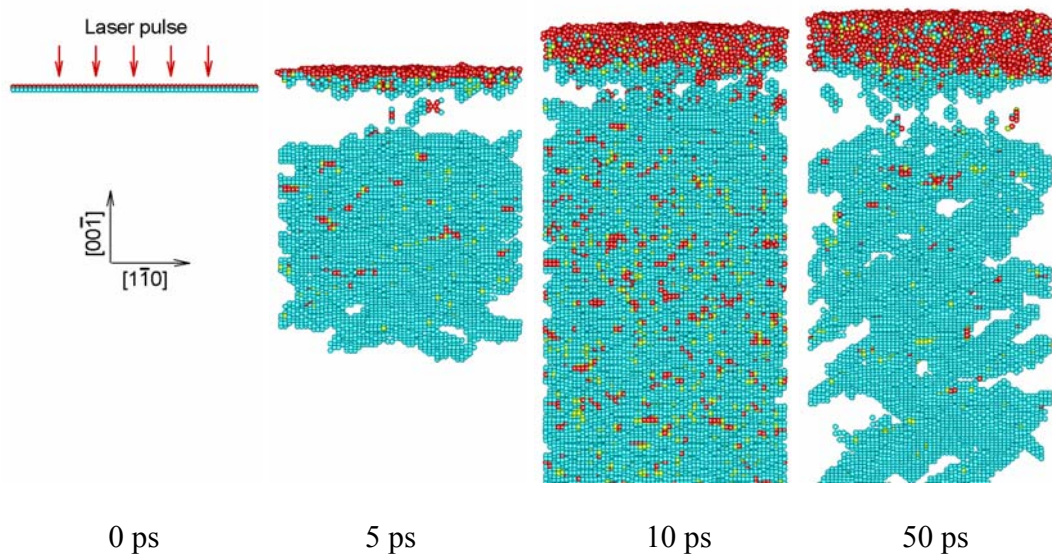
The result of the calculation of the generalized stacking fault energy curves is shown in Fig. 5-7. There are no local minima in the curves obtained for the strain-free BCC lattice, confirming that, in agreement with earlier studies [53,54], any stacking fault generated by a displacement in a $\langle 110 \rangle$ direction along a $\{110\}$ plane is unstable in the EAM Cr material. The uniaxial expansion, however, decreases of the generalized stacking fault energy and creates a plateau in the vicinity of $X \approx 1/8$. In particular, the

GSF energy at $X = 1/8$ decreases from 0.360 J/m^2 at $\alpha = 0$, to 0.352 J/m^2 at $\alpha = 0.01$, to 0.175 J/m^2 at $\alpha = 0.05$ and to 0.093 J/m^2 at $\alpha = 0.07$. The development of the plateau, and even a shallow local minimum observed at 7% strain, suggests that the stacking fault at $X \approx 1/8$, predicted with the hard sphere model, can be stabilized by the laser-induced uniaxial expansion of the target. Indeed, the analysis of the atomic configurations shown in Fig. 5-5 suggests that the uniaxial strain reaches its maximum value of 6.5% by the time of 20 ps at a depth of $\sim 50 \text{ nm}$ below the surface.

The analysis of the stacking fault energy provided above is consistent with the results of the simulation discussed above, where the transient appearance of the stacking faults can be clearly correlated with the expansion of the lattice associated with the propagation of the tensile component of the laser-induced stress wave. Indeed, the spreading of the region where the stacking faults are observed (shown by the dashed line in Fig. 5-3) follows closely the propagation of the tensile stress wave, Fig. 5-3b. The uniaxial expansion of the lattice in the $[001]$ direction activates multiple shifts in four out of six $\{110\}$ crystallographic planes oriented at 45° with respect to the $[001]$ axis of expansion, namely $(0\bar{1}1)$, (011) , $(10\bar{1})$, and (101) . The intersections of these planes with the (010) view plane in Fig. 5-5 are seen as stripes oriented in three directions (horizontal and tilted by $\pm 45^\circ$ with respect to the horizontal direction). The stacking faults on the $\{110\}$ planes start to disappear as soon as the tensile stress wave leaves the surface region and the lattice expansion partially relaxes. The second, much weaker pressure oscillation in the surface region, occurring at around 40 to 90 ps, is also affecting the evolution of the stacking faults, with the stacking fault region experiencing a small additional growth during the time interval when the lattice expands, from 65 to 90

ps (see Fig. 5-3b and snapshots for 60-90 ps in Fig. 5-5). As discussed above, this additional lattice expansion takes place on the background of quasi-static thermoelastic stresses defined by the lateral confinement of the lattice and does not result in the negative pressure values. The stacking faults continue to withdraw at later times and completely disappear by the time of 115 ps.

The correlation between the tensile stresses and the appearance of the stacking faults can be further illustrated by the virtual absence of the stacking faults in the top ~ 5 nm part of the target, where the tensile stresses are low, Fig. 5-3b. The stacking fault-free region can be seen in the snapshots shown in Fig. 5-5, as well as in the enlarged views of the surface part of the irradiated target, shown in Fig. 5-8, where the low energy BCC atoms are blanked in order to expose the crystal defects and the view direction is changed to $[\bar{1}\bar{1}0]$.



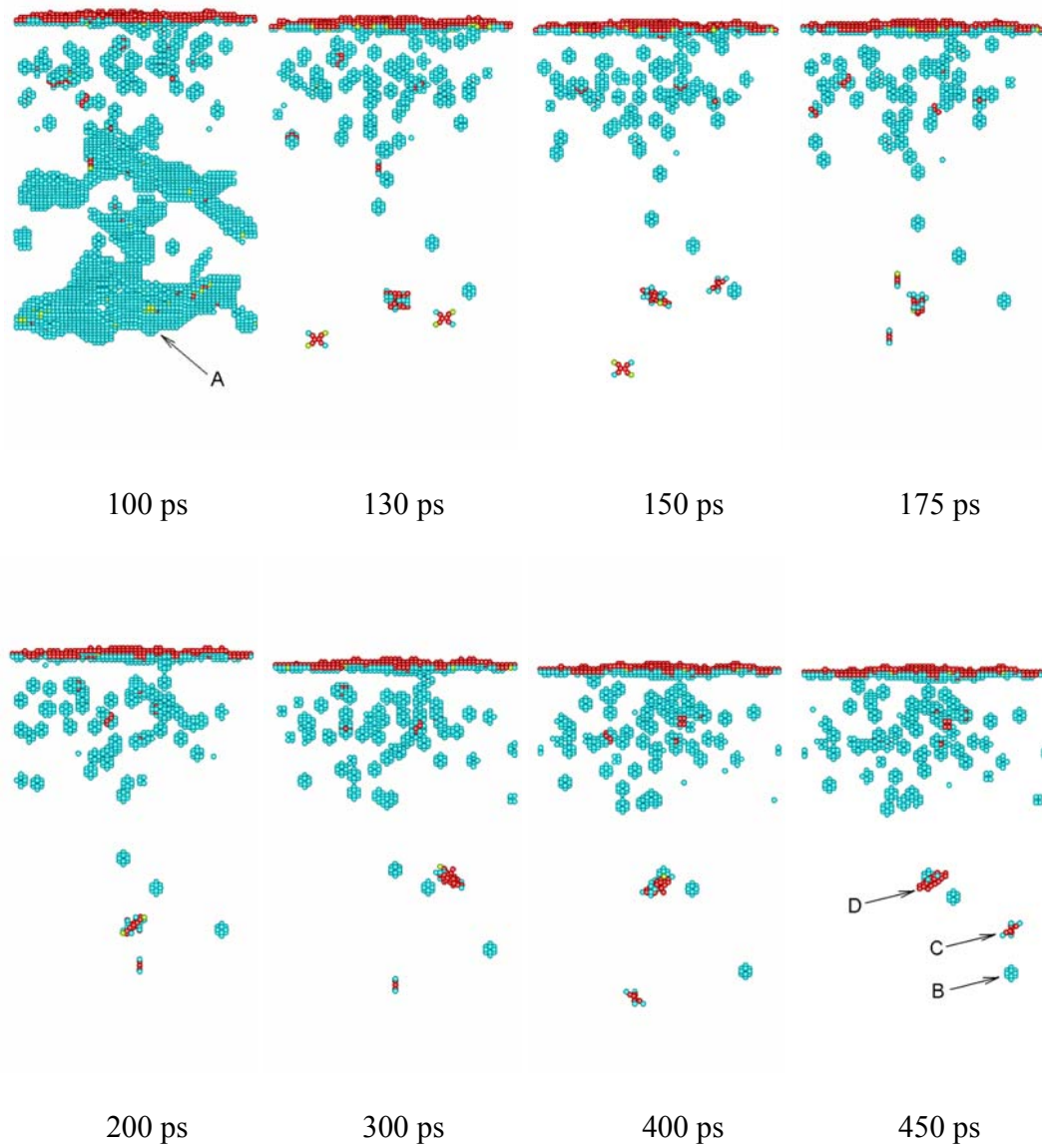


Figure 5-8. Snapshots of the surface regions of atomic configurations obtained in a TTM-MD simulation of a bulk Cr target irradiated with a 200 fs laser pulse at an absorbed fluence of 638 J/m^2 . The snapshots are taken along the $[\bar{1} \bar{1} 0]$ view direction and are shown down to the depth of 20 nm below the level of the initial surface. The configurations are quenched to 0 K in order to reduce thermal noise in atomic positions

and energies. The same coloring scheme as in Fig. 5-5 is used here, with atoms that have energies below -3.99 eV (shown in dark blue in Fig. 5-5) blanked to expose crystal defects. The red atoms in the top parts of the snapshots belong to the melted region (5, 10, and 50 ps) or are located at the surface of the crystalline target (0, 100 - 450 ps). Typical defect configurations marked by “A” in a snapshot shown for 100 ps and “B”, “C”, and “D” in a snapshot shown for 450 ps correspond to a stacking fault, a vacancy, an interstitial, and a cluster of four interstitials, respectively. The atomic arrangements corresponding to these defects are shown in Fig. 5-6.

5.4.3 Generation of vacancies and self-interstitials

The inspection of Fig. 5-8 indicates that a large number of point defects are generated by the laser irradiation and many of the defects still remain in the surface region of the target after the disappearance of the stacking faults. Analysis of the atomic configurations reveals that the defects are vacancies, interstitials, di-vacancies, and a cluster of interstitials. With the visualization method used in Fig. 5-8, when only atoms with elevated potential energy are shown in the quenched configurations, each vacancy shows up as a cluster of 14 atoms that includes the 8 nearest neighbors and 6 second-nearest neighbors of the missing atom. A close up on an atomic arrangement around a vacancy is shown in Fig. 6c, where a single (101) plane is shown. Four out of eight nearest neighbors and two out of six second-nearest neighbors are located in this plane and are shown in light blue color. The individual interstitials are found to always take a $\langle 110 \rangle$ -dumbbell configuration, that is illustrated in Fig. 5-6d. In Fig. 5-8, the interstitials appear as planar cross-like configurations with red atoms in the middle, oriented in one of the $\{110\}$ planes. The $\langle 110 \rangle$ -dumbbell configuration has been predicted to be the most

stable self-interstitial configuration in calculations performed for many BCC metals with pair-wise [55] and EAM [56] potentials. The energies of the relaxed $\langle 110 \rangle$ and $\langle 111 \rangle$ self-interstitial configurations predicted by the EAM Cr potential used in this work are 5.02 eV and 5.89 eV, respectively. Recent DFT calculations [57,58,59] predict similar values for the formation energies of different self-interstitial configurations, in the range of 5.66 – 5.85 eV, suggesting that $\langle 110 \rangle$ and $\langle 111 \rangle$ -configurations are almost degenerate [59]. The MEAM Cr potential, however, predicts the $\langle 110 \rangle$ -dumbbell configuration to be the stable one, with a smaller formation energy of 3.9 eV [27].

The appearance of point defects can be seen as early as 5 ps after the laser pulse, e.g. two vacancy-interstitial pairs can be identified close to the surface in a snapshot shown for 5 ps in Fig. 5-8. Due to a much higher mobility of interstitials as compared to vacancies, most of the interstitials quickly diffuse and escape to the melting front or the surface of the target, leaving behind a high concentration of vacancies in the near-surface region. By the time of 150 ps there are only two interstitials located 12.7 nm and 17 nm below the surface and one cluster of three interstitials located 13.3 nm below the surface. There are no interstitials by this time in the top 10 nm region of the target, and the atoms of high potential energy (shown in red) observed in the top half of Fig. 5-8 belong to the configurations where two vacancies are located close to each other. Between 175 ps and 200 ps one of the interstitials joins the cluster, increasing the number of interstitials in the cluster from three to four. Both the 3- and 4-interstitial clusters have $\langle 111 \rangle$ -crowdion configurations, illustrated in Fig. 5-8e for the 4-interstitial cluster. This observation is consistent with earlier results [60,61,62] suggesting that small clusters of interstitials arrange themselves into sets of $\langle 111 \rangle$ -crowdions/dumbbells. At a sufficiently large size,

a $\langle 111 \rangle$ -crowdion cluster can be described as a dislocation loop with a Burgers vector $a/2\langle 111 \rangle$. The high mobility of such dislocation loops was demonstrated in a recent in situ transmission electron microscopy study [63], where a nanometer-sized dislocation loop in α -Fe was shown to undergo an active one-dimensional diffusion at a temperature as low as 575 K.

Indeed, although the temperature at the depth of the location of the interstitial and the cluster of interstitials drops down to ~ 1100 K ($\sim 0.46 T_m$) by the end of the simulation, both the interstitial and the cluster remain very mobile, as can be seen from changes in the positions and orientations of the $\langle 110 \rangle$ -dumbbell interstitial and the four $\langle 111 \rangle$ -crowdion cluster in Fig. 5-8. The mechanisms of interstitial diffusion observed in MD simulations performed for different BCC metals include reorientation of the $\langle 110 \rangle$ -dumbbell in $\langle 111 \rangle$ direction followed by low-energy barrier jumps along the close-packed $\langle 111 \rangle$ direction [60,64], as well as rotation and translation of $\langle 110 \rangle$ dumbbell [55,65]. While the mobility of the interstitials and their clusters at low temperatures can be strongly affected by relatively small variations in the values of the energy barriers separating different self-interstitial configurations, at high temperatures realized in our simulations ($T \sim 1100\text{--}2650$ K; $k_B T \sim 0.1\text{--}0.2$ eV) different types of jumps and reorientations of the interstitial configurations can be readily activated, making the diffusion pathways more complex [59,66] and, at the same time, less sensitive to the detailed energy landscape predicted with a particular interatomic potential.

The high mobility of the interstitial cluster observed in Fig. 5-8 is consistent with the decrease of the migration energy with increasing cluster size reported in MD simulations performed with different interatomic potentials [61,62,64,65]. The diffusion

of a small interstitial cluster is typically described as a combination of a rapid one-dimensional migration along the crowdion direction and rotations to equivalent $\langle 111 \rangle$ directions. The frequency of the rotations is increasing with temperature and decreasing with the size of the cluster [61,62,64,65]. For the cluster of four interstitials observed in the present simulation, the temperature of the surface region of the target remains sufficiently high during the time of the simulation to induce occasional reorientations of the cluster, resulting in a three-dimensional migration of the cluster, Fig. 5-8.

The high mobility of the remaining interstitial and the interstitial cluster suggests that they are likely to recombine with vacancies or escape to the surface as the cooling process continues. The positions of the vacancies, on the other hand, become relatively static by the end of the simulation. The distribution of vacancies in the top 8 nm surface region of the target is shown in Fig. 5-9. There is total of 53 vacancies in this region, with three more vacancies located below the region shown in the plot, at 10.3 nm, 11.2 nm, and 15.1 nm below the surface. Despite the high concentration of vacancies in the surface region of the target (1.7×10^{-3} in a layer between 1 and 5 nm below the surface) we do not observe any tendency of vacancies to form clusters or small dislocation loops. Only three pairs of vacancies occupying adjacent second nearest-neighbor lattice sites, one pair in fourth nearest-neighbor lattice sites and one pair in fifth nearest-neighbor lattice sites have been identified at 500 ps after the laser pulse. The absence of any pronounced clustering of vacancies can be explained by relatively low (as compared to clusters of interstitials) binding energies of di-vacancies and larger vacancy clusters [55,59,61,62], as well as by the high temperature of the surface region of the irradiated target during the time of the simulation, Fig. 5-4.

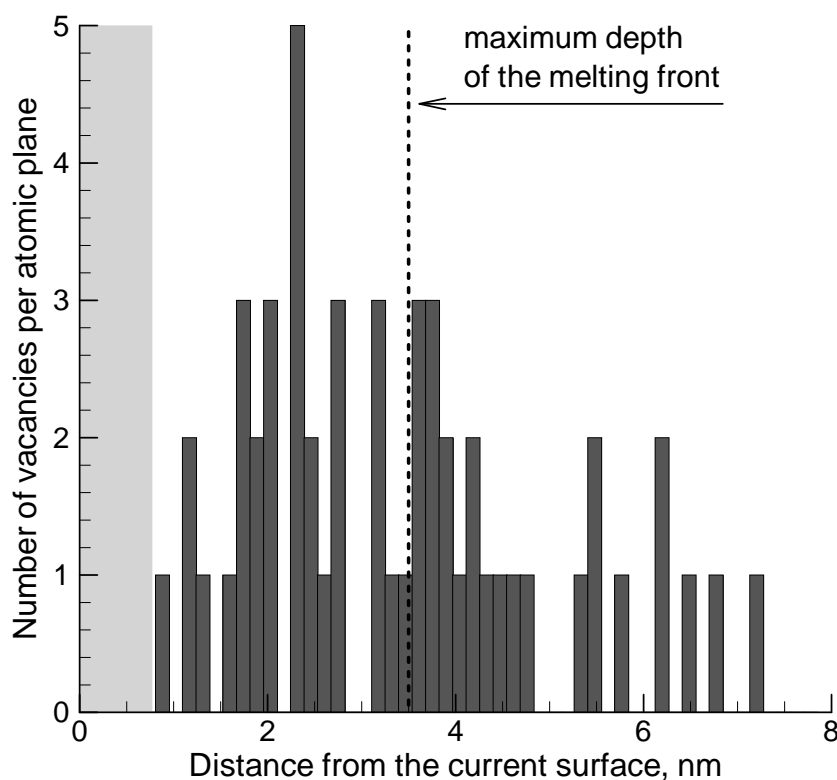


Figure 5-9. Distribution of vacancies in the top 8 nm surface region of a bulk Cr target irradiated with a 200 fs laser pulse at an absorbed fluence of 638 J/m^2 at 500 ps after the laser pulse. The width of an individual bar in the histogram corresponds to the distance between (001) planes, with each bar showing the number of vacancies in an individual (001) atomic plane. The gray area in the left part of the figure corresponds to the surface layer where identification of vacancies is not possible. The dashed line marks the depth of the region that experiences a transient melting and resolidification during the first 85 ps of the simulation.

The fact that a large fraction of the vacancies (52% at 500 ps) are located in the part of the target that experienced a transient melting and resolidification (Fig. 5-9) suggests that, in addition to the thermally-activated generation of vacancy-interstitial pairs, a significant number of vacancies can be left behind by the quickly advancing solidification front. The lattice distortions associated with the transient laser-induced stresses and the quasi-static uniaxial thermal expansion of the surface region may also affect the elementary processes responsible for the generation and mobility of the point defects [67]. A more detailed analysis of the relative contribution of different factors to the generation and evolution of the defect structures in short pulse laser processing is the subject of our ongoing work.

5.4.4 Long-term evolution of the vacancy configuration

To evaluate the possible long-term evolution of the vacancies generated in the surface region of the irradiated target, we calculate the diffusivity of a vacancy and estimate the characteristic diffusion length of a vacancy during the cooling process. The diffusion coefficient of a vacancy, D_v , is calculated based on a series of MD simulations performed for BCC crystals containing a single vacancy at several temperatures in the range from 1000 to 1500 K. The diffusion coefficient for each temperature is calculated using the Einstein relation, $D_v = \frac{1}{6t} \left\langle \left| \vec{R}_i(t_0 + t) - \vec{R}_i(t_0) \right|^2 \right\rangle_{i, t_0}$, where $\vec{R}_i(t)$ is the vacancy position at time t in the i^{th} simulation. The averaging over starting times t_0 along the MD trajectories is used to improve statistical accuracy of the calculation. Fitting the values of the diffusion coefficient obtained for different temperatures to the Arrhenius dependence, $D_v(T) = D_v^0 \exp(-E_v^m / k_B T)$, yields the vacancy migration energy $E_v^m = 0.81$ eV and the

pre-exponential factor $D_v^0 = 0.39 \times 10^{-2} \text{ cm}^2/\text{s}$. The value of the migration energy predicted with the EAM Cr potential is higher than the values of 0.70 eV [27] and 0.73 eV [29] predicted with MEAM Cr potential, but is somewhat lower than the value of 0.91 eV evaluated in DFT calculations [57] and the experimental value of 0.95 eV [35].

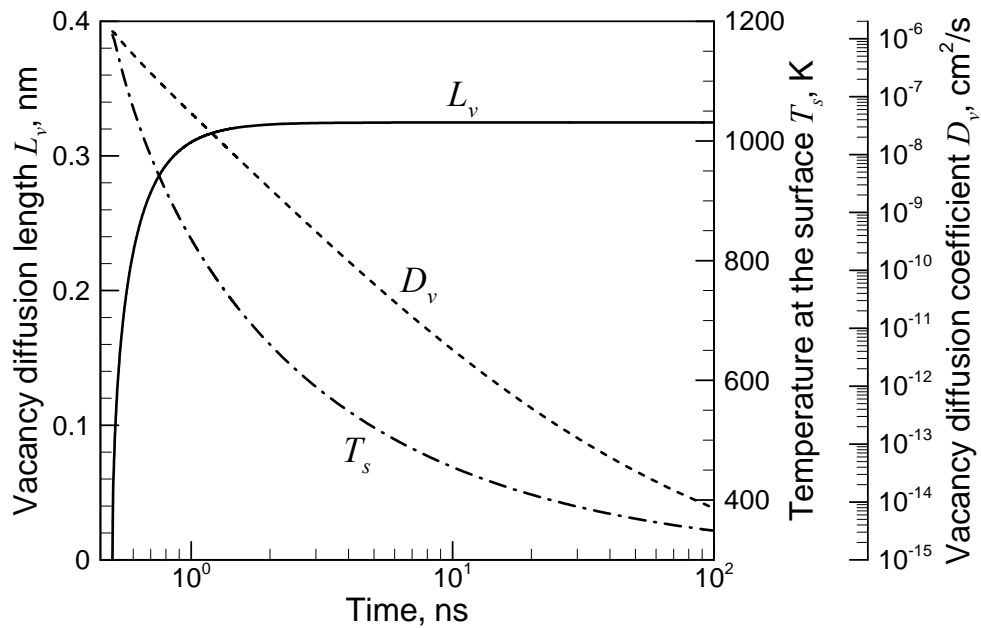


Figure 5-10. Long term evolution of the surface temperature, vacancy diffusion coefficient, and vacancy diffusion length (root mean square displacement of vacancies) in the surface region of a bulk Cr target irradiated with a 200 fs laser pulse at an absorbed fluence of 638 J/m^2 during the late stage of the cooling process, starting from 500 ps after the laser pulse. The temperature is obtained by numerical integration of the heat conduction equation, starting from the temperature profile predicted in the TTM-MD simulation at the time of 500 ps. Surface temperature variation during the first 500 ps is shown in Fig. 5-4.

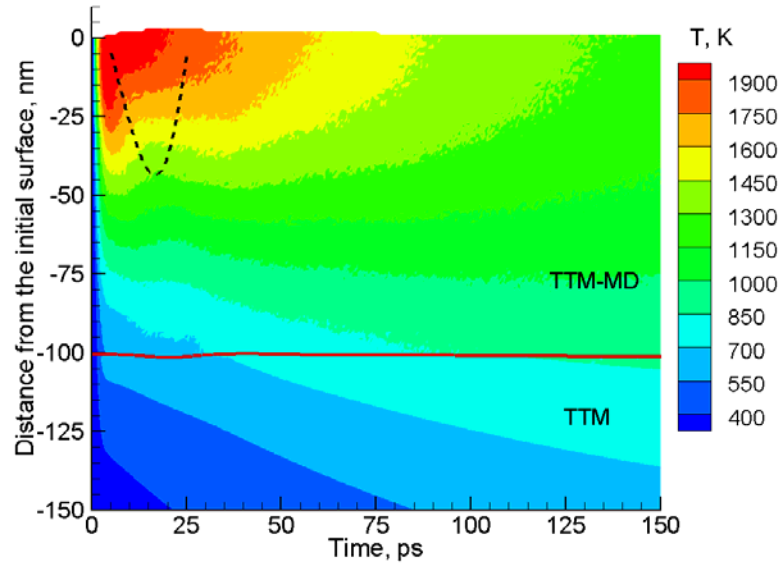
The knowledge of the vacancy diffusivity at different temperatures allows us to back-calculate the vacancy jump rates. For random thermally-activated jumps to the nearest neighbor lattice sites, the jump rate can be calculated as $1/\tau = 6D_v / r_1^2 = 8D_v / a^2$, where $r_1 = \sqrt{3/4}a$ is the nearest neighbor distance in the BCC lattice and τ is the characteristic time between jumps of a vacancy. For the surface temperature of 1180 K predicted in the TTM_MD simulation for 500 ps after the laser pulse, Fig. 5-4, the above equation gives $1/\tau = 37$ GHz, or $\tau = 27$ ps, explaining the slow pace of changes in the vacancy configuration observed during the last hundred picoseconds of the simulation.

To extend the estimations beyond the duration of the TTM-MD simulation, we take the temperature profile predicted at the end of the simulation, 500 ps after the laser pulse, and follow the further temperature evolution in the target by numerically solving a one-dimensional heat conduction equation in a wide region of the target extending up to 10 μm , where the temperature is fixed at 300 K. All the active exothermic or endothermic structural transformations in the surface region of the target are ceased by 500 ps, making the description of the long-term temperature evolution by the heat conduction equation adequate. A contribution of the heat conduction in the radial directions can be expected to increase with time and the cooling rate predicted by the one-dimensional heat conduction equation can be considered to be the lower-end estimate corresponding to the infinitely large laser spot size. The solution of the heat equation predicts that the surface temperature drops down to 900 K by 835 ps, 700 K by 1.65 ns, 500 K by 6.1 ns, and 350 K by 95 ns after the laser pulse, as shown in Fig. 5-10.

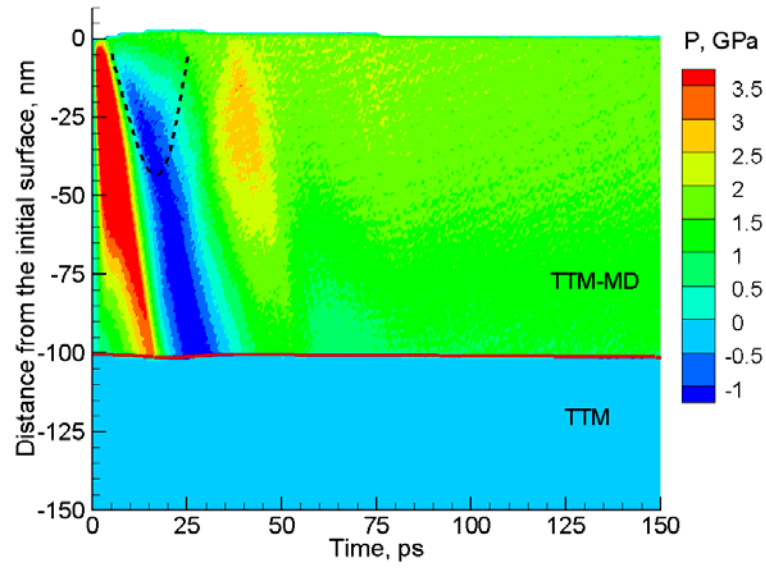
The knowledge of the temperature evolution in the surface region of the target and the temperature dependence of the vacancy diffusion coefficient allows us to predict

the extent of the rearrangements the vacancy configuration generated by the end of the TTM-MD simulation would undergo during the remaining part of the cooling process. The root mean square displacement of vacancies during the cooling process can be estimated by integrating the Einstein relation over the cooling time, with the result of the integration shown in Fig. 5-10. The average diffusion length traveled by a vacancy increases during the time from 0.5 to 1.5 ns and saturates at later times at a level not exceeding 0.33 nm. The saturation of the vacancy diffusion length occurs when the temperature drops below 700 K and the vacancy diffusion coefficient, D_v , drops below 10^{-8} cm²/s. The relatively small, on the order of an interatomic distance, vacancy diffusion length after 500 ps suggests that the configuration of mostly individual vacancies observed at the end of the TTM-MD simulation, Fig. 5-8, is unlikely to undergo any significant changes during the remaining part of the cooling process.

The high supersaturation of the surface region of the target with vacancies can lead to slow atomic rearrangements and eventual vacancy clustering at longer times. Indeed, the binding energies of compact three-dimensional clusters [62] and vacancy loops [61,68] increase with the cluster size and the stability of the clusters increases with decreasing temperature. The formation of vacancy clusters can be accelerated by annealing at an elevated temperature or by reheating of the target in the multi-pulse laser irradiation regime. The long term structural evolution of the surface region is defined by the mobility of vacancy clusters that is not fully understood at this time [69] and depends on the types of the clusters. In particular, the vacancy clusters can transform into small glissile dislocation loops exhibiting one-dimensional thermally activated motion [61,63] or can become immobile compact/spherical nanovoids [62].



(a)



(b)

Figure 5-11. Contour plots of the spatial and temporal evolution of (a) temperature and (b) pressure in a TTM-MD simulation of a bulk Cr target irradiated with a 200 fs laser pulse at an absorbed fluence of 425 J/m^2 . Laser pulse is directed along the Y axes, from the top of the contour plots. Red solid line separates the continuum (TTM) and atomistic

(TTM-MD) parts of the computational system. Black dashed line marks the depth of the region where stacking faults are observed.

The accumulation of vacancies, vacancy clusters, and generation of nanovoids in multi-pulse irradiation regime may weaken the material and result in the incubation effect, when the laser fluence threshold for ablation/damage decreases significantly with increasing number of laser pulses applied to the same area, e.g. [70,71,72,73,74]. In particular, the generation of sub-surface defects may reduce the ability of material to withstand the dynamic loading associated with the laser-induced stress wave, Fig. 3b, leading to the decrease of the fluence threshold for photomechanical spallation [14] of the target in the multi-pulse irradiation regime. The decreased stability of the surface region supersaturated with vacancies against melting [44,75,76] may result in the increase in the depth of the region affected by the transient melting and, in turn, facilitate generation of the higher densities of the surface defects by subsequent laser pulses. The effect of the vacancy generation may be also tuned to a useful account, providing avenues for controlled redistribution/incorporation of impurities or mixing/alloying in multi-component/composite targets.

5.4.5 Simulation at laser fluence below the threshold for surface melting

To study the effect of the laser fluence on the structural changes in the surface region of the target, an additional simulation has been performed at a lower fluence of 425 J/m^2 . The overall picture of the evolution of the lattice temperature and pressure in the surface region of the target, Fig. 5-11, is similar to the one discussed above for the higher fluence, Fig. 5-3. The maximum temperature of 2140 K, reached at the surface of

the target at 5 ps, however, is below the equilibrium melting temperature of the model EAM Cr material, 2381 K, and no surface melting takes place. The lower temperatures result in the lower levels of the compressive and tensile stresses, with the latter does not exceeding -1.5 GPa.

Similarly to the higher fluence simulation discussed above, the expansion of the lattice associated with the unloading tensile wave causes multiple internal shifts in the surface region of the target and generation of stacking faults along $\{110\}$ planes, Fig. 5-12. The depth of the region where the stacking faults are observed in this simulation, however, does not exceed 45 nm and the stacking faults quickly disappear as soon as the tensile stress wave leaves the surface region of the target. Visual analysis of the snapshots of atomic configurations, shown in Fig. 5-12, indicates that the stacking faults completely disappear by 30 ps. Moreover, not a single point defect is generated in this simulation. This observation suggests that the generation of stable crystal defects and possible accumulation of damage in multi-pulse irradiation regime, discussed above for the higher-fluence simulation, take place only at or above the threshold fluence for surface melting.

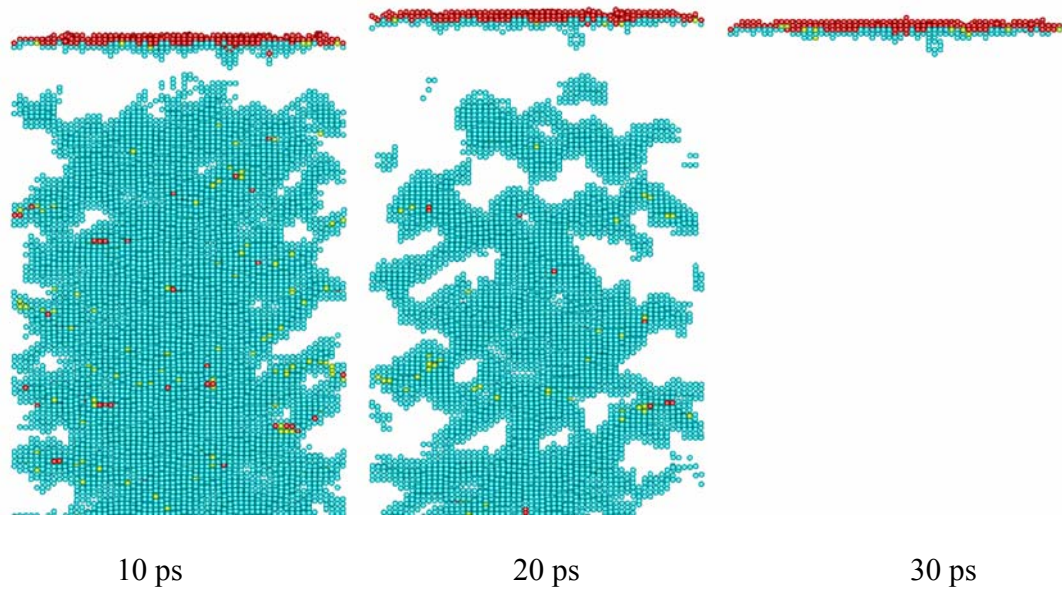


Figure 5-12. Snapshots of the surface regions of atomic configurations obtained in a TTM-MD simulation of a bulk Cr target irradiated with a 200 fs laser pulse at an absorbed fluence of 425 J/m^2 . The snapshots are taken along the $[\bar{1} \bar{1} 0]$ view direction and are shown down to the depth of 15 nm below the level of the initial surface. The configurations are quenched to 0 K in order to reduce thermal noise in atomic positions and energies. The same coloring scheme as in Figs. 5-5 and 5-8 is used here, with atoms that have energies below -3.99 eV blanked to expose crystal defects.

5.5 Summary

A detailed analysis of the structural changes in a surface region of a BCC Cr target irradiated by a femtosecond laser pulse is performed based on the results of large-scale atomic-level simulations. The simulations are enabled by a new parameterization of EAM potential for Cr, which provides a computationally efficient yet sufficiently accurate description of the structural and thermodynamic properties of the real Cr. Some

of the parameters of the model EAM Cr material, such as vacancy migration energy, temperature dependence of the elastic moduli, and the equilibrium melting temperature, are calculated and related to experimental data and predictions of DFT calculations. A description of the laser excitation of conduction band electrons, electron-phonon coupling, and electron heat conduction in the irradiated target is included in the computational model by incorporating a continuum description of the evolution of the electron temperature into the atomistic MD method.

A combined effect of the fast temperature variation and strong thermoelastic stresses produced by the laser energy deposition cause both transient structural changes and the generation of permanent crystal defects in the surface region of the irradiated target. The transient structural changes include fast surface melting and resolidification, as well as the generation of a high density of stacking faults along $\{110\}$ planes. At an absorbed laser fluence of 638 J/m^2 , the surface melting and subsequent epitaxial resolidification affects only a thin $\sim 3.5 \text{ nm}$ layer of the target and the resolidification process is completed by the time of 85 ps after the laser pulse. The stacking faults appear as a result of internal shifts in the crystal undergoing a rapid uniaxial expansion in the direction normal to the irradiated surface. The growth of the region where the stacking faults are observed follows closely the propagation of the tensile component of the laser-induced stress wave. The stacking faults are unstable and quickly disappear when the tensile stress wave leaves the surface region and the lattice deformation partially relaxes.

An important prediction of the simulations is that a high density of vacancies, on the order of 10^{-3} per lattice site, can be produced in the surface region of the irradiated target at laser fluences close or above the surface melting threshold. The thermally-

activated generation of vacancy-interstitial pairs during the laser-induced temperature spike, when the crystalline part of the target can be transiently overheated up to more than 20% above the equilibrium melting temperature [12,51,46,77], serves as the initial source of the point defects. Due to the high mobility of self-interstitials, they quickly escape to the melting front or the free surface of the target, leaving behind a large number of vacancies. A significant number of vacancies can also be produced at the advancing solid-liquid interface during the fast resolidification process. The strong temperature gradient created in the surface region of the target by femtosecond laser irradiation, and associated ultrafast cooling rates exceeding 5×10^{12} K/s at the time of resolidification (Fig. 5-4), provide the conditions for stabilization of the highly non-equilibrium vacancy concentration. The cooling rate, together with the original microstructure and presence of impurities, controls the long-term evolution of the defect structures.

The generation of vacancies and vacancy clusters may result in damage accumulation, generation of nanovoids, and degradation of the mechanical properties of the surface region of the target in the multi-pulse irradiation regime. The generation of crystal defects may be, thus, related to the incubation effect observed in laser ablation and damage [70,71,72,73,74]. The high density of vacancies generated in the surface region should also play an important role in redistribution of impurities or mixing/alloying in multi-component or composite targets. The small depth of the region where the defects are generated may provide avenues for controlled nanoscale modification of material properties.

References for Chapter 5

- [1]. M. von Allmen and A. Blatter, *Laser Beam Interactions with Materials*, Springer: Berlin, 1998.
- [2]. D. Bäuerle, *Laser Processing and Chemistry*, Springer-Verlag: Berlin Heidelberg, 2000.
- [3]. J. Kaspar and A. Luft, *Surface engineering* **17**, 379-383, 2001.
- [4]. J. G. Hoekstra, S. B. Quadri, J. R. Scully, and J. M. Fitz-Gerald, *Adv. Eng. Mat.* **7**, 805-809, 2005.
- [5]. R. L. Harzic, N. Huot, E. Audouard, C. Jonin, and P. Laporte, *Appl. Phys. Lett.* **80**, 3886-3888, 2002.
- [6]. V. Margetic, K. Niemax, and R. Hergenröder, *Anal. Chem.* **75**, 3435-3439, 2003.
- [7]. Q. Feng, Y. N. Picard, H. Liu, S. M. Yalisove, G. Mourou, and T. M. Pollock, *Scripta Materialia* **53**, 511-516, 2005.
- [8]. T. H. R. Crawford, J. Yamanaka, G. A. Botton, and H. K. Haugen, *J. Appl. Phys.* **103**, 053104, 2008.
- [9]. D. S. Ivanov, B. C. Rethfeld, G. M. O'Connor, T. J. Glynn, A. N. Volkov, and L. V. Zhigilei, *Appl. Phys. A*, in press, 2008.
- [10]. X. W. Wang, *J. Phys. D* **38**, 1805-1823, 2005.
- [11]. D. S. Ivanov and L. V. Zhigilei, *Phys. Rev. B*, **68**, 064114, 2003.
- [12]. D. S. Ivanov and L. V. Zhigilei, *Phys. Rev. Lett.* **91**, 105701, 2003.

- [13]. Z. Lin and L. V. Zhigilei, Phys. Rev. B **73**, 184113, 2006.
- [14]. E. Leveugle, D. S. Ivanov, and L. V. Zhigilei, Appl. Phys. A **79**, 1643-1655, 2004.
- [15]. L. V. Zhigilei, D. S. Ivanov, E. Leveugle, B. Sadigh, and E. M. Bringa, High-Power Laser Ablation V, edited by C. R. Phipps, Proc. SPIE **5448**, 505-519, 2004.
- [16]. E. Ohmura, I. Fukumoto, and I. Miyamoto, Int. J. Jpn. Soc. Prec. Eng. **32**, 248-253, 1998.
- [17]. C. Schäfer, H. M. Urbassek, and L. V. Zhigilei, Phys. Rev. B **66**, 115404, 2002.
- [18]. N. N. Nedialkov, S. E. Imamova, and P. A. Atanasov, J. Phys. D: Appl. Phys. **37**, 638-643, 2004.
- [19]. C. Cheng and X. Xu, Phys. Rev. B **72**, 165415, 2005.
- [20]. M. B. Agranat, S. I. Anisimov, S. I. Ashitkov, V. V. Zhakhovskii, N. A. Inogamov, K. Nishihara, Yu. V. Petrov, V. E. Fortov, and V. A. Khokhlov, Appl. Surf. Sci. **253**, 6276-6282, 2007.
- [21]. S. I. Anisimov, B. L. Kapeliovich, and T. L. Perel'man, Sov. Phys. JETP **39**, 375-377, 1974.
- [22]. L. V. Zhigilei and B. J. Garrison, Mat. Res. Soc. Symp. Proc. **538**, 491-496, 1999.
- [23]. C. Schäfer, H. M. Urbassek, L. V. Zhigilei, and B. J. Garrison, Comp. Mater. Sci. **24**, 421-429, 2002.
- [24]. C. Kittel, Introduction to Solid State Physics, 7th ed. (Wiley, New York, 1996).
- [25]. S. D. Brorson, A. Kazeroonian, J. S. Moodera, D. W. Face, T. K. Cheng, E. P. Ippen, M. S. Dresselhaus, and G. Dresselhaus, Phys. Rev. Lett. **64**, 2172-2175,

1990.

- [26]. Handbook of Optical Constants of Solids I/II, edited by D. Palik (Academic Press, London, 1985/1991).
- [27]. B. Lee, M. I. Baskes, H. Kim, and Y. K. Cho, Phys. Rev. B **64**, 184102, 2001.
- [28]. R. Pasianot, D. Farkas, and E. J. Savino, Phys. Rev. B **43**, 6952, 1991.
- [29]. B. Zhang, Y. Ouyang, S. Liao, Z. Jin, Physica B **262**, 218-225, 1999.
- [30]. R. A. Johnson and D. J. Oh, J. Mater. Res. **4**, 1195-1201, 1989.
- [31]. X. W. Zhou, H. N. G. Wadley, R. A. Johnson, D. J. Larson, N. Tabat, A. Cerezo, A. K. Petford-Long, G. D. W. Smith, P. H. Clifton, R. L. Martens, and T. F. Kelly, Acta Mater. **49**, 4005, 2001.
- [32]. Smithells Metal Reference Book, 7th edition, edited by E. A. Brandes and G. B. Brook (Butterworth-Heinemann, Oxford, 1998).
- [33]. J.-O. Andersson, Int. J. Thermophys. **6**, 411-419, 1985.
- [34]. G. K. White and C. Andrikidis, Phys. Rev. B **53**, 8145-8147, 1996.
- [35]. P. Ehrhart, P. Jung, H. Schulta, and H. Ullmaier, in Atomic Defects in Metals, edited by H. Ullmaier, Landolt-Börnstein, New Series, Group III, Vol. 25 (Springer-Verlag, Berlin, 1991).
- [36]. D. I. Bolef and J. de Klerk, Phys. Rev. **129**, 1063-1067, 1963.
- [37]. J. R. Ray and A. Rahman, Statistical ensembles and molecular dynamics studies of anisotropic solids, J. Chem. Phys. **80**, 4423-4428, 1984.

- [38]. T. Çağın, G. Dereli, M. Uludoğan, and M. Tomak, Phys. Rev. B, **59**, 3468-3473, 1999.
- [39]. M. Karimi, G. Stapay, T. Kaplan, and M. Mostoller, Modelling Simul. Mater. Sci. Eng. **5** 337-346, 1997.
- [40]. K. Yoshimoto, G. J. Papakonstantopoulos, J. F. Lutsko, and J. J. de Pablo, Phys. Rev. B, **71** 184108, 2005.
- [41]. K. W. Katahara, M. Nimalendran, M. H. Manghnani, and E. S. Fisher, J. Phys. F **9**, 2167-2176, 1979.
- [42]. M. Born, J. Chem. Phys. **7**, 591-603, 1939.
- [43]. J. Wang, J. Li, S. Yip, S. Phillpot, and D. Wolf, Phys. Rev. B **52**, 12627, 1995.
- [44]. V. Sorkin, E. Polturak, and J. Adler, Phys. Rev. B **68**, 174102, 2003.
- [45]. Z. H. Jin, P. Gumbsch, K. Lu, and E. Ma, Phys. Rev. Lett. **87**, 055703, 2001.
- [46]. S.-N. Luo, T. J. Ahrens, T. Çağın, A. Strachan, W. A. Goddard, and D. C. Swift, Phys. Rev. B **68**, 134206, 2003.
- [47]. M. Forsblom and G. Grimvall, Phys. Rev. B **72**, 054107, 2005.
- [48]. X.-M. Bai and M. Li, Phys. Rev. B **77**, 134109, 2008.
- [49]. The use of terms “lattice” and “lattice temperature” in this study does not imply the preservation of the crystalline order in the system. By using these terms we merely follow the terminology established in the literature presenting TTM calculations, when the term “lattice temperature” is commonly used to refer to the temperature of the ionic sub-system that can be brought out of equilibrium with

the conduction band electrons by short pulse irradiation or high-energy ion bombardment.

- [50]. W. H. Duff and L. V. Zhigilei, J. Phys.: Conference Series **59**, 413-417, 2007.
- [51]. D. S. Ivanov and L. V. Zhigilei, Phys. Rev. Lett. **98**, 195701, 2007.
- [52]. J. B. Cohen, R. Hinton, K. Lay, and S. Sass, Acta Metallurgica **10**, 894, 1962.
- [53]. V. Vitek, Phil. Mag. **18**, 773-786, 1968.
- [54]. V. Vitek, Phil. Mag. **21**, 1275-1278, 1970.
- [55]. R. A. Johnson, Phys. Rev. **134**, A1329, 1964.
- [56]. G. J. Ackland and R. Thetford, Philos. Mag. A **56**, 15-30, 1987.
- [57]. D. Nguyen-Manh, A. P. Horsfield, and S. L. Dudarev Phys. Rev. B **73**, 020101(R), 2006.
- [58]. P. Olsson, J. Wallenius, C. Domain, K. Nordlund, and L. Malerba, Phys. Rev. B **72**, 214119, 2005.
- [59]. P. M. Derlet, D. Nguyen-Manh, and S. L. Dudarev, Phys. Rev. B **76**, 054107, 2007.
- [60]. B. D. Wirth, G. R. Odette, D. Maroudas, and G. E. Lucas, J. Nucl. Mater. **244**, 185-194, 1997.
- [61]. Yu. N. Osetsky, D. J. Bacon, A. Serra, B. N. Singh, and S. I. Golubov, J. Nucl. Mater. **276**, 65-77, 2000.
- [62]. N. Soneda and T. D. de la Rubia, Phil. Mag. A **78**, 995-1019, 1998.

- [63]. K. Arakawa, K. Ono, M. Isshiki, K. Mimura, M. Uchikoshi, and H. Mori, *Science* **318**, 956-959, 2007.
- [64]. N. Soneda and T. Diaz de La Rubia, *Phil. Mag. A* **8**, 331-343, 2001.
- [65]. D. A. Terentyev, L. Malebra, and M. Hou, *Phys. Rev. B* **75**, 104108, 2007.
- [66]. R. C. Pasianot, A. M. Monti, G. Simonelli, and E. J. Savino, *J. Nucl. Mater.* **276**, 230-234, 2000.
- [67]. F. Gao, D. J. Bacon, P. E. J. Flewitt, and T. A. Lewis, *Nucl. Instr. Meth. B* **180**, 187-193, 2001.
- [68]. V. G. Kapinos, Yu. N. Osetskii and P. A. Platonov, *J. Nucl. Mater.* **173**, 229-242, 1990.
- [69]. B. D. Wirth, *Science* **318**, 923-924, 2007.
- [70]. D. Ashkenasi, M. Lorenz, R. Stoian, and A. Rosenfeld, *Appl. Surf. Sci.* **150**, 101-106, 1999.
- [71]. P. T. Mannion, J. Magee, E. Coyne, G. M. O'Connor, and T. J. Glynn, *Appl. Surf. Sci.* **233**, 275-287, 2004.
- [72]. S. E. Kirkwood, A. C. van Popta, Y. Y. Tsui, and R. Fedosejevs, *Appl. Phys. A* **81**, 729-735, 2005.
- [73]. J. Krueger, D. Dufft, R. Koter, and A. Hertwig, *Appl. Surf. Sci.* **253**, 7815-7819, 2007.
- [74]. G. Raciukaitis, M. Brikas, P. Gecys, and M. Gedvilas, *Proc. SPIE* **7005**, paper 7005-105, 2008.

- [75]. T. Górecki, Z. Metallk. (Zeitschrift fuer Metallkunde/Materials Research and Advanced Techniques) **65**, 426-431, 1974.
- [76]. T. Górecki, Scripta Metallurgica **11**, 1051-1053, 1977.
- [77]. A. B. Belonoshko, N. V. Skorodumova, A. Rosengren, and B. Johansson, Phys. Rev. B **73**, 012201, 2006.

6. Generation of Crystal Defects in Short Pulse Laser Interaction with FCC Ni

6.1 Introduction

Short pulse laser interaction with materials is finding an increasing use in a diverse area of applications ranging from advanced materials processing, cutting, drilling, surface micro- and nano-structuring, to laser surgery and artwork restoration. In particular, surface modification technique using short pulse laser irradiation has been employed in many modern processing and fabrication, such as surface alloying, annealing, and hardening, e.g. [1,2,3,4]. Further optimization of the experimental conditions suitable for modification of the irradiated surfaces requires a detailed understanding of the microscopic mechanisms responsible for the structural changes in the materials. However the transient nature of the ultrafast structural transformations occurring under conditions of steep temperature gradients and high stress variations brought by the short pulse laser irradiation makes the investigation challenging.

Large scale atomic level simulations employing molecular dynamic (MD) method provides an intriguing opportunity for studying the ultrafast laser-induced structure changes occurring within the time- and length-scales that are readily achieved by the classical MD technique. Indeed, MD simulations have been successfully carried out for investigating the microscopic mechanisms of laser-induced melting [5, 6, 7], photomechanical spallation [8,9], and ablation [10,11,12,13,14,15] in several metal targets. In addition, the generation of crystal defects in a body centered cubic (BCC) Cr target irradiated by a 200 fs, laser pulse has been recently investigated in large scale MD

simulations [16]. It is shown that in BCC Cr a large concentration of vacancies is created within the surface region of the irradiated target after the resolidification, whereas stacking faults, appearing due to internal shifts in the crystal undergoing a rapid uniaxial expansion, are energetically unstable and disappear shortly after the laser-induced tensile stress wave leaves the surface region of the target. Although it is clear that for a face centered cubic (FCC) crystal the generation of dislocations is easier as compared to BCC crystals and the dislocations could be activated in four different $\{111\}$ slip planes, the atomic-level mechanisms leading to the possible generation of the crystal defects in FCC metals under short pulse laser irradiation remains largely unknown.

In this study, we will investigate the generation of crystal defects in the surface region of an FCC metal, Ni, irradiated by a 1 ps laser pulse. Large scale MD simulations are performed at laser fluences chosen to be above the threshold for the onset of surface melting, but well below the ablation threshold for Ni. This choice of the range of fluences is made to avoid any significant removal of the material since in this study we are focusing on the microstructure changes in non-ablative laser surface modification. The conditions leading to the generation of transient structural changes are discussed based on the simulation results and numerical analysis of the stacking fault stability in the FCC structure. The computational approach used in the simulations is briefly described below, in Section 6.2. The results of the simulations of the generation of crystal defects in the surface region of a bulk Ni target irradiated by a short laser pulse are presented and discussed in Section 6.3 and summarized in Section 6.4.

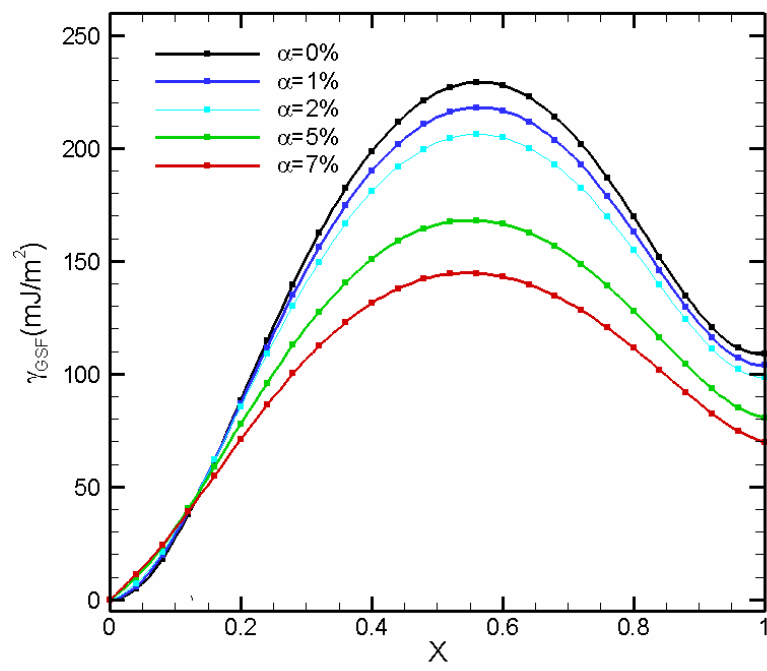
6.2 TTM-MD model for laser interaction with Ni

In this section, we will briefly discuss the computational model used in the simulations of short pulse laser irradiation of a bulk Ni target. The computational model is based on the well-known two-temperature model (TTM) [17] and combines the classical MD method with a continuum description of the laser excitation and subsequent relaxation of the conduction band electrons. The TTM consists of two coupled nonlinear differential equations that describe the time evolution of the lattice and electron temperatures. In the combined model (TTM-MD), the MD method substitutes one of the TTM equations for the lattice temperature in the surface region of the target, where the laser-induced structural and phase transformations are expected to take place. The diffusion equation for the electron temperature is solved by a finite difference method simultaneously with the integration of the equations of motion of atoms in MD. To account for the energy exchange between the electrons and the lattice, a coupling term is added to the MD equations of motion for atoms. While the TTM accounts for the laser energy deposition in the electron system, the energy exchange between the electrons and phonons, and the fast electron heat conduction in metals, the representation of the surface region of the target through MD provides a detailed atomic-level information of laser-induced structural and phase transformations. A complete description of the TTM-MD model is given elsewhere [5].

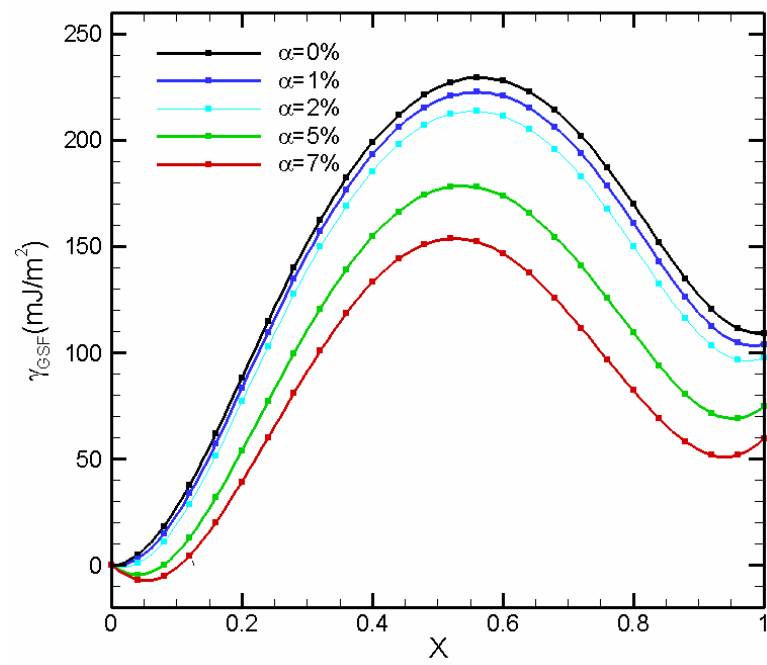
Here we provide the details of the computational setup for the simulation of laser interaction with a bulk Ni target. The computational domain in the TTM-MD model consists of two parts: atomistic (TTM-MD) part and continuum (TTM). The atomistic part of the model corresponds to the top 100 nm surface region of the Ni target and is

composed of 1 811 200 atoms initially arranged in an FCC crystalline lattice with dimensions of $14.1 \text{ nm} \times 14.1 \text{ nm} \times 100 \text{ nm}$. Periodic boundary conditions are applied in the directions parallel to the (100) free surface of the target. In order to correctly reproduce the propagation of the laser-induced pressure wave from the surface region of the target through the boundary between atomistic part and the continuum part of the model, a dynamic non-reflecting boundary condition [18,19] is applied at the bottom of the MD computational cell. In addition, the energy carried away by the pressure wave is monitored to allow for control over the total energy conservation in the combined model. In the continuum part of the model, the evolution of the electron and lattice temperatures is described by the two coupled equations of the conventional TTM. The size of the continuum (TTM) region, below the atomistic part, is chosen to be $1 \text{ }\mu\text{m}$, so that little changes in the electron and lattice temperatures are observed at the bottom of the continuum region during the time of the simulations. Before the laser irradiation, the system is equilibrated at 300 K for 50 ps.

The parameters used for Ni in the TTM equation for the electron temperature are as follows [20]. The electronic heat capacity is $C_e = \gamma T_e$ with $\gamma = 1063 \text{ Jm}^{-3}\text{K}^{-2}$, the electron-phonon coupling constant is $G = 3.6 \times 10^{17} \text{ Wm}^{-3}\text{K}^{-1}$, and the dependence of the electron thermal conductivity on the electron and lattice temperatures is described as $K_e = K_0 T_e / T_l$ with $K_0 = 91 \text{ Wm}^{-1}\text{K}^{-1}$. In order to describe the absorption of a 1 ps laser pulse inside the target, a source term with a Gaussian temporal profile and exponential attenuation of laser intensity with depth under the surface (Beer-Lambert law) is added to the TTM equation for the electron temperature.



(a)



(b)

Figure 6-1. Generalized stacking fault energy, γ_{GSF} , of EAM Ni for a (111) slip plane as a function of the magnitude of the fault vector : (a) $\bar{u} = X \times \frac{1}{6}[2\bar{1}\bar{1}]$ and (b) $\bar{u} = X \times \frac{1}{6}[11\bar{2}]$, where the degree of the uniaxial expansion of the lattice in [001] direction is characterized by the coefficient, α , shown in the figure.

Contrary to the unstable intrinsic stacking faults in $\{110\}$ planes in the BCC structure [21,22], dislocations can be activated in four different active $\{111\}$ slip planes by emission of Shockley partial dislocations, leaving stable stacking faults behind. This is noted by the local minimum in the generalized stacking fault energy curve shown in Fig. 6-1 for zero uniaxial expansion at the place where the displacement vector reaches the distance corresponding to the Burgers vector for a Shockley partial dislocation in FCC: $a/6\langle 112 \rangle$. The generalized stacking fault energy curves for $[2\bar{1}\bar{1}]$ and $[11\bar{2}]$ direction, shown in Fig. 6-1, are calculated for the FCC Ni for various degrees, 0-7%, of the uniaxial expansion. Similar to the stacking fault stability analysis done by Vitek [21,22], the calculations of the generalized stacking fault energy curves are done in a 4000 atom simulation cell that is divided into two parts by the (111) plane with one half of the cell kept fixed and the other half of the cell displaced in the $[2\bar{1}\bar{1}]$ or $[11\bar{2}]$ direction in small increments. After each incremental displacement, the relaxation of atoms is done along the direction perpendicular to the slip plane, $[111]$. After the relaxation, the generalized stacking fault energy is obtained by dividing the difference between the energy of the displaced system and the energy of a perfect lattice by the area of the slip plane. For a perfect FCC lattice, the intrinsic stacking fault energy obtained

for EAM Ni is 0.110 J/m^2 , in a reasonable agreement with the experimental value for the intrinsic stacking fault energy for Ni, 0.125 J/m^2 [23], values calculated using various EAM potentials for Ni, 0.125 J/m^2 [24] and 0.129 J/m^2 [25] as well as the density functional theory (DFT) results, 0.137 J/m^2 [26], 0.183 J/m^2 and 0.145 J/m^2 [27]. As shown in Figure 1, the uniaxial expansion of the lattice in $[001]$ direction leads to the decrease in both the maximum value in the generalized stacking fault energy curve (unstable stacking fault energy defined by Rice [28]) and the intrinsic stacking fault energy at $X=1$. This suggests that it is relatively easier to create stacking faults by shearing the crystal in a highly uniaxially deformed FCC lattice than in a perfect one. It is also worth to point out that, due to the anisotropic lattice expansion, the stacking fault energy curves vary in slightly different ways for two displacement directions, $[2\bar{1}\bar{1}]$ and $[11\bar{2}]$, as shown in Fig. 6-1.

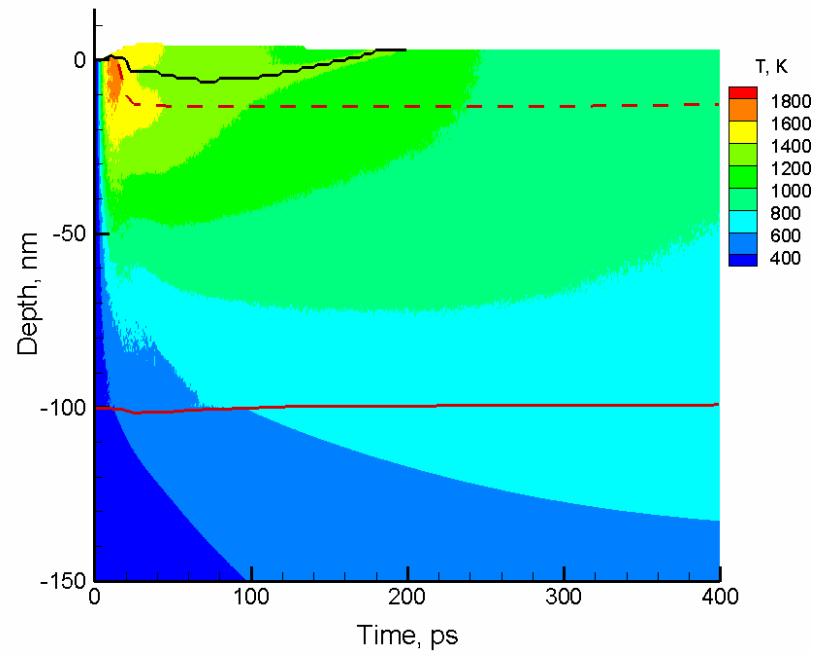
The laser-induced structural changes and crystal defects in the target are identified with the help of the centrosymmetry parameter [29] calculated for each atom, $\Phi = \sum_{i=1}^6 |\bar{\mathbf{R}}_i + \bar{\mathbf{R}}_{-i}|^2$, where \mathbf{R}_i and \mathbf{R}_{-i} are the a pair of vectors that connect to opposite nearest neighbors in the FCC lattice for a given atom. For a perfect FCC lattice, there are six pairs of these nearest neighbors. The value of the centrosymmetry parameter provides a measure of the local atomic environment of an atom away from the FCC centrosymmetry. For reference, the centrosymmetry parameter is zero for atoms with a perfect FCC surrounding whereas for liquid atoms, the parameter is well above zero due to the disordered structure. For crystal defects such as vacancy, interstitials, stacking faults and partial dislocations, the centrosymmetry parameter lies between the values for

perfect lattice and the liquid structure. For instance, point defects (vacancy/interstitial) will lead to nonzero centrosymmetry parameter of atoms surrounding the point defect. Using the lattice constant of EAM Ni at 300 K, 3.53 Å, it can be verified that stacking faults bounded by two Shockley partial dislocations with the Burgers vector $b=a/6\langle 112 \rangle$ have a centrosymmetry parameter of 6.2 Å². Following the laser irradiation, uniaxial expansion of the lattice will lead to slight changes in the centrosymmetry parameters of the stacking faults and partial dislocations as the lattice spacing is changing. One can use this parameter for distinguishing the crystalline and disordered/liquid regions in the melting and resolidification processes. To avoid the contribution from the thermal motions of atoms to the value of the centrosymmetry parameter, the atomic configurations obtained from the simulation are quenched for a period of 2 ps to quickly remove the kinetic energy of the system. During these quenching simulations, the atoms are allowed to relax only to their local energy minima while most of the kinetic energy of the system is removed. The short time of the quenching procedure ensures that the transient structure of the system is captured by the analysis based on the centrosymmetry parameter.

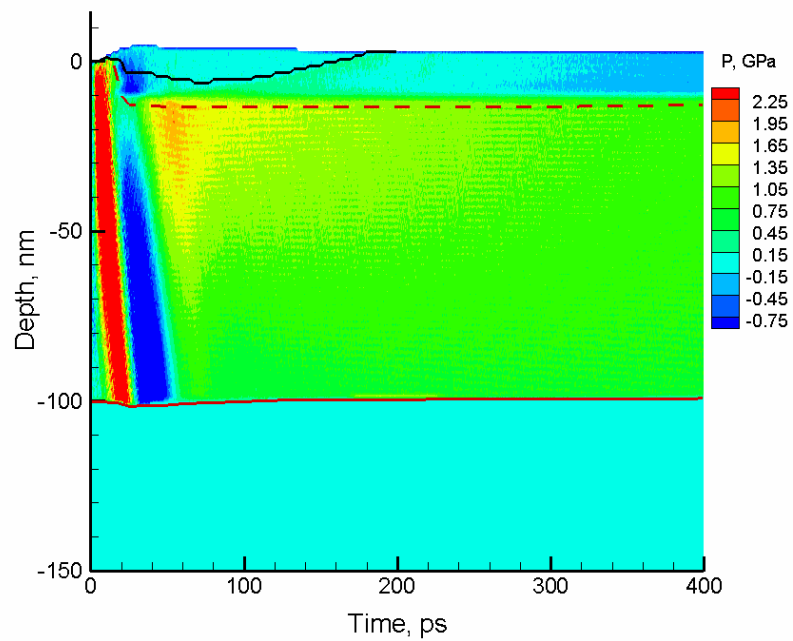
6.3 Simulation results and discussions

In this section, transient structural changes including the appearance of crystal defects, namely point defects and partial dislocations, in a Ni target irradiated with a 1 ps laser pulse are investigated based on the results of large-scale TTM-MD simulations performed at three absorbed laser fluences of 400, 430 and 645 J/m². For all three fluences, partial dislocations and stacking faults are found to appear during the initial

stage of the relaxation of laser-induced thermoelastic stresses and remain in the surface region of the target, along with a large concentration of vacancies, after the resolidification process.



(a)



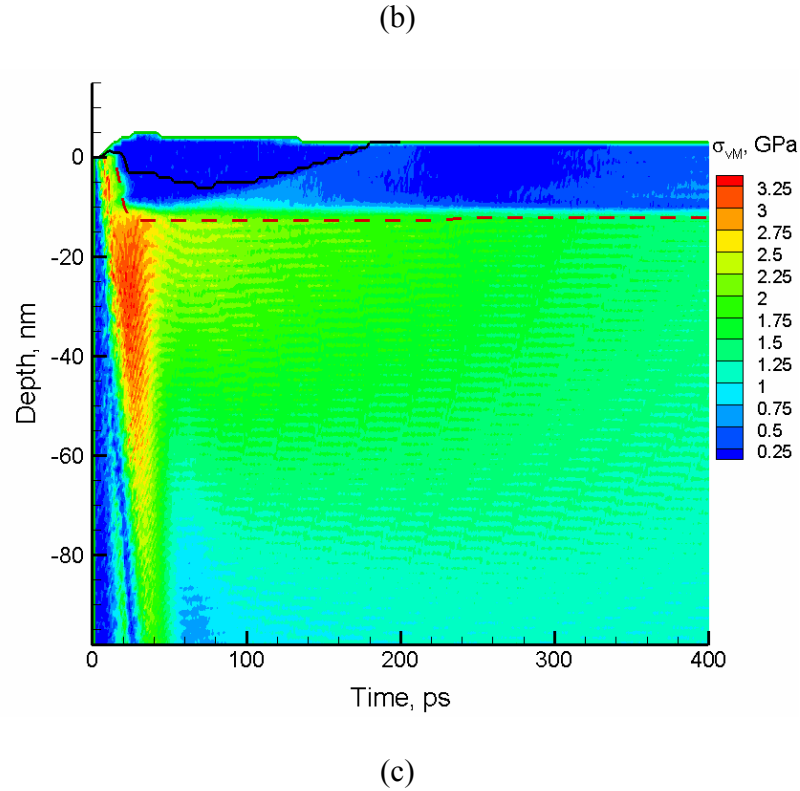


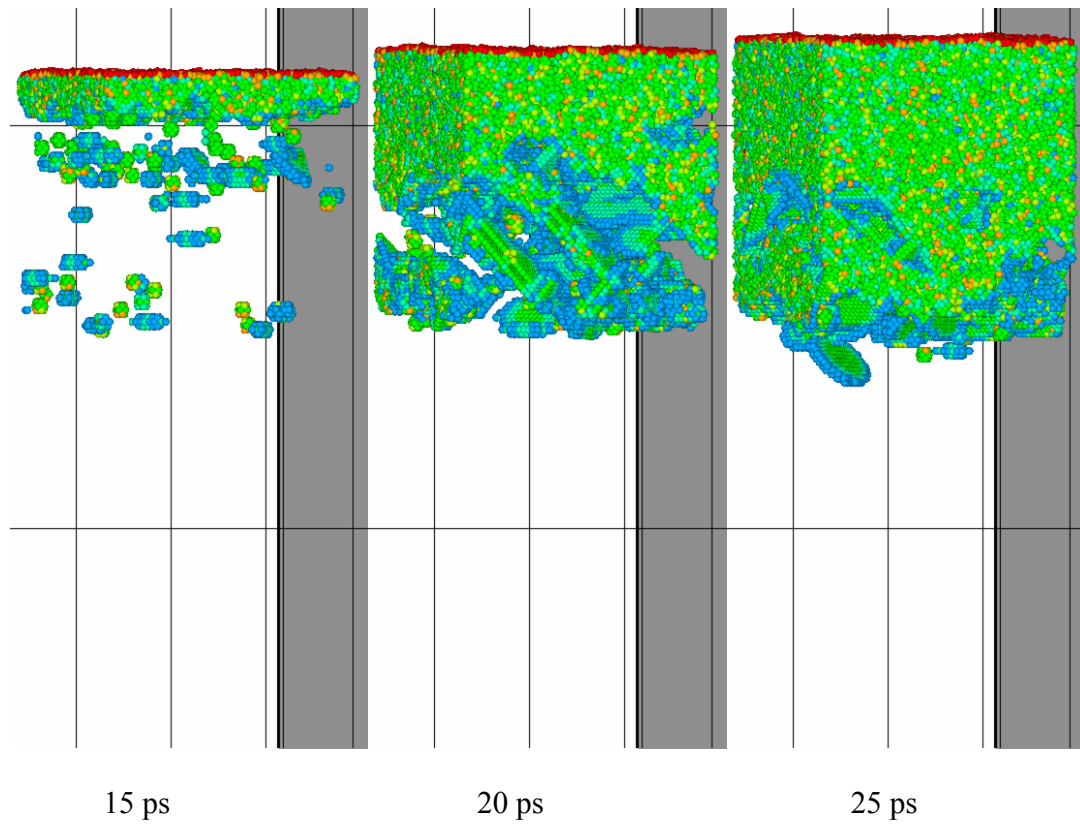
Figure 6-2. Contour plots of the spatial and temporal evolution of (a) temperature, (b) pressure and (c) von Mises stress in a TTM-MD simulation of a bulk Ni target irradiated with a 1 ps laser pulse at an absorbed fluence of 400 J/m^2 . The laser pulse is directed along the Y axes, from the top of the contour plots. The red solid line in (a) and (b) separates the continuum (TTM) and atomistic (TTM-MD) parts of the computational system. The red dashed line marks the maximum depth of the location where stacking faults and partial dislocations are observed. The black solid line separates the transiently melted surface region from the solid bulk of the target.

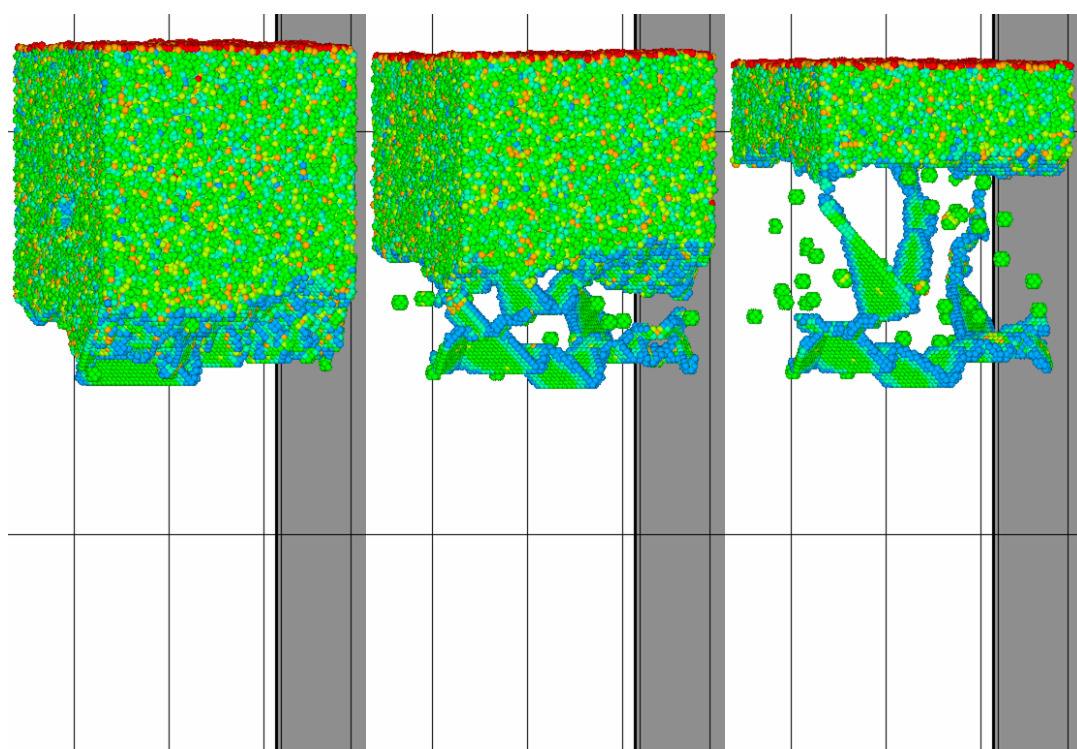
6.3.1 Generation of crystal defects during resolidification

Due to the small heat capacity of electrons as compared to the lattice, the laser energy absorption by the conduction band electrons creates a strongly non-equilibrium between the electrons and the lattice, in which the electron temperature is much higher

than the lattice one. The energy transfer from the hot electrons to the lattice vibrations due to the electron-phonon coupling could lead to the fast increase in the lattice temperature in the surface region of the target. The fast lattice heating within a few ps, occurring under conditions of the inertial stress confinement [30], results in the buildup of strong compressive stresses in the surface region of the irradiated target. The evolution of the temperature and pressure in the surface region of a bulk Ni target irradiated by a 1 ps pulse at an absorbed fluence of 400 J/m^2 is illustrated by the contour plots in Fig. 6-2 (a-b). The value of pressure, shown in Fig. 2b, is obtained from the three principal components of the stress tensor, $P = -(\sigma_{xx} + \sigma_{yy} + \sigma_{zz})/3$. Since a typical laser spot diameter is on the order of $\sim 100 \text{ }\mu\text{m}$, the fast relaxation of the laser-induced thermoelastic stresses can only proceed in the direction normal to the surface. As the compressive stresses relax through the propagation of the compressive pressure wave into the bulk region of the target, the lattice experiences an uniaxial expansion of the lattice in the direction perpendicular to the free surface, leading to the development of an unloading (tensile) wave. An interesting observation in the pressure plot shown in Fig. 6-2(b) is that at $\sim 20 \text{ ps}$ after the laser pulse the unloading tensile stresses are reduced in the region $\sim 10\text{-}20 \text{ nm}$ below the surface. This could be related to the appearance of partial dislocations and stacking faults as shown in a series of snapshots of the atomic configurations at 15, 20 and 25 ps in Fig. 6-3. As the crystal undergoes a rapid uniaxial expansion in the direction normal to the irradiated surface, the partial dislocations and stacking faults occur as a result of internal shifts of the crystal along $\{111\}$ planes. The plastic deformation reduces the level of the tensile stresses in the unloading wave. The

tensile stresses increase again as the unloading wave moves away from the region affected by the plastic deformation.

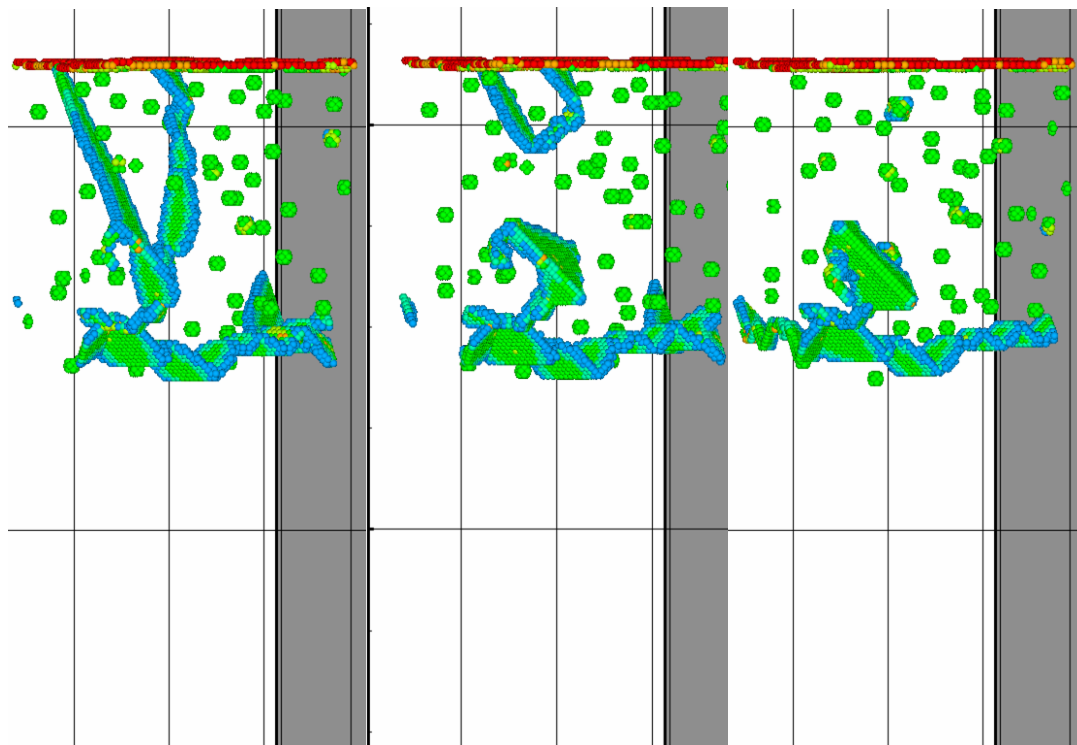




50 ps

100 ps

150 ps



200 ps

215 ps

400 ps

Figure 6-3. Snapshots of the atomic configurations in a TTM-MD simulation of a bulk Ni target irradiated with a 1 ps laser pulse at an absorbed fluence of 400 J/m². Only atoms with the value of the centrosymmetry parameter, Φ , higher than 0.5 are shown in the figure. Red atoms are located at the free surfaces while blue and green atoms correspond to atoms that have a defected local atomic environment within the first nearest neighbor distance. In particular, mono-vacancies show up as clusters of 12 atoms since these atoms have non-zero values of the centrosymmetry parameter due to the absence of one atom in their first nearest neighbor shells. Blue atoms are located along the partial dislocation core while green atoms bounded by the blue atoms correspond to the stacking faults which are left behind by the Shockley partial dislocations. The configurations are quenched to 0 K in order to reduce thermal noise in calculating the centro-symmetry parameter. The atomic configuration is shown down to the depth of 31 nm in the target.

In order to characterize the plastic deformation in the target induced by the relaxation of laser-induced stresses, we calculate the von Mises stress, σ_{vm} , which has been shown to be a good indicator of the onset of plastic deformation under conditions of shock loading [31] and nanoindentation [32]. The von Mises stress is defined in Eq. (6.1)

$$\sigma_{vm}^2 = \frac{1}{2} [(\sigma_{xx} - \sigma_{yy})^2 + (\sigma_{yy} - \sigma_{zz})^2 + (\sigma_{zz} - \sigma_{xx})^2] \quad (6.1)$$

As seen in Fig. 6-2(c), the anisotropic lattice deformation resulted from the unloading tensile pressure wave leads to the buildup of the von Mises stress in the target. For instance, at ~5 nm below the original surface the von Mises stress reaches ~3.9 GPa at ~10 ps. However the high von Mises stress accumulated within ~10 nm below the

surface quickly relax within a few ps. The transition of the magnitude of the von Mises stress from high values, on the order of a few GPa, to nearly zero is related to the structural transformations occurring in this region. At 20 ps, a large density of dislocations and stacking faults, as well as many small liquid nuclei, appear in this region as shown in the snapshot of the atomic configuration in Fig. 6-3. This also suggests that plastic deformation initiates when the von Mises stress exceeds the critical yield stress as a result of uniaxial tension.

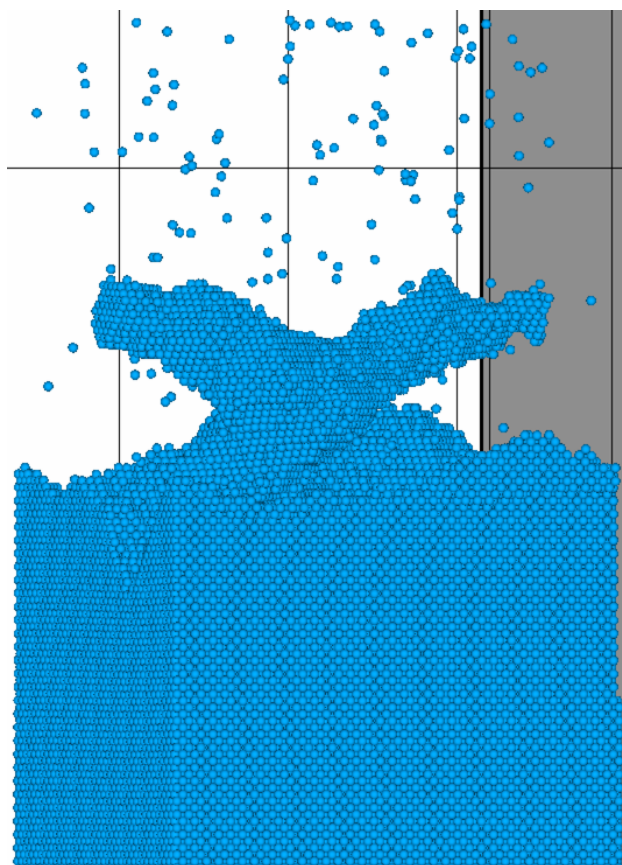


Figure 6-4. Rough morphology of the melting front at 50 ps in a TTM-MD simulation of a bulk Ni target irradiated with a 1 ps laser pulse at an absorbed fluence of 400 J/m². Only atoms with a local FCC atomic surrounding are shown ($\Phi < 0.5$) while defected or

liquid atoms are blanked. The atomic configuration is shown down to the depth of 20 nm in the target.

It is important to point out that at later time the von Mises stress also achieves the level as high as ~ 3.5 GPa at ~ 30 nm below the original surface where no stacking faults or dislocations are observed in the atomic snapshot. This is probably due to the fact that the stress is not high enough to create stacking faults and dislocations without preexisting dislocation sources or defects in this region. The situation is quite different in the region close to the melting front where the melting front could act as the nucleation site for the dislocation emission. Furthermore, thermal softening of the crystal due to the elevated temperature, Fig. 6-2(a), and the generation of a large amount of point defects in the target as shown in the snapshots could also facilitate the appearance of the dislocations and stacking faults in this region. The thermal softening also reduces the image forces that resist the emission of the dislocation.

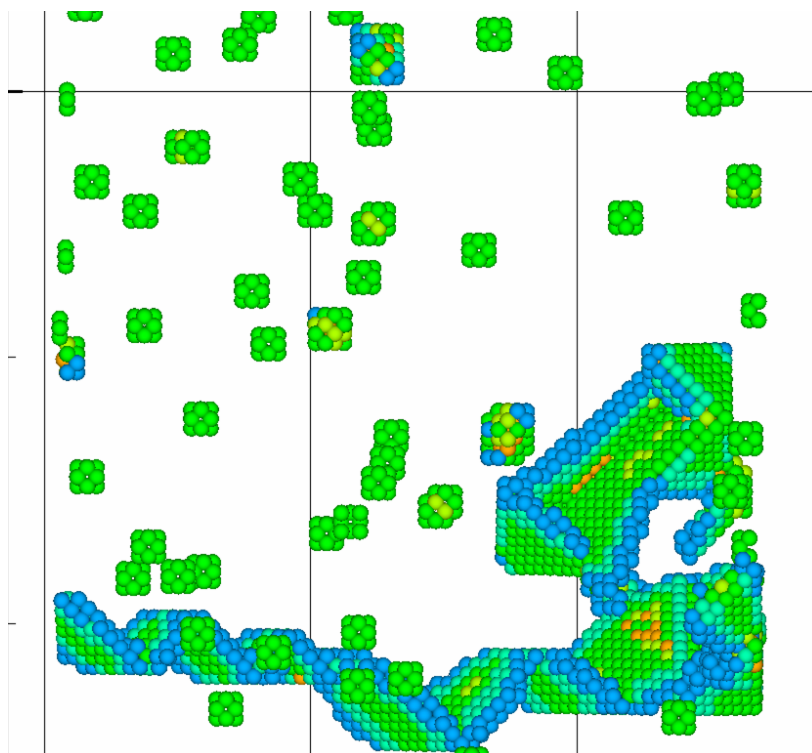


Figure 6-5. A close snapshot of the atomic configuration of defects at 400 ps in a TTM-MD simulation of a bulk Ni target irradiated with a 1 ps laser pulse at an absorbed fluence of 400 J/m².

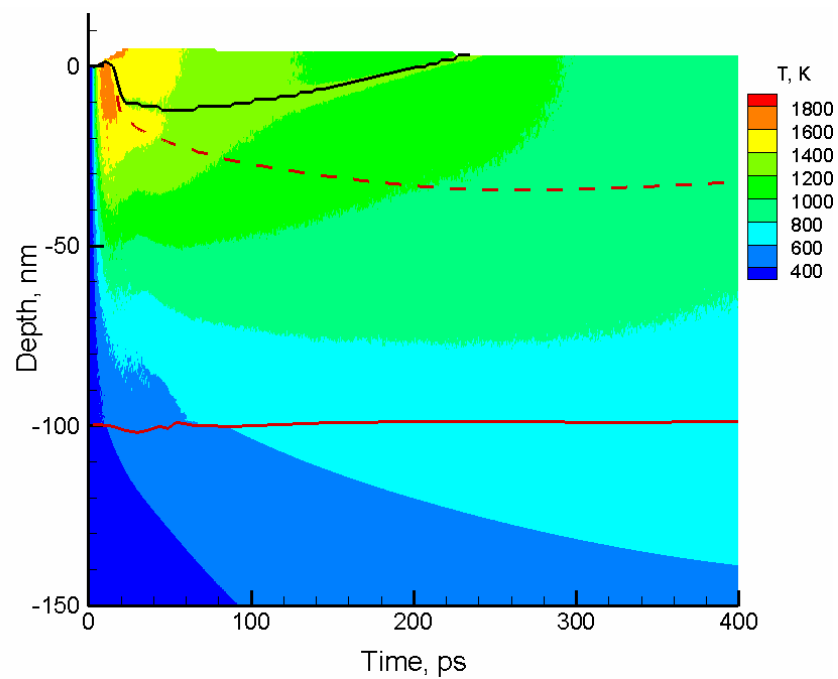
The snapshots of the atomic configurations shown in Fig. 6-3 demonstrate that the processes of generation of crystal defects and melting are intertwined during the first ~25 ps after the laser pulse. The active generation of point defects and partial dislocations in the transiently strained and overheated surface region of the target is clearly assisting the melting process, which continues in a highly defected region even after the temperature drops below the equilibrium melting temperature of the EAM Ni (1439 K) at ~40 ps. The melting process proceeds selectively in the regions of highest defect densities,

leading to the complex non-planar morphology of the “melting front” as shown in Fig. 6-4.

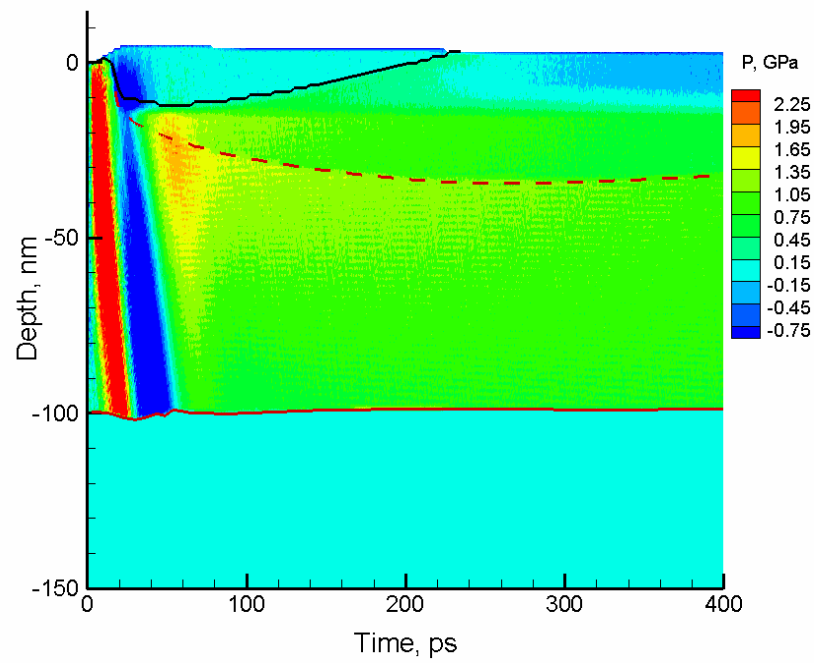
At the time of the beginning of the recrystallization process, ~ 70 ps, there is a pattern of partial dislocations immobilized by sessile stair rod dislocations [23] formed as a result of the interaction of dislocations propagating along different $\{111\}$ glide planes. For example, the dislocation observed at the highest depth in snapshots starting from 50 ps is located at the $[110]$ intersection of (111) and $(\bar{1}\bar{1}1)$ glide planes. The retreating melting front leaves behind dislocations that extend down to the surface by the time of 200 ps. Shortly after that time, these dislocations separate from the one located at ~ 11 nm, quickly retreat to the surface and disappear.

While the remaining configuration of partial dislocations undergoes only slight variations from 215 ps to 400 ps, the generation of a large number of vacancies in the surface region is also observed during the resolidification, Fig. 6-5. We compare the snapshots at 400 ps and 600 ps in the extended simulation and find that the configuration of these vacancies does not undergo any significant changes during the period of 200 ps. This could be explained by the fast cooling of the surface region due to the heat conduction into the bulk of the target. As the surface temperature drops, Fig. 6-2(a), the mobility of the remaining vacancies becomes very small, as expected from the Arrhenius temperature dependence of the vacancy diffusion, similar to the case for BCC Cr [see Chapter 5 and Ref. 16]. Therefore, the ultrafast cooling rate (on the order of 10^{12} K/s), measured from the surface temperature of the target, ensures the high supersaturation of the surface region of the target with vacancies, which are unlikely to undergo any significant motions during the rest of the cooling process.

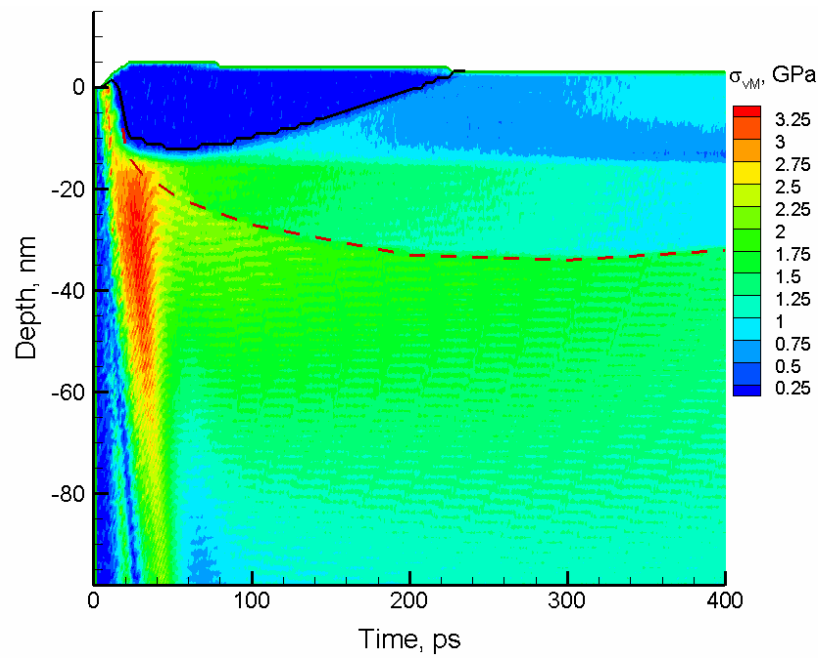
The remaining crystal defects in the surface region of the irradiated target could influence the mechanical properties of the surface region and could play an important role in the incubation effect often observed in multi-pulse irradiation regime [33,34,35,36,37]. At the same time, the presence of a high concentration of vacancies in the surface region of the target may play a role in atomic mixing/alloying in multi-component/composite materials.



(a)



(b)



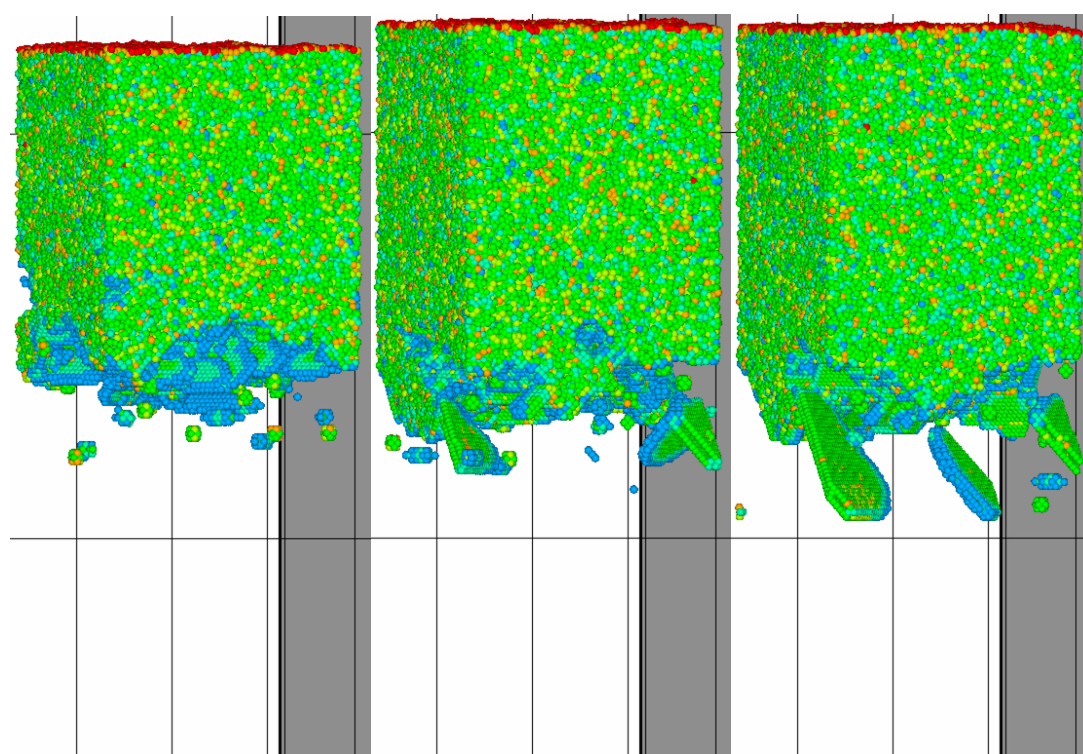
(c)

Figure 6-6. Same as in Figure 6-2 but with absorbed laser fluence of 430 J/m^2 .

6.3.2 Emission of partial dislocation at higher laser fluences

As the absorbed laser fluence of the laser pulse increases, it is observed that the melting front goes deeper into the target as more energy is supplied for the melting process in the surface region of the target. As expected, the melting brings the von Mises stress within the liquid region down to zero as seen from Fig. 6-6, whereas the propagation of a partial dislocation also decreases the level of von Mises stress. It can be seen that in the region between the melting front and the front of the partial dislocations, marked by the red dashed line in Fig. 6-6(c), there are still rather strong von Mises stresses, ~ 2 GPa, from 50 to 100 ps. The less significant, as compared to the simulation discussed above (Fig. 6-2(c)), reduction of von Mises stresses in the region below 15 nm can be explained by the fact that this reduction is caused by propagation of a single partial dislocation, Fig. 6-7. At later times, this partial dislocation slowly retreats towards the surface due to the gradual cooling of the lattice as well as the reduction in the uniaxial lattice expansion.

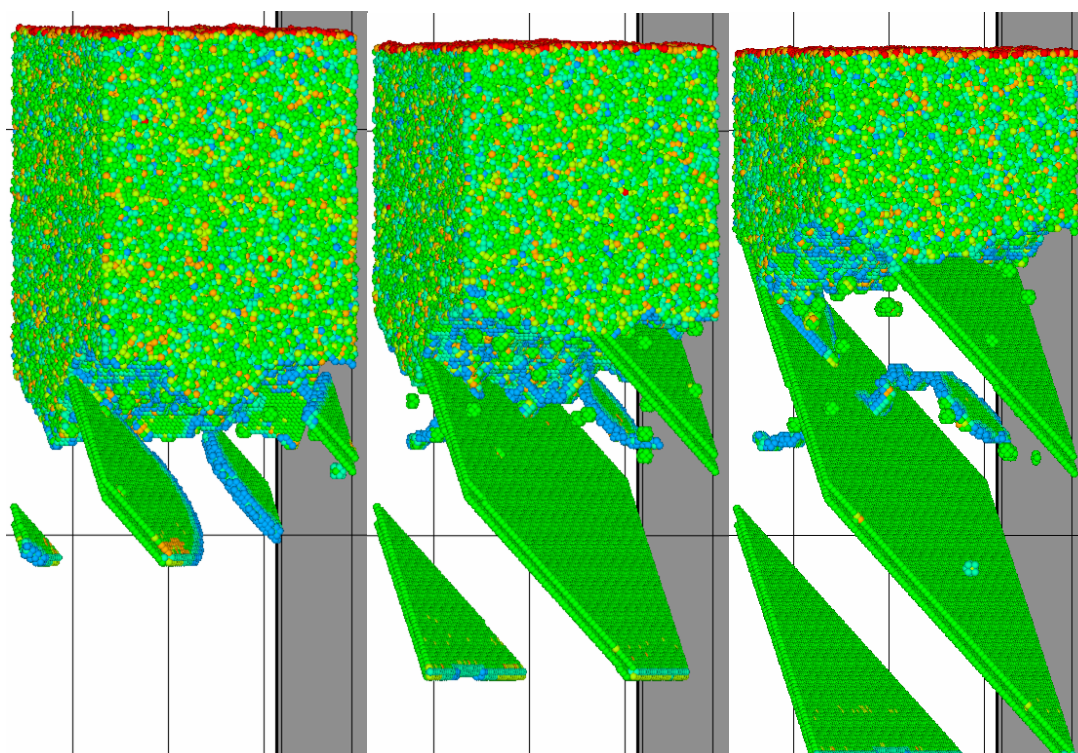
It is interesting to note that a stacking fault stripe corresponding to a dissociated dislocation appears during the resolidification at ~ 15 nm. The atomic snapshots show that the dislocation has a zig-zag shape and bends over from one glide plane to another, similar to the dislocation observed in the simulation discussed in Section 6.3.1. Each transition from one glide plane to another is associated with a sessile stair-rod dislocation that immobilizes the dissociated dislocation at the depth where it is created.



20 ps

30 ps

40 ps



50 ps

100 ps

150 ps

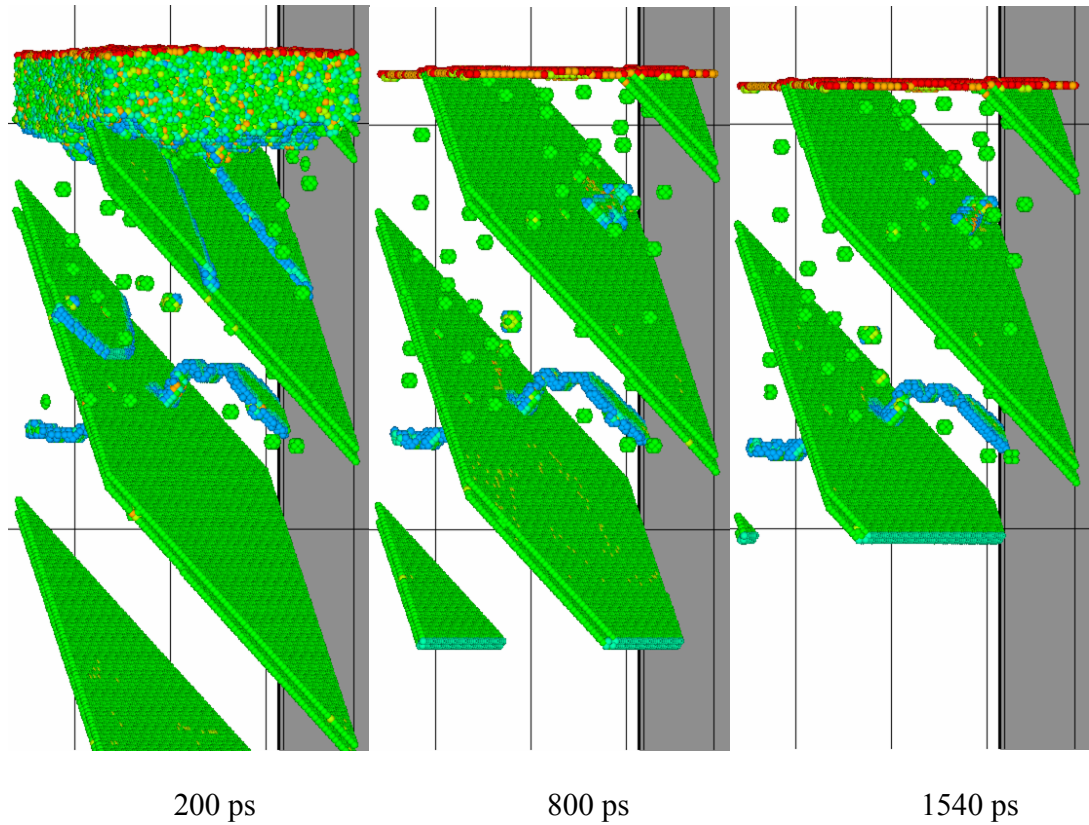
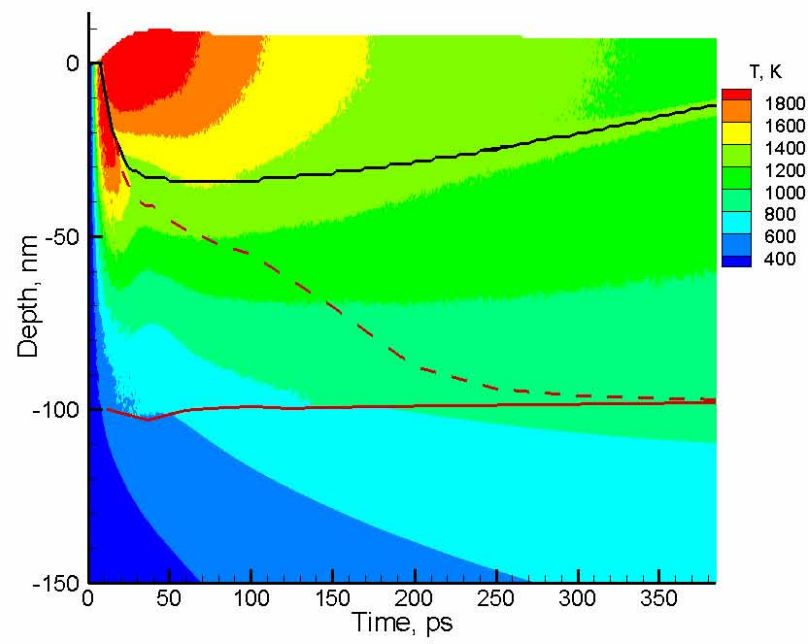
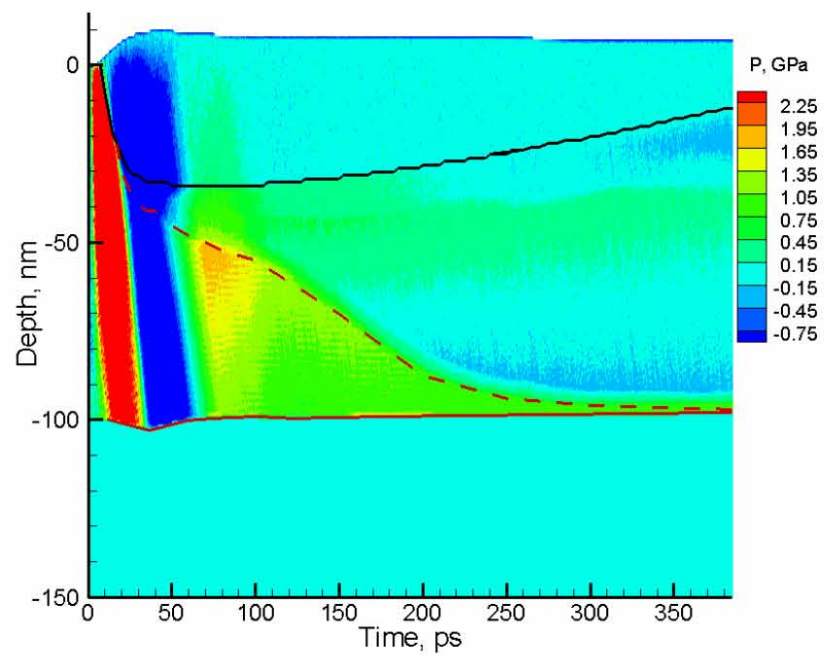


Figure 6-7. Same as in Figure 6-3 but with absorbed laser fluence of 430 J/m^2 . The atomic configuration is shown down to the depth of 31 nm in the target.

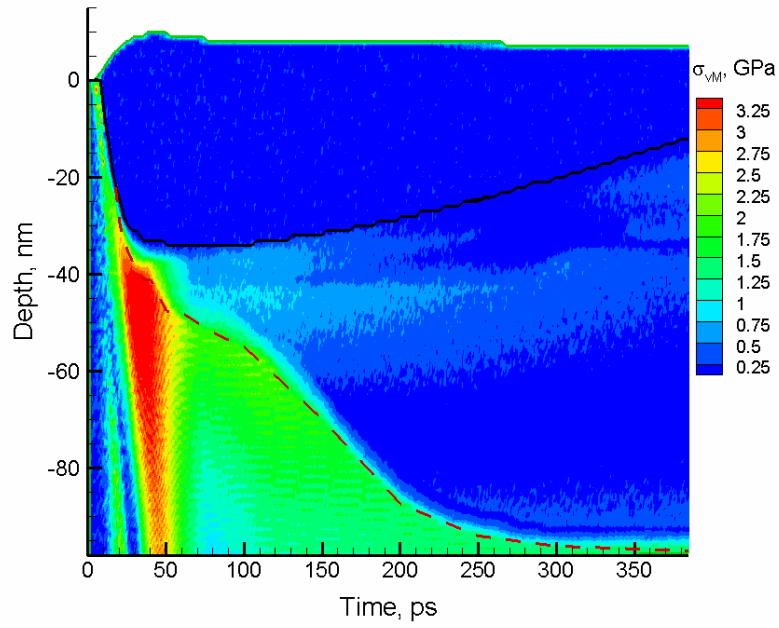
In the simulation performed at the highest fluence in this study, 645 J/m^2 , a large number of partial dislocations and stacking faults are propagating ahead of the melting front during 25-35 ps, as shown in Fig. 6-9. This observation can be related to high tensile stresses, up to $\sim 4 \text{ GPa}$, in this region. The calculation of the generalized stacking fault energy curves, shown in Fig. 6-1, indicates that the barrier for the formation of the stacking faults in the target is significantly reduced at high uniaxial expansion. As a result, partial dislocations are emitted in those directions, for which the residual shear stress is high, on four (111) glide planes in the FCC structure, leaving multiple stacking faults behind the dislocations (25-35 ps in Fig. 6-9).



(a)



(b)



(c)

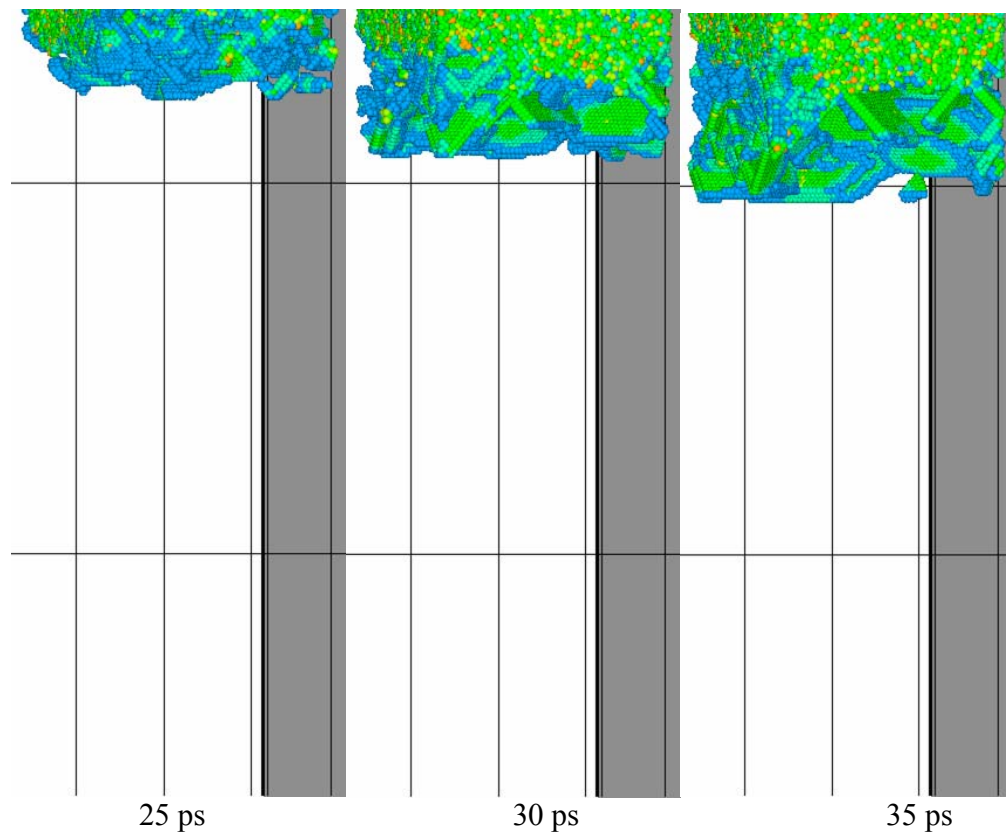
Figure 6-8. Same as in Figure 6-2 but with absorbed laser fluence of 645 J/m².

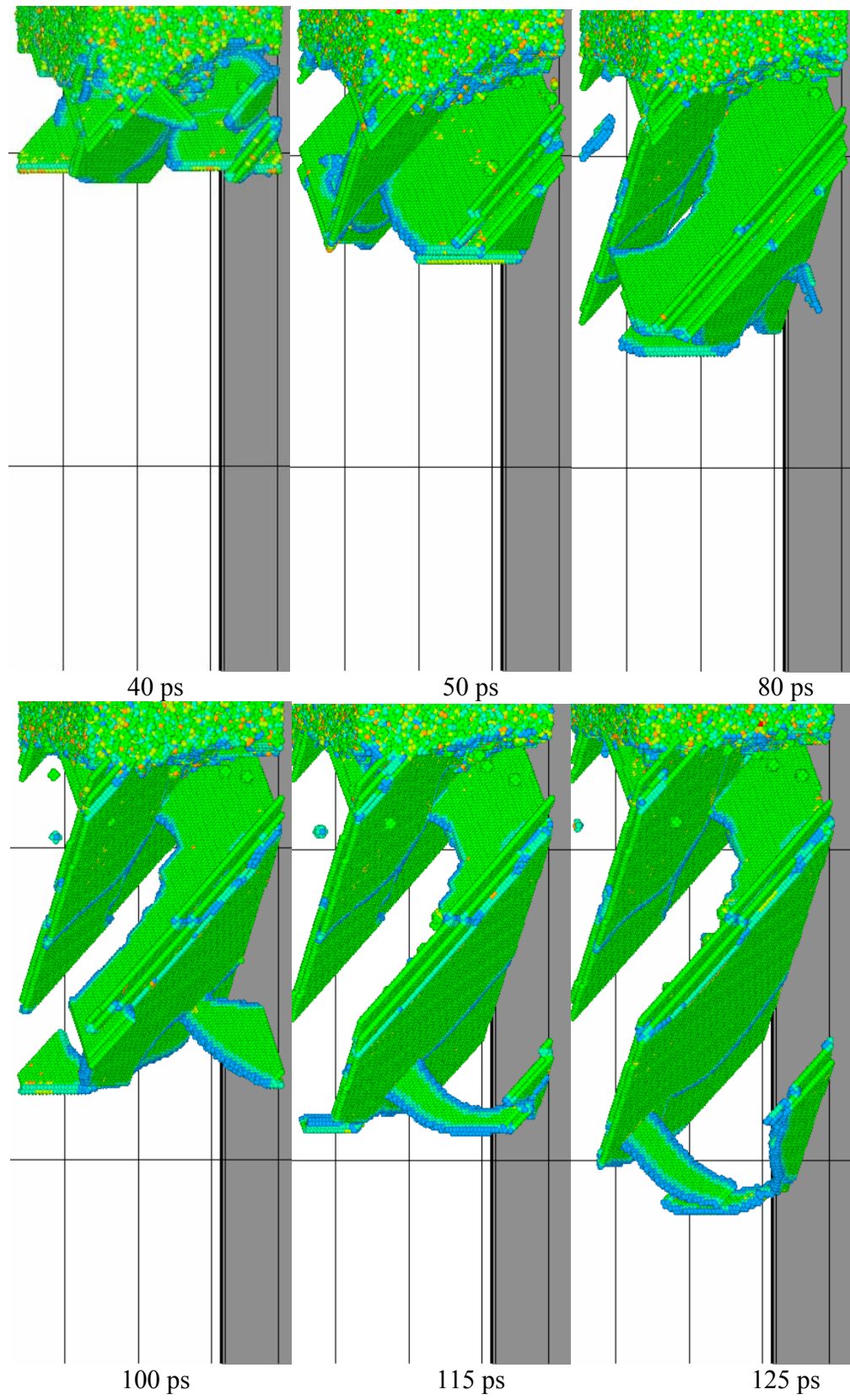
In order to characterize the stress state inside the target, we calculate the maximum shear stress to the slip system with both slip plane and slip direction oriented at 45° to the [001] direction at 50 and 100 ps, as shown in Fig. 6-10. The shear stress is taken as the form described in Eq. (6.2).

$$\sigma_{shear} = \frac{1}{2} [\sigma_{zz} - 0.5(\sigma_{xx} + \sigma_{yy})] \quad (6.2)$$

Fig. 6-10 clearly shows that there is a sharp drop of the shear stress behind the front of the propagating dislocations, indicating that the propagation of dislocations effectively reduces the shear stress. The gradual decrease of the shear stress in front of the dislocation at 100 ps is related to the decreasing residual thermoelastic stresses that remain in the surface region of the target after the laser-induced stress wave leaves this

region. This is directly reflected in the distribution of three principal components of the stress tensor in Ni at 150 ps, shown in Fig. 6-11. As can be seen, the principle component of the stress tensor corresponding to the direction perpendicular to the surface of the irradiated target, σ_{zz} , is fluctuating around zero throughout the region ~ 100 nm below the surface, while the other two principle components have nonzero values due to the residual lattice heating under conditions of the lateral confinement.





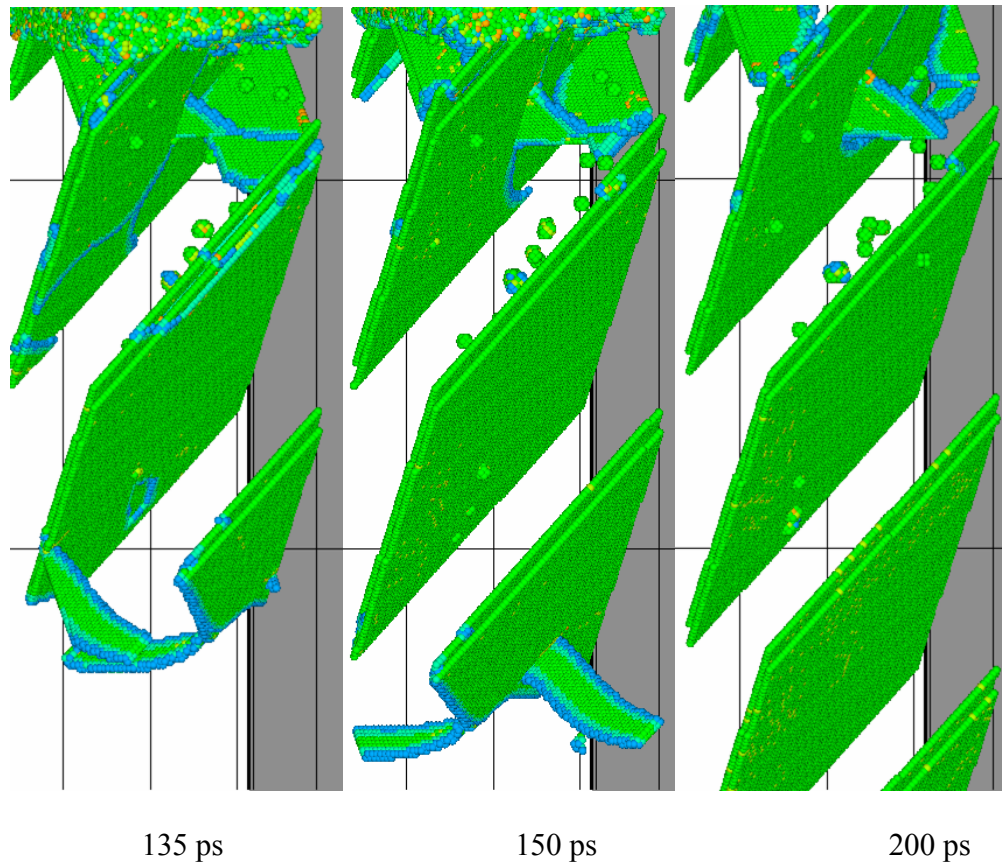


Figure 6-9. Same as in Figure 6-3 but with absorbed laser fluence of 645 J/m^2 . The atomic configuration is shown down to the depth of 72 nm in the target.

From the inspection of the atomic configuration in Fig. 6-9 along with the von Mises stress plot in Fig. 6-8(c), it can be seen that the propagation of two dislocations deeper into the target reduces the von Mises stresses down to about zero. One of the partial dislocations is followed by a trailing partial that propagates in the same plane and removes the stacking fault, as can be seen from the series of snapshots in Fig. 6-9. By 135 ps, we observe a configuration where a partial dislocation propagating along $(1\bar{1}1)$ plane is moving together with a complete dislocation dissociated into two partials. The Burgers vector of the dissociated dislocation can be identified from the atomic

arrangement in Fig. 6-12. It is clear that it is a perfect dislocation with a Burgers vector of $a/2[\bar{1}0\bar{1}]$, dissociated into two Shockley partial dislocations. The fast motion of the propagating dislocation reflects the glissile nature of the Shockley partial dislocations of the type $\frac{1}{6}\langle 112 \rangle$ on $\{111\}$ planes.

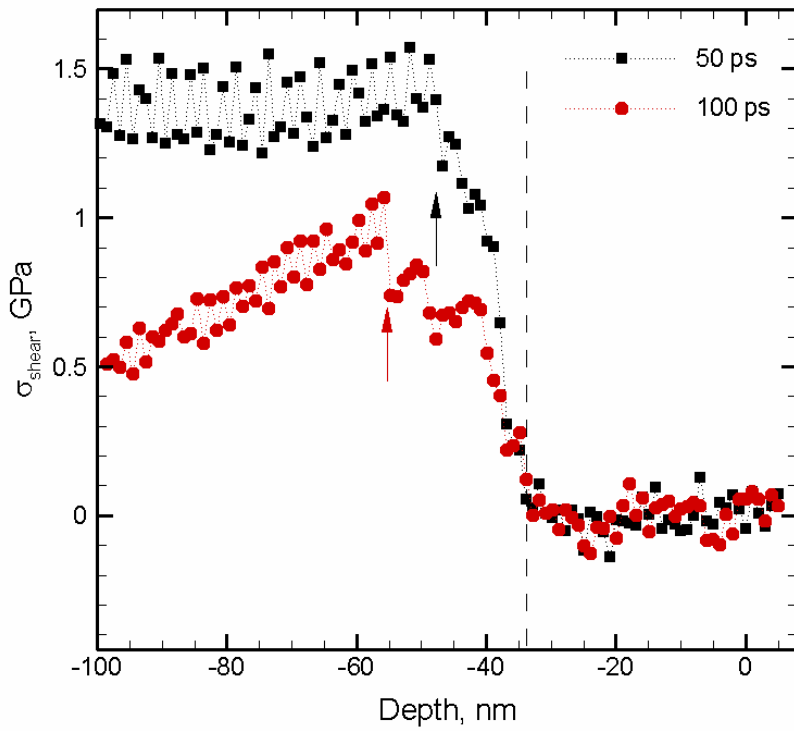


Figure 6-10. The distribution of the shear stress at 50 and 100 ps in Ni irradiated by a 1 ps laser pulse at an absorbed fluence of 645 J/m^2 . Dashed line marks the solid-liquid interface at 50 and 100 ps that separates the solid from the melted region. Black and red arrows indicate the front of propagating partial dislocations at 50 and 100 ps, respectively.

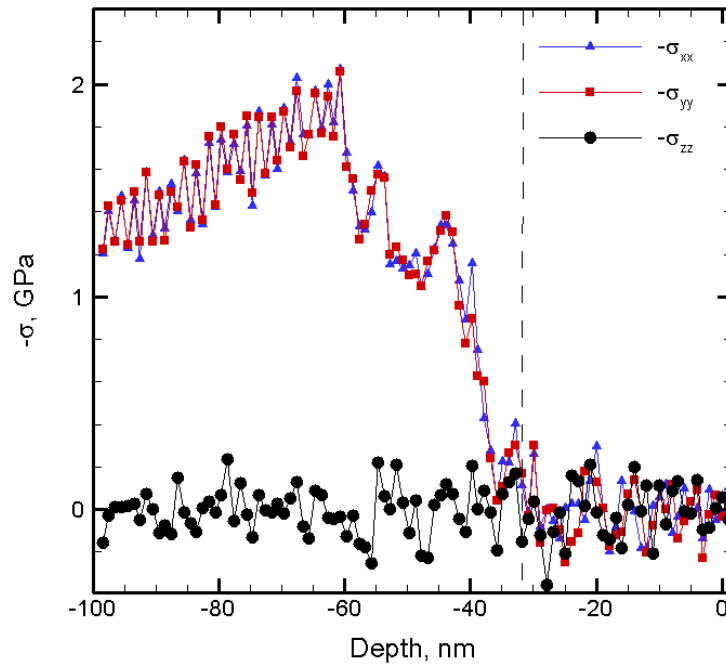


Figure 6-11. The distribution of the three principal components of the stress tensor, taken with a negative sign, at 150 ps in Ni irradiated by a 1 ps laser pulse at an absorbed fluence of 645 J/m^2 . Dashed line marks the solid-liquid interface at 150 ps that separates the solid from the melted region.

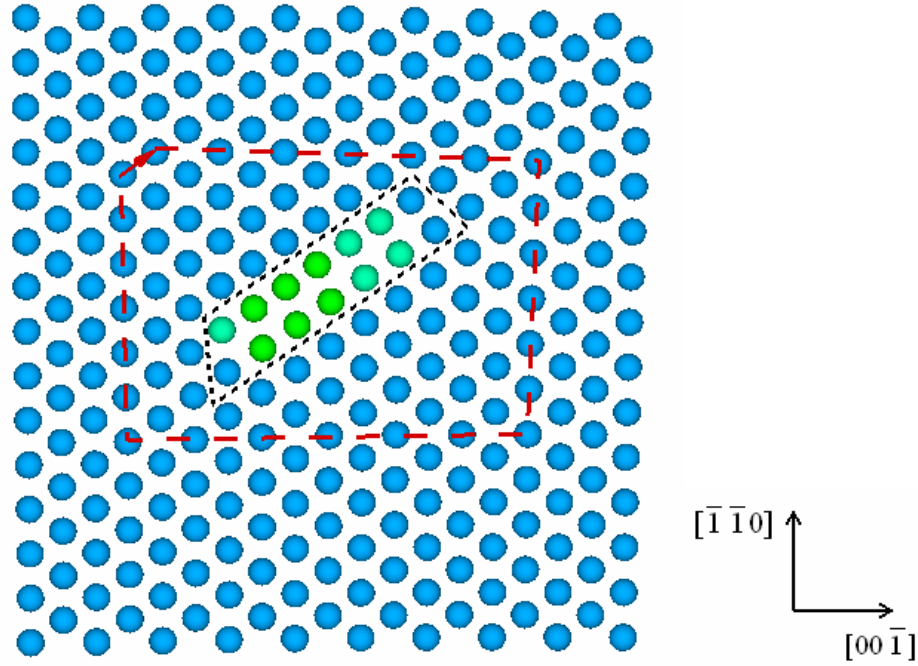


Figure 6-12. The atomic arrangement around a dissociated dislocation at 125 ps in Fig. 6-9. Atoms with a perfect FCC local structure are also shown in this figure, while only atoms enclosed by the dashed black line are shown in the snapshot of Fig. 6-9. The atomic configuration is viewed along the $[110]$ direction. The red arrow indicates the Burgers vector of $a/2[101]$.

6.4 Summary

Short pulse laser-induced structural transformations in the surface region of a bulk Ni target are investigated through a hybrid computational model that combines the atomic level MD method with a continuum description of laser-excited electrons. The model adequately accounts for the laser absorption in the conduction band electrons and subsequent hot electron relaxation through the electron-phonon energy transfer and electron heat conduction in the irradiated target. Computer simulations based on this

model are performed with three values of absorbed fluences above the threshold for surface melting for Ni.

A detailed analysis of the structural changes in the surface region of the irradiated target for all three fluences suggest that Shockley partial dislocations, stacking faults and a large number of vacancies are generated in the target after the laser-induced melting and resolidification processes. The appearances of Shockley partial dislocations and stacking faults in this region are associated with the strong transient thermoelastic stresses induced by the laser irradiation. Numerical analysis of the generalized stacking fault energy of two partial dislocations of the type $1/6\langle 112 \rangle$ reveal that the uniaxial expansion of the crystal in the [001] direction leads to an overall decrease in the energy barrier for slips in the FCC crystal, supporting the observation of the emission and fast propagation of dislocation during the dynamic lattice expansion, followed by a partial retreat of the dislocation after the tensile unloading wave leaves the surfaces.

For the lowest laser fluence applied in the simulation, the partial dislocations in the target do not move significantly with respect to the location where they are generated, whereas for higher laser fluences strong thermoelastic stresses due to the intense laser irradiation result in the fast propagation of partial dislocations emitted from the melting front away from the surface, leaving the stacking fault behind. In particular, analysis of the stress in the target indicates that the propagation of the two interacting dislocations effectively reduce the shear stress remained in the materials, leading to a three dimensional relaxed state.

A significant amount of vacancies are found to appear during the resolidification as the solid-liquid interface retreats back to the surface. The ultrafast cooling rate, on the

order of 10^{12} K/s, helps to stabilize the highly non-equilibrium vacancy concentration. For low fluence, vacancies are found to appear below the depth that the melting front can reach, whereas for high fluences, in addition to the region where melting and resolidification occurs, a number of vacancies also form in the region where partial dislocations annihilate and remove the stacking faults.

References for Chapter 6

- [1] M. von Allmen and A. Blatter, *Laser Beam Interactions with Materials*, Springer: Berlin, 1998.
- [2] D. Bäuerle, *Laser Processing and Chemistry*, Springer-Verlag: Berlin Heidelberg, 2000.
- [3] J. Kaspar and A. Luft, *Surface engineering* **17**, 379-383, 2001.
- [4] J. G. Hoekstra, S. B. Quadri, J. R. Scully, and J. M. Fitz-Gerald, *Adv. Eng. Mat.* **7**, 805-809, 2005.
- [5] D. S. Ivanov and L. V. Zhigilei, *Phys. Rev. B*, **68**, 064114, 2003.
- [6] D. S. Ivanov and L. V. Zhigilei, *Phys. Rev. Lett.* **91**, 105701, 2003.
- [7] Z. Lin and L. V. Zhigilei, *Phys. Rev. B* **73**, 184113, 2006.
- [8] E. Leveugle, D. S. Ivanov, and L. V. Zhigilei, *Appl. Phys. A* **79**, 1643-1655, 2004.
- [9] L. V. Zhigilei, D. S. Ivanov, E. Leveugle, B. Sadigh, and E. M. Bringa, *High-Power Laser Ablation V*, edited by C. R. Phipps, *Proc. SPIE* **5448**, 505-519, 2004.
- [10] X. W. Wang, *J. Phys. D* **38**, 1805-1823, 2005.
- [11] E. Ohmura, I. Fukumoto, and I. Miyamoto, *Int. J. Jpn. Soc. Prec. Eng.* **32**, 248-253, 1998.
- [12] C. Schäfer, H. M. Urbassek, and L. V. Zhigilei, *Phys. Rev. B* **66**, 115404, 2002.
- [13] N. N. Nedialkov, S. E. Imamova, and P. A. Atanasov, *J. Phys. D: Appl. Phys.* **37**, 638-643, 2004.
- [14] C. Cheng and X. Xu, *Phys. Rev. B* **72**, 165415, 2005.
- [15] M. B. Agranat, S. I. Anisimov, S. I. Ashitkov, V. V. Zhakhovskii, N. A. Inogamov,

- K. Nishihara, Yu. V. Petrov, V. E. Fortov, and V. A. Khokhlov, *Appl. Surf. Sci.* **253**, 6276-6282, 2007.
- [16] Z. Lin, R. A. Johnson, and L. V. Zhigilei, *Phys. Rev. B*, in press, 2008.
- [17] S. I. Anisimov, B. L. Kapeliovich, and T. L. Perel'man, *Sov. Phys. JETP* **39**, 375-377, 1974.
- [18] L. V. Zhigilei and B. J. Garrison, *Mat. Res. Soc. Symp. Proc.* **538**, 491-496, 1999.
- [19] C. Schäfer, H. M. Urbassek, L. V. Zhigilei, and B. J. Garrison, *Comp. Mater. Sci.* **24**, 421-429, 2002.
- [20] J. Hohlfeld, S.-S. Wellershoff, J. Gu'dde, U. Conrad, V. Ja'hnke, and E. Matthias, *Chem. Phys.* 251, 237, 2000.
- [21] V. Vitek, *Phil. Mag.* **18**, 773-786, 1968.
- [22] V. Vitek, *Phil. Mag.* **21**, 1275-1278, 1970.
- [23] J.P. Hirth and J. Lothe, *Theory of Dislocations* (New York: Wiley), 1982.
- [24] J.E. Angelo, N.R. Moody and M.I. Baskes, *Modelling Simul. Mater. Sci. Eng.* **3** 289-307, 1995.
- [25] Y. Mishin, D. Farkas, M.J. Mehl and D.A. Papaconstantopoulos, *Phys. Rev. B* **59** 3393-407.
- [26] C. Brandl, P. M. Derlet, and H. Van Swygenhoven, *Phys. Rev. B*, **76**, 054124, 2007.
- [27] J.A. Zimmerman, H. Gao, and F. F. Abraham, *Modelling Simul. Mater. Sci. Eng.* **8** 103-115, 2000.
- [28] J.R. Rice, *J. Mech. Phys. Solids* 40 239-71, 1992.
- [29] C. Kelchner, S.J. Plimpton and J.C. Hamilton, *Phys. Rev. B* **58**, 11085, 1998.

- [30] E. Leveugle, D. S. Ivanov, and L. V. Zhigilei, *Appl. Phys. A* **79**, 1643-1655, 2004.
- [31] E. M. Bringa, A. Caro, Y. Wang, M. Victoria, J. M. McNaney, B. A. Remington, R. F. Smith, B. R. Torralva, and H. Van Swygenhoven, *Science* **309**, 1838-1841, 2005.
- [32] Y. R. Jeng and C. M. Tan, *Phys. Rev. B* **69**, 104109, 2004.
- [33] D. Ashkenasi, M. Lorenz, R. Stoian, and A. Rosenfeld, *Appl. Surf. Sci.* **150**, 101-106, 1999.
- [34] P. T. Mannion, J. Magee, E. Coyne, G. M. O'Connor, and T. J. Glynn, *Appl. Surf. Sci.* **233**, 275-287, 2004.
- [35] S. E. Kirkwood, A. C. van Popta, Y. Y. Tsui, and R. Fedosejevs, *Appl. Phys. A* **81**, 729–735, 2005.
- [36] J. Krueger, D. Dufft, R. Koter, and A. Hertwig, *Appl. Surf. Sci.* **253**, 7815-7819, 2007.
- [37] G. Raciukaitis, M. Brikas, P. Gecys, and M. Gedvilas, , *Proc. SPIE* **7005**, paper 7005-105, 2008.

7. Summary

The study of short (femto- and pico-second) pulse laser interaction with metals presented in this dissertation has provided rich information of the material response to the extreme conditions created by short pulse laser irradiation. By performing MD simulations using a combined atomistic-continuum approach, microscopic mechanisms of the ultrafast structural and phase transformation, as well as the generation of crystal defects, in the irradiated metals are revealed. The connections between the electronic band structure and the electron temperature dependences of the thermophysical properties, namely the electron-phonon coupling and the electron heat capacity, under strong laser-induced electron-phonon non-equilibrium are established through *ab initio* electronic structure calculations for several representative metals.

The diffraction profiles and density correlation functions are calculated for transient atomic configurations generated in MD simulations of a 20 nm Au film irradiated with 200 fs laser pulses of different intensity. The results of the calculations provide an opportunity to directly relate the detailed information on the atomic-level structural rearrangements available from the simulations to the diffraction spectra measured in time-resolved x-ray and electron diffraction experiments. Three processes are found to be responsible for the evolution of the diffraction profiles. During the first several picoseconds after the laser excitation, the decrease of the intensity of the diffraction peaks is largely due to the increasing amplitude of thermal atomic vibrations and can be well described by the Debye-Waller factor. The effect of thermoelastic deformation of the film prior to melting is reflected in shifts and splittings of the

diffraction peaks, providing an opportunity for experimental probing of the ultrafast deformations. Finally, the onset of the melting process results in complete disappearance of the crystalline diffraction peaks. The homogeneous nucleation of a large number of liquid regions throughout the film is found to be more effective in reducing long-range correlations in atomic positions and diminishing the diffraction peaks as compared to the heterogeneous melting by melting front propagation. For the same fraction of atoms retaining the local crystalline environment, the diffraction peaks are more pronounced in heterogeneous melting. A detailed analysis of the real space correlations in atomic positions is also performed and the atomic-level picture behind the experimentally observed fast disappearance of the correlation peak corresponding to the second nearest neighbors in the FCC lattice during the laser heating/melting process is revealed.

In addition to the ultrafast laser-induced melting processes in metals, the generation of crystal defects in BCC Cr and FCC Ni irradiated by short pulse laser is also investigated in large scale TTM-MD simulations. For BCC Cr, the parameterization of the EAM potential is done in collaboration with Prof. R.A. Johnson in the Department of Materials Science and Engineering at the University of Virginia. The potential is tested by comparing properties of the EAM Cr material with experimental data and predictions of density functional theory (DFT) calculations. The simulations of a Cr target irradiated by a short, 200 fs, laser pulse are performed at laser fluences close to the threshold for surface melting. Fast temperature variation and strong thermoelastic stresses produced by the laser pulse are causing surface melting and epitaxial resolidification, transient appearance of a high density of stacking faults along $\{110\}$ planes, and generation of a large number of point defects (vacancies and self-interstitials). The stacking faults

appear as a result of internal shifts in the crystal undergoing a rapid uniaxial expansion in the direction normal to the irradiated surface. The stacking faults are unstable and disappear shortly after the laser-induced tensile stress wave leaves the surface region of the target. Thermally-activated generation of vacancy-interstitial pairs during the initial temperature spike and quick escape of highly mobile self-interstitials to the melting front or the free surface of the target, along with the formation of vacancies at the solid-liquid interface during the fast resolidification process, result in a high density of vacancies, on the order of 10^{-3} per lattice site, created in the surface region of the target.

For FCC Ni, TTM-MD simulations are performed at three laser fluences above the threshold for surface melting for Ni, but well below the ablation threshold. A detailed analysis of the microstructure changes in the surface region of the irradiated target show that Shockley partial dislocations appear in response to the internal stresses in the FCC crystal undergoing a fast uniaxial expansion in the direction normal to the irradiated surface. The dislocations are emitted from the melting front and propagate away from the surface, leaving the stacking faults behind. Stacking fault stability analysis for EAM Ni suggests that the energy barrier for creating intrinsic stacking faults is reduced under uniaxial expansion, facilitating the generation of partial dislocations in the surface region of the target irradiated by short pulse laser. In addition, a large concentration of vacancies is found to be present in the surface region after the fast resolidification process.

The strong supersaturation of vacancies, observed in both BCC Cr and FCC Ni after the resolidification in the surface region of the irradiated target, can be related to the incubation effect in multi-pulse laser ablation/damage in metals and may play an important role in mixing/alloying of multi-component or composite targets.

The characteristics of the melting process are also investigated for of a nanocrystalline Au film irradiated by a short laser pulse. In particular, it is shown that a complete melting of the nanocrystalline film is achieved at a lattice temperature below the equilibrium melting temperature. In order to explain this behavior, the classical nucleation theory is applied for the investigation of the thermodynamic stability of the nanoclusters in a liquid environment. It is shown that the melting process starts at the grain boundaries and leads to the decrease of the sizes of the nanocrystalline grains. As a result, due to the contribution of the interfacial energy of grain boundaries to the Gibbs free energy of the system, the remaining grains are thermodynamically unstable in a liquid environment at a lattice temperature below the equilibrium melting temperature for EAM Au.

Thermophysical properties of metals (electron-phonon coupling, electron heat capacity and thermal conductivity) under conditions of strong laser-induced electronic excitation are investigated by first principles electronic structure calculations. Surprisingly, under strong electron excitations the electron-phonon coupling and electron heat capacity are found to undergo large transient variations, deviating from commonly accepted descriptions. It is shown that the strength of the electron-phonon coupling can either increase (Al, Au, Ag, Cu, W), decrease (Ni, Pt), or exhibit non-monotonic changes (Ti) with increasing electron temperature. The electron heat capacity can exhibit either positive (Au, Ag, Cu, W) or negative (Ni, Pt) deviations from the linear temperature dependence. It is the thermal excitation of the lower d band electrons upon the laser irradiation that gives rise to the large variations in these thermophysical properties that are found to be very sensitive to the details of the electronic structure of the material.

It is illustrated through two sets of simulations, performed with the TTM-MD model and continuum TTM equations, that large variations of the thermophysical properties for the range of electron temperatures typically realized in femtosecond laser material processing applications have important practical implications for quantitative computational analysis of ultrafast processes associated with laser interaction with metals. A TTM-MD simulation, performed for a 20 nm Au film irradiated with a 200 fs laser pulse, demonstrates that the increase in the strength of the electron-phonon coupling at high electron temperatures leads to a faster lattice heating, generation of stronger thermoelastic stresses, and a significant decrease in the time of the onset of the melting process. The timescale of the melting process predicted in the simulation accounting for the thermal excitation of lower d band electrons in Au is in excellent agreement with the results of recent time-resolved electron diffraction experiments. In comparison, a simulation performed with commonly used approximations of a constant electron-phonon coupling factor and a linear temperature dependence of the electron heat capacity significantly overpredicts the time of the beginning of the melting process. It is also shown in TTM simulations of short pulse laser irradiation with a bulk Ni target that the temperature dependence of the thermophysical parameters that accounts for the thermal excitation of d band electrons leads to higher maximum lattice and electron temperatures achieved at the surface of an irradiated Ni target. And it also brings the threshold fluences for surface melting closer to the experimentally measured values as compared to the predictions obtained with commonly used approximations of the thermophysical parameters. These results support the importance of accounting for the thermal excitation of lower band electrons for realistic modeling of short pulse laser processing in metals.